UNIVERSITÀ DELLA CALABRIA

Dipartimento in INGEGNERIA PER L'AMBIENTE, IL TERRITORIO E INGEGNERIA CHIMICA

(sede amministrativa del Corso di Dottorato)

Scuola di Dottorato in Scienze Ingegneristiche "PITAGORA"

Dottorato di Ricerca in

INGEGNERIA IDRAULICA PER L'AMBIENTE E IL TERRITORIO

Con il contributo di:

SECRETARIA NACIONAL DE EDUCACIÓN SUPERIOR, CIENCIA, TECNOLOGIA E INNOVACION (SENESCYT – ECUADOR)

CICLO

XXVII

CHARACTERIZATION OF REAL AQUIFERS USING HYDROGEOPHYSICAL MEASUREMENTS. AN APPLICATION TO THE CHAMBO AQUIFER (ECUADOR).

Settore Scientifico Disciplinare ICAR/02

Coordinatore: Ch.mo Prof. FRANCESCO MACCHIONE

Supervisore: Ing. Prof. SALVATORE STRAFACE

Dottorando: Ing. Benito Guillermo Mendoza Trujillo

El amor y la ternura de tu presencia lo es todo para mi, haces que cada día quiera ser siempre mejor, con mucho amor.

Para ti

Benito Andrés

INTRODUCTION

Groundwater is the most important water supply for drinkable and irrigational use. The strong interconnection between hydrologic, soil and atmospheric systems allows the circulation of different pollutants. Pollution strongly reduces useful water supply which should be able to satisfy community needs. The combination of the classical disciplines of hydrogeology with the technological development of geophysics, allows rapid acquisition and interpretation of high-resolution information, using noninvasive, nondestructive and low cost techniques. The purpose of this thesis is the adoption of new approaches to improve aquifer characterization and monitoring by means of hydrogeophysical methodologies.

Several experimental tests have been performed both at a laboratory and field scale: we started from the study of the hydrodispersive parameters of the soil through the execution of tracer tests carried out within flow cells, and we continued with the monitoring of the hydrocarbons concentration performed with Ground Penetrating Radar (GPR) techniques in a sandbox, to finish with Self Potential (SP) measurement in the Experimental well field of University of Calabria.

The acquired data, have been interpreted by means of an iterative inverse procedure based on a finite element model simulating multiphysical problems. Depending on the case, you can solve coupled equations systems describing the experiment under examination, i.e. the transport and groundwater flow phenomena, or the two-phase flow for immiscible fluids, or the Poisson-Darcy model for the evaluation of the electrical potential generated by the water flowing into a porous medium.

The Know-how acquired studying laboratory and experimental field tests, has been than applied in a real problem, regarding the water supply of the Chambo Aquifer in the Province of Chimborazo – Ecuador. The main goal of the study was the determination of the aquifer recharge over time, to demonstrate that that is the groundwater system is not fossil. The first step of the analysis, was the reconstruction of the basin domain through the interpretation and interpolation of different data types. A geographic

information system (GIS) of the area was performed through the processing of satellite images (ASTER) together with the information provided by the Ecuadorian Confederation of Agricultural Services (CESA), allowing the reconstruction of the Chambo basin, which has an approximate area of 3589.55 km2. The superficial hydrological system of the basin consists of thirty-three tributaries that come from different directions and fed the Chambo River. The main tributaries are the Cebadas River, which comes from the southern boundary of the basin, and the Guano River coming from the north. The Alao and Guamote Rivers are major tributaries coming from the West and East, respectively. The superficial water balance was calculated in the ArcGIS environment, using average temperature and rainfall data for the entire year. These data come from the Meteorological Annuary of the National Institute of Meteorology and Hydrology (INAMHI). The aquifer boundaries were defined through the information derived from the geological map of the basin. This process allowed to locate the aquifer within the Riobamba Formation, which includes incoherent pyroclastic rocks , gravel and sand. The demarcation of the boundaries allowed the identification of a potential groundwater recharge coming from the Chimborazo Volcano. The reconstruction of the model surface was obtained from Digital Terrain Model (DTM)data , while the bottom was obtained from the ordinary kriging of the information collected during a Vertical Electrical Sounding (VES) campaign. The spatial distribution of the hydraulic conductivity was derived from the ordinary kriging of puctual valuesobtained from the interpretation of the several pumping tests conducted in the aquifer area. The hydrological forcings included in the model are: a) the principal rivers: Guano, Chibunga and Chambo; b) the complex system of wells with a total pumping rate of 600 l/s, this withdrawal guarantees the water supply of drinkable water for the cities of Riobamba and Guano; c) and the net-infiltration determined by the superficial water balance. The boundary conditions adopted in the model are: a) Neuman boundary conditions, on the side from which a water flowrate it's expected from the Chimborazo volcano, whose estimation is the goal of the study; b) a Dirichlet boundary condition applied to sides influenced by the rivers; c) and a no-flow boundary conditions in the other contours. The water volume of lateral recharge was obtained from the model calibration , in which hydraulic head data supplied by springs and ponds (points where the watertable outlooks on the ground surface) and the ones measured in the piezometers have been adopted to condition the inversion process. Once the mathematical model has been set up, the inversion of twelve different

scenarios representing the monthly groundwater variation during a year, was carried out. The results show the existence of a water flow coming from the north-western part of the model, representing the contact point with the southern slope of the Chimborazo volcano, with an approximate monthly value of 2 m^3/s. The hydro-geological model was built and executed with the MODFLOW code, while the inverse procedure was conducted by the PEST software. This approach, gave back a very good fitting between the calculated and observed hydraulic heads, demonstrating that the Chimborazo Volcano contributes with a 63% of the volume to the groundwater recharge, compared with the 37% coming from other hydrological forcings, moreover, the rivers receive the largest volume of water leaving the aquifer with 82% of the total outgoing volume .

This study demonstrates that the Chambo aquifer is not fossil , i.e. is fed by a lateral recharge of approximately 2 m^3/s, which come from the glaciers of Chimborazo Volcano. The results of this study, together with the ones coming from the ^{14}C analyses, suggest that the reserve of ancestral ice of the Chimborazo glacier are dissolving, highlighting the influence of the climate change in Ecuador and, hence, in the world.

INTRODUZIONE

Le acque di falda costituiscono la più preziosa riserva idrica ad uso potabile ed irriguo. La forte interconnessione esistente tra sistemi idrici sotterranei e superficiali e fra questi e il suolo e l'aria, favorisce la messa in circolo di inquinanti di svariata natura e composizione. Di conseguenza, l'inquinamento riduce notevolmente la possibilità di utilizzazione di risorse idriche che dovrebbe sarebbero quantitativamente in grado di soddisfare le esigenze della comunità. L'unione tra le discipline classiche dell'idrogeologia ed i recenti sviluppi tecnologici della geofisica, consente l'acquisizione e l'interpretazione rapida di informazioni ad alta risoluzione sfruttando tecniche non invasive e non distruttive con minori oneri economici rispetto alle indagini dirette. Il lavoro di tesi si inserisce in tale contesto, con l'obiettivo di sviluppare e adottare nuove metodologie idrogeofisiche, per migliorare la caratterizzazione ed il monitoraggio degli acquiferi.

A tale scopo sono stati eseguiti diversi test sperimentali a scala di laboratorio e di campo: partendo dallo studio dei parametri idrodispersivi del suolo mediante l'esecuzione di prove di tracciamento effettuate su celle di flusso, si è passati ad esperimenti di monitoraggio della concentrazione di idrocarburi con l'uso del Ground Penetrating Radar (GPR) in un sandbox, per giungere al monitoraggio della falda del campo Prove dell'Università della Calabria sito a Montalto Uffugo, attraverso l'interpretazione di misure di potenziale spontaneo (SP).

I dati acquisiti, sono stati invertiti attraverso una procedura iterativa basata su un modello agli elementi finiti che consente l'implementazione di problemi multifisici. A seconda dei casi, è possibile accoppiare e risolvere le equazioni che descrivono i fenomeni che avvengono negli esperimenti, come il flusso ed il trasporto delle acque sotterranee, il flusso bifase per fluidi immiscibili o ancora il potenziale elettrico generato dall'acqua che scorre in un mezzo poroso (modello Darcy-Poisson)

Le metodologie studiate in laboratorio e su campo sperimentale, sono state quindi applicate per lo studio di un problema reale inerente alla falda acquifera del Chambo nella provincia di Chimborazo – Ecuador. Il duplice obiettivo dello studio è stato quello di determinare la ricarica idrica della falda nel tempo e dimostrare che quest'ultima non

è fossile. Il primo passo è stato la ricostruzione del dominio del bacino attraverso l'interpretazione e l'interpolazione di dati di varia natura. Attraverso l'elaborazione, in ambiente GIS, di immagini satellitari di tipo ASTER e delle informazioni fornite dal Central Ecuatoriana de Servicios Agricolas CESA, è stata effettuata la ricostruzione del bacino del fiume Chambo e la determinazione della sua superficie, che è risultata pari a circa 3589.55 Km^2. Il sistema idrologico superficiale del bacino è costituito da trentatre affluenti che provenendo da direzioni differenti alimentano il fiume Chambo. I principali affluenti sono il rio Cebadas, che proviene dal confine meridionale del bacino, ed il rio Guano che proviene da Nord. I fiumi Guamote e Alao sono invece i principali affluenti che provengono rispettivamente da Ovest ed Est. Inserendo i dati di temperatura e pioggia, provenienti dall'annuario metereologico dell'Istituto di Metereologia e Idrologia (INAMHI), nella ricostruzione del bacino in ambiente GIS, è stato possibile determinare il bilancio idrico superficiale, valutato mensilmente nel corso di un anno. La falda acquifera presente nel bacino, è stata invece delimitata utilizzando le informazioni provenienti dalla carta geologica del bacino, che ha consentito la localizzazione del bacino sotterraneo all'interno della formazione detta Riobamba, la quale comprende per lo più rocce piroclastiche incoerenti, ghiaia e sabbia. La delimitazione dei confini della falda, ha quindi consentito di individuare il dominio di modellazione per la stima di un eventuale ricarica idrica sotterranea proveniente dal versante del vulcano Chimoborazo. La ricostruzione della parte superficiale del modello del flusso idrico sotterraneo è stata ottenuta dai dati provenienti dal DTM, mentre il bottom attraverso l'ordinary kriging delle informazioni ricavate da una campagna di Sondaggi Elettrici Verticali (SEV). La distribuzione spaziale della conducibilità idraulica è stata derivata da un ordinary kriging dei valori puntuali di K, ricavati dall'interpretazione di diverse prove di emungimento realizzate nel bacino. Le forzanti idrologiche inserite nel modello sono rappresentate a) dai fiumi principali: il Guano, il Chibunga ed il Chambo; b) dal complesso sistema di pozzi presenti nell'area che, per garantire l'approvvigionamento idrico di acqua potabile alle città di Guano e Riobamba, emungono complessivamente una portata di 600 l/s; c) l'infiltrazione netta determinata attraverso il bilancio idrico superficiale. Per quanto riguarda le condizioni al contorno adottate nel modello, sono state adottate, una condizione alla Neuman sul confine da cui dovrebbe entrare un flusso idrico proveniente dal vulcano Chimborazo, la cui stima è l'obbiettivo dello studio, una condizione alla Dirichlet sui contorni interessati dalla presenza dei fiumi ed una condizione di flusso nullo sui restanti contorni. La

calibrazione del modello e quindi la stima della ricarica idrica laterale, è stata ottenuta utilizzando i dati di carico idraulico forniti da sorgenti, e stagni (punti in cui la falda acquifera si affaccia sulla superficie del suolo) e quelli misurati nei piezometri. Una volta aver definito l'impostazione del modello matematico, è stata effettuata l'inversione di dodici scenari mensili differenti, che hanno tutti mostrato l'esistenza di un flusso d'acqua di circa 2 m^3/s, proveniente dalla zona Nord-occidentale del modello che rappresenta il punto di contatto con il versante Sud del vulcano Chimborazo. Il modello idrogeologico è stato implementato ed eseguito con il codice MODFLOW, mentre la procedura di inversione è stata condotta attraverso il software PEST. Il loro uso congiunto sui dodici modelli implementati, ha restituito un ottimo fitting tra i carichi idraulici calcolati e quelli osservati. Si è dimostrato quindi che il Chimborazo contribuisce al 63% del volume di ricarica idrica sotterranea contro il 37% proveniente dalle altre forzanti idrologiche, e che il maggior volume di acqua esce dalla falda attraverso i fiumi con 82% in uscita.

Questo studio dimostra che l'acquifero del Chambo non è di natura fossile ma viene alimentato da una ricarica laterale di circa 2 m^3/s proveniente dal ghiacciaio del vulcano Chimborazo. I risultati di questo studio, insieme a quelli ottenuti da un analisi effettuata con il ^{14}C, suggeriscono che le riserve di ghiaccio ancestrale sul vulcano si stanno sciogliendo, mettendo in evidenza il possibile impatto dei cambiamenti climatici in Ecuador e quindi nel mondo.

Contents

List of Figures

List of Tables

CHAPTER 1

1.1 HYDROGEOPHYSICS

1.1.1 New frontiers in the characterization of Porous Media parameters

The aim of this chapter is to present an overview of the geophysical methodologies for the measurement, characterization and modeling of porous media parameters. Special emphasis is given to electric and electromagnetic measurements which strongly depend on soil characteristics and water content, but other geophysical techniques which are very promising for hydrologic studies are also taken into consideration. The principles and field applications of these methodologies are briefly discussed, including main concerns and limitations. In last few years, geophysics techniques have driven the attention of many researchers interested to the investigation of near surface hydrology problems. These techniques are based on easy geophysical measurements which can be used to monitor fundamental hydrologic processes (Rubin and Hubbard 2005).

Conventional hydrologic technologies, normally applied to characterize the shallow subsurface, typically involve piezometric measurements in carved wells. Such measurements are usually sparsely distributed and do not consent, in many cases, to take into an appropriately consideration the hydrologic heterogeneity of the sites, specially when the area under investigation is very large with respect to the size of typical homogeneous region of the investigated sites. In these cases geophysics

measurements can be used to acquire complementary data to better define the problem under investigation. In fact these techniques are not invasive and can be taken at a much big density with respect to piezometer measurements. For this reason they consent to obtain more precise bidimensional and tridimensional picture of the investigate sites. The main categories of hydrologic problems that can be solved by geophysics techniques are:

Hydrological Mapping.

Under this denominations are be classified actions such as: the definition of aquifers geometry; the determination of water table level, basement and boundaries; the fresh and salt water interfaces, contaminant plumes, fracture zones etc. (Goldman, 2003; Arango 2005; Mcpheeet al. 2006). In mapping studies, the integration of sparse borehole measurements with continuous geophysics data is usually used in order to overcome the problems arising from the heterogeneity of the subsoil. An excellent review of such a strategic approach to obtain reliable volumetric hydraulic permeability is due to Sanchez-Vila et. al. (2006)

Hydrologic parameter estimation

That is to say the estimation of the water content, water quality and effective-volumetric parameter. In these case geophysical information are calibrated with directly measured hydrological data both at field scale or at laboratory level, in such a way that they can provide a more complete estimation of hydrological parameters (Ferrè et. al. 2005; Tullen et.al. 2006). Usually aquifer flow and transport properties are derived by numerical models where geophysical data are also inserted. For instance, the Hydraulic conductivity K and porosity φ defined as:

$$K = \frac{\rho_w g k}{\mu} \qquad \varphi = \frac{V_p}{V_t}$$

Where ρ_w is the density of the pore fluid g is the gravitational acceleration μ the fluid dynamic viscosity and K is the hydraulic permeability, Vp and Vt are the pore volumes and total volume respectively Now, it is assumed that the parameters inserted into the above equations can be derived from measurable geophysical properties such us electrical resistivity, dielectric constant, acoustic porosity.

Hydrologic processes monitoring of subtle geophysical property changes, caused by natural or forced systems: common examples are the changes of water content and water quality (Slater et al., 1997; Singha and Gorelick, 2005; Tezkan et al., 2005). Dynamic transformations in flow and transport processes are monitored by time-lapse measurements of geophysical properties at the same location. Generally the, conventional Hydrological measurement suffer by the lack of a total survey repeatability at different time at a given sounding location, and these problems may introduce uncertainty into the results while looking for quantitative rates of change. When using geophysical measurement, which consent a more precise sounding location, the repeatability uncertainty of time-lapse models decreases, at benefit of the data inversion procedures, especially if constraining unchanging targets are retrieved on all the models. It must be considered that in shallow surface studies identical positioning plays a major role in performing quantitative investigations. The following table shows the main application of geophysics methodologies to hydrologic problems in different scale application.

Geophysical Methods		**Obtained properties**	**Hydrogeological objectives**
Airborne	Remote sensing	Gamma radiation, Thermal radiation, Electromagnetic	Bedrock mapping, faults, hydrothermalism, aquifer characterization and regional water quality
Satellite	Aeromagnetic	Reflectivity, gravity	
	Electromagnetic	Electrical resistivity	
Surface	Seismic Refraction	P-ware velocity	Bedrock mapping, water table, faults
	Seismic Reflection	P-ware reflectivity and velocity	Stratigraphy, bedrock and faults delineation
	Electromagnetic (TDEM, FDEM, CSEM, AMT)	Electrical resistivity	Aquifer zonation, water table, bedrock, fresh and salt-water interfaces and plume boundaries, estimation of hydraulic conductivity, estimation and monitoring of water content and quality
		Electrical resistivity	
	IP	Complex electrical resistivity	Hydraulic conductivity

	GPR	Dielectric constant values and dielectric contrast	Stratigraphy, water table, water content estimation and monitoring
	NMR		Water content, mobile water content, pore structure
Cross hole	Electrical Resistivity DC	Electrical resistivity	Aquifer zonation, estimation monitoring of water content and water quality
	GPR	Dielectric constant	
	Seismic	P-wave velocity	Lithology, estimation and fracture zone detection
Well bore	Geophysical well logs	Many properties such as electrical resistivity, seismic velocity, and gamma ray	Lithology water content, water quality, fracture imaging

Table 1. 1: Geophysical Methods, **Obtained properties** and **Hydrogeological objectives**

It must be also considered that the strong improvement in geophysical techniques, over the last decade, is surely linked to the exponential increase in the number and diversity of available advanced instruments, adapted to different study scales. The study scales range from satellite, remote sensing and airborne, to surface and cross-hole, and, at a more detailed scale, well logs and laboratory measurements. Satellite, remote sensing and airborne geophysics work at regional scales, providing data which can be used to draw conclusions about the regional subsurface architecture. It could also be used to identify areas of interest for carrying out more detailed ground based surveys. At the other extreme, borehole geophysics provides continuous profiling or point measurements at discrete depths, and can be related to the physical and chemical properties of the surrounding wall rock, the fluid saturation of the pore spaces in the formations, the fluid in the borehole, the well casing, or any combination of these factors.

1.1.2 Work scale

In the following figure 1.1 (modified from Rubin and Hubbard, 2005) a schematic diagram of field geophysical length scale resolution and study objective scale, is reported.

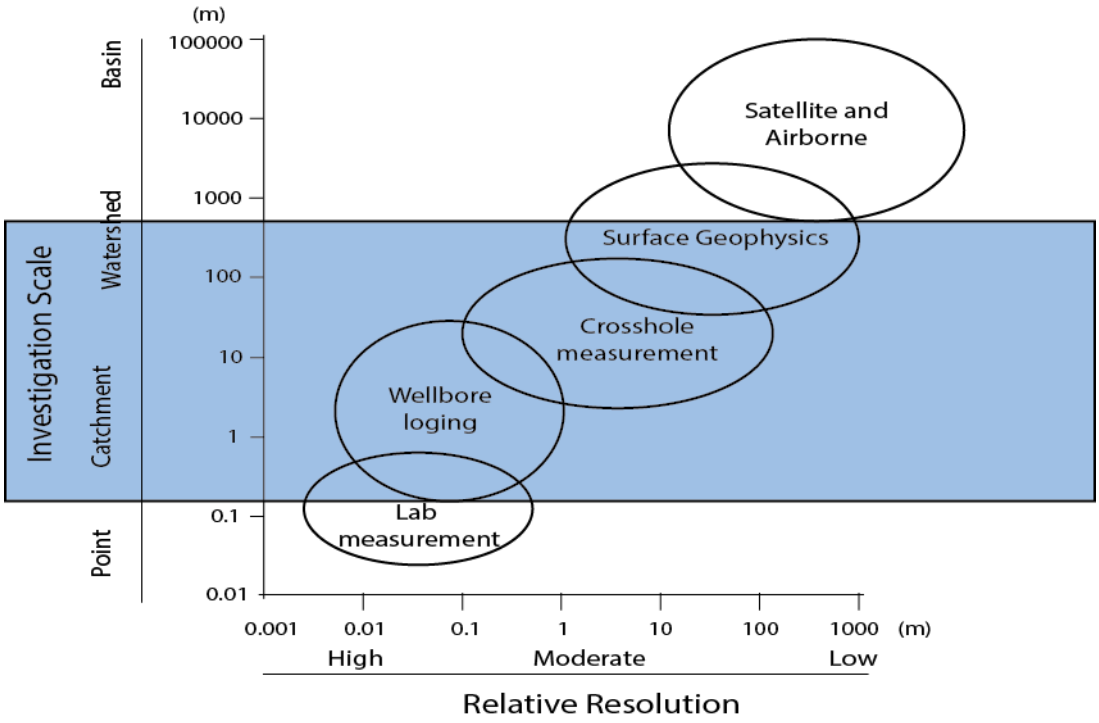

Figure 1. 1: (modified from Rubin and Hubbard, 2005) a schematic diagram of field geophysical length scale resolution and study objective scale.

Before performing any geophysical investigation, a good compromise between resolution and work scale needs to be chosen in order to identify the instrumentation and field survey design, required to achieve the wanted results. A combination of different geophysical techniques and equipments, each sensitive to a given property and/or field scale, could be required, in order to characterize, in the better way, the investigated system. Further, a combination of geophysical data with direct hydrogeological measurements could be used to get a better characterization of the subsurface at different resolutions and scales (Meju, 2000; Choudhury and Saha, 2004; Pedersen *et al.,* 2005).

1.1.3 Modeling and inversion problems

Geophysical data can be used to extract either qualitative or quantitative estimates of the subsurface characteristics. The qualitative approach uses raw geophysical data and it is often used for preliminary mapping or to assess relative changes. These raw data images give generally a smooth image of the subsurface. The values of the investigated properties and the corresponding depth locations cannot be considered reliable at this

stage. Geophysical data require specific data processing and analysis for each given technique before modelling and inversion processes can be performed. Careful data analysis can provide further accuracy of the final models or constrain the specific modelling approach, such as the dimensionality inversion (Ledo *et al.*, 2002 a; Martí *et al.,* 2004; Ledo, 2006). The transformation from raw data to an estimated geophysical model is usually achieved using numerical forward modelling and inversion procedures, to provide a description of the subsurface fitting the observed data. Joint inversion of different geophysical sets (Gallardo and Meju, 2003; Bedrosian, 2006; Linde *et al.*, 2007) is used to constrain the possible subsurface models with multiple independent data, using either a deterministic approach, or a probabilistic approach such as stochastic inversion methods (Deutsch and Journel, 1998; Rubin and Hubbard, 2005; Gómez-Hernández, 2005).

The interpretation of the experimental data obtained from geophysical measurementis normally made according to a procedure which can be defined as Modelling and Inversion. As a first step the researcher need to make a model of the subsurface structure, and calculate with a forward procedure the corresponding geophysical information. Then the calculated data are compared with the theoretical one, and the model is gradually changed in order to minimize the deviation of the calculated data from the experimental. This second step is considered a reverse step (Tarantola, 1987). The next figure 1.2 shows schematically the procedure. Forward modelling is a typical trial and error process that computes the responses of an input model, comparing the responses with measured data, modifying the model where the data are poorly fitted and then re-computing the responses until a satisfactory fit is obtained.

The inverse problem involves an automatic iterative process that searches for the best model, progressively reducing the misfit between the measured data and synthetic data from the model with each iteration. The iterative process proceeds until either a predefined threshold misfit value is reached or until an acceptable model is obtained. Inversion strategies used aim to achieve better numerical convergence, more stable solutions, three-dimensionality inverse modelling, and to reduce the computational time (Spichak and Popova, 2000; Zyserman and Santos, 2000; Haber *et al.*, 2004; Siripunvaraporn *et al.*, 2004; Avdeev, 2005; Haber, 2005; Siripunvaraporn *et al.*, 2005 a).

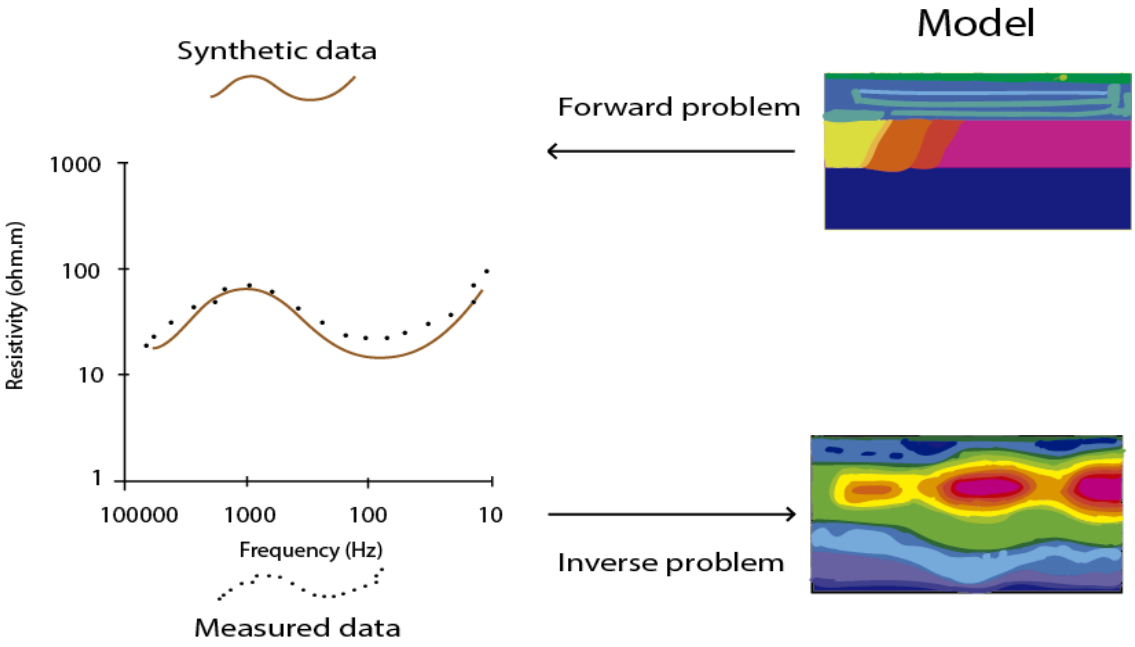

Figure 1. 2: Flux diagram showing the forward and inverse processes. On the left an example of calculated and observed data and on the right created and inverted models.

The model resulting from the above described process provides an image that has to be considered an approximation of the real physical situation. First of all geophysical data are subject to measurement errors and the beginning trial model generally contains semplifications of the physical reality. Cure must be taken do not overfit data, introducing artifacts into the models. Moreover, numerical processes and coarse discretization tend to provide regionally smooth models.

Finally, a study of the sensitivity of the model is required to provide confidence in the subsurface image. It is also desirable for the estimated model to be in accord with any available previous investigation of similar problems (Binley and Kemma, 2005).

1.1.3 Base Concepts of Electrical and Electromagnetic Geophysical Techniques

General tools

Most part of the following discussion has strongly suggested the excellent scientifical contributes of Pellerin 2002, Guerin (2005), Hubbard and Rubin (2005), Aukenet.al (2006). Electrical (E) and electromagnetic (EM) methods are the most commonly used in geophysical approaches to determine hydrogeological parameters and processes.

E&EM are particularly suitable for hydrological studies in the vadose and saturated zones, since the electrical properties of subsurface materials are highly dependent on lithology, water saturation, biochemistry of the fluid and movement of this fluid. Figure 1.3 presents the electrical resistivity of the different geological materials.

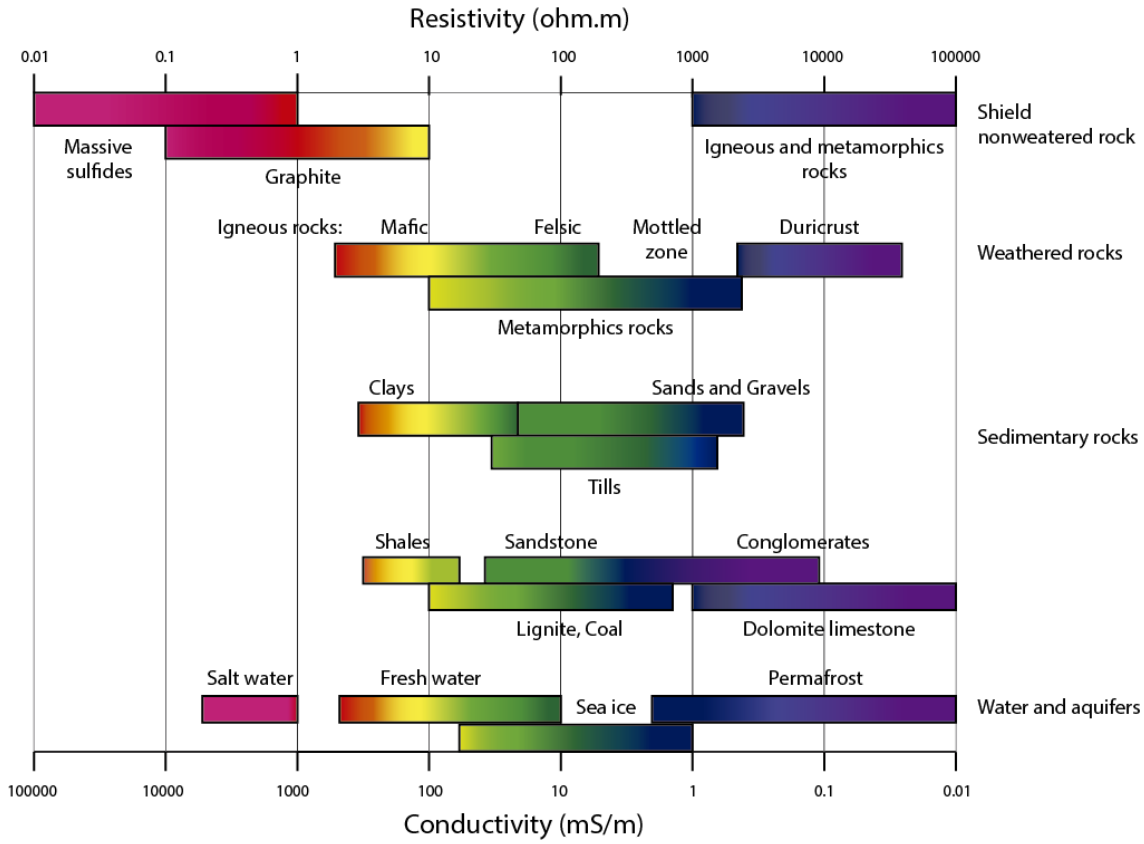

Figure 1. 3 : Electrical resistivity and conductivity of Earth materials (modified from Palacky, 1988).

When an electrical current naturally exists or is externally applied, the mobile charge carried within the soil starts to flow, and the differential charge distribution in the soil generates space differences of the electric potential. The base equation governing the current densities *J* and electric displacement *D* are:

$$\vec{J} = \sigma\vec{E} \qquad \vec{D} = \varepsilon\vec{E}$$

Electrical conductivity (σ) describes how free charges flow to form a current when an electric field is present and the electrical permittivity (ε) describes how charges are displaced in response to an electric field.

The measured geoelectrical properties of materials, under the application of oscillating field depend on the of frequency (ω) of the applied signal:

$$\sigma(\omega) = \sigma'(\omega) - i\sigma''(\omega) \qquad \varepsilon(\omega) = \varepsilon'(\omega) - i\varepsilon''(\omega)$$

Conductivity and similarly permittivity can be expressed as a magnitude and a phase angle that relates the in-phase and the out-of-phase components:

$$|\sigma| = \sqrt{(\sigma')^2 + (\sigma'')^2} \qquad \theta = \tan^{-1}\left(\frac{\sigma''}{\sigma'}\right)$$

where σ', σ", ε' and ε" denotes the real' and imaginary" electrical components known as ohmic conduction, faradic diffusion, dielectric polarization, and energy loss due to polarization, respectively. The above equations show that there is more than ohmic conduction contributing to what is measured as electrical conductivity, and there is more than dielectric polarization contributing to what is measured as effective permittivity or stored energy in the system. A point of divergence in the literature is found in the assumptions that are made about the relative importance of these four parameters in order to extract values from the measured data.

Complex electrical conductivity or, the inverse parameter, resistivity and complex permittivity contain the same information expressed differently and are related by the following expression:

$$\sigma^* = i\omega\varepsilon^*$$

where * indicates a complex number and the complex components are related as:

$$\sigma(\omega) = \sigma'(\omega) + \omega\varepsilon''(\omega) \qquad \varepsilon(\omega) = \varepsilon'(\omega) + \frac{\sigma''(\omega)}{\omega}$$

σ' represents the ohmic conduction current (energy loss) detected by the DC resistivity and EM induction methods. This conduction is due to the pore-filling electrolyte and the surface conduction generated by the ion migration at the electrical double layer (EDL) (Purvance and Andricevic, 2000). σ" is related solely to the fluid-grain interface (Slater, 2006), related to the polarization (energy storage) term measured with induced polarization techniques.

When modelling electrical behaviour of soil materials at frequencies greater than 100 kHz it is commonly assumed that $\frac{\sigma''(\omega)}{\omega}$ =0 and $\sigma'(\omega) = \sigma_{DC}$ (Knight and Endres, 2006) therefore above relations can be rearranged as:

$$\sigma(\omega) = \sigma'_{DC} + \omega\varepsilon''(\omega) \quad \text{and} \quad \varepsilon(\omega) = \varepsilon'(\omega)$$

For low frequency measurements, $\sigma'(\omega) \neq \sigma_{DC}$ and $\sigma'(\omega)$ *is* considered the source of the frequency dependence governing the electrical response, where two specific final cases can be defined:

1) When fluid conductivity dominates the electrical behaviour, that is ionic conduction Dominates, $\sigma'(\omega) \gg \omega\varepsilon''(\omega)$ thus the electric loss term $\varepsilon''(\omega)$ can be neglected and effective resistivity can be formulated as:

$$\sigma = \sigma'(\omega) \quad ; \quad \varepsilon(\omega) = \varepsilon'(\omega)$$

2) When energy loss dominates the electrical behaviour (fluid grain interface effects, ionic migration on the EDL), $\sigma''(\omega)/\omega \gg \varepsilon'(\omega)$, the electrical parameters can be written as:

$$\varepsilon(\omega) = \frac{\sigma''(\omega)}{\omega} \quad ; \quad \sigma(\omega) = \omega\varepsilon''(\omega)$$

Further insights into the influence of type of electric characteristic of the system under investigation will be given in paragraph 1.4.2 of this chapter. This particular aspect of the problem represent one of the most important research topic still underdevelopment.

Electric potential differences is actually measured in Electric and electromagnetic geophysical investigation. These parameters can be expressed as a function resistivity and permittivity values, which in turn can interpreted in terms of a geological model of the investigated site. The following sections present the main electric and electromagnetic methods used where resistivity or permittivity can be inferred.

1.1.4 Electromagnetic fundamentals

The principle behind electromagnetic methods (EM) is governed by Maxwell's equations that describe the coupled set of electric and magnetic fields change with time: changing electric currents create magnetic fields that in turn induce electric fields which drive new currents (Figure 1.4). The EM techniques presented here (CSAMT, TDEM, FDEM, GPR and NMR) use a controlled artificial electromagnetic source as a primary field that induces a secondary magnetic field. However, other EM methods use the Earth's natural electromagnetic fields as well (AMT). Natural EM waves are generated

by thunderstorm activity in the frequency range of interest to hydrogeophysical studies 1Hz to 1 MHz. Combining the laws of Ohm, Ampere, and Faraday and the constitutive relationships results in a wave equation, which relates electromagnetic responses to rock physics in order to quantify material properties (Everett and Meju, 2005):

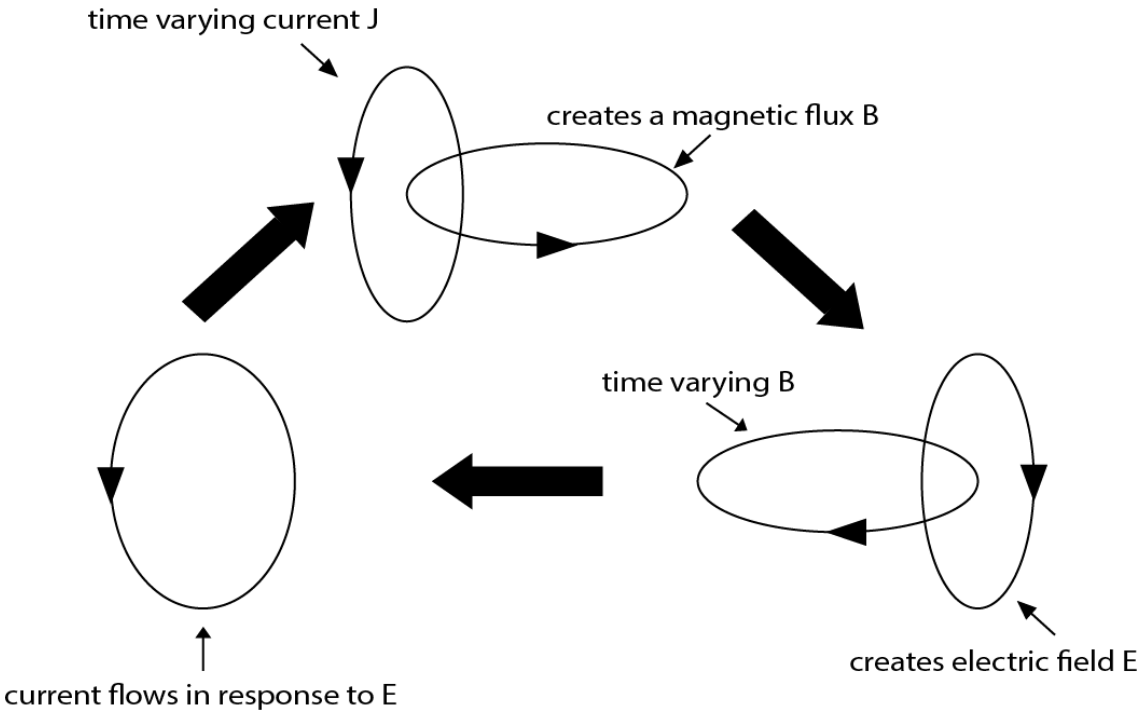

Figure 1. 4: Wave nature of electromagnetic fields. A moving charge of current creates a magnetic field B which induces an electric field E which in turn causes electric charges to move and so forth (modified after Annan, 2005).

$$\nabla^2 B - \underbrace{\mu_0 \sigma \frac{\partial B}{\partial t}}_{I} - \underbrace{\mu_0 \varepsilon \frac{\partial^2 B}{\partial t^2}}_{II} = \mu_0 \nabla J_s$$

where B (T) is the magnetic field, μ_0 (H/m) is the magnetic permeability, σ is the electrical conductivity (S/m), ε (F/m)is the electric permittivity, J (A/m2) is the source current distribution, and t (s) is time. For most hydrogeophysical applications the Earth is generally considered to be nonmagnetic and μ_0 taken as the magnetic permeability of free space $\mu_0 = 4л \times 10^7$ H/m. In highly magnetic soils or in the presence of ferrous metal objects this assumption can break down. Referring to the above equation, term I is the energy dissipation relating to the electromagnetic diffusion and term II is the energy storage describing wave propagation. The frequency of the electromagnetic waves controls the contribution of both diffusion and propagation phenomena through the Earth. The diffusion regime (ω < 100 kHz) is prevalent when term I is larger by several

orders of magnitude than the wave propagation term (II). Such condition is also called the quasi-stationary approximation. In the diffusion regime the propagation term II could be ignored and the electric permittivity plays no further role in the discussion of the AMT, TDEM, FDEM methods. In a similar manner, when the propagation term is bigger than the diffusion one (ω >1MHz), the conductivity effect is minor; in this situation the GPR is highly effective. However, problems can occur when both effects make contributions to the response of the recorded induced currents. The electromagnetic methods are sensitive to electrical resistivity and electric permittivity over a volume of ground where induced electric currents are present. Among the subsurface based geophysical methods that sense bulk electrical and effective properties of the ground, EM provides deeper penetrations depth capability and greater resolving power (Everett and Meju, 2005). EM methods are cost effective, relatively easy to operate in the field, and a variety of data processing options are available, ranging form the construction of apparent resistivity curves or pseudo-sections for a fast subsurface evaluations, to 1-D and 2D forward and inverse modelling. 3D inverse modelling is not yet fully developed although research is moving forward rapidly in this field, where new codes are being tested. However, the main concerns in all EM methods are cultural noise sources such as power lines, pipelines and DC trains among others, that screen and disturb the geophysical signal.

Electromagnetic induction methods are the most widely used and versatile geophysical methods in hydrogeology studies at different scale ranges. This diverse set of techniques and instruments available provides the possibility of conducting cross-scale investigations. Airborne electromagnetic methods are used to obtain regional survey information from watershed to basin scales and can be implemented either from a helicopter or a fixed-wing aircraft and operated in either the frequency or the time domain. Surface geophysical methods can investigate greater depths and on higher resolution (from local studies to basin scale). At a detailed resolution scale in depth there are borehole and cross-hole arrays available. Selection of the appropriate technique will be strongly influenced by study objectives, time, founds and computational facilities.

1.1.5 Methods for geophysical data acquisition

Direct Current methods (DC)

DC methods are based on the injection of a current into the ground, to measure the generated electrical field as a potential difference. The experimental configuration of the electric resistivity method consists of four electrodes. Two of them, A and B, are the current electrodes, where a current I is injected, while the other two, M and N, are the potential electrodes, where a potential difference ΔV is recorded. The potential difference measured depends on the current applied, the resistivity of the subsurface medium and the geometric factor (k) determined by the array configuration (distance between electrodes). The following expression relates these parameters to the apparent resistivity ρ_a:

$$\rho_a = k\frac{\Delta V}{I}$$

defined as the resistivity of a homogenous site to which the real site is equivalent. The apparent resistivity has to be inverted to obtain estimated resistivity versus depth. Many electrode configurations are commonly used for ground-surface surveys,

Schlumberger, Wenner, Dipole-dipole, where the electrode separations relate to the investigation depth and lateral resolution, according to the sensitivity distribution of each arrangement (Roy and Apparo, 1971; Edwards, 1977; Gabàs, 2003). There are numerous electric prospecting arrays depending on number of electrodes and its distribution on the ground. The most appropriate survey configuration (vertical electrical sounding, electrical resistivity tomography ERT or DC surface, cross-borehole) will strongly depend on the specific objectives of the project. DC resistivity surveying is one of the most widely used methods given that field survey acquisition, processing and interpretation are relatively easy to perform. DC resistivity cannot easily determine the relative importance of electrolyte and surface conductivity on the bulk-measured resistivity (Slater, 2006; Binley and Kemma, 2005; Purvance and Andricevic, 2000). However procedures for estimating hydraulic permeability and porosity have been attempted widely and will be discussed below.

Vertical electrical soundings (VES)

Vertical electrical sounding (VES) consists of a symmetric geoelectrical array that can be used to determine the electrical resistivity of the subsurface. Increasing progressively the spacing between the current electrodes AB, while keeping the potential electrodes

MN at the same position, provides a sounding curve corresponding to the apparent resistivity versus depth of at single location. The wider the electrode spacing, the deeper is the investigation depth. Although the VES method is still widely used (Choudhury and Saha, 2004), nowadays VES is regarded as an out-dated technique as there are alternative instrumentation and electrode configurations that can provide 2D or 3D images of the subsurface more time-effectively.

Electrical surface imaging (DC or ERT)

Electrical surface imaging (DC surface) called as well Electrical Resistivity Tomography (ERT), combines surface profiling with vertical soundings using a multi-electrode array to produce 2D or 3D images of the subsurface resistivity. The measurements are acquired along profiles using a large number of electrodes placed equidistantly, allowing the electrodes to be current and potential electrodes alternately. The procedure is repeated for as many combinations of source and receiver electrode positions as is defined by the survey configuration to create a full set of measurements (Figure 1.5). In new instrumentation developments continuous recording systems has been implemented that consist of fixed electrode configurations taking measurements continuously as the instrument is towed over the ground such as for example the "Ohm-mapper" system (Geometrics) or "Paces" system (Sørensen, 1996).

Measured data are presented as a pseudo-section in which the apparent resistivity is assigned to the midpoint of the four electrodes for each survey level (related to the spacing between current and potential electrodes) (Figure 1.5). The pseudo-section provides a smooth image of the 'true' resistivity structure with depth, so does not reproduce correctly either the electrical resistivity contrast between structures, or its exact spatial position.

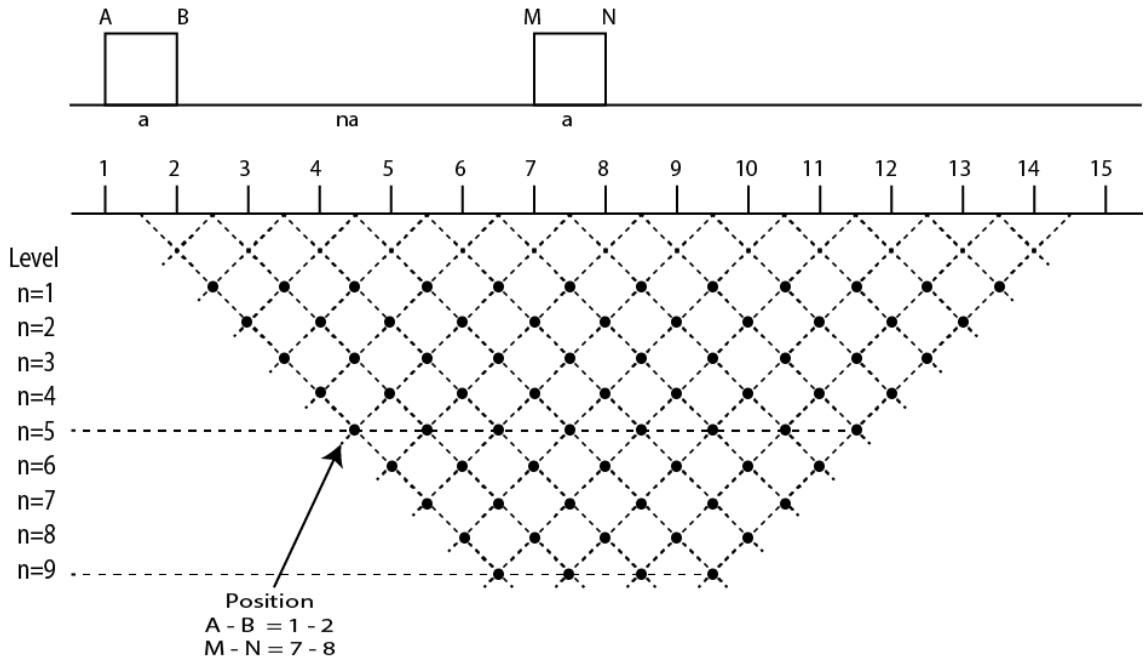

Figure 1. 5: Measurement distribution of a surface resistivity arrangement that built the resistivity pseudosection.

Solving the inverse problem is necessary to obtain the estimated resistivity with depth. ERT is widely used in applications relating to hydrogeological problems (Slater *et al.*, 2002; Mota *et al.,* 2004; Auken *et al.,* 2006 a; Wilson *et al.*, 2006). Work scales may vary from2-5 m up to 50-100 m depending on the electrode spacing and the resistivity of the ground, and limited by the strength of the current injected. DC has been used mainly to map static hydrological properties, structure or hydraulic pathways as well as to monitor temporal properties associated with changes in moisture or water quality.

Induced Polarization (IP)

Induced Polarization, IP, allows the spatial distribution of the subsurface resistivity characteristics to be determined in a similar manner to the DC method. However, IP is capable of determining the geophysical signal contribution from the pore fluids and from the fluid-grain interfaces that contribute to the real and imaginary parts of the electric conductivity. Given that IP is sensitive to the processes at the fluid-grain interface (effective clay content or internal surface area), it has been used to establish petrophysical relationships with hydraulic permeability (Knight and Nur, 1987; Purvance and Andricevic, 2000; Slater, 2006).

IP measurements are made in the field using a four electrodes arrangement using non-polarizing electrodes. The measurements are based on recording the polarization and

potential difference that occurs after applying a current in either the time or the frequency domain. Time domain IP measures the decay voltage as a function of time after stopping the current injection (Figure 1.6, left). The gradual voltage decrease as a complex function of the electrical charge polarization at the fluid-grain interface and the conduction within the pore fluid (Binley and Kemma, 2005). The measurements are used to obtain an IP apparent resistivity and an apparent chargeability m_a:

$$m_a = \frac{1}{(t_2 - t_1)Vp}\int_{t1}^{t2} V(t)dt$$

where *Vp* is the primary voltage and the integral measure the decay secondary voltage withtime.In the frequency-domain mode, after injecting an alternating current of characteristic angular frequency, the resistivity magnitude and the phase-shifted voltage of the complex electrical resistivity is measured (or the time delay between the transmitter current signal and the received voltage signal is measured) (Figure 1.6). A more challenging method is the Spectral Induced Polarization (SIP) involving the injection of current at different frequencies normally ranging between 0.1 to 1000 Hz. The complex resistivity, composed by a spectrum of impedances is obtained after applying a Fourier transform to derive apparent resistivity and phases as a function of frequency.

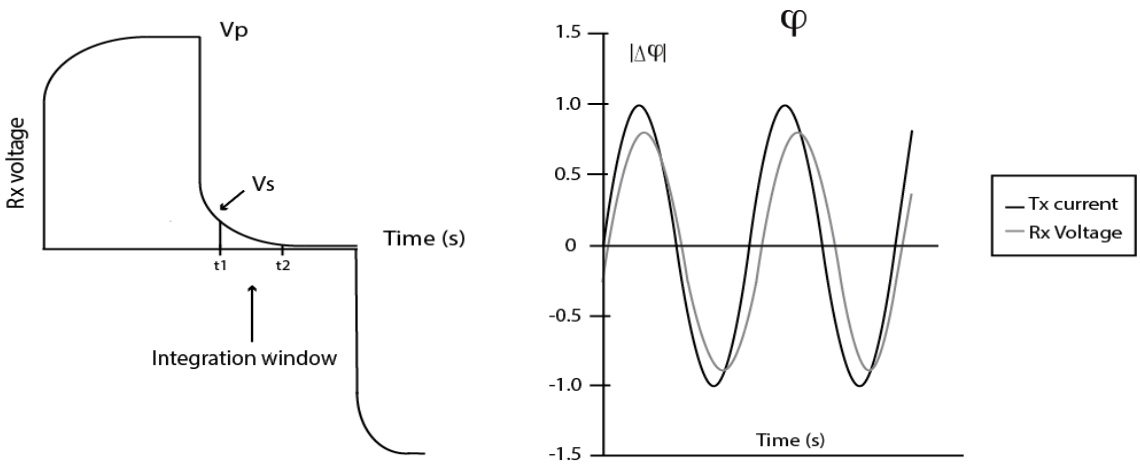

Figure 1. 6: Left, Time domain IP waveform showing the primary voltage Vp, the secondary voltage Vs, and the integration window. On the right, frequency domain IP waveform showing IP response defined as a phase lag in the received waveform (Modified after Zonge et al., 2006).

SIP has been reported to provide better results for extracting information on the pore-fluid-conductivity and the fluid-grain interface (specific surface area) (Slater and

Lesmes, 2002). It has been found to show a very close dependence on the specific surface area of pore volume ratios of soils, which represents the inverse of the hydraulic radius and exerts a critical control on hydraulic permeability (Slater, 2006). Although SIP provides better predictive estimates of hydraulic permeability, great disadvantages exist when compared to the DC applications due to the fact that 1) data acquisition and interpretation is more complex, 2) coupling effects and high-noise-signal ratio and 3) physiochemical interpretation is still not fully understood (Slater and Lesmes, 2002).

Self-Potential (SP)

SP is a geoelectrical natural field method based on the measurement of electric potentials generated by natural electrokinetic processes (composed by electrocinetism, electrothermalism and electrochemism among other phenomenon) usually when an electrolyte flows in a porous medium (Revil and Pezard, 1999). The spatial distribution of electric potential measured using non-polarizable electrodes allows the mapping of the steady-state current flow.

A pore fluid is in chemical equilibrium with the rock matrix, resulting in an ion accumulation at the pore fluid interface known as the electrical double layer (EDL). Thus, when a fluid flows through a porous medium, so do the charged ionic species, resulting in the generation of an electrical current. If no other external electric current sources exist, the convection current is balanced by conduction current so as to maintain a constant electric charge. The conduction current is responsible for the measured SP signal. In this case, the measured potential V is related to the fluid pressure, P, through the Helmholtz–Smoluchowski equation, (Darnet and Marquis, 2003):

$$\overline{\nabla} V = C \overline{\nabla} P$$

where C is the SP cross-coupling coefficient which depends mainly on the water content, electrical conductivity, permittivity and dynamic viscosity.

SP has been commonly used for the monitoring of hydraulic processes and consists of the continuous measurement of the electric potential differences between two un-polarizable electrodes using high impedance voltmeter. This dipole is usually aligned along the direction of the water flow. In addition, to ensure a good electrical contact between the electrode and the medium, an electrically conductive solution (e.g. salty water with clay) is usually added around the electrode. The electrokinetic effects of water flow during pumping tests have been shown to generate surface Streaming

Potential (SP) anomalies of several tens of millivolts that are well correlated with the geometry of the water table (Darnet, 2003). SP measurements have been used to estimate aquifer hydraulic properties, flux direction, and hydrothermal circulation near volcanic zones to forecast or characterize possible volcanic crises (Sailhac and Marquis, 2001). However, the main concerns about the method relate to low signal-to-noise ratios, and scale issues. In addition, more detailed investigations need to be conducted on the specific contribution of each elecrokinetic effect on the final measurement in order to have a better understanding of the results.

Time Domain Electromagnetic (TDEM)

TDEM is an inductive method in which a strong direct current is usually introduced through an ungrounded loop, Tx, and is abruptly interrupted after a specific time. The secondary fields due to the induced eddy currents in the ground are measured with a suitable receiver loop, Rx, in the absence of the primary field. Changes in the polarization of the vertical, and sometimes also the horizontal components of the secondary magnetic fields are measured within different time gates after the primary inducing current is turned off. The signal recorded by the receiver is called the transient, and several hundreds of transients are typically recorded and averaged to reduce the effect of EM background and instrumentation noise. The transmitter and receiver loops (Tx, Rx) can either be separated by some distance, as in offset-loop sounding, or not, as in a central loop configuration, which is most commonly used and where no reversal sign is recorded (Figure 1.7). The amplitude of the current flow decreases as a function of time both downwards and outwards away to the Tx due to the resistivity of the soil. The magnitude and distribution of the decaying transient depends on the resistivity of the ground and the instrument configuration. In the early stages (after the shutdown), the induced voltage is time-invariant and proportional to the near surface resistivity value, whereas at later times the time dependent voltage v(t) decay asymptotically (Spies and Frischknecht,1991).

Conversion of v(t) to apparent resistivity curves at late stages depends on the loop configuration, and for instance in a central loop configuration is defined by:

$$\rho_a = \frac{kM^{2/3}}{v(t)^{2/3}\, t^{5/3}}$$

where k is a constant, M is the transmitter coil moment (current per area transmitted: for a circular loop M = 2лr2I), t is time and v(t) is the output voltage from a single- turn receiver coil of area of $1m^2$.

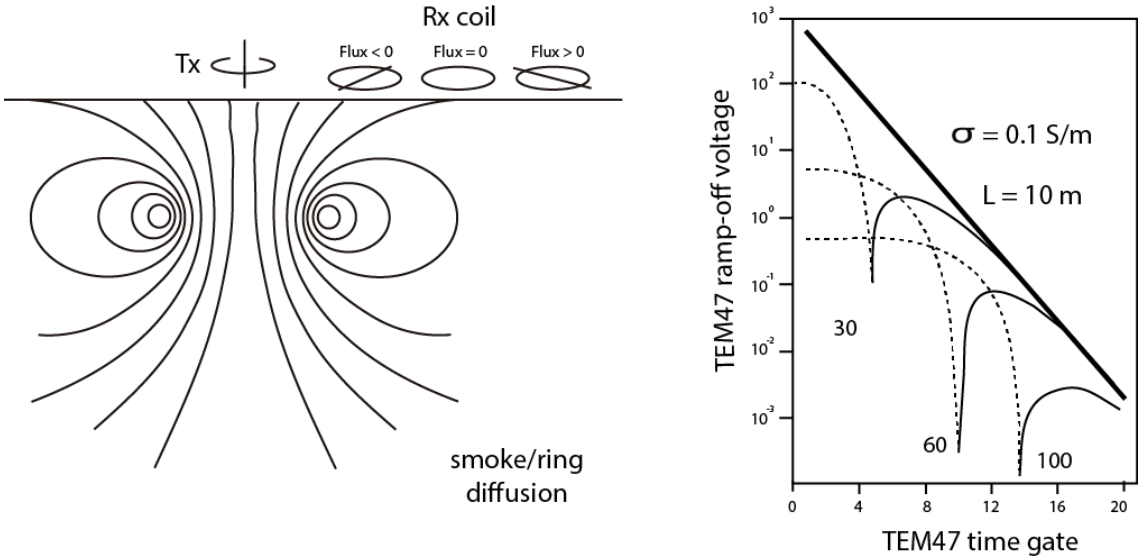

Figure 1. 7: On the left, transmitter and receiver coil and electromagnetic waves distribution in the Earth's interior. On the right, transient decay curves for a loop-loop system at different separation distances over a uniform halfspace (0.1 S/m). The transient time of the sign reversal increases with increasing Tx-Rx separation from 10, 30, to 60, to 100 m. Dashed line negative voltage, solid line positive voltage (from Everett and Meju, 2005).

Investigation depth is function of recording time and loop radius (transmitter moment and turn-off time) at the expense of shallow resolution; however the signal must be strong enough compared with the EM background and instrumental noise in order to be measurable (Fitterman and Stewart, 1986, Nabighian and Macnae, 1991). The extent of the EM noise limits the recording time length and consequently limits the investigation depth. Enlarging the transmitting loop affects the sounding curve at early times, making the calculations difficult for the first layer where mathematical approaches assumes late stage decay at all the times. Furthermore the first layer has to have a minimum thickness to be detectable due to the inherent instrumentation delay in starting sampling after the current turnoff.

Time-domain electromagnetic data can provide information from shallow to relatively deep, up to 500 m and are used mostly for qualitative preliminary interpretation of the resistivity distribution in an estimated range depth. Inversion methods are established only for 1Dparametrization due to a more stable solution. TDEM is still limited by the

lack of applicability of the algorithms for the inference of 2D and 3D structures. TDEM is a good method for resolving the position of conductors; however it is a poor technique for distinguishing resistivity contrasts in high resistivity ranges (Auken et al, 2006 b). Transient electromagnetic systems have also been adapted to helicopter and aircraft, used to acquire extensive and dense surveys (Sørensen and Auken, 2004). TDEM has been used to delineate the depth to basement, hydrostratigraphy (Fitterman and Stewart, 1986; Krivochieva and Chouteau 2003) and buried valley aquifers (Steuer, 2006). It is particularly good at mapping conductive targets, such asclays (Auken *et al.*, 2006 b) or seawater. It has been used to determine clays as a structural indicator of aquifer pollutant susceptibility, or to detect salt-water freshwater interfaces (Guérin *et al.*, 2001; Goldman and Kafri, 2004), where porosity and site specific relationships have been studied using measured water resistivity.

Frequency domain electromagnetic (FDEM)

The frequency domain electromagnetic method, FDEM, is based on the injection of an alternating current of a given angular frequency through an ungrounded loop with a characteristic frequency. The primary field of the Tx loop will induce eddy currents in all conductors present in the Earth. The response at the Rx loop contains contributions from both the primary magnetic flux from the transmitter loop and the secondary magnetic fluxes generated by the induced currents. The out of phase ratio of the secondary to the primary magnetic fields are used to estimate the apparent conductivity σ_a:

$$\sigma_a = \frac{4}{\omega \mu_0 L^2} \frac{H_{si}}{H_{pj}}$$

The primary field, Hpj, is known precisely since the Tx and Rx characteristics are under the control of the experiment. Profiling is performed by measuring the apparent resistivity of the depth volume as a function of frequency at the Tx-Rx midpoint positions (Figure 1.8). There are many different coil configurations, which include both horizontal co-planar for mapping horizontal features and vertical co-axial to delineate vertical structures. The different configurations provide different sensitivities in the horizontal and vertical directions.

Investigation depth depends on the coil separation as well as the frequency of the applied current and has been qualitatively determined as the 0.75 times the transmitter-

receiver loop spacing for a horizontal electromagnetic dipole configuration and 1.5 times the spacing for a vertical dipole (CUAHSI, 2005) at a fixed frequency.

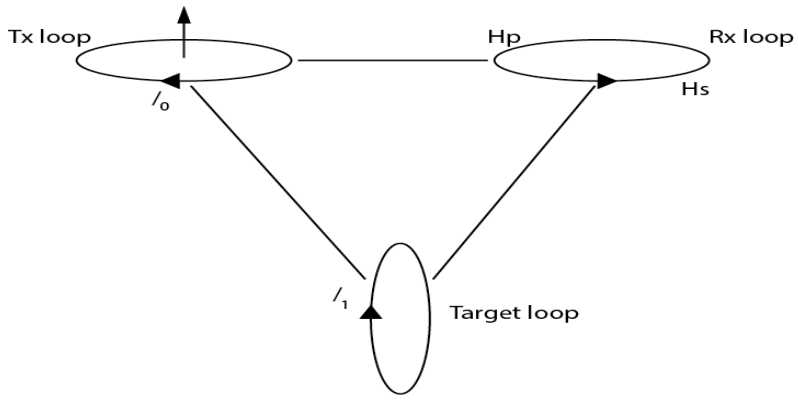

Figure 1. 8: Geometry of a typical loop-loop system. Coils can operate either in a vertical or horizontal configuration, achieving different investigation depth and lateral resolution.

Systems have been improved by the development of multiple frequency transmitter capabilities. In general, new instrumentation can measure from 3 to 6 frequencies that provide different effective penetration depths, and providing better resolution in depth. FDEM has been widely used as profiling method mainly for providing qualitative interpretation or 1D smooth inversion. Quantitative inversion is complex due to the coupling effects of the primary and secondary fields and calibration of the coil interferences is therefore complex. Other concerns relate to the problem of extremely low resistive first layer limiting penetration depth. While frequency domain electromagnetic method has a lower penetration than TDEM, the surveys are easy to perform and the instruments are light and easily portable with a fixed coil separation. Airborne frequency domain electromagnetic methods, similar to TDEM, provide fast data acquisition, and therefore more time and cost effective surveys. FDEM surveys have been used for qualitative preliminary interpretation of subsurface resistivity distribution for an estimated depth range depending on each frequency. Research fields currently focus on imaging the first tens of meters of the subsurface and to identify flow pathways (Geonics, 1999), saline soils (Himi *et al.,* 2002; Arranz *et al.,* 2004), mapping clay content, UXO, and is often used in precise agriculture investigations (Pellerin and Wannameker, 2005).

Audiomagnetotelluric (AMT)

Audiomagnetotelluric (AMT) is a natural source electromagnetic technique working in the frequency domain that allows the determination of the resistivity distribution of the

subsurface. The fundamentals are common to the magnetotelluric method (Simpson and Bahr, 2005). AMT is based on the simultaneous measurement of the temporal fluctuations of the horizontal electric and magnetic fields on the Earth's surface.

The transformation from the time to the frequency domain is achieved by a Fourier type transform or a wavelet transform (Trad and Travassos, 2000; Arango 2005) that computes the frequency content of the signal within a particular time interval.

AMT instrumentation consists of two pair of electrodes laid out perpendicularly to each other and two coil magnetometers aligned in the orthogonal directions. From the ratios of any of the electric and magnetic field components in the frequency domain we can define the complex impedance as Zij(ω) = Ei(ω)/Hj(ω), where i and j are two perpendicular directions. The relation between the horizontal electrical and magnetic fields in the frequency domain can be written as:

$$\begin{pmatrix} E_x(\omega) \\ \\ E_y(\omega) \end{pmatrix} = \begin{pmatrix} Z_{xx}(\omega) & Z_{xy}(\omega) \\ \\ Z_{yx}(\omega) & Z_{yy}(\omega) \end{pmatrix} \begin{pmatrix} H_x(\omega) \\ \\ H_y(\omega) \end{pmatrix}$$

The impedance components can be scaled to obtain the apparent resistivity, similar to that used in DC resistivity techniques, and the impedance phase:

$$\rho_{a,xy}(\omega) = \frac{1}{\omega\mu}\left|\frac{E_x(\omega)}{H_y(\omega)}\right|^2 \quad ; \quad \varphi_{xy}(\omega) = \tan^{-1}\left(\frac{E_x(\omega)}{H_y(\omega)}\right)$$

The investigation depth is a function of the electrical resistivity of the Earth and angular frequency, ω, of the EM field. A reasonable measure of the penetration scale length is the skin depth, which corresponds to the distance in which the amplitude of the incident electromagnetic field has attenuated by a factor of 1/e. In a uniform half-space the skin depth, in meters, is given by:

$$\delta \approx 501\sqrt{\frac{\rho}{f}}$$

The measured apparent resistivity and phase data must be inverted to obtain the Earth's electrical resistivity distribution. Plane wave methods, of which AMT is an example, have significant advantage in comparison to other EM methods. Multidimensional

modelling capabilities are well developed from traditional crustal-scale MT studies and are directly applicable to hydrological problems, at higher frequencies. Presently there are several 2D inversion codes (Siripunvaraporn and Egbert, 2000; Rodi and Mackie, 2001), and 3D inversion codes are beginning to be used (Siripunvaraporn *et al.,* 2005 a).

In hydrogeophysical applications, the AMT method is starting to be used. It has been used for the delineation of static properties, aquifer geometries and boundaries (Krivochieva and Chouteau, 2003; Linde and Pedersen, 2004 b), structural and stratigraphycal characterization, in thermal aquifers (Manzella *et al.,* 2004; Arango, 2005), and seawater intrusion problems (Falgàs *et al.*, 2005; Unsworth, 2006). Monitoring of dynamic processes has recently been implemented on oil leakages (Tezkan *et al.*, 2005) and seawater-freshwater dynamic interface movement. AMT is ideally suited for hydrogeological investigations given the sensitivity of electrical resistivity to the subsurface lithology, the presence of water and its quality. It can be implemented rapidly, it can achieve high investigation depths with reasonable resolution and it provides a true 3D measurement. In this thesis AMT plays a significant role used as the principal geophysical technique that, together with complementary information is used to improve our knowledge of aquifer systems.

Ground Penetrating Radar (GPR)

The ground penetrating radar (GPR) is an electromagnetic method that measures the transmission and reflection of high frequency (1MHz to 1 GHz) electromagnetic waves within the Earth. The method is effective in low-loss materials in which energy dissipation is small compared to the energy storage, and therefore GPR waves respond within the propagation regime.

When the EM waves reach a boundary, the incident wave is partially transmitted and partially reflected, and GPR measures the velocity, v, and the energy attenuation, α, as the arrival time of reflected energy. Electromagnetic wave velocity and the reflection of the EM energy are primary controlled by the dielectric constant, ε, and the conductivity, σ, of the medium.

$$v = 1/\sqrt{\varepsilon\mu} \quad ; \quad \alpha = 0.5\sigma/\sqrt{\mu/\varepsilon}$$

GPR data provide a subsurface reflection time versus spatial position. Variations in the reflection amplitude and time-delay indicate variations in the propagation velocity and

energy attenuation. Resolution and penetration depth of the resulting GPR images depend on the use of different antenna frequencies and the conductivity of the medium. Typically, higher frequencies increase the resolution at the expense of the depth of penetration, while electrical conductivity of the subsurface has a significant impact on the attenuation of the EM energy. In general investigation depth is not greater than 10-20 m for most geological media. GPR instruments are commonly composed of a transmitter and a receiver, with a fixed spacing among them. Surveys usually are organized in regular grid to achieve 2D and 3D coverage. GPR surveys can be performed using a surface-based system where the transmitter and receiver antennas are moved across the Earth's surface (reflection survey), in a cross-hole system where the antennas are positioned in separate boreholes (trans illumination survey) or a combination of the two.

There are many GPR contributions to hydrogeological applications (Knight, 2001) since the presence or absence of water dominates the GPR response through the dielectric constant, ε, where many time lapse GPR surveys focus on moisture-fluid movement recognition (Loeffler, 2005). GPR has also been considered useful because of its ability to delineate fine scale stratigraphic structures which have importance on the groundwater flow. However, clayey materials and saline soils provide low penetration and conductivity estimation has been recently derived from observations of the energy attenuation. Quantitative interpretation is a subject of current research, and typically site-specific relationships have been developed.

Nuclear Magnetic Resonance (NMR)

Nuclear Magnetic Resonance (MNR) is a fairly new electromagnetic geophysical technique used for directly investigating the water content, mobility, and pore-structure parameters controlling the hydraulic permeability. The fundamentals of the method rely on the excitement of the hydrogen protons of water with an external electromagnetic source transmitting at the resonance frequency of the protons (Larmor frequency, fL, around 1-3 kHz), depending on the local Earth magnetic field) (Figure 1.9). The Larmor frequency is defined by:

$$f_L = \gamma B_0 / 2\pi$$

Where γ =0.2675 Hz/nT, is the gyromagnetic ratio of hydrogen protons and _L= 2л *f*L is the angular frequency.

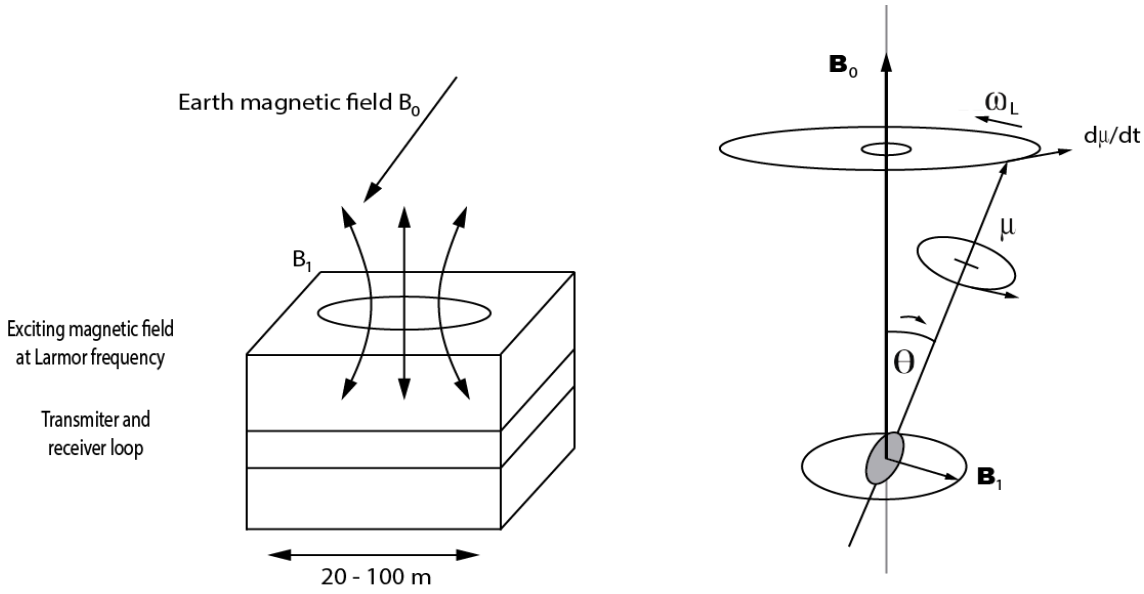

Figure 1. 9: On the left NMR instrument application. On the right detail of the hydrogen proton deflection due to the induced current at the Larmor frequency (from Yaramanci et al., 2005).

Protons of hydrogen atoms in the water molecules have a magnetic moment which processes along the local magnetic field B0. When another magnetic field, B1, is applied, perpendicular to B0, the axis (magnetic moment) of the precession movement is deflected (Figure 1.10, right). When B1 is removed the magnetization relaxes back to the equilibrium position, emitting an electromagnetic signal that decays with time (Figure 1.10).

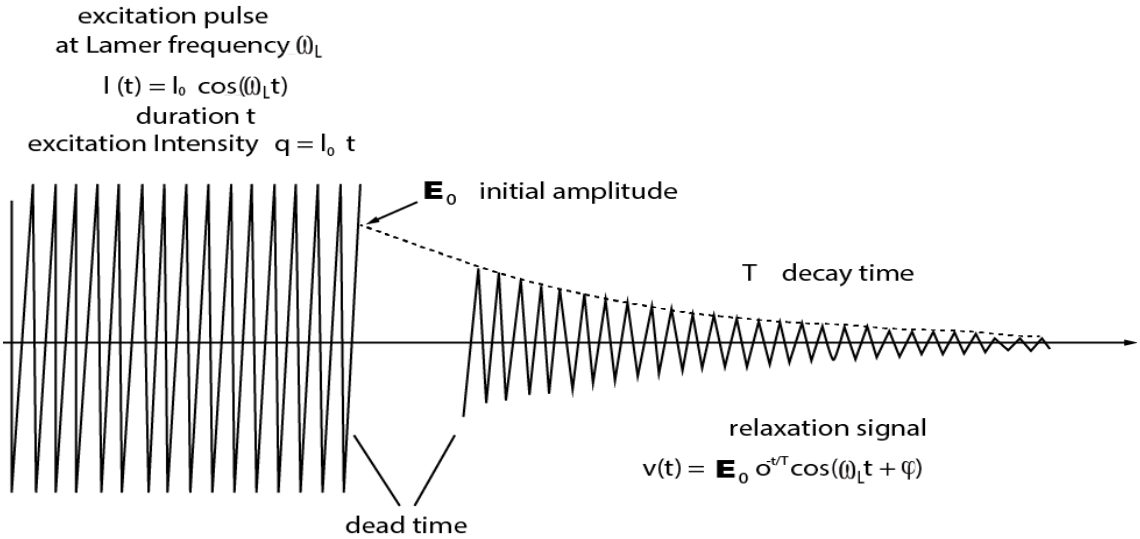

Figure 1. 10: Input and output signals of NMR (from Yaramanci et al., 2005).

The device is composed by a single coil which works both as a transmitter and a receiver system. An alternating current is applied within the coil with the angular

Larmor frequency at specific intensity. After the current is switched off, a potential difference or voltage v(t), which is frequency and time dependent, is induced in the coil. The output signal v(t) is usually approximated by:

$$v(t) = E_0 e^{-t/T} \cos(\omega_L t + \varphi)$$

The initial amplitude E_0 at t=0 is related to the water content for a non-conductive medium, while the decay time, T, is related to the mean pore size (or grain size), and the hydraulic conductivity of the material. Decay times are shorter for materials with finer grains sizes (60ms-300ms) than for the coarser sizes (300-600 ms for gravels). At the other extreme, in clay materials water is bounded by a strong molecular attraction and has a very short relaxation time (< 30 ms) that can not be detected by the NMR.

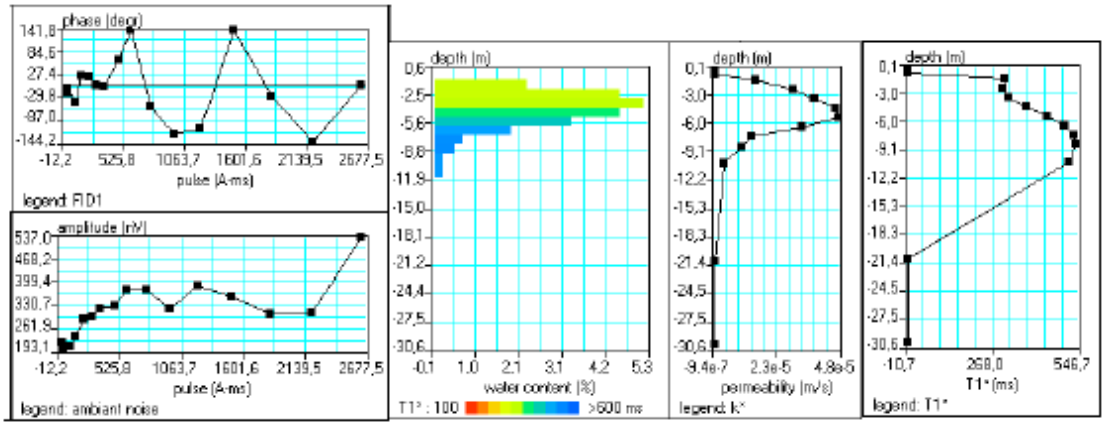

Figure 1. 11: Typical data (left) and inversion models (right) of an NMR sounding on La Soutte (Behaegel 2006), where water content and permeability have been estimated.

NMR measurements are conducted for different excitation intensities (q), recording the initial amplitude $E_0(q)$ and the decay time T(q). The primary parameter obtained through inversion of the NMR data is the density distribution of hydrogen atoms, which is directly related to the water content (Figure 1.11). In terms of petrophysical approaches, the currently available quantitative expressions that describe of the relationship between the decay time and flow-property parameters are of an empirical nature. Approximation of the hydraulic conductivity relationships can be addressed simply by the pore size hydrologic relationship and site specific proves. For instance, Yaramanci *et al.* (1999) have proposed an hydraulic conductivity estimation given by $K \sim T^4$, where K is hydraulic conductivity in m/s, and T is decay time in milliseconds.

The resolution and accuracy of the NMR method decreases with depth, and depends mainly on the intensity of the current applied (i.e., higher strength and/or longer pulse time). Increasing the intensity increases the investigation depth as long as the injected current time << decay time. In the studies carried out by Lubczynsky and Roy (2003) the high intensity of the applied current allowed subsurface characterization to more than 80 m depth. Nonetheless, the

main concerns are related with EM noise given the low signal to noise ratio. NMR has the potential to become a powerful tool for groundwater exploration, with many contributions to date having produced petrophysical characterization, data inversions procedures and successful case studies (Lubczynski and Roy, 2003; Legchenko and Shushakov, 1998; Plata and Rubio, 2002; Keating and Knight, 2007). Yaramanci *et al.* (2005), considering the capability of NMR as a direct indicator of water and soil properties, suggest that an improvement will be achieved through the development of joint inversions or joint interpretations of NMR with electric and electromagnetic methods as a means of decresing the uncertainty in the results in conductive media. The induction effects need to be considered to improve the inversion and modeling process in order to account for the primary field modification in the presence of conductive structures. Other important research are the regularization and inversion procedures considering that nowadays only 1D inversion are mainly used.

Shallow seismic methods

Seismic is a commonly used geophysical method that can provide structural and additional complementary information about the aquifer systems. Seismic methods are based on the generation of an elastic wave field that propagates through the ground, returning to the surface where several detectors record its spatial-temporal variation. Developed for locating and mapping oil reservoirs, seismic methods can also be used as a tool for high-resolution mapping of shallow geologic targets (Hunter *et al.*, 1984; Steeples and Miller, 1990).

Seismic waves include body waves (P-waves and S-Waves) that travel three dimensionally trough solid volumes, and surface waves (Love waves and Rayleigh waves) that travel as a boundary wave near the Earth's surface. P-waves are the first waves recorded due to their higher velocity, and are the most commonly used and easiest waves type to work with. The velocity of propagation of various types of elastic waves, and their frequency content, are related to both the elastic properties and mass

density of the medium in which the waves are travelling. The propagation velocity is given by the product of the wave frequency and the wavelength, $v=f\lambda$, where the P-wave and S-wave propagation velocities are defined respectively by:

$$v_p = \sqrt{\frac{k + \mu\frac{4}{3}}{\rho}} \quad ; \quad v_s = \sqrt{\frac{\mu}{\rho}}$$

where k is the bulk modulus, μ is the shear modulus, and ρ is the density of the material through which the waves are propagating. Fluids have no shear strength, their shear modulus is zero, and S-waves therefore cannot propagate through fluids. Since the velocity is a physical property intrinsic to each Earth material, higher frequencies result in shorter wavelengths and better resolution. The upper frequency limit for near surface studies is generally about 1KHz.

Seismic involves measurement of the travel time between the generation of a seismic pulse and its arrival as a wave train at different geophones located at known distances away from the source. Wave propagation is described by several mechanisms: time delay, dispersion, attenuation, reflection, refraction and interference. When a seismic energy source (e.g. sledgehammers, explosives or vibration devices) is activated, energy radiates in all directions prompting wave refraction or reflection at geological interfaces (Figure 1.12). When the seismic refraction method is used, the waves corresponding with head waves originating at geological interfaces are recorded at the surface as the first arrivals (Figure 1.12).

Surface seismic refraction methods are focused on travel-time data sets which provide information about seismic velocity. Inversion routines are used to determine velocity as a function of depth, and are based on Snell's law and ray theory (Pelton, 2006). From an hydrogeological point of view, P-wave seismic velocity can improve our understanding of changes in fluid saturation (e.g. mapping water table) and locate interfaces with large acoustic contrasts, such as the bedrock-soft sediment interface. Velocity changes are related to lithology, pore-fluid type and pressure changes (Rubin *et al.,* 1992).

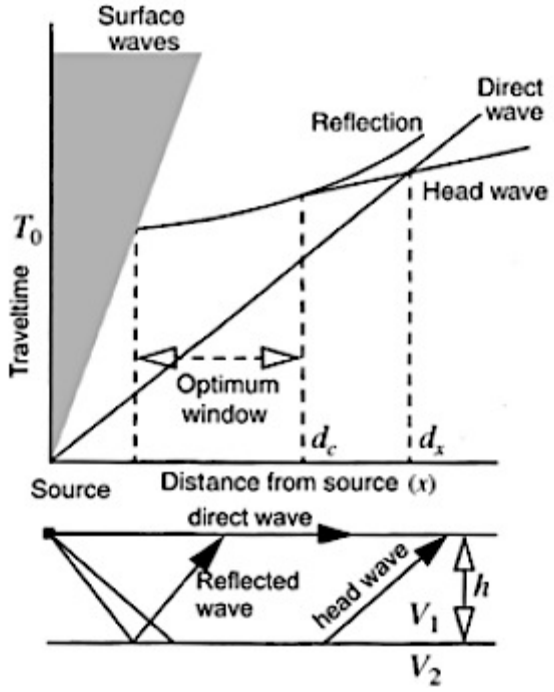

Figure 1. 12: Geometric relationships between surface, reflected, direct and refracted (headwave) waves (From Pelton, 2006).

Seismic reflection methods are based on the isolation and processing of reflections from the boundaries of geologic units to provide a time image of the subsurface called seismic section. The amount of seismic energy that crosses an interface depends upon the acousticimpedance, Zi :

$$Z_i = \rho_i v_i$$

where ρi is the density and vi is the seismic velocity of each layer i. Reflection seismic will provide a direct image of the impedance contrasts within the subsurface, in two-way-travel time, provided three criteria relating to the subsurface materials are satisfied: acoustic impedance contrasts must be present, the dominant frequency of the data must be high enough so the direct waves and refractions will not interfere with the reflections, and finally the wave-field must be sampled adequately in space and time, using appropriate experimental design (Figure 1.12). The generally accepted vertical-bed resolution limit is given by the ¼ _ wavelength criterion for the dominant frequency. The dominant wavelength for seismic reflections normally increases with depth due to the velocity typically also increasing with depth. The dominant frequency always decreases with depth due to the attenuation of high frequencies.

When possible, vertical seismic profiling, VSP, is conducted in boreholes, allowing the accurate determination of the one-way travel time of seismic waves to various geologic units, as well as the attenuation and acoustic impedances. Surveying is preformed using a string of hydrophones placed in a borehole, with the source placed on the surface. In shallow seismology, the main concerns are the interference of refractions with reflections, the presence of air-waves, and the presence of surface waves that need to be efficiently filtered or muted (Steeples, 2005). Inaccurate velocity estimations also induce errors in the depths estimated in the seismic profiles.

Seismic applications to hydrologic problems have focused on mapping the bedrock, delineating confining units, resolving sedimentology and stratigraphy, detection of geologic faults, evaluating karst conditions, mapping landslides' base, determining the degree of saturation and the water table depth which may help constrain other geophysical techniques (Gallardo and Meju, 2003; Jarvis and Knight, 2002; Rubin *et al.*, 1992). Novel approaches also include S-wave methods, three-component recording methods with orthogonal mounted geophones, surface wave analysis (SASW, MASW), acquisition and processing of 3D surveys, the combined use of GPR and high-resolution seismic and development of relationships between seismic properties and rock physical properties.

Gravity and Magnetic field application

Gravity and magnetic fields are good potential tools in hydrogeophysical applications, and are generally used in support of the regional interpretations of other geophysical measurements. An extensive review of both methods can be found in Blakely (1995).

Gravimetry consents to measure the variations in the vertical component of the gravitational field of the Earth. The acquired data require extensive processing and correction for non-geological effects and for subsurface geological variation (e.g. topography, location, day and time) before they can be modelled. Gravity data traditionally have been used to determine the subsurface configuration of structural basins, made possible by the large density contrast between basin infill and bedrock. Gravity data inverted to produce basement depth are more sensitive to shape than depth (i.e. Jachens and Moring, 1990). The main hydrogeological applications of gravity concern the investigation of maximum aquifer thickness in basins to constrain water flow models, to distinguish carbonate from sandstone aquifers (difficult discrimination when using geoelectrical methods), and in the case of microgravity, to measure the total

mass of water in a conceptual column and therefore to examine changes in the mass balance of water (Gehman *et al.*, 2006).

The magnetic method uses the variation in the strength of the Earth's magnetic field that reflects the spatial distribution of magnetized material throughout the subsurface.

Magnetization occurs naturally in materials and rocks, and depends on the quantity of the magnetic minerals and on the strength and direction of the permanent magnetization carried by these minerals (magnetite, pyrrhotite). Although magnetic data do not respond directly to the presence of water, they can contribute to the understanding of the geologic controls on the groundwater systems. Magnetic surveys can be useful in hydrogeological studies due to their ability to determine basin geometry, to delineate igneous intrusions that my affect groundwater flow, and to identify shallow local magnetic anomalies caused by faults, paleochannels, eolian deposits or man-made features, intra sedimentary faults, and hence the compartimentation or connection within the aquifer system (Grauch, 2001).

Well logging

Borehole geophysics includes all methods that make continuous profiles or point measurements at discrete depths down a borehole. The measurements are made by lowering different types of probes into the borehole. Logging probes enclose the sensors that are connected to a cable that is pulled upward while data are recorded. The measurements are related to the physical and chemical properties of the surrounding rock, to the pore fluid, to the fluid in the well, the well casing or any combinations of these factors. Many geophysical logging techniques were initially developed by the petroleum industry, and later adapted for the hydrogeological discipline. Once a well is drilled, geophysical well logging is able to make several different physical measurements (acoustic, electric, nuclear) that can provide information on lithology, thickness, continuity of aquifers, porosity, bulk density, resistivity, groundwater chemical and physical characteristics, fluid movement parameters, and integrity of the well construction. The most commonly used log types that provide those properties are SP, resistivity, gamma-ray, gamma-gamma, neutron, elastic wave propagation, cement bond log, acoustic televiewer, borehole television, caliper, temperature, fluid conductivity, flowmeter, fluid transparency or turbidity. Korb *et al.* (2005) present a complete summary of hydrogeophysical applications of log probes facilities.

In terms of the limitations of borehole geophysics, the main concerns are related to borehole characteristics, most of the logs need uncased wells, fluid-filled wells, or require isolation packers. Laboratory analysis of cores and fluid is essential either for direct calibration of the logs or to verify calibrations used to estimate hydrological parameters.

1.1.6 Hydrogeophysical challenges

There are three main research topics where special effort is required in order to fulfil the potential of hydrogeophysics: 1) Petrophysical relationships, 2) Integration of geophysical and hydrogeological measurements and 3) Improvement on the geophysical methodologies.

Petrophysical relationships

Estimation of hydrogeological parameters using geophysical data is a new and current area of research, still under strong development. Firstly, geophysical properties may be associated with more than one hydrogeologic condition (effective conductivity versus fluid conductivity and surface specific conductivity, or electrokinetic effects) that can lead to misinterpretation. Secondly, the scale of sampling from the hydrogeologic data can be different from that of the geophysical data (cores, well lithology description, seismic, DC, GPR). In addition, geophysical data are often dependent on the array geometry and measurement direction. However to estimate hydraulic parameters over the space the dense, cost-effective geophysical datasets are needed to provide a better understanding of the hydrologic systems and processes. The link between the hydrogeological parameters and the geophysical properties is non-universal for geological materials. The most common strategy is to infer a site-specific empirical relationship between the geophysical measurement and the parameter of interest, using collocated hydrogeological and geophysical data. Under controlled laboratory conditions petrophysical parameters can often be defined more completely and more accurately (Ferré *et al.*, 2005). For example, soil and water resistivity measurements and granulometric analysis of core samples can be performed in the laboratory and used to extrapolate the geophysical results over the entire basin site (Keller, 1988; Mazáck *et al.*, 1990; Purvance and Andricevic, 2000; Guérin *et al.*, 2001) (Figure 1.13). Similarly,

geophysical well logs can be used to define hydrogeologic parameters such as hydraulic conductivity and effective porosity that neutron density or acoustic logs can be calibrated in porosity units (used basically in oil reservoir modeling).

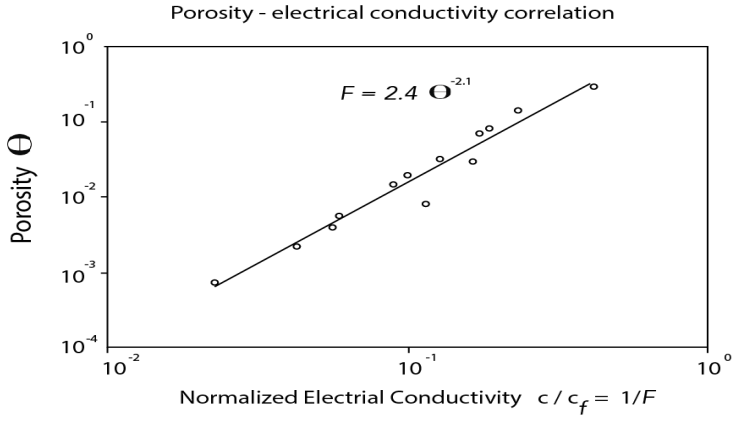

Figure 1. 13: Archie type petrophysical relationship. F is formation factor and is porosity extracted from laboratory studies. C is conductivity and Cf is the fluid conductivity. Linial regression is derived and subsequently applied at the same locality, when only one of the two variables is known (from Purvance and Andricevic, 2000).

Resistivity models

While electrical resistivity is the most commonly used property from which to infer porosity, Φ, or hydraulic permeability, *k*; no general petrophysical relationship has been reported. The well knows Kozeny-Carman equation has been commonly used to estimate the hydraulic permeability in a porous medium, replacing the porosity and/or the specific surface area Sp with an electrical measurement. Kozeny-Carman relationship states:

$$k = \frac{\phi \cdot r^2}{aT}$$

where r is the radius of the pore space (inverse of specific surface area Sp of the porous volume), a is a shape factor and T is the tortuosity defined as the ratio between the effective fluid transmission path length (*La*) and the macroscopic length of the sample (*L*). The tortusosity has been related (Nelson, 1994) to the electrical formation factor F (defined below).

$$T = \left(\frac{L_a}{L}\right)^2 \propto \phi F$$

and consequently equation k can be rewritten as:

$$k = \frac{1}{aFS_p^2}$$

Quantitatively, the rock resistivity response is principally due to the pore fluid conductivity (related with F) and pore surface conductivity (related with the Sp) since most of the rock materials are fundamentally electrical insulators (Purvance and Andricevic, 2000). However defining the correct equivalent effective property of the geophysical measurement is not simple. For a clay free environment the widely used relationship that relates porosity, formation resistivity ρ and fluid resistivity ρw can be approached with Archie's law (Archie, 1942):

$$\rho = a\rho_w\phi^{-m}$$

The formation factor is a structural parameter defined by:

$$F = \phi^{-m} \Big/ a$$

where m is the Archie cementation factor. Keller (1988) among others, provides tables for the a and m parameters for different materials obtained by analysis of a collection of samples analysis. Considering the above two equations the fluid resistivity and the formation resistivity is simply correlated to the structural parameter F (see also Figure 1.13).

$$F = \frac{\rho}{\rho_w}$$

In this free clay case, pore fluid resistivity provides the main contribution to the bulk resistivity. Inverse and direct relationships between hydraulic permeability and resistivity could be established. In a saturated media the higher the hydraulic permeability the lower the electric resistivity, within the same rock type, due to increasing effective porosity and to a negative linear log K-logρ relationship results (continuous lines in Figure 1.15).

On the other hand, hydraulic permeability and electrical resistivity are directly proportional to the grain size (the rock type), and increasing grain size increases both the electrical resistivity and the hydraulic permeability and a positive linear log K-log ρ relationship results (dashed line in Figure 1.14).

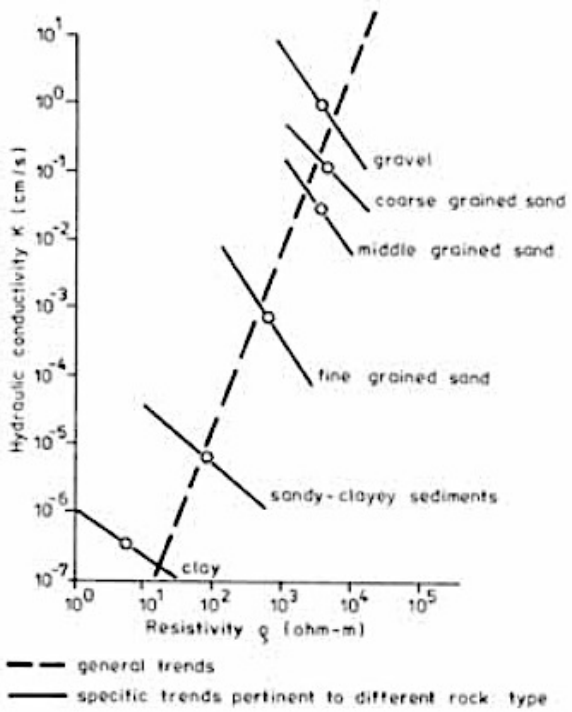

Figure 1. 14: Relationships between hydraulic conductivity and resistivity for different rock types (direct correlation) and within a specific rock types (inverse correlation) (from Mázac et al., 1990).

In addition, Archie's law fails on predicting where clay minerals are present. The presence of clay strongly influences porosity, permeability and resistivity given that clay is characterized by a high cation exchange phenomenon (Waxman and Smits, 1968), and high specific surface area. In clayey environments the dominant contribution to the bulk resistivity is due to surface conductivity. In general, the higher the clay content the lower the resistivity and the lower the hydraulic permeability (Figure 1.14, Figure 1.15, left). Porosity decreases with increasing clay content until the effective porosity is reduced due to the reduced connected porosity. Thereafter the porosity as non-connected porous space increases increasing clay content (Figure 1.15, right), reflecting the total porosity.

In Figure 1.15 shows the relative impact on resistivity provided by clay content and salinity (fluid resistivity). For a given clay content two types of behaviours are seen, 1) when the effect of high clay content dominates the bulk resistivity, even with increasing salinity (horizontal trend line in Figure 1.15 left), and 2) when salinity dominates the bulk resistivity, which follows the 0% clay content and water line trends. In low clay materials, fluid dominated behaviour is attained at lower salinity concentrations.

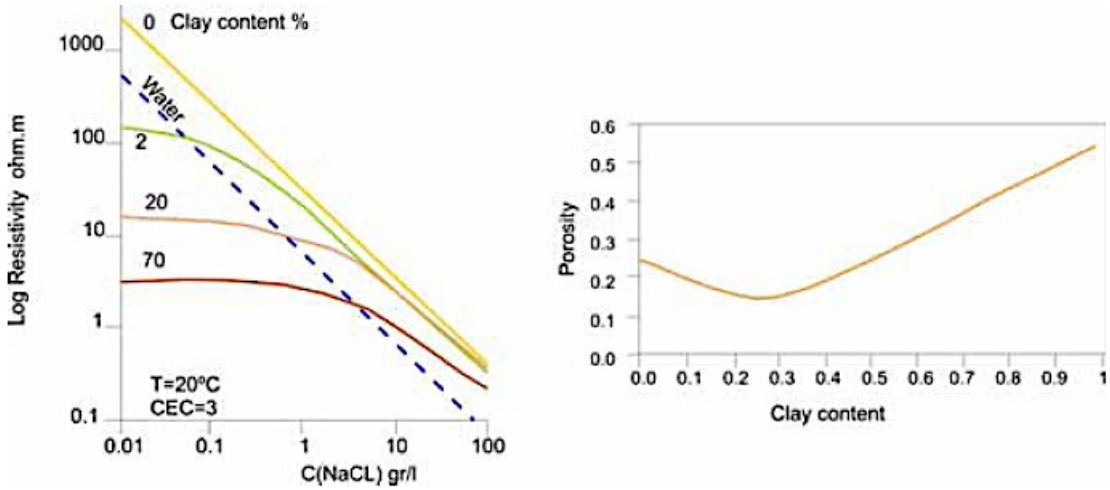

Figure 1. 15: Left, resistivity versus salinity concentration (CNaCl) for samples with different clay content samples showing two different dominant resistivity process. Right, the relationship between porosity and clay content. Total porosity decreases due to increasing clay content up to a critical point, where after it starts to increase, and conversely effective porosity decreases (modified form Shevnin, 2006).

The fundamental limitation of most of the effective resistivity geophysical measurements is to determining the relative importance of the both resistivity contributions, due to the electrolyte or the surface specific conductivity, thus the real and imaginary parts of the complex resistivity. In many studies the Hashin-Shtrikman bounds (HS) are used to restrict the solutions (Hashin and Shtrikman, 1962; Wempe, 2000). The theoretical (HS) bounds for electrical resistivity provide upper and lower limits for the resistivity–porosity relationship in a multi-constituent media. The upper bound HS+, describes the case where the conductive material is perfectly interconnected, whilst the lower bound HS- describes de case where the conductive material is confined within isolated pockets.

Several research groups are working on the improvements in determining k based on IP and SIP, where the real an imaginary parts of the electric conductivity can be inferred independently and used in the Koezeny-Carman relationship for F and Spor respectively (Purvance and Andricevic, 2000; Binley *et al.*, 2005; Slater, 2006) (Figure 1.16).

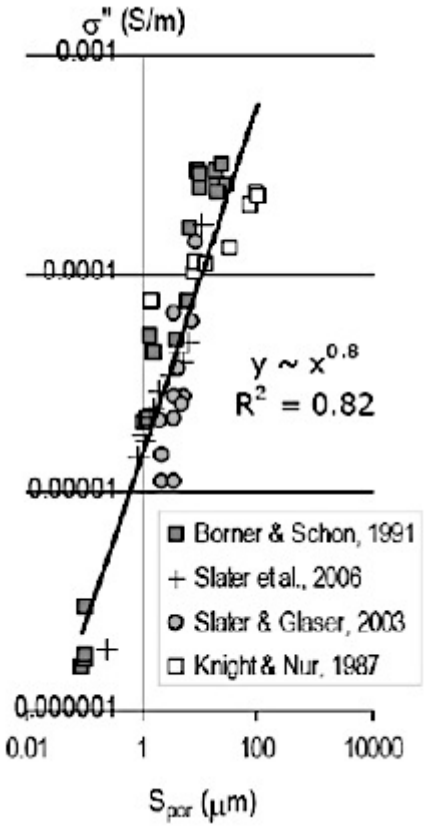

Figure 1. 16: Compilation of measurements of specific porous surface area Spor and imaginary electric component σ'' from different materials and studies, showing a consistent relationship (from Slater, 2006).

Permittivity models

There is no general theoretical relationship between permittivity and hydraulic conductivity. Since permittivity is strongly controlled by water content due to the large contrast between the permittivity of the water (80), the air (1) and minerals (aprox 5), the apparent permittivity data contain information about the water content variation or water-filled porosity. Secondary factors affecting the permittivity responses of rocks and soils include the effective shapes of the pores and grains, fine scale lamination, temperature and salinity of the saturated solution (Lesmes and Friedman, 2005). The Complex Refractive Index Model expressed as in CRIM equation (Wharton *et al.*, 1980), is one of the most widely used models to predict the porosity of water saturated materials from their measured permittivity:

$$\sqrt{k^*} = (1-\phi)\sqrt{k_s^*} + \phi\sqrt{k_w^*}$$

where k* denotes the dielectric constant as a complex number defined by the ratio of $k = \varepsilon/\varepsilon_0$, with ε_0 being the permittivity of a vacuum. The dielectric constants k_s, k_w, and k_a are the dielectric constants of the solid grains, pore water and air respectively. In saturated soils, permittivity ε *and* ε_s, depend on the porosity and effective pore/grain shapes, and therefore permittivity measurements can potentially be used to constrain parameters in a permeability prediction formula, that is calibrated by using laboratory measured pore/grain sizes. Introducing grain shape and porous space permittivity considerations in CRIM equation, more complex models MG (Maxwell-Garnett) and SS models (self-similar) have been developed. Lesmes and Friedman (2005) made and extensive review of permittivity models on both saturated and unsaturated media. In the later condition, Topp relationship (Topp, 1980) relates the permittivity and the volumetric water content as a three-phase model. Topp equation expresses the effective relative permittivity as a function of volume water content θ :

$$k_{eff} = 3.03 + 9.3 \cdot \theta + 146 \cdot \theta^2 - 76.6 \cdot \theta^3$$

Although Topp model gives, generally, the most reliable relationship (Lesmes and Friedman, 2005), Archie's law, Topp and CRIM equations all fail in the estimation of k in fine textured soils, where these latter equations under predict the water content.

Integration of geophysical and hydrogeological measurements

To perform the integration of geophysical measurements with hydrogeological measurements, the scale problem has to be considered, as well as the non-uniqueness and uncertainty of the geophysical models. Further a specific appropriate petrophysical relationship must be chosen. Thereafter, integration and estimation approaches can be applied that focus on defining the spatial distribution and the magnitude on the aquifer system. The first step is to obtain reliable geophysical models with which to translate geophysical properties into hydraulic parameters. The second step is the quantitative conversion of the geophysical property to hydrological properties that may be obtained 1) via direct mapping using a petrophysical relationship, the so called deterministic approach, or 2) by applying stochastic methods, such as geostatistics or Bayesian techniques (Deutsch and Journel, 1998; Gómez-Hernández, 2005; Rubin and Hubbart, 2005), the so called probabilistic approach.

The most general way to integrate a priori information and data for non-linear problems is to apply stochastic inversion methods where the resulting models parameters is given

by a probability distribution. The probabilistic weight of each element is considered in the iterative posterior inversions to improve the models. These geostatistical and simulating methods include Montecarlo simulation, neural networks, fuzzy logic, and Bayesan methods. Computational time and a priori distributions of model parameters are the main concerns. Hydrogeophysical research is increasingly turning to joint inversion strategies in which multiple geophysical datasets and/or geophysical-hydrological datasets, are processed simultaneously to produce more realistic estimates of the hydrologic parameters that satisfy all the available datasets, e.g., DC+GPR, DC+NMR, DC+AMT, GPR+Seismic (Bedrosian, 2006; Linde *et al.*, 2006; Gallardo and Meju, 2003). Thus joint inversion methods are configured either as a coupled inversion of geophysical and hydrological data or as a coupled inversion of multiple geophysical data. When two datasets are both sensitive to the same physical property, the simultaneous inversion is achieved by minimizing the misfit of both datasets (Linde, 2005). On the other hand, if the geophysical data sets are sensitive to different physical property final models will provide complementary information at the same location point. Joint inversion of hydrogeological and geophysical data is expected to improve the final hydrogeological final model. Hydrogeological data calibrates the hydrogeophysical variables based on the assumption that any relevant hydrogeological structure has a geophysical signature (Slater, 2006).

Geophysical methodology improvement

Over the last decade instrumentation has gone through a significant improvement in many aspects. Guérin (2005) has reviewed the novel instrument prototypes within the hydrogeophysical scientific community, and the case studies carried out with them, showing its potential. Remarkable effort has expended in the diversification of the measurable properties recorded from the subsurface that can provide independent complementary information at different time and scales. However, further advances in the geophysical technology are required to improve the sensors, sensitivity, depth resolution, and portability. Few remarks about geophysical improvement are listed below:

1) Development of multidimensional inversion and 3D acquisition devices to providevalid 3D models. Currently, 3D environments (except from a few cases of 3D DC or AMT measurements) are approached using 2D profiles or dense 1D spatial sampling that only provide partial information of the study area.

2) Better resolution at all depths. Geophysical methods usually results in and inverse relationship between depth of investigation and target resolution, which is high resolution at shallow depths and vice versa. Multiscale measurements will provide more detailed models at greater depths.
3) Advancements will provide very large datasets due to high-resolution sampling or due to more continuous data acquisition. Therefore inverse modelling processes need to improve in order to handle these large datasets with less computational time.
4) Cultural noise is one of the main geophysical concerns during data acquisition in urban areas, where most environmental hydrogeophysical problems are investigated. Much more research is needed to minimize coupling effects and noise limitations (Guérin, 2005; Post, 2005).
5) Geophysical instrumentation is usually composed of several components: transmitter, receiver, console, and batteries, which results most of time in large devices with significant total weight that are not easy to transport. Smaller and more portable equipment would contribute greatly to improve field procedures.

New communication capabilities such as satellite or mobile phone technology will provide data in real time from permanent arrays used to monitoring hydrodynamic processes. While some projects have had access to these technologies, is currently not economically viable for more modest projects.

CHAPTER 2

2.1 TRACERS TRANSPORT EXPERIMENTS: Estimating porous media transport parameters.

2.1.1 Introduction

Tracer tests, in hydrogeology, concern the fate and the way with which a certain quantity of matter or energy is carried by the groundwater flow. Their interpretation return information about the flow direction and/or the water velocity, and also how and where potential contaminants could be transported by the water. If enough information are collected, the study of the behavior of a tracer can also help with the determination of the hydraulic conductivity, porosity, dispersivity, chemical distribution coefficients, and other hydrogeologic parameters of the porous medium (Davis et al., 1980).

Examples of studies involving gas phase dispersion cases are the radon migration into buildings (Wang and Ward 2002), the remediation and movement of volatile contaminants for instance at contaminated soil sites (Arands et al. 1997; Gidda et al. 2006; Atteia and Hohener 2010), the sequestration of CO_2 in saline aquifers and the depletion of oil and gas reservoirs (White et al. 2003). Gas dispersion also plays an important role in the migration and emission of methane from landfills and wetlands (El-Fadel et al. 1997; De Visscher et al. 1999; Liang et al. 2000; Pangala et al. 2010; Pennock et al. 2010; Schaufler et al. 2010), and during composting of

organic material in aerated piles (Fukumoto et al. 2003; Thummes et al. 2007). Solute dispersion instead, is the most important mechanism in the propagation of dissolved contaminants, in both the vadose and the saturated zones of the soil, and its knowledge is crucial when estimating contaminant migration or selecting appropriate remediation strategies at a contaminated site (Gerke and van Genuchten 1996; Thomson et al. 1997; Domenico and Schwartz 1998; Silva and Grifoll 2009; Lewis and Sjostrom 2010).

Gas dispersion in porous media has been studied extensively since the late 1960s. Examples are Sinclair and Potter (1965), Evans and Kenney (1966), Edwards and Richards (1968), Suzuki and Smith (1972), Han et al. (1985), Coelho and Guedes de Carvalho (1988), Tan and Liou (1989), Popovicova and Brusseau (1997), Costanza- Robinson and Brusseau (2002), Poulsen et al. (2008), Sharma and Poulsen (2010) and Pugliese et al. (2012). Solute dispersion in porous media has been studied since about 1950. Examples are Bear (1961), Whitaker (1967), Greenkor and Kessler (1969), Rose (1973), Scheidegger (1974), Brenner (1980), Brusseau (1993). Delgado (2006) has published an excellent review of the existing knowledge about dispersion of gases and solutes in homogeneous porous media.

Both gas and solute dispersion generally increases with fluid phase velocity, distance travelled, porous medium particle size range, anisotropy ratio, and pore system tortuosity as confirmed by several earlier studies referred in Delgado (2006), but it is also in agreement with more recent studies such as Gidda et al. (2006), Bromly et al. (2007), Poulsen et al. (2008), and Sharma and Poulsen (2010). Pugliese et al. (2012) observed that the dispersion depends on particle shape. In general, it is agreed that gas and solute dispersion are controlled by the same parameters and that they are affected in a similar manner.

For an equal pressure gradient, gases travel faster than liquids through a given porous medium. It is therefore generally faster and easier to measure gas dispersion compared to solutes. Solute dispersion measurements, in coarse-grained materials such as sand, usually take 10-100 times longer than gas dispersion measurements performed under identical conditions. In finer materials, such as fine sand or silt, this difference will be even larger. As gas and solute dispersion in porous media are controlled by the same parameters they are likely related. This relation allows the estimation of the solute dispersion coefficients based on gas dispersion

measurements resulting in a considerable time saving. The main problem in establishing a relationship between gas and solute dispersion, is the difference in their flow patterns within a porous medium. This has been documented by Schjonning (1986), and Loll et al. (1999), who showed that the intrinsic gas permeability can be orders of magnitude larger than the liquid permeability, depending on porous medium characteristics.

However, no studies presenting corresponding measurements of gas and liquid dispersion coefficients, under identical conditions, have been published. Thus, the knowledge of the link between gas and solute dispersion is at present very limited. The goal of the experiments presented in this thesis is to evaluate the possibility of estimating solute transport and mass transfer parameters based only on the initial part of the breakthrough curves in combination with porous medium characteristics, such as particle shape and particle size distribution. The evaluation will be based on previously conducted breakthrough measurements (Pugliese, 2013b) in a set of porous media covering a wide range of particle shapes and particle size distributions.

2.1.2 Theory

Transport of conservative solutes in porous and fractured media is often described, at the continuum scale, by the advection dispersion equation (ADE). In case of one-dimensional flow through a column containing a homogeneous porous medium, under assumption of uniform flow and dispersion, and in presence of both a mobile and an immobile solute phase, the ADE is expressed as:

$$\frac{\partial C_m}{\partial t} = D\frac{\partial^2 C_m}{\partial x^2} + u\frac{\partial C_m}{\partial x} + k(C_{im} - C_m) \qquad [1]$$

where C_m and C_{im} are the tracer concentrations in the mobile and immobile solute phases (M L^{-3}), respectively, u is the pore velocity (interstitial velocity) in the mobile solute phase (L T^{-1}), k is the tracer mass transfer coefficient (T^{-1}) for mass transfer between the mobile and immobile solute phases, and x and t are the space (L) and time (T) variables (Pugliese et al., 2012). D is the overall dispersion-diffusion coefficient (L^2 T^{-1}), given as:

$$D = D_{mol} + D_{mech} \qquad [2]$$

where D_{mol} is the molecular diffusion coefficient ($L^2\ T^{-1}$), D_{mech} is the contribution by mechanical dispersion ($L^2\ T^{-1}$). For one-dimensional flow, D_{mech} is generally expressed as:

$$D_{mech} = u\alpha \qquad [3]$$

where α is the tracer mechanical dispersivity in the mobile phase (L). At very low flow velocities flow dispersion is negligible and the linear relation (Eq. (3)) does not hold (Delgado 2006).

Single phase modeling

When treating a porous medium by means of a single phase model, despite the presence of both a mobile and an immobile fluid phase, no mass transfer between the two phases is considered. This means that the media is seen as a large and unique region characterized by a single value of (active) porosity.

If it is assumed that there is local equilibrium between the tracer concentrations in the mobile and immobile (i.e. $C_m = C_{im}$) regions, the porosity in Eq. (1) represents the total porosity, otherwise, if it is assumed null the concentration in the immobile region (i.e. $C_{im} = 0$), the porosity in the Eq. (1) equals the kinematic porosity. However, the ADE in both cases is given as:

$$\frac{\partial C_m}{\partial t} = D\frac{\partial^2 C_m}{\partial x^2} - u\frac{\partial C_m}{\partial x} \qquad [4]$$

Dual phase modeling

When treating a porous medium by means of a dual phase model, the medium pore space is considered as a dual region system. Therefore, two values of porosity are considered (one for the mobile and one for the immobile region). In this case solute transport in the mobile region is described by Eq. (1), while tracer concentration in the immobile region is described as:

$$\frac{\partial C_{im}}{\partial t} = \frac{\varepsilon_m}{\varepsilon_{im}} k(C_{im} - C_m) \qquad [5]$$

where ε_m and ε_{im} are the mobile and immobile solute-filled porosities ($L^3\ L^{-3}$) in the porous medium, respectively. These are mutually linked by the following relation:

$$\varepsilon_{im} = \varepsilon_{tot} - \varepsilon_m \qquad [6]$$

2.1.3 Description of the experiment

The Dispersion coefficients were measured in three different media: (1) granite pebbles, (2) gravel and (3) Leca®. The granite pebbles are characterized by an irregular and very angular particle shape, gravel consists of somewhat rounded rock fragments and Leca® consists of rounded particles. Granite and gravel does not have any internal porosity (single porosity material), while Leca® consists of highly porous particles (double porosity material) although this internal porosity is inaccessible by air as it consists of closed vesicles very similar to those produced by soap foam. All three materials were initially sieved into six particle size fractions with uniform particle size distributions. Each of these fractions was characterized by a particle size range (R) of 2 mm, in the range between 2 and 14 mm. Particle diameters (D) were $2 \leq D < 4$, $4 \leq D < 6$, $6 \leq D < 8$, $8 \leq D < 10$, $10 \leq D < 12$, and $12 \leq D < 14$ mm corresponding to mean particle diameters (D_m) of 3, 5, 7, 9, 11, and 13 mm respectively. Additional fractions with $R = 4$ mm ($D_m = 4, 6, 8, 10, 12$ mm), $R = 6$ mm ($D_m = 5, 7, 9, 11$ mm), $R = 8$ mm ($D_m = 6, 8, 10$), $R = 10$ mm ($D_m = 7, 9$), and $R = 12$ mm ($D_m = 8$), with uniform particle distributions, were produced by combining appropriate quantities of the six $R = 2$ mm fractions. Uniform particle size distributions were chosen to ensure well-defined distributions across all the used fractions. A total of 63 particle size fractions were produced (21 fractions for each material)and packed into 100 cm long and 14 cm inner diameter acrylic columns, taking care to reduce variations and differences in the packing density of each column. A stainless steel mesh with 2-mm openings and 1-mm thickness was installed at both ends of the columns, to support and prevent movements of the porous media. Polyethylene lids, sealed using rubber O-rings, were used at both ends. Soft Teflon tubings with an inner diameter of 4 mm were used to connect each component of the system.

Different sets of flow rates were applied for both gas and solute dispersion experiments, in order to obtain comparable results for each fluid covering the same range of Reynolds numbers ($\mathrm{Re} = \rho V d/\mu$) ($0.004 \leq \mathrm{Re} \leq 2.13$).

Gas dispersion measurements were carried out for granite following the approach of Poulsen et al. (2008). The inlet (at the bottom) section of each column was connected to an air/nitrogen supply via a three-way valve and a precision ball flow

meter (model F150, Porter Instruments, Inc., Hatfield, PA) to control gas flow rate. The outlet lid was equipped with an oxygen sensor (KE-12 galvanic oxygen electrode, GS Yuasa Power Supply Ltd., Japan) with a 5 s response time for the determination of effluent oxygen concentrations. Readings from the oxygen sensor (sampling every 5 s) were recorded by a data logger (CR-1000, Campbell Scientific, Logan, UT). Atmospheric air and nitrogen were used as tracer gases. A scheme of the experimental setup is shown in Figure 2.1 (a), while details are given in Poulsen et al. (2008).

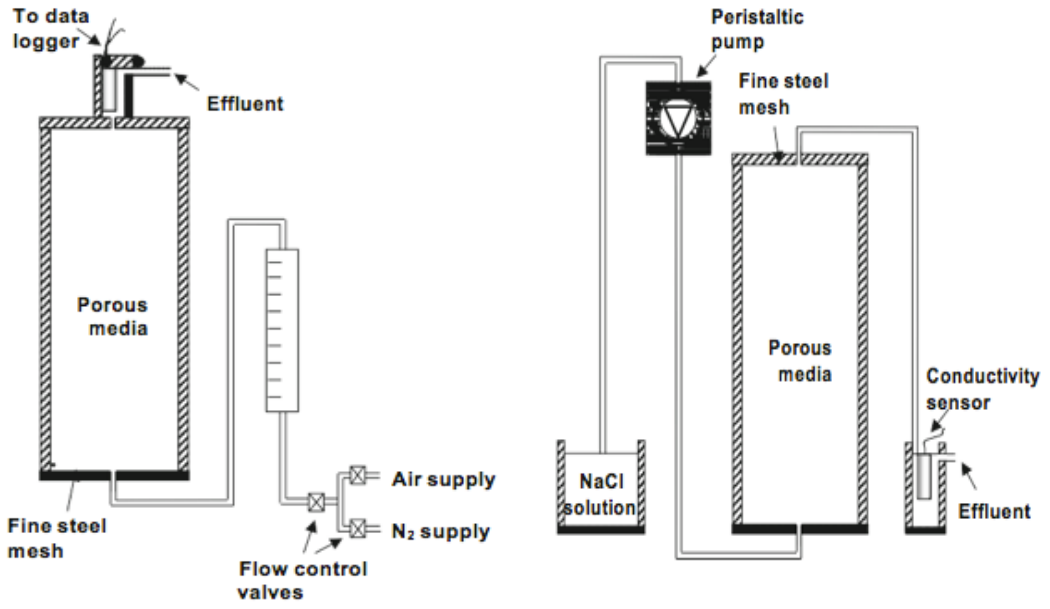

Figure 2. 1: Experimental setup for a gas dispersion and b solute dispersion measurements

Columns were initially saturated with atmospheric air (78 % N2 and 21 % O2), and the flow adjusted to the desired values. Once the effluent O2 concentration was stable, the inlet gas was switched to N2. Care was taken to make sure that gas flow remained constant during the switch. A constant flow of N2 was maintained until the effluent O2 concentration reached zero. After that, the gas supply was switched back to atmospheric air and the flow maintained until a stable O2 concentration was once again observed. Oxygen and nitrogen breakthrough curves were measured in duplicate for granite, at gas flow rates of 0.2, 0.5, 1.0, 1.5, 2.0, and 2.3 L/min. Gas dispersion data for gravel and Leca® measured using an identical procedure, were taken from a previous study (Sharma and Poulsen 2010). All experiments were carried out twice. For the solute dispersion measurements, the inlet (at the bottom) of the column was connected to a

peristaltic pump (model PD 5101, Heidolf). The outlet was connected to a measuring tube holding 12 mL of liquid, equipped with a TETRACON 325 conductivity-meter. A scheme of the experimental setup is shown in Figure 2.1 (b).

The column was initially saturated with demineralized water, after which NaCl solution of 5 g L^{-1} was injected continuously at a specific flow rate. Effluent NaCl concentration was measured every 10 s. Experiments were carried out for all three materials with the following flowrates 0.015, 0.05, 0.075, 0.1, 0.125, 0.15 L/min, and terminated when inlet and outlet NaCl concentrations were identical. Measurements were conducted for all three porous materials, but only nine of the 21 particle size fractions ,resulted in a solute dispersion measurement longer than the gas ones (about 12 times longer).

For the single phase model, measured BTC's were fitted using Eq. (4), by optimizing D and ε_{tot} (i.e. assumption of local equilibrium between the trace concentrations in the mobile and immobile regions). Only the first part of the breakthrough curves (BTC's) ($C/C_0 \leq 0.6$) was analyzed because D influences only the steepness and not the tailing of the BTC's. The curve fitting was carried out using an analytical solution of the ADE, solved inside an inverse procedure based on the Non Linear Least Square Method. The procedure has been implemented through the Matlab® code

For the dual phase model, measured BTC's were fitted using Eq. (1) and Eq. (5), by optimizing values of k and ε_m. D and ε_{tot} values were in this case taken from the single porosity model and used as known values. The dual porosity model was built in the COMSOL Multiphysics® environment and inverted using the full BTC measurements (including the tails).

For both the single and dual phase models, the corresponding initial and boundary conditions were:

Initial condition	$t = 0, x \geq 0$	$C = 0$	[7a]
Boundary condition	$t > 0, x = 0$	$C = C_0$	[7b]

where C_0 is the concentration of the tracer (NaCl).

Optimal fitted values presented were all determined by minimizing the sum of the squared errors (SSE) between calculated and fitted/predicted values (by the numerical model) as:

$$SSE = \sum \left[P_{Calculated} - P_{fitted} \right]^2 \quad [8]$$

where, $P_{calculated}$ and $P_{fitted/predicted}$ are the calculated and fitted (by the model) or predicted (by the partial analysis) transport parameters, respectively.

2.1.4 Results

Measured BTC's at a solute flow rate of 0.125 l/min, for the 2-14 mm particle size fraction, for all three materials, are shown in Figures 2.2, 2.3 and 2.4, together with the best-fit curves for the single phase model (Eq. (4)) and the dual phase model (Eq. (1) and (5)).

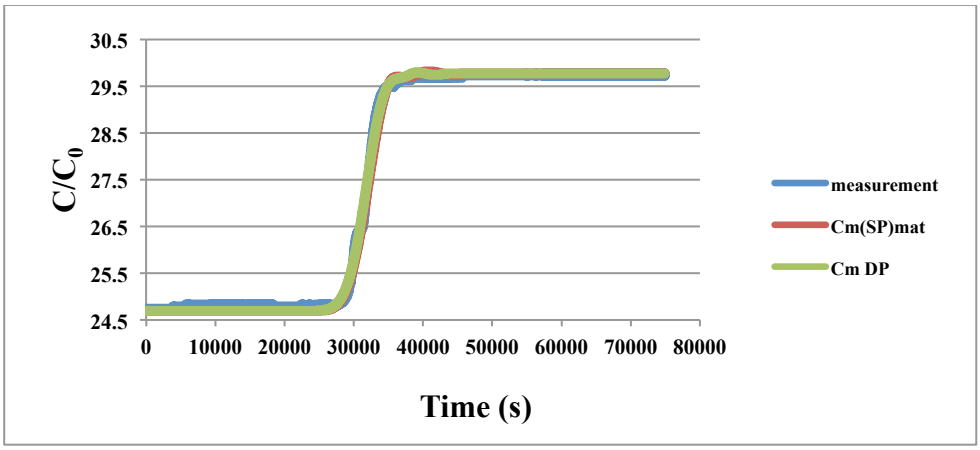

Figure 2. 2: Best-fit curves for the single and the dual phase model (Granite)

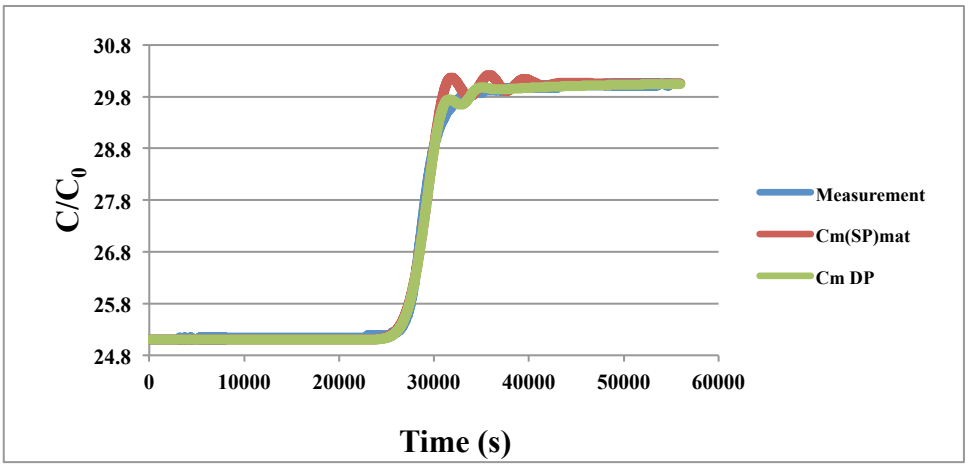

Figure 2. 3: Best-fit curves for the single and the dual phase model (Gravel)

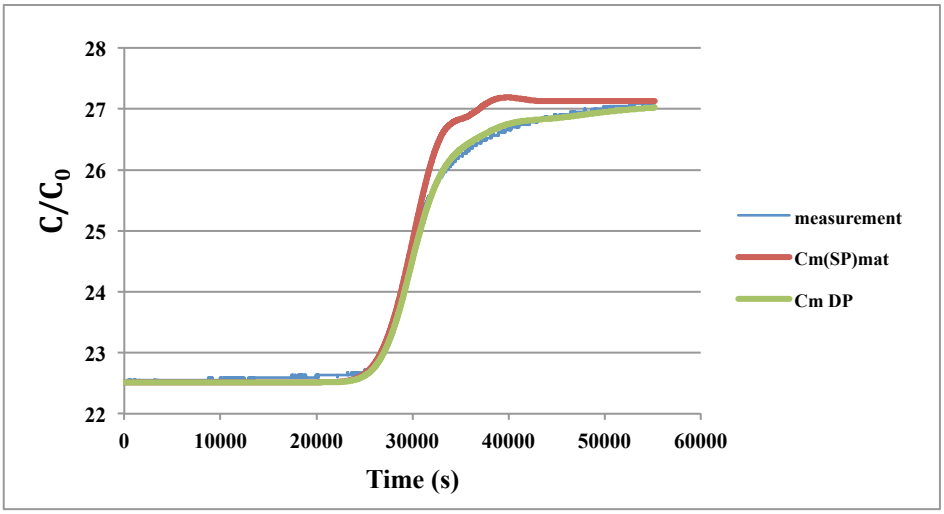

Figure 2. 4: Best-fit curves for the single and the dual phase model (Leca®)

All the three data sets exhibit the typical sigmoid shape characterizing this type of process. In all three cases some tailing is evident, with granite showing the least and Leca® the most amount of tailing.

This was also the case for the remaining 321 BTC's. The relatively poor tailing phenomenon exhibited by the granite data represents a reduced solute exchange between the mobile and immobile phases indicating a quasi-equilibrium condition between the two phases. On the other hand, gravel and Leca® exhibit an important tailing occurrence, resulting in a larger immobile water content. The estimation procedure provided the values of the effective porosity (n_c), dispersivity (α) and tortuosity (λ), including the values of the linear regression coefficient for the single and the dual phase model (Table 2.1):

Size range (mm)	*Single Phace Model*			*Double Phace Model*		
	n_c	*α (m)*	R^2	*n*	*λ*	R^2
2_4	*5.13E-01*	*1.64E-03*	*9.99E-01*	*5.21E-01*	*5.00E-04*	*9.99E-01*
2_8	*4.58E-01*	*1.86E-03*	*9.99E-01*	*4.64E-01*	*4.65E-05*	*9.99E-01*
2_14	*4.25E-01*	*2.04E-03*	*9.99E-01*	*4.33E-01*	*3.27E-05*	*9.99E-01*
4_12	*4.39E-01*	*1.78E-03*	*9.98E-01*	*4.42E-01*	*-8.26E-05*	*9.99E-01*
6_8	*4.82E-01*	*1.76E-03*	*9.98E-01*	*4.99E-01*	*4.27E-05*	*9.57E-01*

6_10	*4.61E-01*	*1.49E-03*	*9.98E-01*	*4.65E-01*	*8.72E-05*	*9.99E-01*
8_10	*4.78E-01*	*1.41E-03*	*9.97E-01*	*4.33E-01*	*1.54E-04*	*8.32E-01*
8_14	*4.99E-01*	*1.30E-03*	*9.96E-01*	*5.00E-01*	*1.22E-04*	*9.97E-01*
12_14	*5.01E-01*	*1.30E-03*	*9.95E-01*	*4.59E-01*	*4.26E-02*	*9.96E-01*

Table 2. 1: Values of effective porosity (n_c), dispersivity (α), tortuosity (λ) and linear regression coefficient for the single phase model (SP) and the double phase model (DP)

The results of this approach have been compared with the values of total porosity and dispersivity of the materials described by Pugliese et al. 2013a and Pugliese et al. 2013b. Table 2.2

Size range	***Granite***		***Gravel***		***Leca®***	
(mm)	***n***	***α (cm)***	***n***	***α (cm)***	***n***	***α (cm)***
2_4	*0.45*	*0.296*	*0.42*	*0.64*	*0.88*	*0.71*
2_8	*0.44*	*0.398*	*0.41*	*0.54*	*0.89*	*0.79*
2_14	*0.44*	*0.669*	*0.39*	*0.791*	*0.9*	*1.03*
4_12	*0.45*	*0.39*	*0.41*	*0.473*	*0.9*	*0.96*
6_8	*0.45*	*0.326*	*0.42*	*0.56*	*0.91*	*0.74*
6_10	*0.44*	*0.371*	*0.42*	*0.6*	*0.91*	*0.77*
8_10	*0.46*	*0.32*	*0.41*	*0.27*	*0.91*	*0.73*
8_14	*0.46*	*0.249*	*0.41*	*0.361*	*0.91*	*0.8*
12_14	*0.47*	*0.186*	*0.41*	*0.276*	*0.91*	*0.61*

Table 2. 2: Values of Total porosity (n) and dispersivity (α) for Granite, Gravel and Leca Pugliese et al. 2013a and Pugliese et al. 2013b.

Also, a graphical comparison between the dispersivities (α), estimated in this thesis and in Pugliese works is presented below.

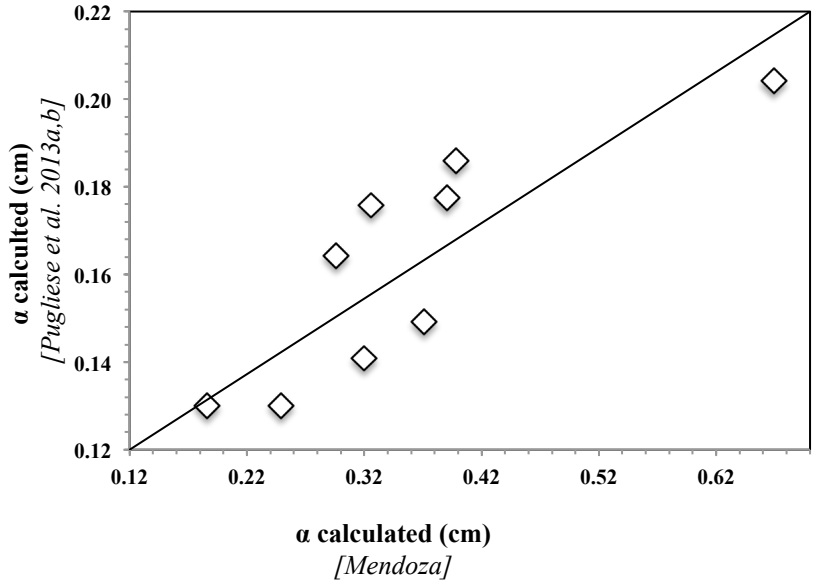

Figure 2. 5: α calculated (cm) [Pugliese et al., 2013a,b] vs α calculated (cm) [Mendoza] for the Granite

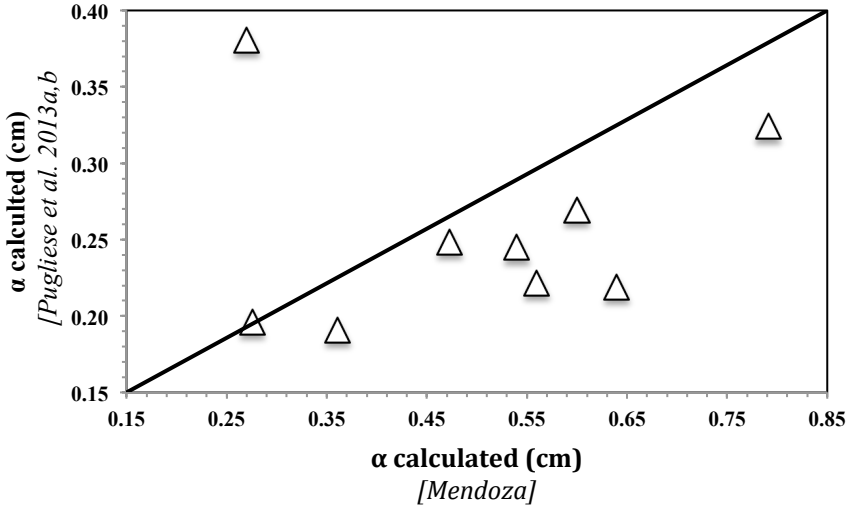

Figure 2. 6: α calculated (cm) [Pugliese et al., 2013a,b] vs α calculated (cm) [Mendoza] for the Gravel

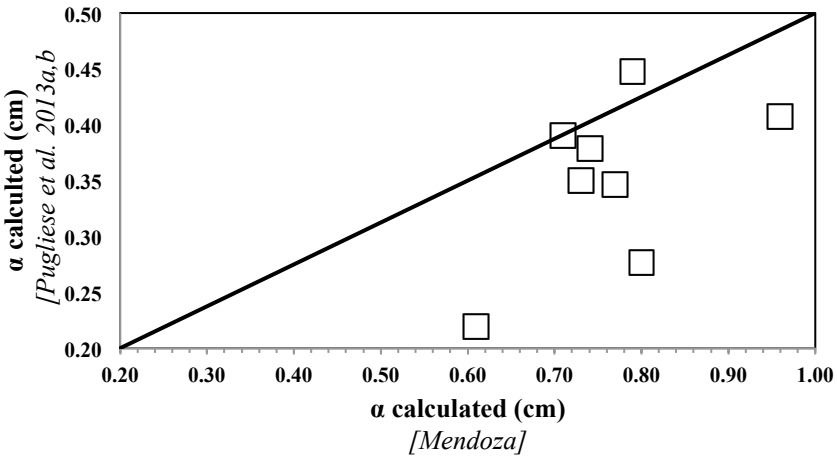

Figure 2. 7: α calculated (cm) [Pugliese et al., 2013a,b] vs α calculated (cm) [Mendoza] for the Leca®

2.1.5 CONCLUSIONS

The solute transport in three different granular media (granite pebbles, gravel and Leca®), exhibiting similar particle sizes but different particle shapes, was analyzed in this study. Solute transport data, using chloride as a tracer, for 27 particle size fractions (9 for each material), at 6 different pore flow velocities (corresponding to a total of 324 breakthrough curves (BTC's)), were acquired during the analysis.

The measured BTC's were fitted to both single porosity and dual porosity models. Results of the fitting confirm that both models can be accurately fitted to the initial part of the breakthrough curves. However, as expected, significant deviations between measured and fitted values occur for the single porosity model when fitting the tail end of the BTC's, while the dual porosity model is able to achieve accurate fits for the entire curve. This suggests the presence of non-equilibrium solute mass transfer between a mobile and an immobile phase, as also often seen in previous studies. Among the three materials, BTC's for Leca® (having the most rounded particles) exhibit the largest amount of tailing while granite (having the least rounded particles) exhibit the smallest amount of tailing suggesting that particle shape has a significant impact on mass transfer.

Values of dispersion coefficient D were determined by fitting the single porosity model to the initial part of the BTC's. The D-values were then used in the dual porosity model together with the entire BTC's to estimate values of mass transfer coefficient k and mobile porosity (εm). Leca® showed the highest k-values (a consequence of the higher amount of tailing in the BTC's), while granite showed the lowest, values. This indicate that the more spherical the particles, the greater the mass transfer between the mobile and immobile phases. Round particles in fact expedite the exchange between mobile and immobile phases, while particles with more angular shapes (mainly granite) hinder it. The results further indicated that the slope, th more angular shapes (mainly granite) hinder rsivity), the slope, further indicated that the slope, th more angular shapes (mainly granite) hinder rsivity) particle size fractions), could be predicted from particle size distribution characteristics and particle shape using a simple linear expression. This means that dual porosity model parameters (k and ε_m) may be estimated using only the initial part of the BTC's, in combination with porous medium characteristics, which in

turn mean that significant time can be saved as the time consuming measurements of the tail end of the curves can be excluded. As the quantity of data used in the analyses presented here are somewhat limited, however, additional measurements on other media, having different particle size distributions and particle shapes are needed to verify and improve the relationships presented in this study.

2.2 HYDROGEOPHYSICAL EXPERIMENTS: Study of Hydrocarbon Saturation with GPR and Chemical Methods.

2.2.1 Introduction

LNAPLs are widely used in the industrial production, they are responsible of the contamination of soil and groundwater. Their location and behavior in the groundwater systems have been studied through invasive methods which are expensive and high impact makers for the environment. The aim of this work is to integrate a noninvasive hydrogeophysical method as the Ground Penetrating Radar (GPR) with chemical analysis (Infrared Spectrophotometry – IR) to localize contaminant distribution and quantify Total Petroleum Hydrocarbons (TPH) concentrations.

2.2.2 Theory

Hydraulic theoretical background

The two-phase flow numerical model, establishes the governing equations and constitutive relationships that define fluid retention and permeability in the natural media. The governing equations for two-phase flow in porous media, follow separate mass conservation equations for the wetting and non-wetting fluids. Water is considered to be the wetting fluid since it promotes the contact with the solid matrix (i.e. mineral grains making up the aquifer). LNAPL is the non-wetting fluid, which means it has a lower tendency to interact with the solid matrix with respect to water (Charbeneau, 2000). The governing equations for the multiphase flow, are coupled nonlinear partial differential equations (PDEs). Constitutive relationships are also integrated into the PDEs to account for fluid retention and aquifer permeability. The following equations are based on Mualem (1976) and Van Genuchten (1980). The mass conservation equations for the wetting (w) and non-wetting (nw) fluids, assuming two incompressible fluids, are:

$$\theta_s \frac{\partial S_{e,w}}{\partial t} + \nabla \cdot \left(-\frac{K_0 K_{r,w}}{\eta_w} \nabla (p_w + \rho_w g z) \right) = 0 \qquad [1]$$

$$\theta_s \frac{\partial S_{e,nw}}{\partial t} + \nabla \cdot \left(- \frac{K_0 K_{r,nw}}{\eta_{nw}} \nabla (p_{nw} + \rho_{nw} g z) \right) = 0 \qquad [2]$$

where θ_s is the porosity of the porous medium, S_e is the saturation degree of wetting and non-wetting phase, K_0 is the intrinsic permeability of porous medium [L^2], K_r is the relative hydraulic conductivity of wetting and non-wetting phase [LT^{-1}], η is the dynamic viscosity of wetting and non-wetting phase [$ML^{-1}T^{-1}$], p is the hydraulic pressure of wetting and non-wetting phase [$ML^{-1}T^{2}$], ρ is the density of wetting and non-wetting phase [ML^{-3}], g is the gravity acceleration [LT^{-2}], and finally z is the depth [L]. Equations (1) and (2) are subject to the constraint:

$$S_{e,w} + S_{e,nw} = 1 \qquad [3]$$

This constraint assumes that the void space of the porous media is completely filled by water and/or LNAPL. The saturation of either fluid phase can range from 0 to 1. Capillary pressure (*pc*) is the pressure difference between the non-wetting and wetting phase interfaces and is mathematically defined as:

$$p_c = p_{nw} - p_w \qquad [4]$$

Capillary pressure results from the density difference between two fluids and is a function of the fluid phase saturations. Effective saturation changes with capillary pressure. This relationship is quantified as:

$$C_{p,w} = -C_{p,nw} = \theta_s \frac{\partial S_{e,w}}{\partial p_c} \qquad [5]$$

where C_p is the specific capacity of the wetting and non-wetting phases at a given pressure. In order to simplify the model, Equations (3), (4) and (5) are substituted in Equations (1) and (2), so that the governing equations become:

$$C_{p,w} \frac{\partial}{\partial t} (p_{nw} - p_w) + \nabla \cdot \left[- \frac{k_0 k_{r,w}}{\eta_w} \nabla (p_w + \rho_w g z) \right] = 0 \qquad [6]$$

$$C_{p,w} \frac{\partial}{\partial t} (p_w - p_{nw}) + \nabla \cdot \left[- \frac{k_0 k_{r,nw}}{\eta_{nw}} \nabla (p_{nw} + \rho_{nw} g z) \right] = 0 \qquad [7]$$

GPR theoretical background

Ground Penetrating Radar (GPR) is an electromagnetic technique designed primarily to investigate the shallow subsurface of the earth, building structures, roads, and bridges. GPR utilizes the transmission and reflection of high frequency

electromagnetic (EM) waves in the range between 10MHz to 2GHz. The propagation of the radar signal depends on the frequency-dependent electrical properties of the ground. When the radiated energy encounters an inhomogeneity in the electrical and magnetic properties of the subsurface, part of the incident energy is reflected back to the radar antenna and part is transmitted through the inhomogeneity (Daniels, 2004).

The GPR data are presented as a two or three dimensional depth profile along a single or more scanned traverse line in which the vertical axis corresponds to the two-way travel-time measured in nanoseconds. If the propagation velocity of the electromagnetic waves is known, the depth of the reflector (d) can be determined from:

$$d = \frac{vt_v}{2} \qquad [8]$$

where t_v is the two-way travel time, and v is the EM velocity through the subsurface material. The EM wave velocity of propagation in a medium is equal to:

$$v = \frac{c}{\sqrt{k}} \qquad [9]$$

where c is the light velocity in free space (0,3 m/ns) and k is the relative dielectric permittivity which is a measure of the capacity of a material to store a charge when an electric field is applied to it relative to the same capacity in a vacuum (Sheriff, 1984).

The GPR is one of the techniques that has seen increasing use in the investigation of both unsaturated and saturated hydrogeology. Greaves et al. (1996) used GPR interval velocities gathered from surface common midpoint (CMP) surveys, and coupled their results with Topp's equation (Topp et al., 1980) to estimate moisture content in saturated sediments. Due to the success achieved in the field of hydrogeology, in recent years GPR was used effectively for the study of large areas to search of anomalies into the electromagnetic behavior attributable to the presence of pollutants. GPR is able to detect the level of pollution in vadose zone and to identify the plume in groundwater (Atekwana et al., 1998; Godio et al. 1998). Furthermore, several researches were conducted aimed at identifying mainly the correlation between soils electromagnetic properties and water and hydrocarbons content. Laboratory experiments have allowed to verify the complex interaction

between electromagnetic properties, conductivity and dielectric permittivity (Santamarina et al., 1997). Most of the studies were controlled injections of contaminants in which GPR surveys were performed before, during and following the injections. In addition to controlled injections of LNAPLs there have been several GPR studies of accidental spill sites (Bermejo et al., 1997; Sauck et al., 1998).

In presence of contaminants in the subsurface, it is possible to record changes in the electrical behavior of contaminated rocks and soils. However, for a good understanding of the pollution phenomenon the use of GPR in the analysis and monitoring of contaminants in the environment cannot be separated from knowledge of the chemical and physical dispersed contaminants. Even though, GPR is able to provide relatively high spatial resolution, on the other hand its penetration depth will in many cases be insufficient because of attenuation related to clays or high pore water conductivity.

The physical properties of the most common contaminants have been tabulated in a rigorous manner by Lucius (1992). From the study of these tables has been possible to obtain reference parameters for the characterization of LNAPL used in laboratory. The electrical properties are defined in terms of dielectric permittivity, magnetic permeability, and electrical conductivity. The attenuation of the signal generated by the EM antennas is particularly affected by both the dielectric permittivity and electrical conductivity. For this reason, the estimation of these parameters is very important for the understanding of the investigated problem.

Dielectric permittivity for the GPR frequencies is determined by the physical properties of the materials of the medium, which usually consists of a matrix of air, water, minerals and NAPL. The mechanism that most influences GPR measurement is characterized by displacement of the water (k=80) naturally contained in the matrix when is replaced by NAPL characterized by permittivity values much lower (k= 2-10). In general, when NAPL replaces water in the pore space of rock or soil, the relative dielectric permittivity of the media decreases, thereby increasing the wave velocity. The electrical properties of rock and soil, containing mixtures of air, water and NAPL have been estimated using volumetric mixing laws such as the complex refractive index model (CRIM) (Birchak et al., 1974) and effective media theory (Sen et al., 1981). The accuracy of quantitative estimates of the LNAPL content affected significantly the

specific distribution of the voids and the volume fraction of variable liquid and gaseous substances present in the medium. Overcoming this difficulty is probably the most important challenges in the field of environmental research conducted in geophysics.

Chemical background

The Spectrophotometry InfraRed (IR) methodology is used to investigate the composition of a sample or to identify a compound. This method analyzes the electromagnetic spectrum, i.e. the absorbed infrared spectrum of a material within a whole frequency range of the spectrum. Because each chemical element has its own absorption band or wavelength associated with the energy differences of its different atomic orbitals, knowing the absorbed infrared spectrum it is possible to measure the sample composition. For the TPHs, this method measures the absorption caused by changes in vibration-rotation of the C-H bonds of hydrocarbons. In particular, in our experiment we used the 8440 U.S. EPA (1996) method in a wavelength range of 3200 – 2700 cm^{-1} and with detection limit of 10 to 600 mg kg^{-1} of TPH.

The quantification is obtained by comparing the sample absorption against a calibration curve made with a reference oil, and in case of more concentrated extracts it is advisable to make the necessary dilutions to obtain measurements of absorbance between 0.1 and 0.8. (Fernández et al., 2006). The TPHs signal in IR method is represented by three characteristic peaks at 2956, 2926 and 2855 cm^{-1}; however, in this study to calculate the TPHs concentration we only consider the peak at 2956 cm^{-1}. The TPH values are calculated from the extrapolation of the absorbance value obtained for samples within the calibration curve. Values are expressed in mg L^{-1} and converted to mg kg^{-1} of dry soil (DS), considering the amount of soil removed, the amount of solvent that was used to make a solution, and the amount of sample taken from this solution, as follows:

$$TPHs = \frac{(Abs - b)}{m} \qquad [10]$$

where *TPHs* is the Total Petroleum Hydrocarbons (mg L^{-1}), *Abs* is the absorbance of the sample 2956 cm^{-1}, *b* is the intercept of the calibration curve and m the calibration curve slope. This value can be expressed in mg $kgDS^{-1}$ by:

$$TPHs\left(\frac{mg}{kg_{DS}}\right) = \left[\frac{TPHs\left(\frac{mg}{L}\right)*VT}{FC_1}\right] * \left[\frac{VD}{VE}\right] * \left[\frac{FC_2}{P}\right] \qquad [11]$$

where VD is the total volume of solution (dichloromethane), VE is the volume taken from VD and began to evaporation, VT is the volume of tetrachlorethylene where the sample was dissolved or evaporated, FC_1 is the correction factor for the TPH (mg) in VT equal to 1000, P is the weight (g of dry soil extracted equal to PH*FH), FC_2 is the correction factor to obtain mg of TPH in kg of dry solid, PH is the amount of moisture soil extracted and, finally, FH the correction factor of humidity equal to:

$$FH = 1 - \frac{humidity\ (\%)}{100} \qquad [12]$$

In this sense, the TPH quantitative analysis with infrared spectroscopy is a relatively fast method for determining the approximate LNAPL amount in the soil, in fact the main advantage of the technique is the simplicity, speed and low cost. However, especially for heterogeneous samples it shows limited accuracy and precision and it does not give information concerning the type of hydrocarbons exist in the sample or the presence or absence of toxic molecules (Weisman, 1998).

2.2.3 Experiments set-up

The experiments were performed at the hydrogeophysical Laboratory of University of Calabria (Cosenza, CS, Italy) in collaboration with the Hydrogeosite Laboratory of the CNR-IMAA (Consiglio Nazionale delle Ricerche – Istituto di Metodologia per l'Analisi Ambientale), in Marsico Nuovo (Basilicata Region, Southern Italy). The model is a 2D sandbox made of plexiglass with the following dimensions: 100×60×10 cm^3 (Figure 2.8).

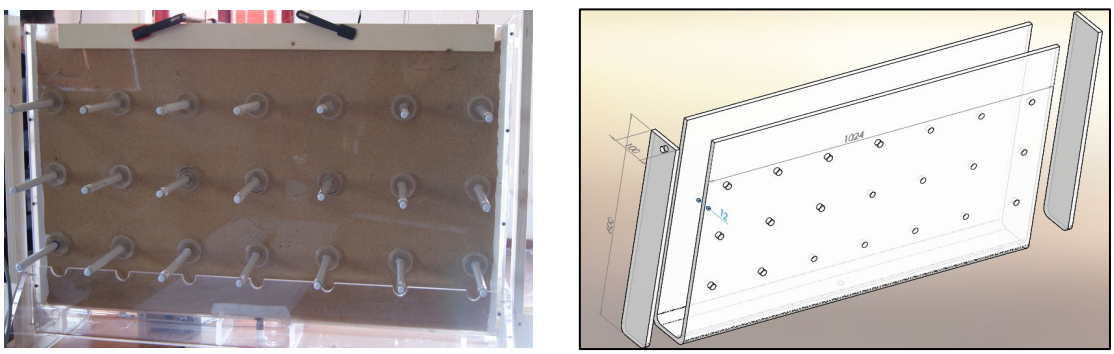

Figure 2. 8: 2D Sandbox in plexiglass

Twenty-one holes with a diameter of 16 mm were realized in one of the vertical walls of the Sand-Box. The holes were ordered in three different levels; the first level is located at 15 cm, the second at 30 cm and the third at 45 cm from the bottom. Each hole is equipped with a sampler (Figure 2.9).

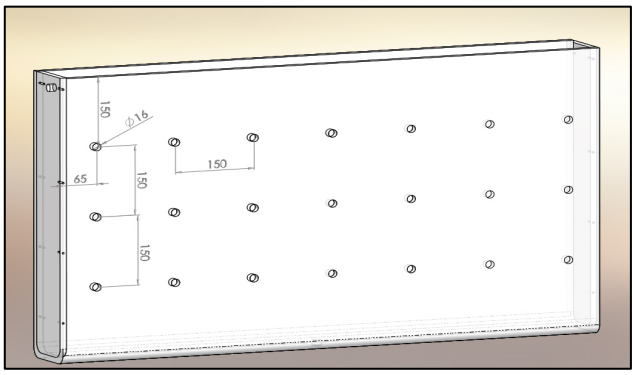

Figure 2. 9: Front side of the 2D Sandbox whit twenty-one extraction holes of 16 mm

The Sandbox was filled by a natural silicic sand rich of quartz, with grain size ranged from 0.15 to 1.2 mm and a characteristic diameter (d_{30}) equal to 0.3 mm. The non-compacted sand had a total porosity of about 0.37 as determined by the water saturation method. A hydraulic conductivity of $4.51 \pm 0.23\ 10^{-4}$ m/s has been obtained by means of constant head permeameter tests.

In order to avoid the entrapment of air bubbles, the sand was saturated with tap water, through a hydraulic loading system, from the bottom up to a level of around 55 cm. (Figure 2.10).

Figure 2. 10: Hydraulic loading system: (a) collection tank; (b) loading tank.

Successively 2000 ml of diesel was injected from the bottom by means of a peristaltic pump (Figure 2.11).

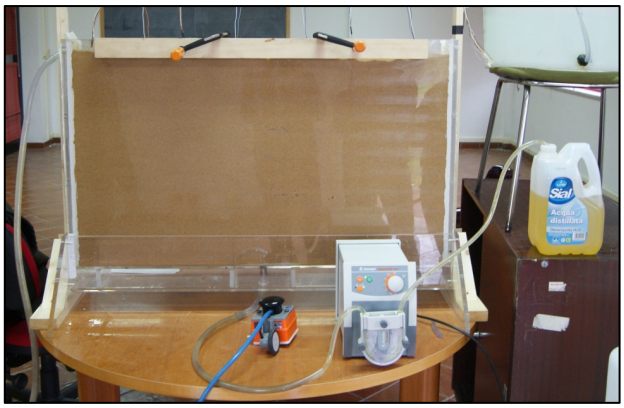

Figure 2. 11: Hydrocarbon injection by means of a peristaltic pump

During the experiment, GPR measurements on the backside of the sandbox were performed. Data were acquired in reflection mode and in continuous by means of the GPR SIR-3000 (GSSI-Instrumentation) equipped by an antenna with an incorporated survey-wheel. Due to the limited size of the box, the experiments were performed by a high resolution antenna with a central frequency of 2Ghz (Figure 2.12).

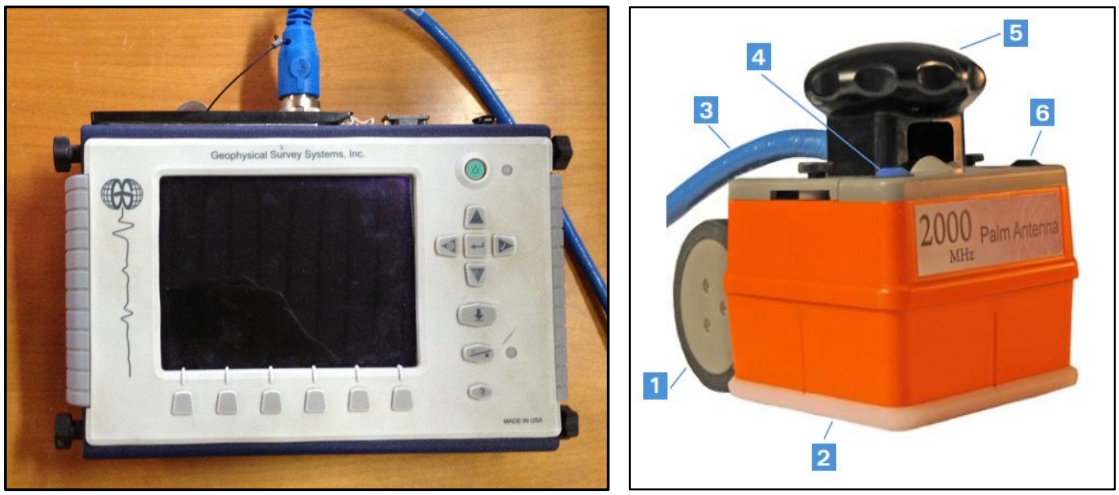

a) **b)**

Figure 2. 12: a) SIR 3000 GPR used for data acquisition. b) Antenna GPR, 2000Hz. 1-wheel equipped with recorder; Mini 2-replaceable plate; 3-Fiber optic cable; 4- Deadman switch (safety switch); 5-removable knob; 6-Marker to switch.

The used antenna has a survey wheel system, which gives the position of each recorded data. The data were acquired along parallel and perpendicular profiles spaced 5 cm from each other (Figure 2.13).

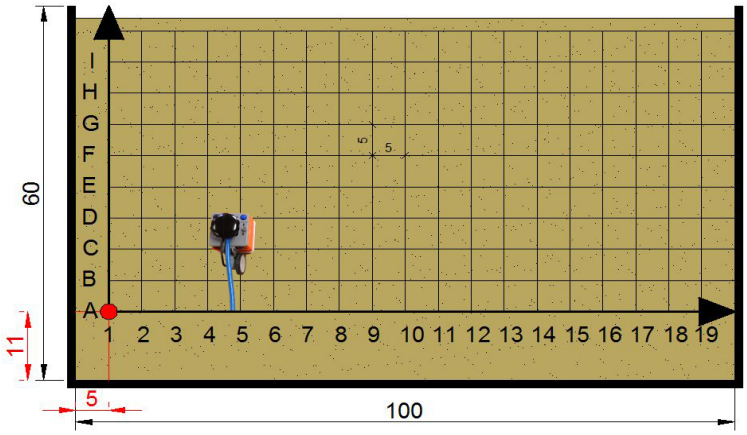

Figure 2. 13: Grid of acquisition located behind the Sandbox.

GPR measurements were carried out in saturated conditions before and after the injection, in order to have some reference data during the unpolluted state. The post-processing data allowed to obtain the best signal/noise ratio and to estimate the distribution of the permittivity values by EM velocity analysis. The permittivity distribution maps allowed to highlight clearly the contaminated area during the hydrocarbon transfer from the bottom to the top. The dielectric constant of a porous material is highly sensitive to its volumetric water content θ_w because the relative dielectric constant of water is higher than the dielectric constant of air and most minerals forming a rock matrix (Topp et al., 1980). Topp et al. (1980) identified an empirical relationship between the dielectric constant k and the volumetric water content θ_w:

$$\theta_w = -5.3x10^{-2} + 2.92x10^{-2}k - 5.5x10^{-4}k^2 + 4.3x10^{-6}k^3 \qquad [13]$$

Moreover the water content (θ_w) is the product of the porosity (Φ) and the water saturation (S_w).

$$\theta_w = \Phi S_w \qquad [14]$$

In our case study, using Topp's empirical relationship, the GPR data allowed to estimate the LNAPL saturation degree using equations 13 and 14.

The three different datasets were processed by removing the effect connected to the coupling between the antenna and the box and the information contained in radargrams outside the area of interest. From processed-data, "significant traces" (one profile every 5 cm) were extracted. They describe the propagation mode on the

high-frequency electromagnetic waves generated in the sandbox. Analyzing the propagation velocity of the waves and knowing the sand box geometry it was possible to estimate the relative dielectric permittivity.

When the steady-state conditions were reached, twenty-one samples, one for each hole realized in the plexiglass, were collected in order to chemically quantify the hydrocarbon content.

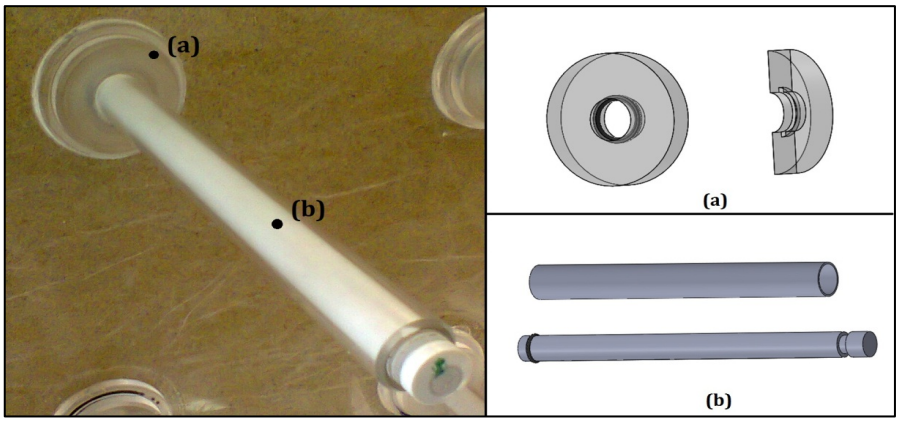

Figure 2. 14: Syringe sampler applied to the front face of the SandBox. a) pierced junction plate applied with perspex liquid (left) and sections of the piece (right). b) Sampling syringe (left) and its components (right).

a)

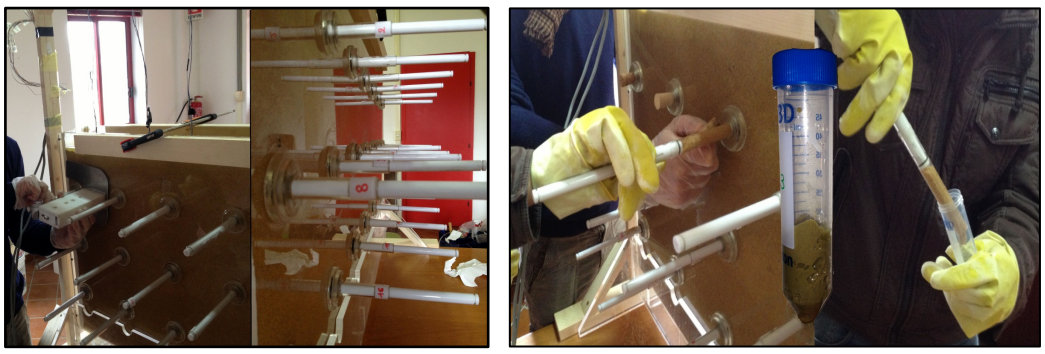

b)

Figure 2. 15: a) Sandbox samplers configuration and b) Sampling operations

All samples were analyzed according to the U.S. EPA (1996) methods. Protocols 3541 and 3540C have been followed for the extraction of Hydrocarbons from the samples, and protocol 8440 for the determination of the TotalPetroleumHydrocarbon (TPH) by means of Infrared Spectrophotometry (IRS).

a) b)

Figure 2. 16: a) Infrared Spectrophotometry Thermo FT-IR Nicolet iS10 b) LNPL samples analysis

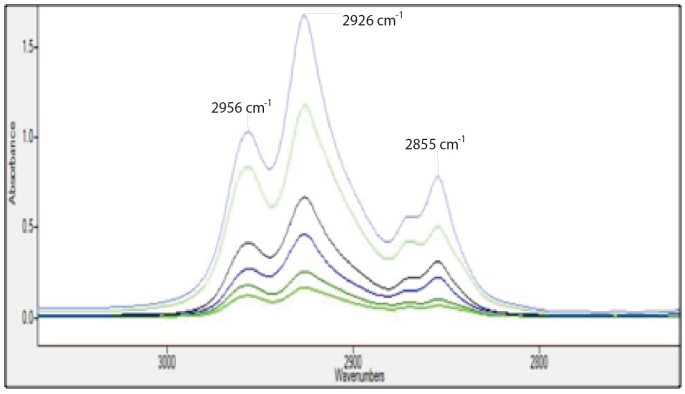

Figure 2. 17: Typical curves of TPHs derived from the infrared spectrophotometer for an absorbance range of 2800 - 3000 cm^{-1}

The measuring system was previously validated by performing three benchmarks with known concentrations of hydrocarbons (0.5, 1, 2 mL), resulting in an error of 2.5% in concentration values. This result shows the potentiality of the IRS method to quantify the TPH. The aim of the chemical analysis is to obtain the distribution of the hydrocarbon content and to validate the LNAPL saturation degree, determined by Topp's formula from the GPR data.

2.2.4 Results

The first GPR acquisition was performed at the end of the water saturation phase, where it was possible to identify a mean baseline value of the dielectric constant k >

20 and an homogeneous distribution of EM waves velocities. The dielectric permittivity map, shown in Figure 2.18, was obtained using a geostatistical approach based on kriging contouring. In Figure 2 it's possible to notice a decrease in the k values moving from the center of the box toward the boundaries, where the bulging effect, produced by the pressure exerted by the inner material, is minimum.

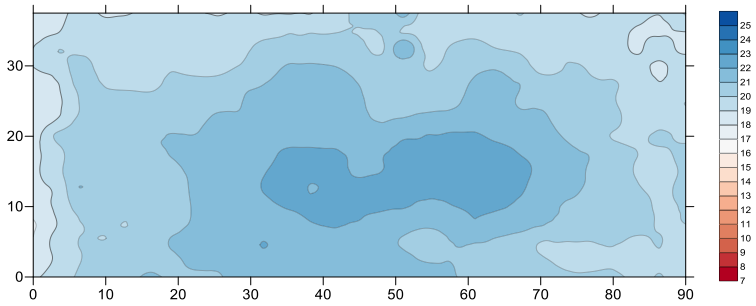

Figure 2. 18: Permittivity map during water saturated conditions.

Figure 2.19 shows the permittivity map obtained from GPR data acquired during the fuel-injection (diesel-LNAPL) (fig. 2.19a) and after six days (fig. 2.19b)

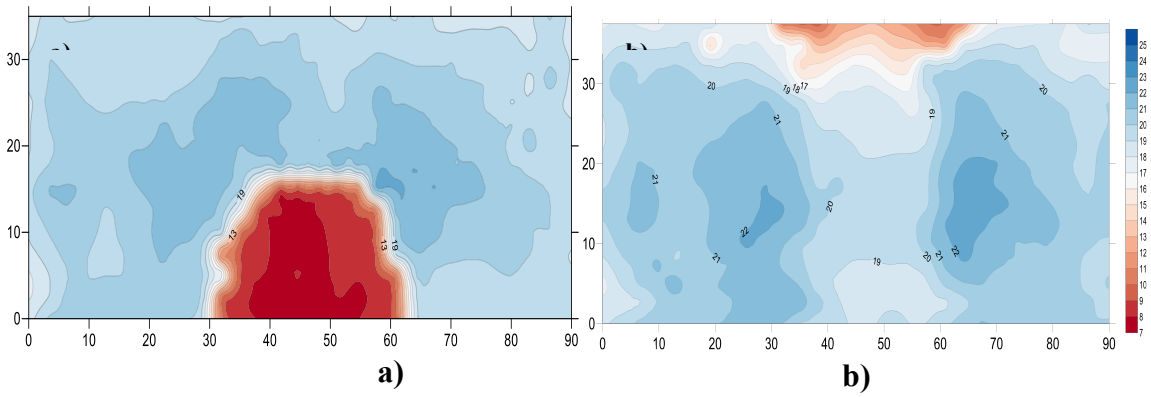

Figure 2. 19: a) Permittivity map during fuel injection, b) Permittivity map after six days

To better highlight the variations induced by the contaminant, a "contrast map" (figure 2.20) has been realized, where the dielectric differences between the two scenarios have been reported. The use of this type of representation allowed the elimination of the effects induced by the box bulging.

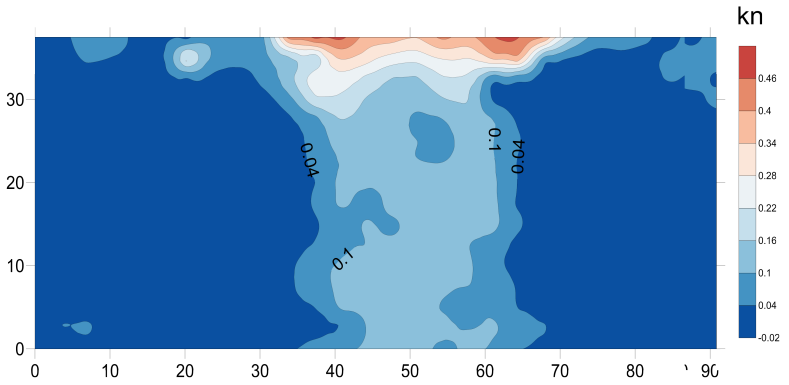

Figure 2. 20: Interpolated contrast permittivity map realized by the differences recorded between the water saturated conditions map and the scenarios acquired the sixth day from the diesel injection.

The final step consisted in the implementation of Topp's equation (13) to quantify the LNAPL saturation degree from the measured dielectric permittivity values. The results are shown in figure 2.21.

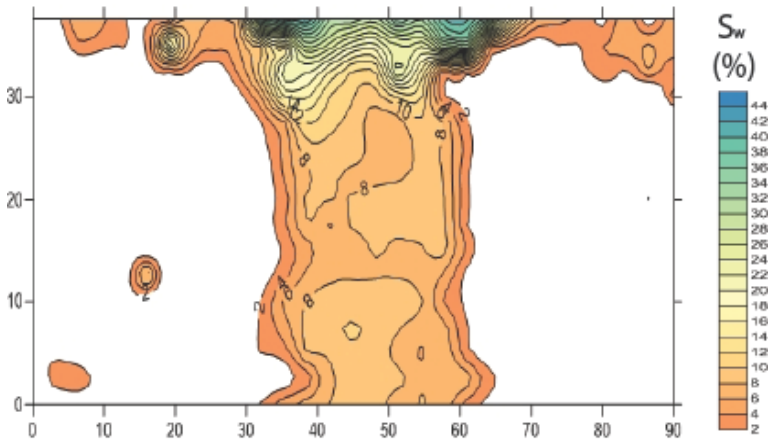

Figure 2. 21: Contrast map expressed in saturation degree S_w percentage.

The results are extremely interesting and allow a clear distinction between an area characterized by low dielectric permittivity values (i.e. high propagation speed of the EM waves), where the diesel saturation is probably greater, and two lateral areas where no significant variations of the electromagnetic behavior of the sand are detectable (i.e. absence of contaminant dispersion). In order to find the correlation between the dielectric permittivity measures and the LNAPL saturation degree, the sand samples, collected by means of the system described in section 2.2.3, were analyzed. The samples located in the central zone of the box were characterized by higher LNAPL concentration values (31,664 $[g\ kg_{DS}^{-1}]$), while, the lateral zones of the box were characterized by a lower concentration (0,109 $[g\ kg_{DS}^{-1}]$). These values converted in the

form of TPH saturation are equal to 11.86% and 0.2% respectively, so we found a good correlation between LNAPL saturation degree obtained by chemical analysis and geophysical data.

2.2.5 CONCLUSIONS

The reliability of GPR as a tool to detect near-surface contaminants is illustrated through a test representing diesel fuel infiltration in a saturated soil, carried out under controlled conditions in a hydro-geophysical laboratory of the University of Calabria. Lots of the performed tests show that GPR may provide an indication of NAPL saturation degree in the saturated zone. In fact, results show significant changes in the responses of electromagnetic measurements in presence of fuel contamination. Moreover, GPR can provide high-density, quantitative data for investigations of vadose zone contaminant hydrogeology. The experimental results show the capability of GPR to identify the contaminant dispersed in the subsoil.

The chemical analysis carried out on the samples, validate the technique of GPR in the study of infiltration process into the soil and provide basic data for the construction of empirical relationships for the estimation of the real amount of contaminants in the subsurface. For this reason, the future of this research will be the evaluation of the capability to estimate the real content of LNAPL from the values of permittivity by geophysical techniques.

2.3 HYDROGEOPHYSICAL EXPERIMENTS: Self Potential Method for the Monitoring of the aquifer of Montalto Uffugo Research Site.

2.3.1 Introduction

Groundwater is the main source of drinkable water, but several human activities have led to a significant reduction of this resource. New research methods are able to identify and monitor groundwater movement and allow the rapid acquisition and interpretation of high-resolution information, through non-destructive and non-invasive techniques, which are less expensive with respect to direct surveys.

The purpose of this study is to experiment a technique, for the location of the watertable of the shallow aquifer, based on the self potential method, without resorting to excavations or other destructive actions on the field.

2.3.2 Experimental well field of University of Calabria

The study area is the well field of the University of Calabria, located in Montalto Uffugo, Cosenza, Italy. The experimental well field is located in an alluvial deposit at the confluence of the Settimo River in the south, the Mavigliano River in the north, and the Crati River in the east. The deposit mainly consists of unconsolidated and highly permeable alluvial sands and conglomerates. The well field of the test site encompasses an area of about 2100 m^2 (Figure 2.22), divided into five areas: offices, laboratory hydraulic models, warehouse, and laboratory analysis of water and field tests, where experiments were conducted.

a) b)

Figure 2. 22: a) Experimental well field of University of Calabria, b) 1 office 2 laboratory hydraulic models 3 warehouse 4 laboratory analysis of water and 5 field tests.

The subsurface geology of the site has been classified into four geological units (Straface et al., 2007) (Figure 2.23). The top unit (formation A) is composed of heterogeneous gravels embedded in a salty sand matrix. This formation extends from the ground surface to a depth of about 7 m. Underlying the top formation is a shale layer (formation B) at approximately 7 to 11 m depth. The third formation (formation C), at approximately 11 to 55 m depth, is the main aquifer of our interest. It is mainly composed of salty sand. Underlying formation C is a low-permeability shale stratum (formation D). A shallow perched aquifer is sometimes present in formation A during a part of the year. This was the case at the time of our experiment. The main aquifer is weakly confined: The piezometric surface was approximately 4 m above the top of formation B.

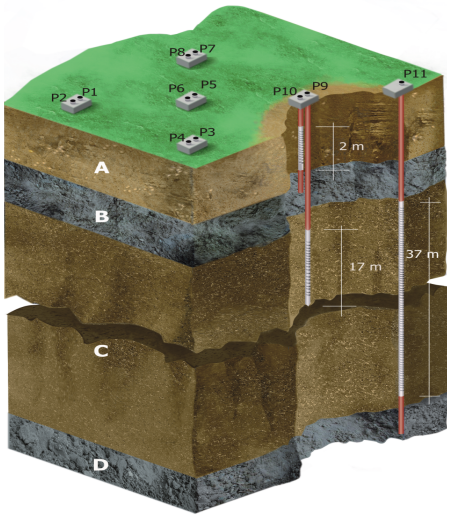

Figure 2. 23: A schematic illustration of the layout of the well field of Montalto Uffugo Scalo and our conceptual model of its geology (Straface et al., 2007)

The groundwater monitoring facility, established in June 1993, consists of five monitoring stations: four additional monitoring stations surround a central monitoring station. Each station includes a borehole reaching a depth of 10 m (i.e., reaching the shallow perched groundwater) and a second borehole reaching a depth of 40 m in the aquifer of interest. All the boreholes have a metal casing; the shallow boreholes are screened over an interval of 2 m, whereas the deep boreholes have a screened portion of 17 m. The boreholes are numbered P1 to P10 (Figure 2.23). A new well was drilled in October 1997 to a depth of 57 m to penetrate the clay bottom of the confined aquifer. This additional borehole, P11, is located 19 m from the central well (P5), and it reaches the impermeable layer at the bottom of the main aquifer. All the wells have a diameter

of 20 cm. Fifty holes with a depth of 25 cm, have been realized on the top soil, (Figure 2.24), to allow the insertion of the unpolarizable electrodes for the self potetial measurements.

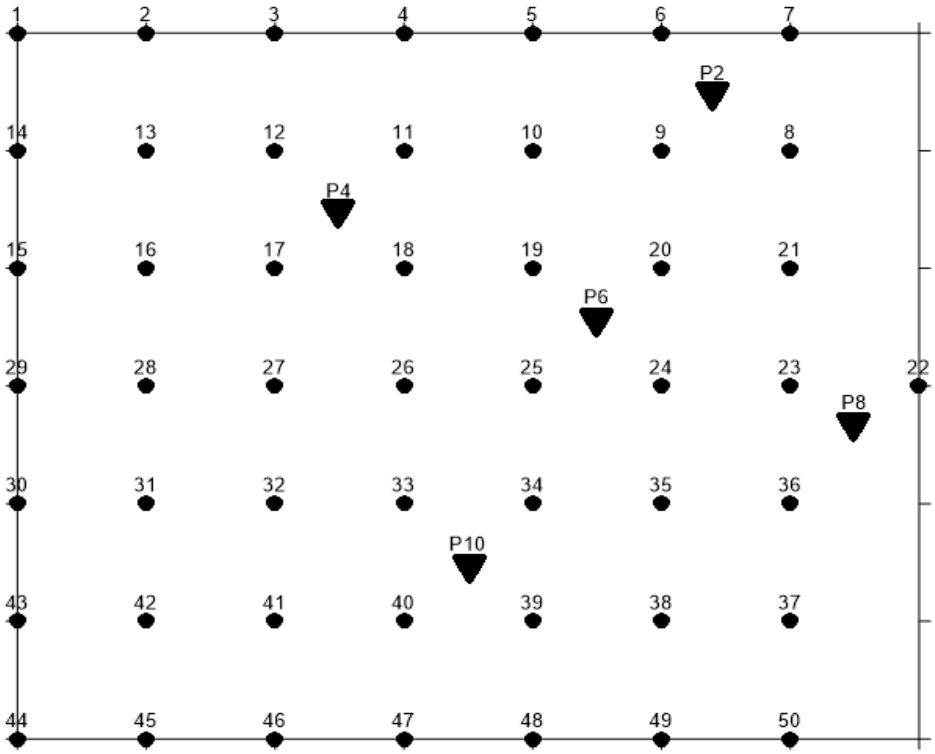

Figure 2. 24: Scheme of arrangement of the SP monitoring points and wells

Hydraulic measuring devices

Phreatimeter

The Corr Tek phreatimeter KL 010 is a quick, simple and economic system for ground water level measurement (distance to water) and is based on the contact between the water table and a probe placed on a white polyethylene measuring tape with meter markings in red, cm division, dm numbering in black. This device is provided by an optical and acoustic signal which indicate the moment in which the probe is in touch with water surface, and the distance between the top of the well and water can be read on the white graduated tape. The contact gauge is powered by four 1.5 Volt batteries (C-cells) and the measuring tape has a length of 30 m (Figure 2.25).

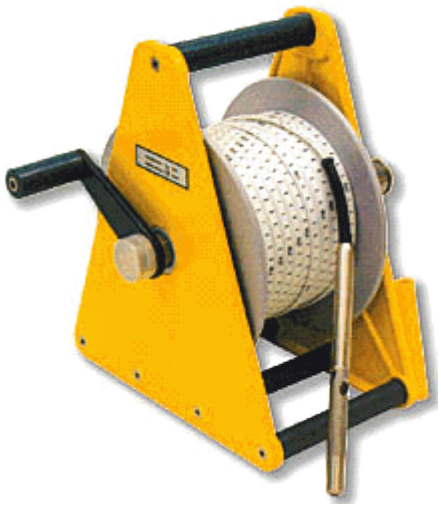

Figure 2. 25: Contact gauge KL 010

Datalogger Mini-Diver

The Mini-Diver (Figure 2.26) is an instrument for the autonomous measuring and recording of groundwater level and temperature. Its internal memory of 24000 measurements per parameter provides sufficient capacity to perform nearly one measurement every ten minutes for six months. For each measurement, the Diver registers the date and time, groundwater level, and temperature.

General Specifications

Dimensions	ø 0.87 in x 3.54 in.
Memory	24000 measurements
Wetted parts	
housing	stainless steel (316L)
o-rings	Viton ®
pressure sensor	ceramic (Al_2O_3)
cap / nose cone	Nylon PA6 30% glass fibre
Battery life	10 years (dependant on usage)
Sample interval	0.5 second to 99 hours
Mass	0.12 lbs

Temperature specifications

range / compensated	-4 °F to 176 °F / 32 °F to 122 °F
accuracy*	±0.18 °F
resolution	0.018 °F

Pressure specifications

Type	DI 501	DI 502	DI 505	DI 510
Range	32.8 ftH_2O	65.6 ftH_2O	164 ftH_2O	328 ftH_2O
- accuracy*	±0.2 inH_2O	±0.4 inH_2O	±0.98 inH_2O	±1.97 inH_2O
- resolution	0.08 inH_2O	0.16 inH_2O	0.4 inH_2O	0.79 inH_2O

Figure 2. 26: Mini-Diver

Datalogger Baro-Diver

The Baro-Diver (Figure 2.27) is an instrument for the autonomous measuring and recording changes in atmospheric pressure, covers a radius of up to 9 miles, depending on the topography, the Baro-Diver has an internal memory capable of storing 24000 measurements per parameter. For each measurement, the Baro-Diver simultaneously registers barometric pressure, air temperature, date and time.

General Specifications

Dimensions	ø0.87 in x 3.54 in.
Memory	24000 measurements
Wetted parts	
housing	stainless steel (316L)
o-rings	Viton ®
pressure sensor	ceramic (Al_2O_3)
cap / nose cone	Nylon PA6 30% glass fibre
Battery life	10 years (dependant on usage)
Sample interval	0.5 second to 99 hours
Mass	0.12 lbs

Temperature specifications

range / compensated	-4 °F to 176 °F / 14 °F to 122 °F
accuracy	±0.18 °F
resolution	0.018 °F

Pressure specifications

Type	DI 500
Range	4.9 ftH_2O
- accuracy	±0.2 inH_2O
- resolution	0.08 inH_2O

Figure 2. 27: Baro-Diver

Geophysic measuring devices

Unpolarizable electrodes for self -potentials measurements

This non-polarizing $Pb/PbCl_2$ (Petiau) electrodes (Figure 2.28), produced by SDEC – France, measure the self-potential at different soil depths, compared to a reference measure. These probes have been used since 25 years in the geophysics field with a great success. They are a kind of "dry" tensiometer (it is running without water inside) with a very long "lifetime" (about 15 years). These great advantages allow to use this probe in soil without maintenance, for high number of measurements once installed.

Technical specifications:

Diameter: 32 mm.

Length: 180 mm.

Weight: 250 g.

Value of the polarization on new electrodes: about 0,2mV.

Drift: ≈ 0.2 mV per month.

Temperature factor: 20 à 30 µV/°C.

Internal resistance (value between 2 electrodes): ≈ 500 Ohm.

Maximum pulling weight acceptable on the wire: 15kg.

Lifetime: 10 to 15 years.

Figure 2. 28: Nonpolarizing Pb/PbCl2 (Petiau) electrodes

Multichannel voltmeter

A multimeter or a multitester, also known as a volt/ohm meter or VOM, is an electronic measuring instrument that combines several measurement functions in one unit, like voltage, current, resistance and temperature measurements. Keithley 2701 multichannel voltmeter (Figure 2.29) is adopted for Self Potential measures. This multimeter is PC interfaced and equipped with 80 channels connected with SDEC electrodes. Keithley voltmeter scans the electrode and acquire SP measures with a desired sampling time.

	2701
No. of differential input channels	80
Matrix crosspoints	96
Ohms resolution	100 $\mu\Omega$
Dry circuit ohms (20mV clamp)	No
No. of slots	2
Memory buffer	450,000 rdgs
Size (2U height)	Half-rack width
Communications	Ethernet, RS-232
Scan-Rate (memory)	500/s
Scan-Rate (bus)	440/s
Max. Internal Trigger Rate	2800/s
Max. External Trigger Rate	2000/s

Figure 2. 29: Keithley 2701 multichannel voltmeter

Multimeter Voltmeter

The handheld Multimeter PCE-DM 22 (Figure 2.30) is an electronic measuring instrument that combines several measurement functions in one unit. Along with determining DCV, ACV, DCA, ACA and resistance accurately, this multimeter also determines capacitance, frequency, revolutions and temperature, as well as does continuity checks and diode tests. This multimeter voltmeter is adopted for Self Potential measures.

Figure 2. 30: Multimeter PCE-DM 22

2.3.3 Experiment Setup

The first experimental step was the groundwater level monitoring through the installation of pressure transducers in the wells marked with the numbers 2, 4, 6, 8, 10 (Figure 2.23). Also the Baro-Diver has been prepared to monitor the atmospheric pressure variation for the compensation of the water level values acquired by the Mini-Divers. The data acquisition lasted for 23 consecutive days, with a sampling interval of one-hour. The hydraulic head values (Z), are obtained by considering the aquifer thickness up to the inlet section of the wells (B), by subtracting to this latter, the height at which the pressure transducers were positioned (S = 7 m) and by adding the height of the water column above the transducers (C), as shown schematically in Figure 2.31

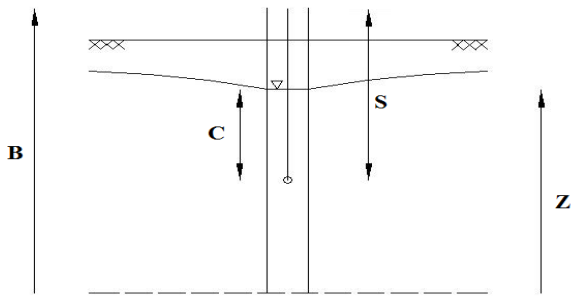

Figure 2. 31: Scheme adopted for the hydraulic heads calculation

A significant rainfall event occurred during the aquifer monitoring phase. The graphs below show the variation in the hydraulic head in all the five wells (Figure 2.32).

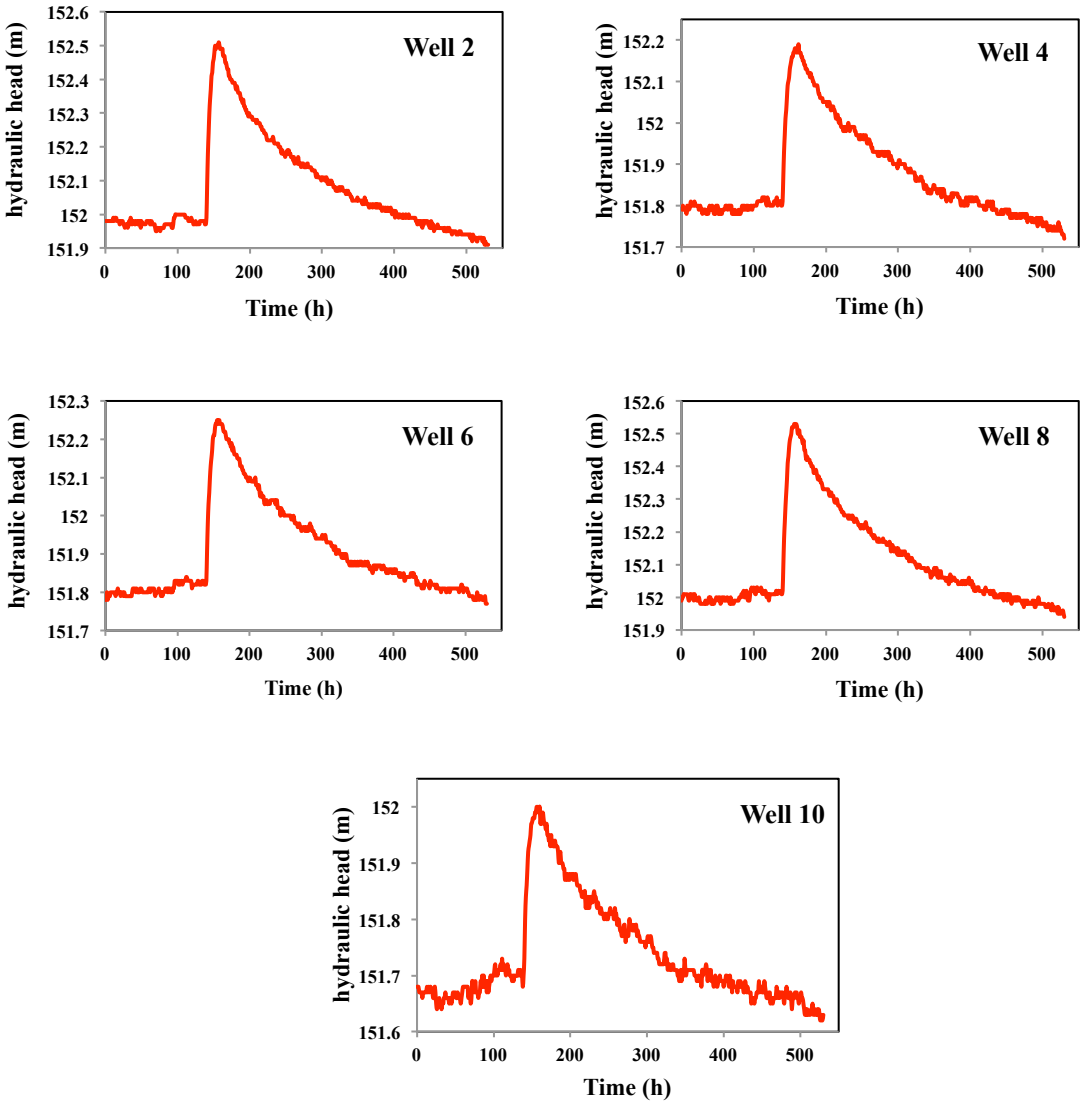

Figure 2. 32: Hydraulic head variations in wells 2, 4, 6, 8, 10

At the same time, the self potential signals have been acquired using a Keithley 2701 multichannel voltmeter and a Multimeter PCE-DM 22. The Self-Potential signal was recorded in 50 locations using only two electrodes; the first electrode was placed far from the study area and kept fixed in the same point, while the second electrode was moved in all the 50 measuring location after an acquisition interval of one minute for each. Bentonite was used into the holes to create a better contact between the ground and the electrode (Figure 2.33 - 2.34).

a) b)

Figure 2. 33: a) Bentonite base b) Electrode with bentonite

Figure 2. 34: Self-Potential measurement with Multimeter PCE-DM 22

Figure 2.33 shows the collected Self Potential signals.

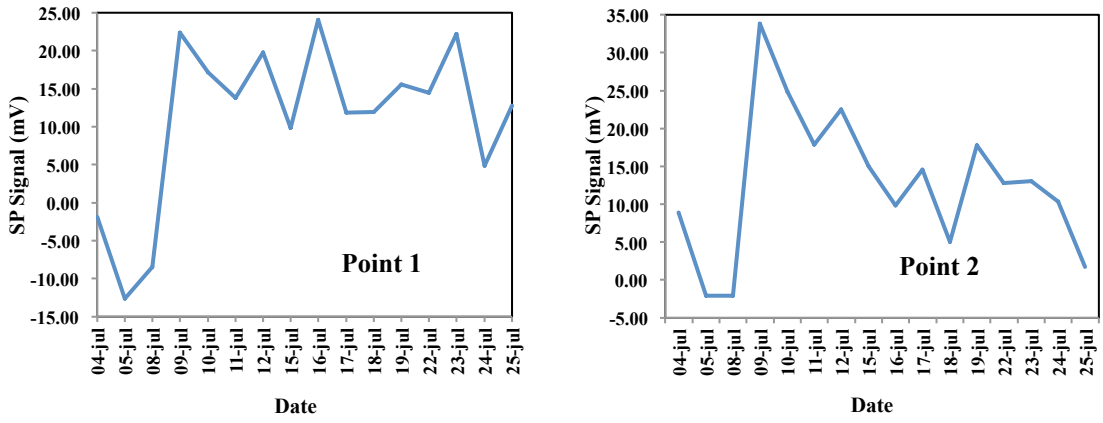

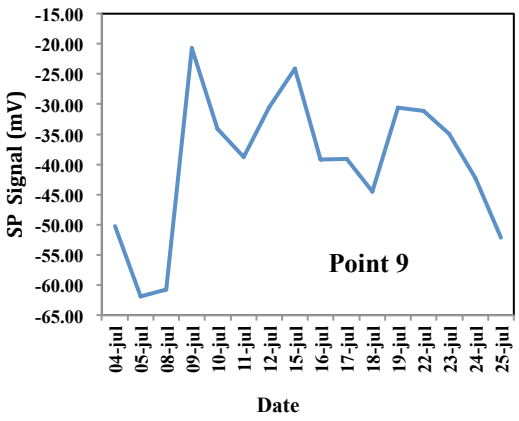
SP Signal (mV)
-15.00
-20.00
-25.00
-30.00
-35.00
-40.00
-45.00
-50.00
-55.00
-60.00
-65.00
Point 9
04-jul
05-jul
08-jul
09-jul
10-jul
11-jul
12-jul
15-jul
16-jul
17-jul
18-jul
19-jul
22-jul
23-jul
24-jul
25-jul
Date

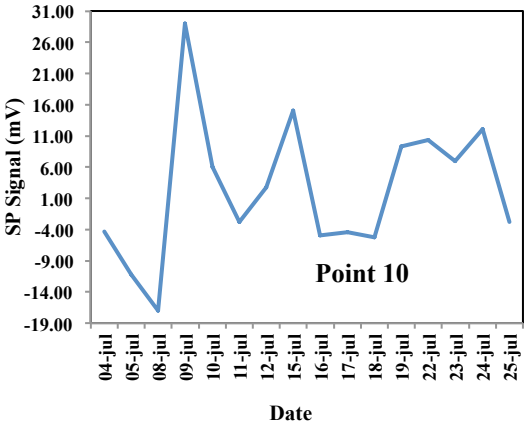
SP Signal (mV)
31.00
26.00
21.00
16.00
11.00
6.00
1.00
-4.00
-9.00
-14.00
-19.00
Point 10
04-jul
05-jul
08-jul
09-jul
10-jul
11-jul
12-jul
15-jul
16-jul
17-jul
18-jul
19-jul
22-jul
23-jul
24-jul
25-jul
Date

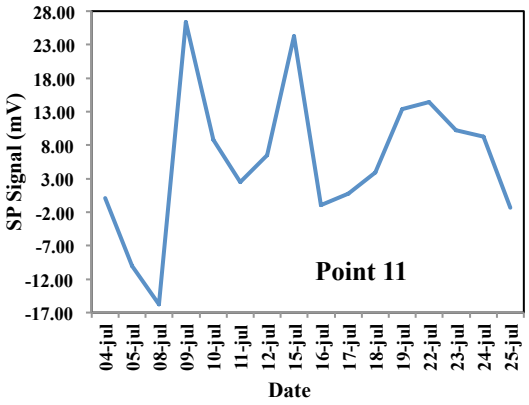
SP Signal (mV)
28.00
23.00
18.00
13.00
8.00
3.00
-2.00
-7.00
-12.00
-17.00
Point 11
04-jul
05-jul
08-jul
09-jul
10-jul
11-jul
12-jul
15-jul
16-jul
17-jul
18-jul
19-jul
22-jul
23-jul
24-jul
25-jul
Date

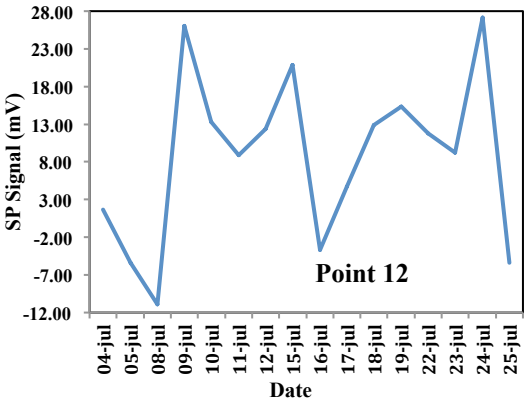
SP Signal (mV)
28.00
23.00
18.00
13.00
8.00
3.00
-2.00
-7.00
-12.00
Point 12
04-jul
05-jul
08-jul
09-jul
10-jul
11-jul
12-jul
15-jul
16-jul
17-jul
18-jul
19-jul
22-jul
23-jul
24-jul
25-jul
Date

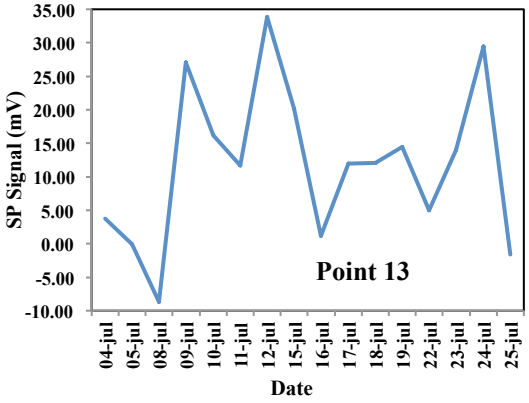
SP Signal (mV)
35.00
30.00
25.00
20.00
15.00
10.00
5.00
0.00
-5.00
-10.00
Point 13
04-jul
05-jul
08-jul
09-jul
10-jul
11-jul
12-jul
15-jul
16-jul
17-jul
18-jul
19-jul
22-jul
23-jul
24-jul
25-jul
Date

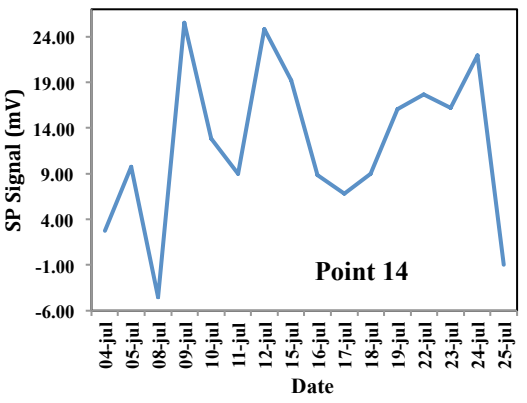
SP Signal (mV)
24.00
19.00
14.00
9.00
4.00
-1.00
-6.00
Point 14
04-jul
05-jul
08-jul
09-jul
10-jul
11-jul
12-jul
15-jul
16-jul
17-jul
18-jul
19-jul
22-jul
23-jul
24-jul
25-jul
Date

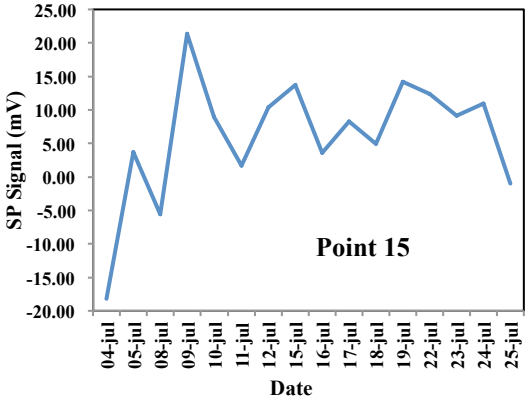
SP Signal (mV)
25.00
20.00
15.00
10.00
5.00
0.00
-5.00
-10.00
-15.00
-20.00
Point 15
04-jul
05-jul
08-jul
09-jul
10-jul
11-jul
12-jul
15-jul
16-jul
17-jul
18-jul
19-jul
22-jul
23-jul
24-jul
25-jul
Date

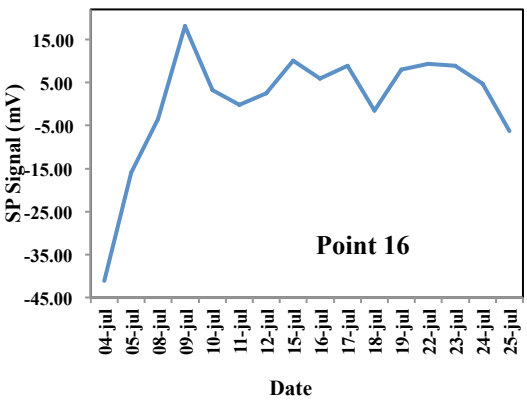
SP Signal (mV)
15.00
5.00
-5.00
-15.00
-25.00
-35.00
-45.00
Point 16
04-jul
05-jul
08-jul
09-jul
10-jul
11-jul
12-jul
15-jul
16-jul
17-jul
18-jul
19-jul
22-jul
23-jul
24-jul
25-jul
Date

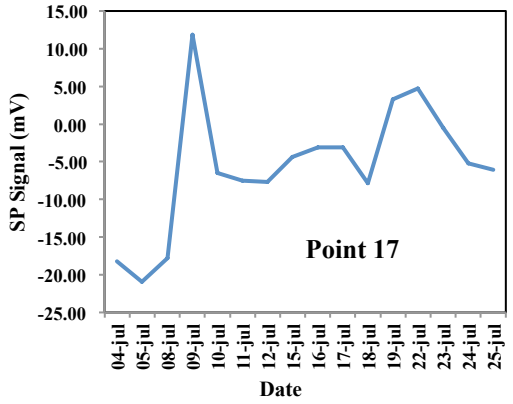
SP Signal (mV)
15.00
10.00
5.00
0.00
-5.00
-10.00
-15.00
-20.00
-25.00
Point 17
04-jul
05-jul
08-jul
09-jul
10-jul
11-jul
12-jul
15-jul
16-jul
17-jul
18-jul
19-jul
22-jul
23-jul
24-jul
25-jul
Date

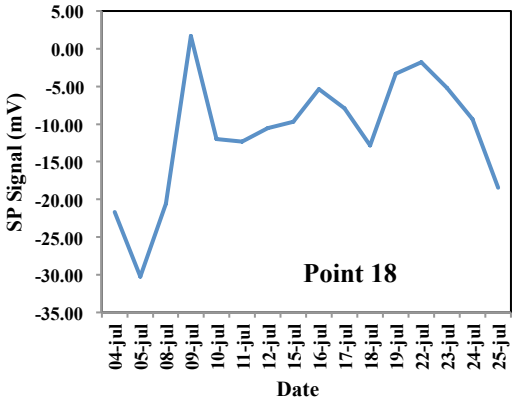
SP Signal (mV)
5.00
0.00
-5.00
-10.00
-15.00
-20.00
-25.00
-30.00
-35.00
Point 18
04-jul
05-jul
08-jul
09-jul
10-jul
11-jul
12-jul
15-jul
16-jul
17-jul
18-jul
19-jul
22-jul
23-jul
24-jul
25-jul
Date

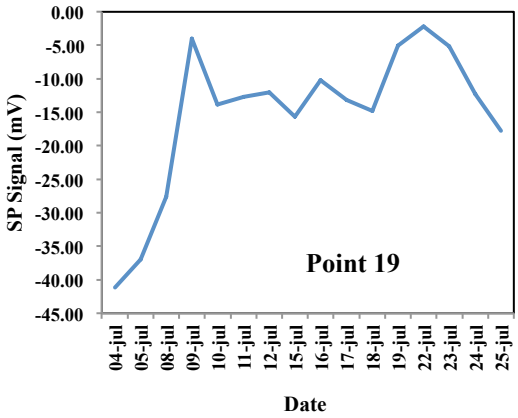
SP Signal (mV)
0.00
-5.00
-10.00
-15.00
-20.00
-25.00
-30.00
-35.00
-40.00
-45.00
Point 19
04-jul
05-jul
08-jul
09-jul
10-jul
11-jul
12-jul
15-jul
16-jul
17-jul
18-jul
19-jul
22-jul
23-jul
24-jul
25-jul
Date

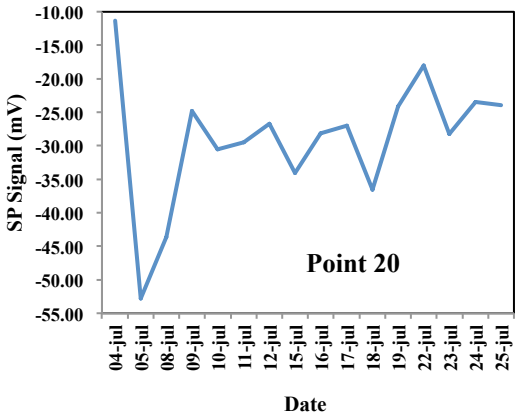
SP Signal (mV)
-10.00
-15.00
-20.00
-25.00
-30.00
-35.00
-40.00
-45.00
-50.00
-55.00
Point 20
04-jul
05-jul
08-jul
09-jul
10-jul
11-jul
12-jul
15-jul
16-jul
17-jul
18-jul
19-jul
22-jul
23-jul
24-jul
25-jul
Date

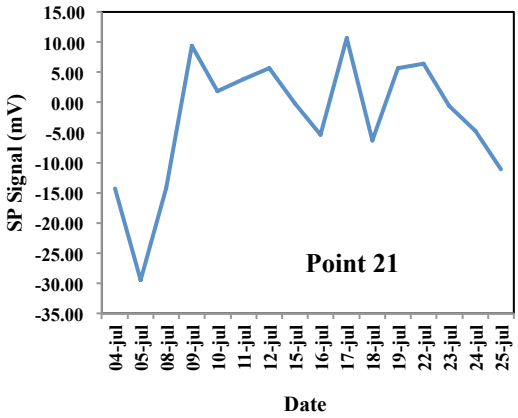
SP Signal (mV)
15.00
10.00
5.00
0.00
-5.00
-10.00
-15.00
-20.00
-25.00
-30.00
-35.00
Point 21
04-jul
05-jul
08-jul
09-jul
10-jul
11-jul
12-jul
15-jul
16-jul
17-jul
18-jul
19-jul
22-jul
23-jul
24-jul
25-jul
Date

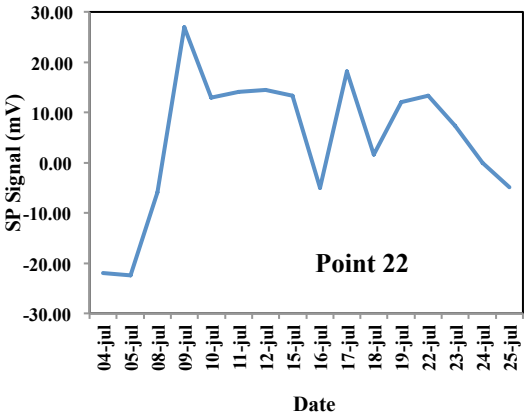
SP Signal (mV)
30.00
20.00
10.00
0.00
-10.00
-20.00
-30.00
Point 22
04-jul
05-jul
08-jul
09-jul
10-jul
11-jul
12-jul
15-jul
16-jul
17-jul
18-jul
19-jul
22-jul
23-jul
24-jul
25-jul
Date

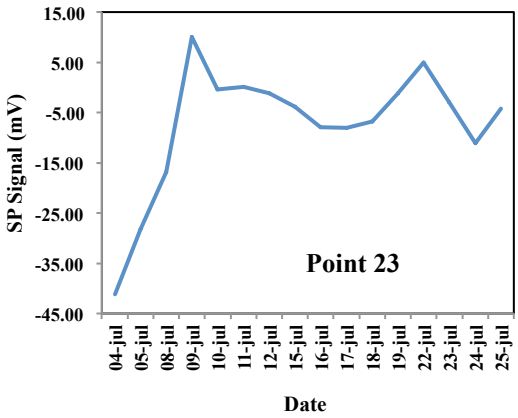
SP Signal (mV)
15.00
5.00
-5.00
-15.00
-25.00
-35.00
-45.00
Point 23
04-jul
05-jul
08-jul
09-jul
10-jul
11-jul
12-jul
15-jul
16-jul
17-jul
18-jul
19-jul
22-jul
23-jul
24-jul
25-jul
Date

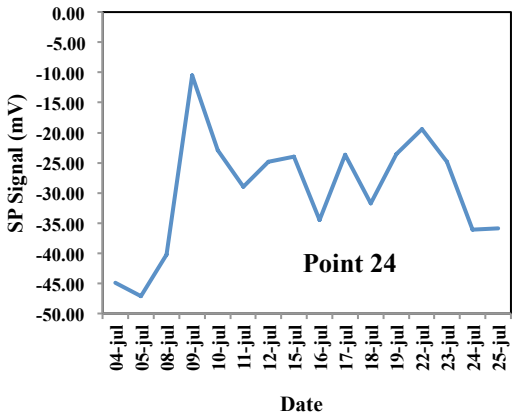
SP Signal (mV)
0.00
-5.00
-10.00
-15.00
-20.00
-25.00
-30.00
-35.00
-40.00
-45.00
-50.00
Point 24
04-jul
05-jul
08-jul
09-jul
10-jul
11-jul
12-jul
15-jul
16-jul
17-jul
18-jul
19-jul
22-jul
23-jul
24-jul
25-jul
Date

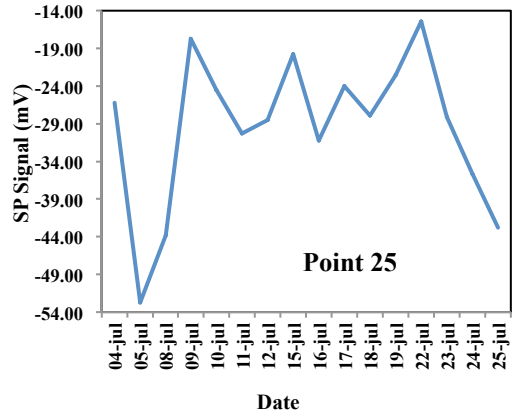
SP Signal (mV)
-14.00
-19.00
-24.00
-29.00
-34.00
-39.00
-44.00
-49.00
-54.00
Point 25
04-jul
05-jul
08-jul
09-jul
10-jul
11-jul
12-jul
15-jul
16-jul
17-jul
18-jul
19-jul
22-jul
23-jul
24-jul
25-jul
Date

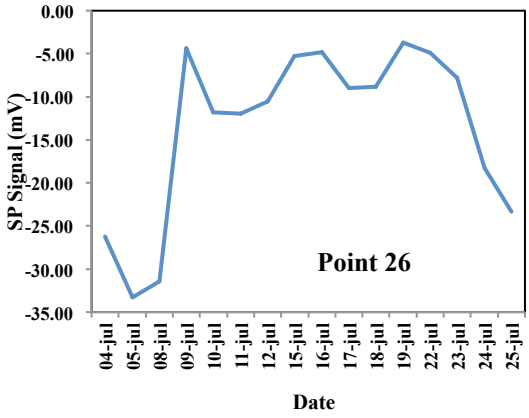
SP Signal (mV)
0.00
-5.00
-10.00
-15.00
-20.00
-25.00
-30.00
-35.00
Point 26
04-jul
05-jul
08-jul
09-jul
10-jul
11-jul
12-jul
15-jul
16-jul
17-jul
18-jul
19-jul
22-jul
23-jul
24-jul
25-jul
Date

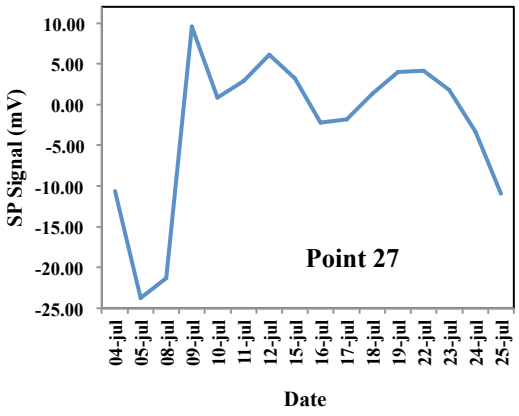
SP Signal (mV)
10.00
5.00
0.00
-5.00
-10.00
-15.00
-20.00
-25.00
Point 27
04-jul
05-jul
08-jul
09-jul
10-jul
11-jul
12-jul
15-jul
16-jul
17-jul
18-jul
19-jul
22-jul
23-jul
24-jul
25-jul
Date

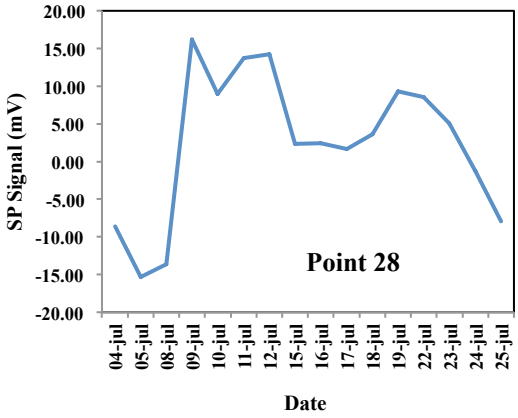
SP Signal (mV)
20.00
15.00
10.00
5.00
0.00
-5.00
-10.00
-15.00
-20.00
Point 28
04-jul
05-jul
08-jul
09-jul
10-jul
11-jul
12-jul
15-jul
16-jul
17-jul
18-jul
19-jul
22-jul
23-jul
24-jul
25-jul
Date

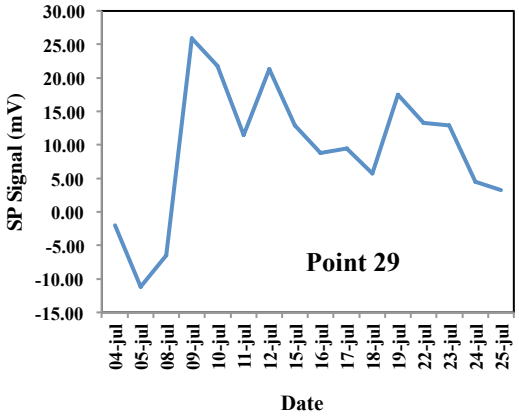
SP Signal (mV)
30.00
25.00
20.00
15.00
10.00
5.00
0.00
-5.00
-10.00
-15.00
Point 29
04-jul
05-jul
08-jul
09-jul
10-jul
11-jul
12-jul
15-jul
16-jul
17-jul
18-jul
19-jul
22-jul
23-jul
24-jul
25-jul
Date

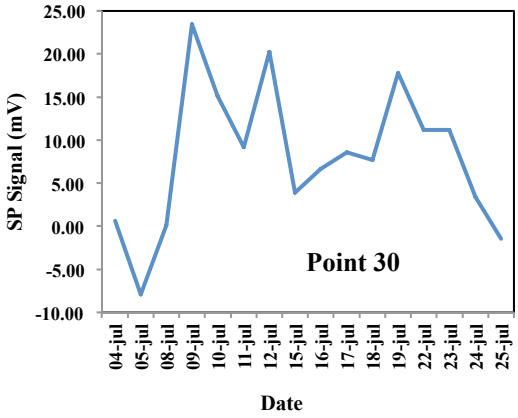
SP Signal (mV)
25.00
20.00
15.00
10.00
5.00
0.00
-5.00
-10.00
Point 30
04-jul
05-jul
08-jul
09-jul
10-jul
11-jul
12-jul
15-jul
16-jul
17-jul
18-jul
19-jul
22-jul
23-jul
24-jul
25-jul
Date

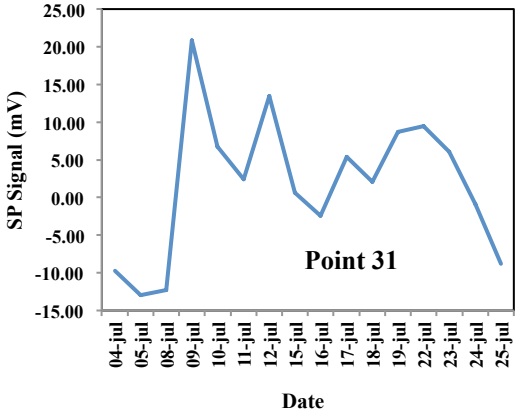
SP Signal (mV)
25.00
20.00
15.00
10.00
5.00
0.00
-5.00
-10.00
-15.00
Point 31
04-jul
05-jul
08-jul
09-jul
10-jul
11-jul
12-jul
15-jul
16-jul
17-jul
18-jul
19-jul
22-jul
23-jul
24-jul
25-jul
Date

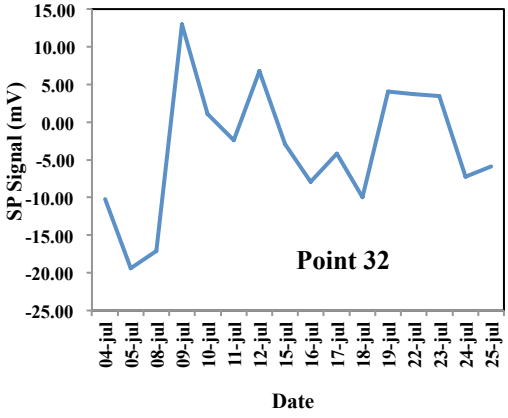
SP Signal (mV)
15.00
10.00
5.00
0.00
-5.00
-10.00
-15.00
-20.00
-25.00
Point 32
04-jul
05-jul
08-jul
09-jul
10-jul
11-jul
12-jul
15-jul
16-jul
17-jul
18-jul
19-jul
22-jul
23-jul
24-jul
25-jul
Date

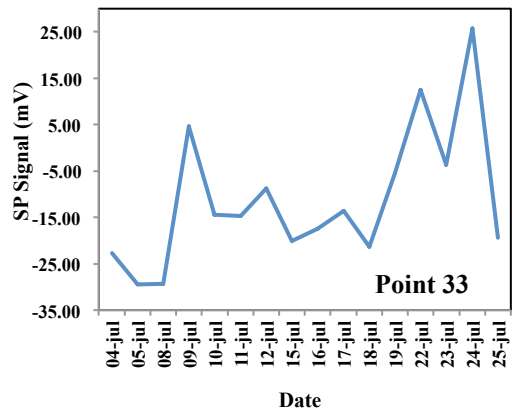
SP Signal (mV)
25.00
15.00
5.00
-5.00
-15.00
-25.00
-35.00
Point 33
04-jul
05-jul
08-jul
09-jul
10-jul
11-jul
12-jul
15-jul
16-jul
17-jul
18-jul
19-jul
22-jul
23-jul
24-jul
25-jul
Date

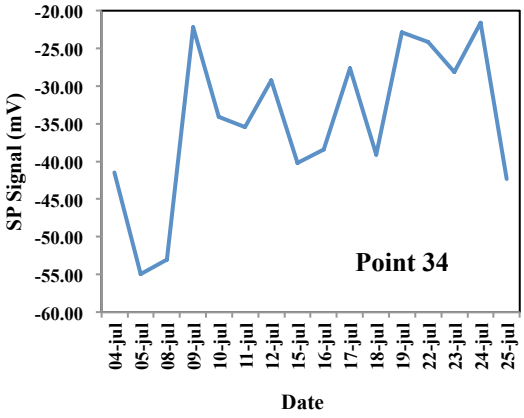
SP Signal (mV)
-20.00
-25.00
-30.00
-35.00
-40.00
-45.00
-50.00
-55.00
-60.00
Point 34
04-jul
05-jul
08-jul
09-jul
10-jul
11-jul
12-jul
15-jul
16-jul
17-jul
18-jul
19-jul
22-jul
23-jul
24-jul
25-jul
Date

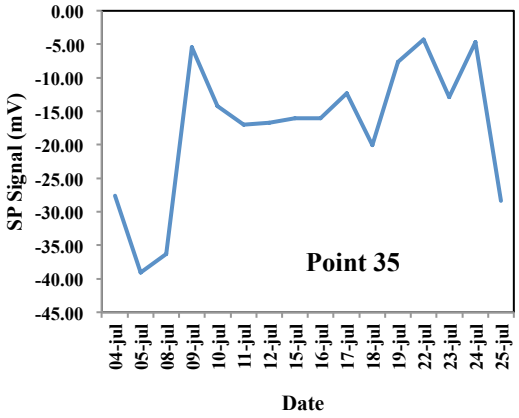
SP Signal (mV)
0.00
-5.00
-10.00
-15.00
-20.00
-25.00
-30.00
-35.00
-40.00
-45.00
Point 35
04-jul
05-jul
08-jul
09-jul
10-jul
11-jul
12-jul
15-jul
16-jul
17-jul
18-jul
19-jul
22-jul
23-jul
24-jul
25-jul
Date

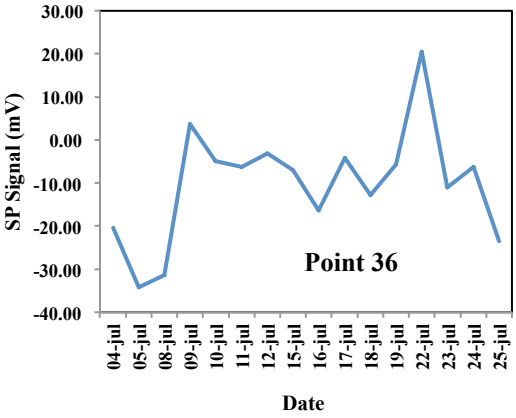
SP Signal (mV)
30.00
20.00
10.00
0.00
-10.00
-20.00
-30.00
-40.00
Point 36
04-jul
05-jul
08-jul
09-jul
10-jul
11-jul
12-jul
15-jul
16-jul
17-jul
18-jul
19-jul
22-jul
23-jul
24-jul
25-jul
Date

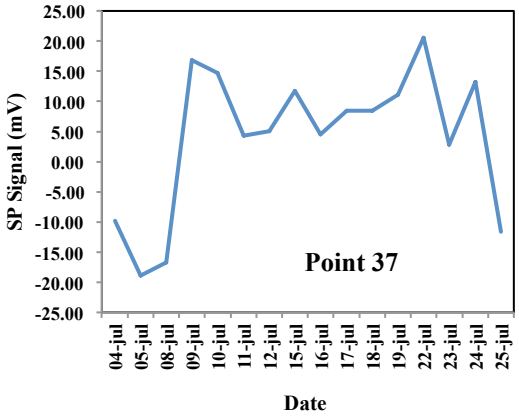
SP Signal (mV)
25.00
20.00
15.00
10.00
5.00
0.00
-5.00
-10.00
-15.00
-20.00
-25.00
Point 37
04-jul
05-jul
08-jul
09-jul
10-jul
11-jul
12-jul
15-jul
16-jul
17-jul
18-jul
19-jul
22-jul
23-jul
24-jul
25-jul
Date

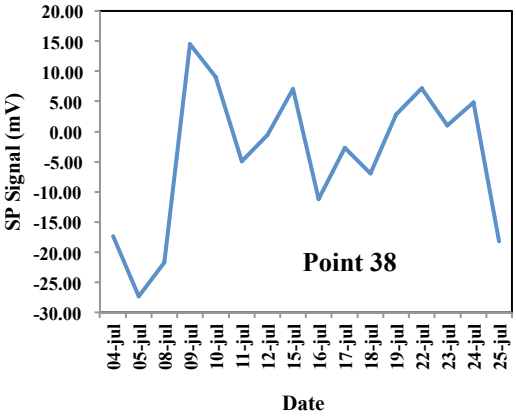
SP Signal (mV)
20.00
15.00
10.00
5.00
0.00
-5.00
-10.00
-15.00
-20.00
-25.00
-30.00
Point 38
04-jul
05-jul
08-jul
09-jul
10-jul
11-jul
12-jul
15-jul
16-jul
17-jul
18-jul
19-jul
22-jul
23-jul
24-jul
25-jul
Date

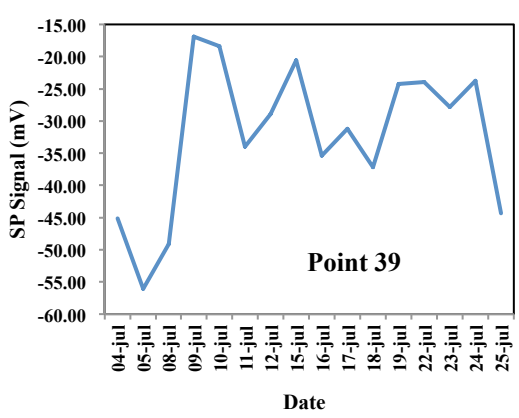
SP Signal (mV)
-15.00
-20.00
-25.00
-30.00
-35.00
-40.00
-45.00
-50.00
-55.00
-60.00
Point 39
04-jul
05-jul
08-jul
09-jul
10-jul
11-jul
12-jul
15-jul
16-jul
17-jul
18-jul
19-jul
22-jul
23-jul
24-jul
25-jul
Date

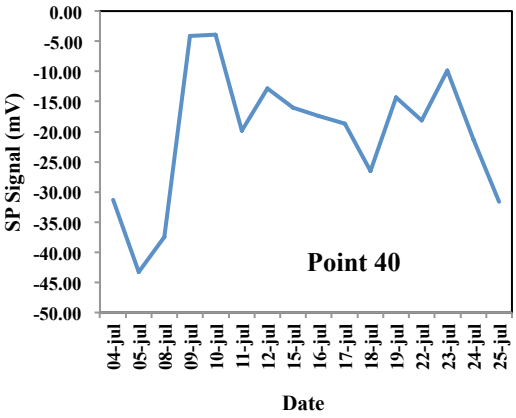
SP Signal (mV)
0.00
-5.00
-10.00
-15.00
-20.00
-25.00
-30.00
-35.00
-40.00
-45.00
-50.00
Point 40
04-jul
05-jul
08-jul
09-jul
10-jul
11-jul
12-jul
15-jul
16-jul
17-jul
18-jul
19-jul
22-jul
23-jul
24-jul
25-jul
Date

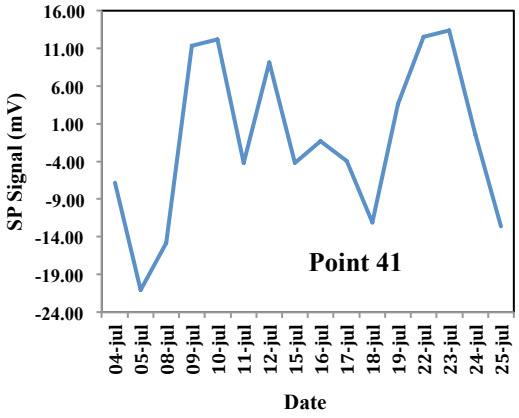
SP Signal (mV)
16.00
11.00
6.00
1.00
-4.00
-9.00
-14.00
-19.00
-24.00
Point 41
04-jul
05-jul
08-jul
09-jul
10-jul
11-jul
12-jul
15-jul
16-jul
17-jul
18-jul
19-jul
22-jul
23-jul
24-jul
25-jul
Date

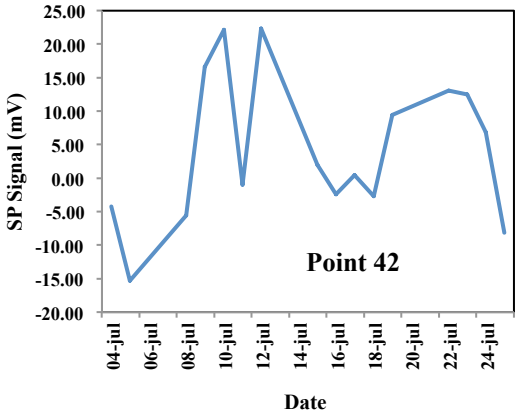
SP Signal (mV)
25.00
20.00
15.00
10.00
5.00
0.00
-5.00
-10.00
-15.00
-20.00
Point 42
04-jul
06-jul
08-jul
10-jul
12-jul
14-jul
16-jul
18-jul
20-jul
22-jul
24-jul
Date

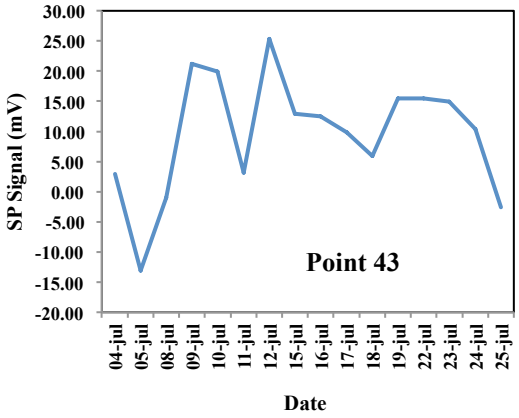
SP Signal (mV)
30.00
25.00
20.00
15.00
10.00
5.00
0.00
-5.00
-10.00
-15.00
-20.00
Point 43
04-jul
05-jul
08-jul
09-jul
10-jul
11-jul
12-jul
15-jul
16-jul
17-jul
18-jul
19-jul
22-jul
23-jul
24-jul
25-jul
Date

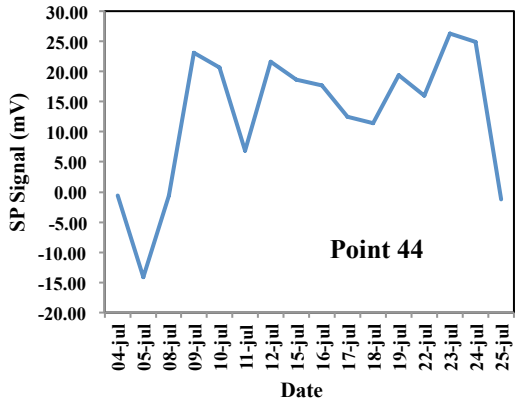
SP Signal (mV)
30.00
25.00
20.00
15.00
10.00
5.00
0.00
-5.00
-10.00
-15.00
-20.00
Point 44
04-jul
05-jul
08-jul
09-jul
10-jul
11-jul
12-jul
15-jul
16-jul
17-jul
18-jul
19-jul
22-jul
23-jul
24-jul
25-jul
Date

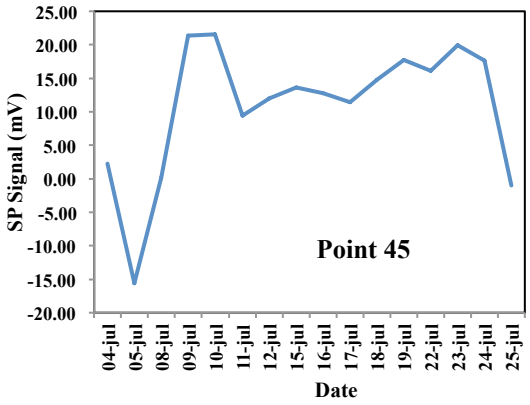
SP Signal (mV)
25.00
20.00
15.00
10.00
5.00
0.00
-5.00
-10.00
-15.00
-20.00
Point 45
04-jul
05-jul
08-jul
09-jul
10-jul
11-jul
12-jul
15-jul
16-jul
17-jul
18-jul
19-jul
22-jul
23-jul
24-jul
25-jul
Date

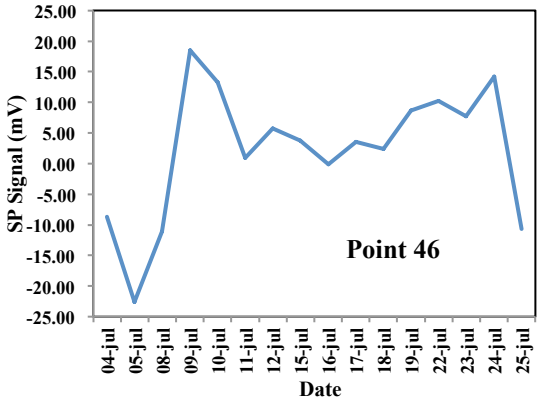
SP Signal (mV)
25.00
20.00
15.00
10.00
5.00
0.00
-5.00
-10.00
-15.00
-20.00
-25.00
Point 46
04-jul
05-jul
08-jul
09-jul
10-jul
11-jul
12-jul
15-jul
16-jul
17-jul
18-jul
19-jul
22-jul
23-jul
24-jul
25-jul
Date

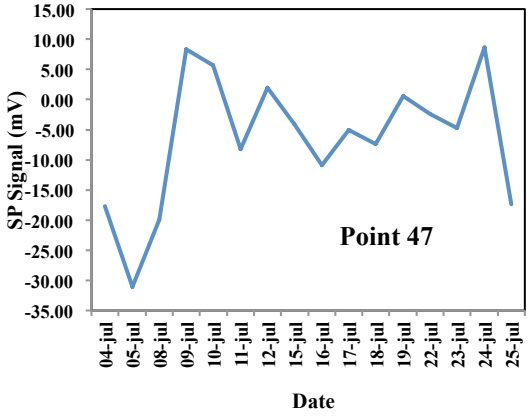
SP Signal (mV)
15.00
10.00
5.00
0.00
-5.00
-10.00
-15.00
-20.00
-25.00
-30.00
-35.00
Point 47
04-jul
05-jul
08-jul
09-jul
10-jul
11-jul
12-jul
15-jul
16-jul
17-jul
18-jul
19-jul
22-jul
23-jul
24-jul
25-jul
Date

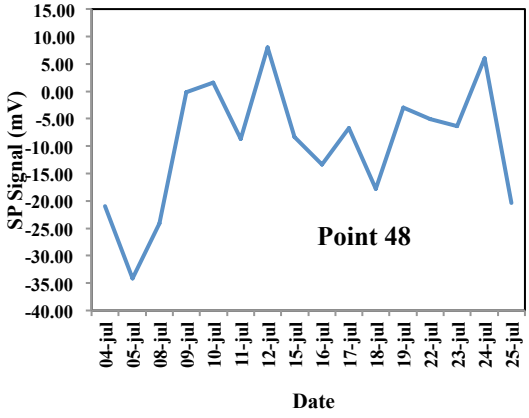
SP Signal (mV)
15.00
10.00
5.00
0.00
-5.00
-10.00
-15.00
-20.00
-25.00
-30.00
-35.00
-40.00
Point 48
04-jul
05-jul
08-jul
09-jul
10-jul
11-jul
12-jul
15-jul
16-jul
17-jul
18-jul
19-jul
22-jul
23-jul
24-jul
25-jul
Date

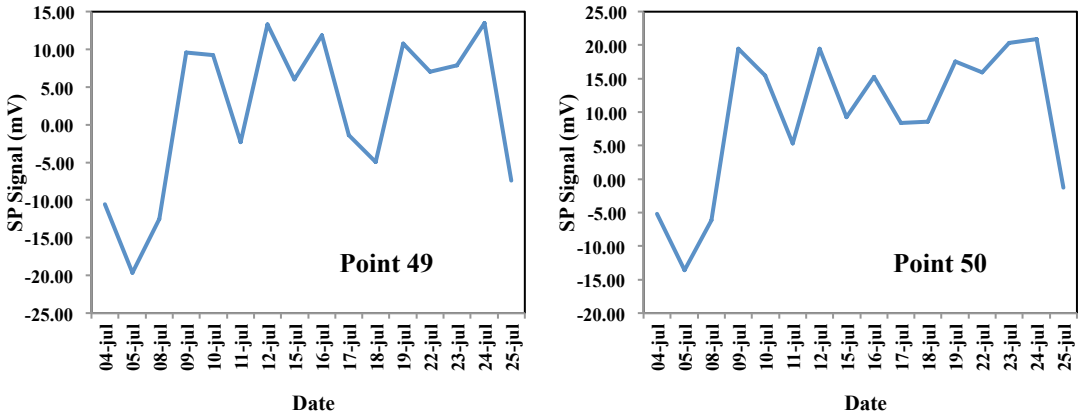

Figure 2. 35: SP signals acquired in the 50 measurement points

Also, the air temperature variation was recorded during watertable monitoring (Figure 2.36)

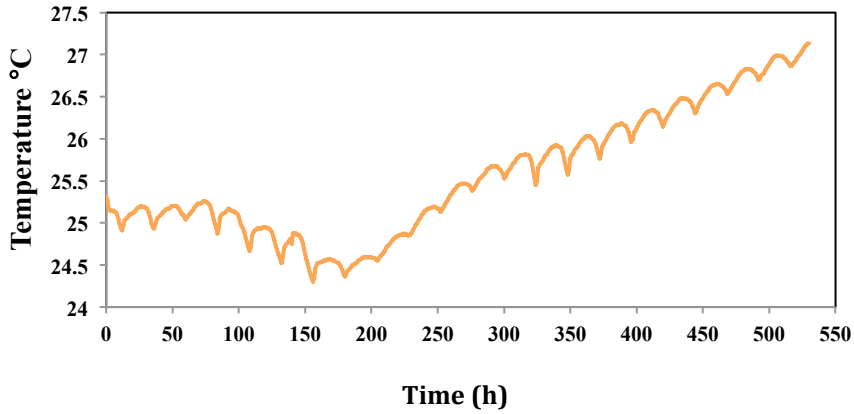

Figure 2. 36: Trend of the temperature values in the time

The precipitation data were provided by the Regional Agency for Environmental Protection of Calabria (ARPACAL) and reported in the following graph (Figure 2.37)

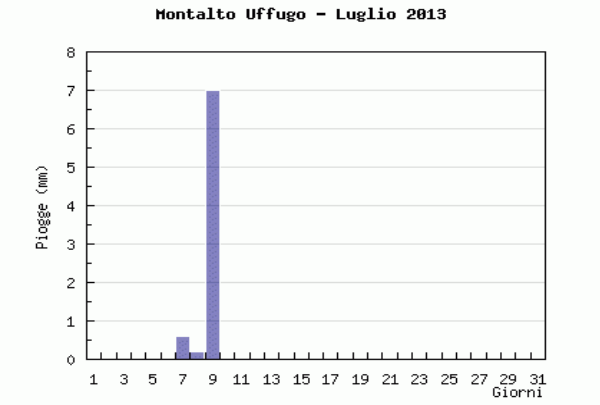

Figure 2. 37: Precipitations during July, Montalto Uffugo – ARPACAL

2.3.4 Measurements interpretation

The trend analysis performed on the SP and hydraulic head values, showed an increasing behavior before July 10th. This change is caused by the rain occurred in the previous days, which produced a water infiltration into the aquifer. After this period of infiltration the water level tended to decrease, while the SP signals showed an irregular behavior. Through the interpolation of the recorded hydraulic head and SP values, the time variation maps have been elaborated (Figure 2.38).

July 4

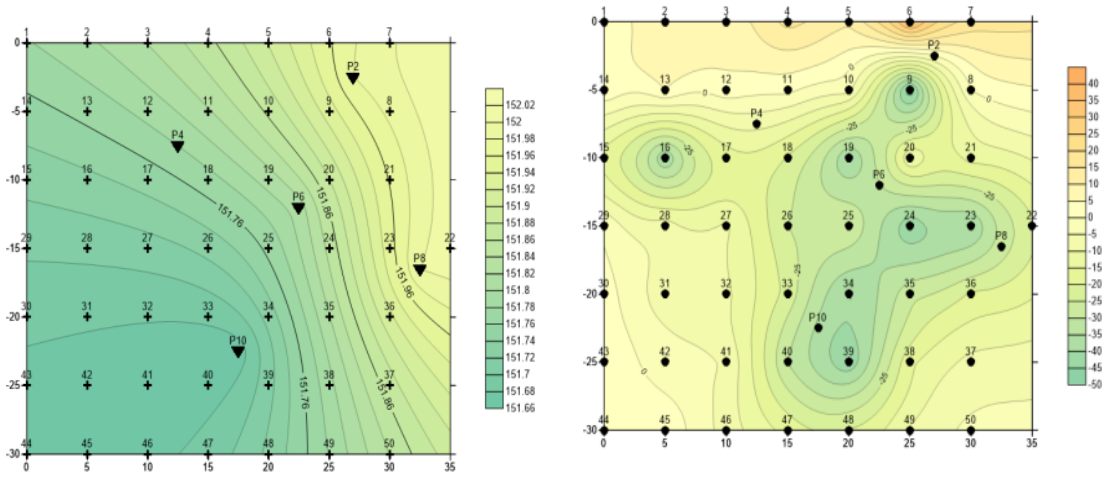

July 5

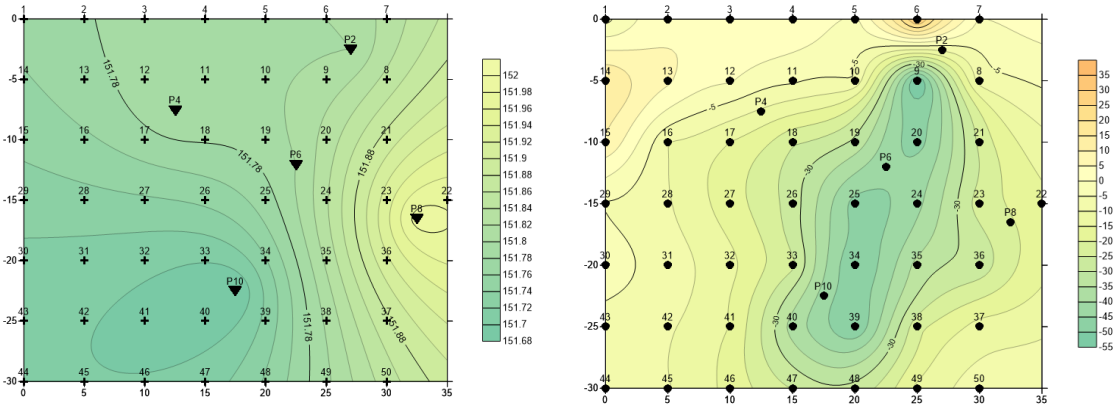

July 8

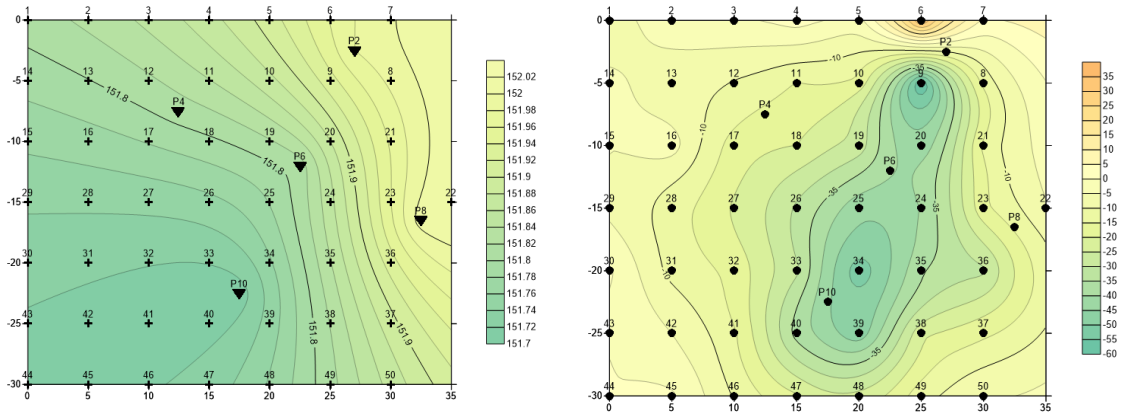

July 9

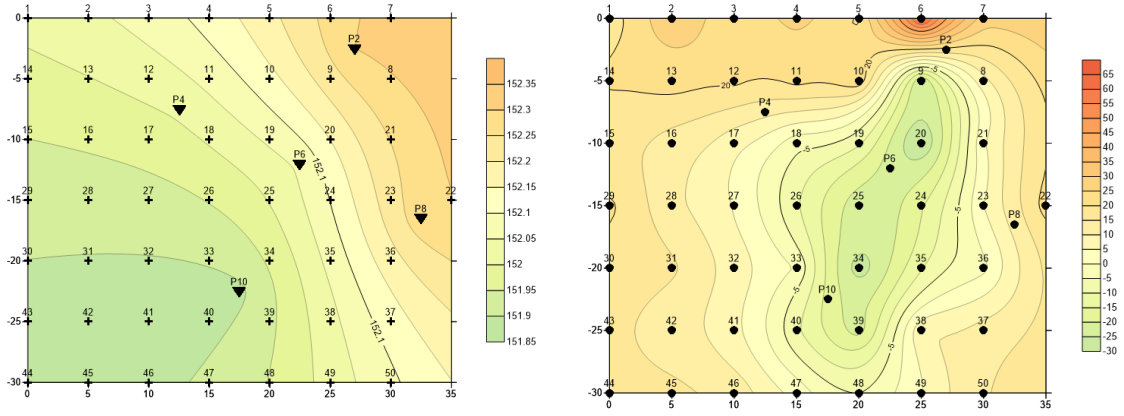

July 10

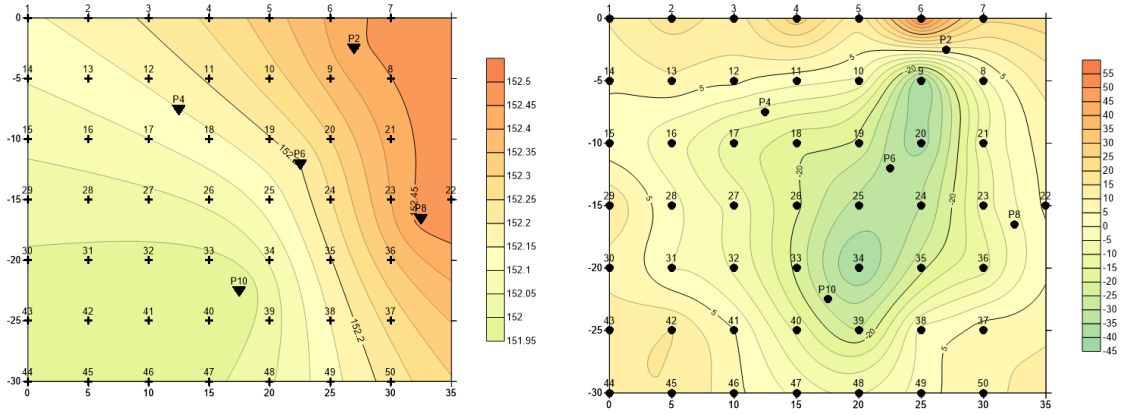

July 11

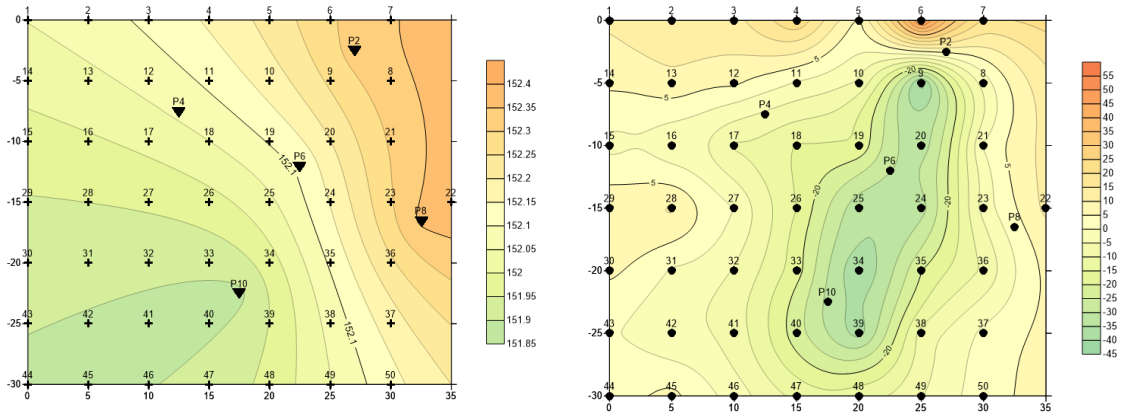

July 12

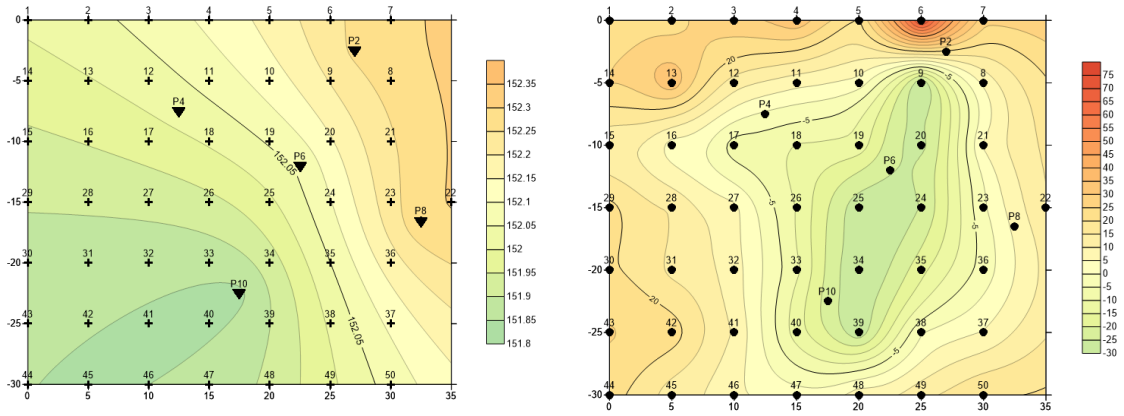

July 15

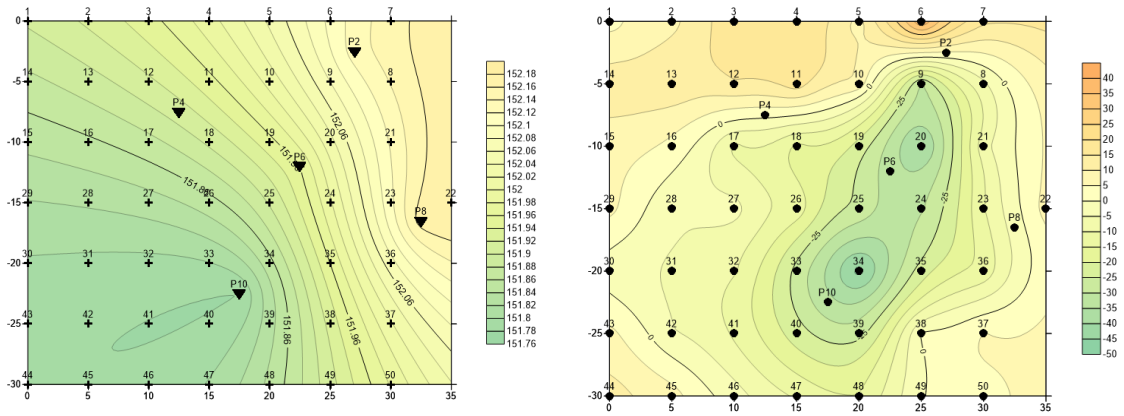

July 16

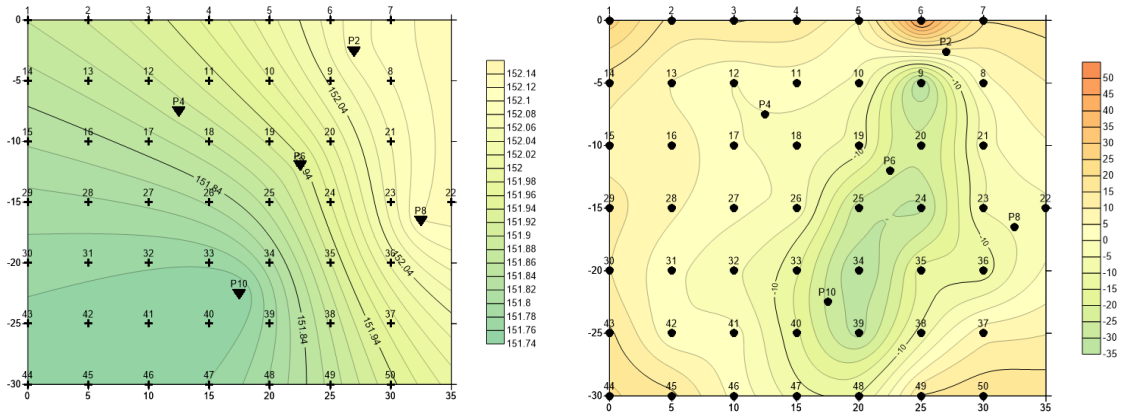

July 17

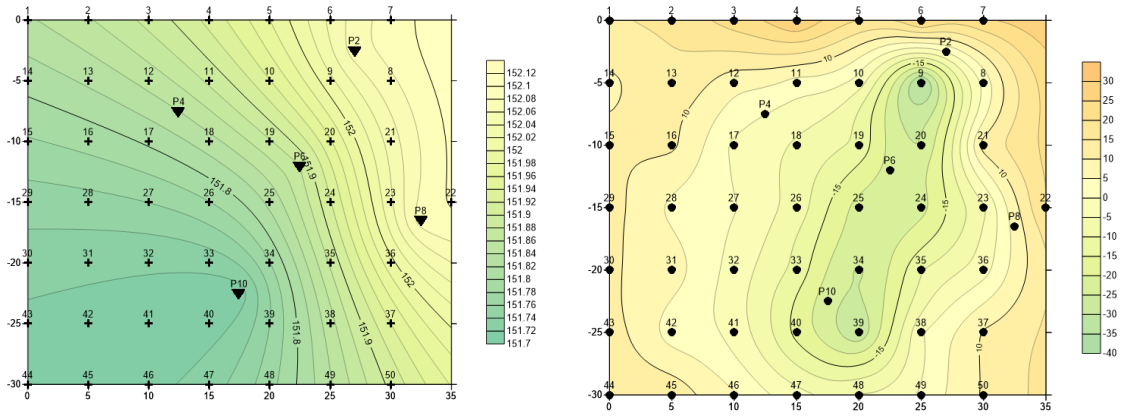

July 18

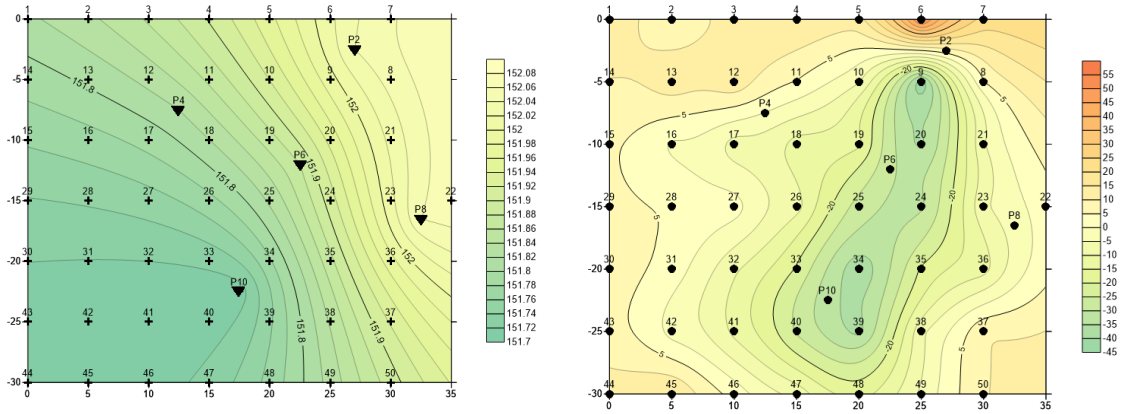

July 19

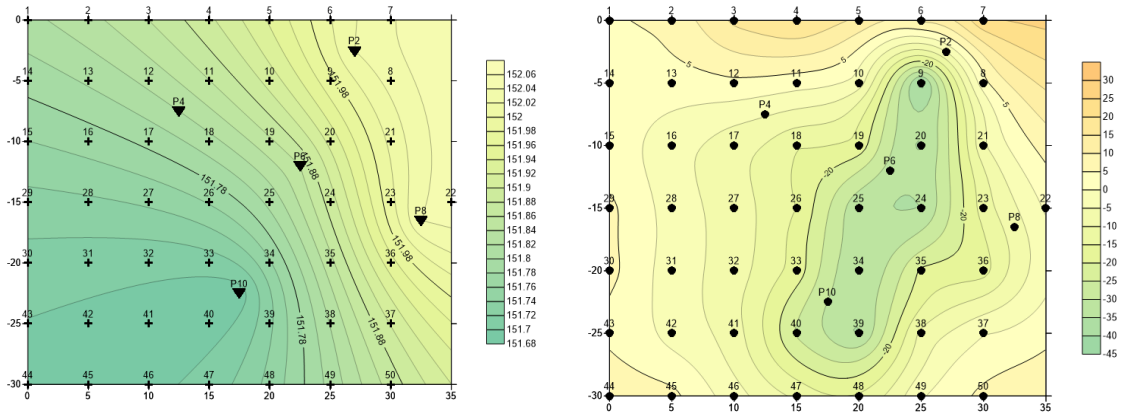

July 22

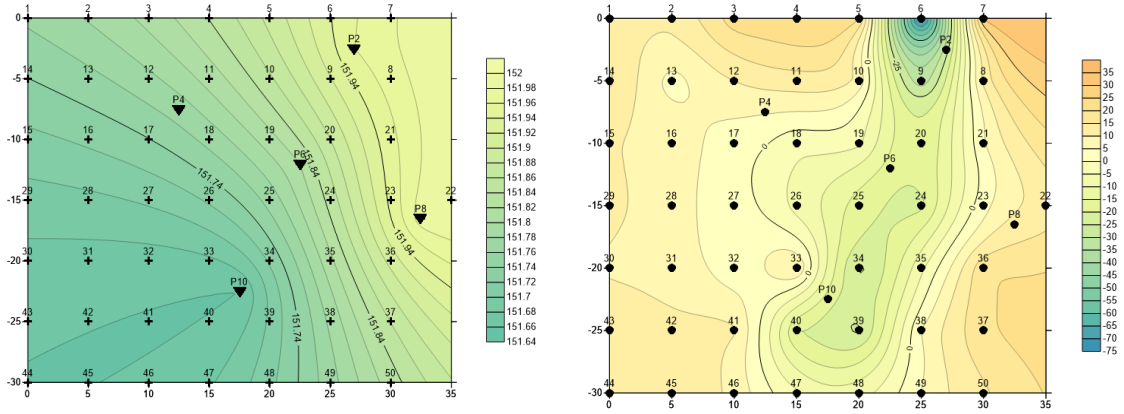

July 23

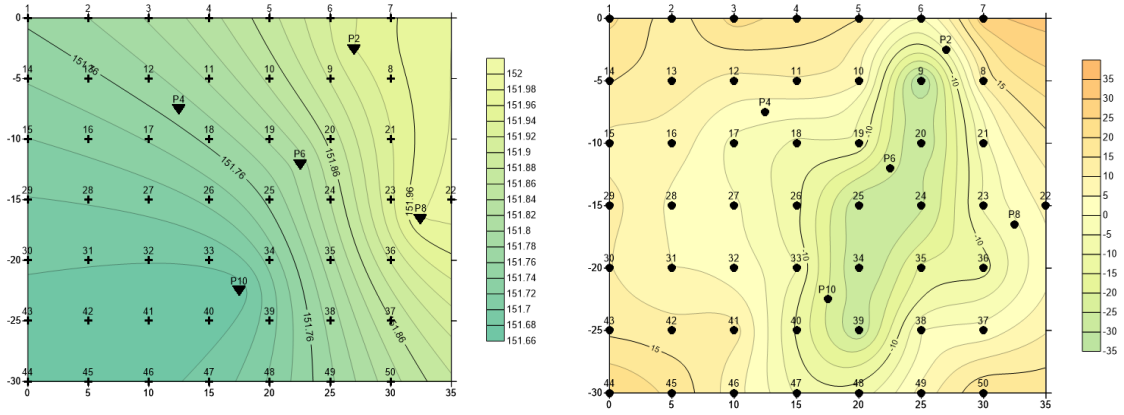

July 24

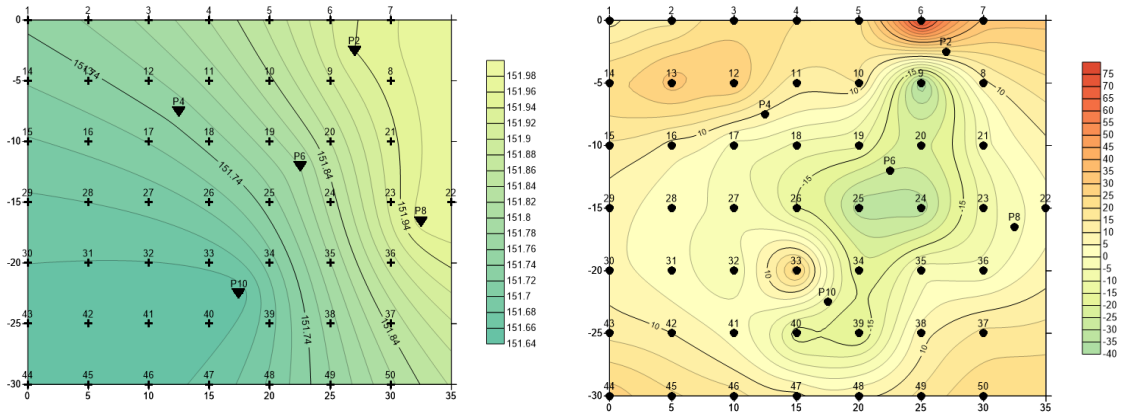

July 25

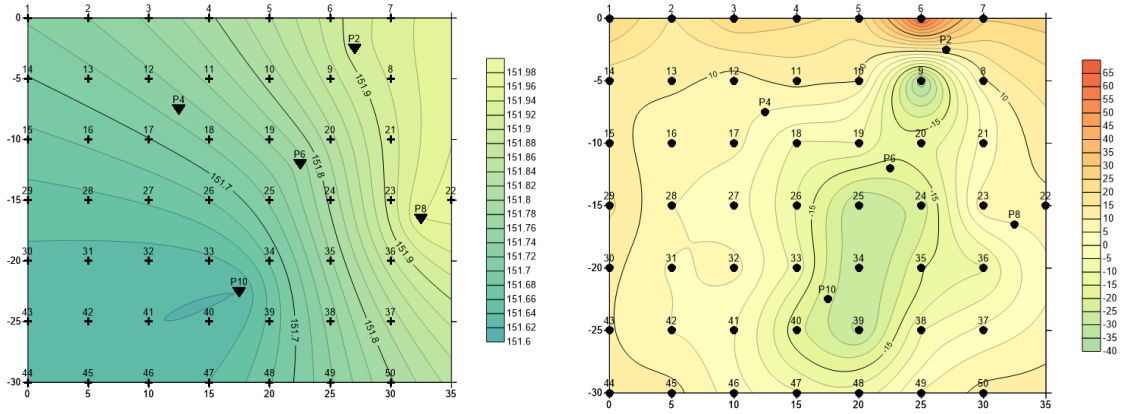

Figure 2. 38: Time evolution maps of the hydraulic head distribution (left) and SP signals (right)

The main aquifer flow direction, has been identified thanks to the maps, Figure 2.38 (left) shows that the groundwater flow goes from the Mavigliano river located in the north of the field, toward the Settimo river in the South.

Furthermore, the SP signals maps showed lower SP values in correspondence of the areas close to the wells (Figure 2.39).

Figure 2. 39: Area with the presence of wells and metal parts

The next step of the study, is represented by the numerical modeling of the experimental experience described before. The aim of the model is the evaluation of the self potential response caused by the rainfall phenomenon, in order to understand the capability of this geophysical technique for aquifers monitoring. The modeling has been performed using the COMSOL Multiphysics software; this is a powerful interactive environment for modeling and solving all kinds of scientific and engineering problems based on the finite element method.

A three-dimensional numerical model, with the following dimensions 250 × 50 × 6 m^3 (Figure 2.40), has been created, wells and SP monitoring points were included. The aquifer has been modeled as a homogeneous and isotropic medium with a uniform saturated thickness. This conceptual scheme is consistent with the lithological features of the area. The coupled (transient) groundwater and electrical flow problems have been solved over a simulation time of 18 days. The following boundary conditions were adopted: Dirichlet boundary conditions were set on the west and east sides of the domain, in which also a null potential condition ($\varphi = 0$) has been adopted for what concerns the electrical flow. No-water and no-electrical flow conditions have been imposed on the north and south boundaries of the model domain (Figure 2.40). A spatial variation law for the hydraulic head has been determined on the basis of the measurements performed in the wells during undisturbed conditions. This law was used to define the initial hydraulic conditions in the model:

$$H = 3{,}92 + 0{,}0212 * y$$

The water amount that infiltrates into the groundwater due to the rain, represents the parameter we want to calibrate, to ensure a correct self potential calculation. This topic will be discussed below in the next section.

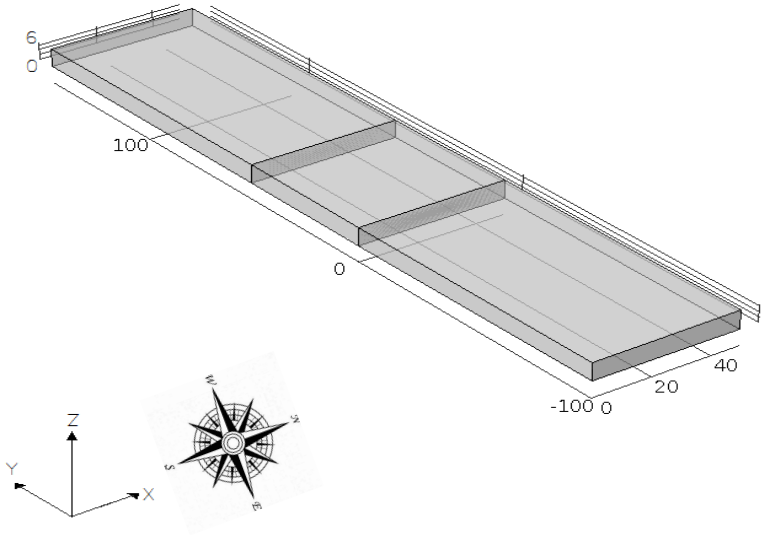

Figure 2. 40: The hydrogeological model

Further details on the modeling assumptions and techniques adopted to simulate the rainfall phenomenon and the resulting response in terms of electric potential, are reported below:

Darcy's law (COMSOL Multiphysics), this law describes fluid flow in porous media driven by gradients in pressure and gravitational potential. The dependent variable in Darcy´s law is always a pressure p but interfaces for inputs in hydraulic head H and pressure head Hp are provided.

The governing equation for fluid flow described by Darcy´s law:

$$\delta_S S\frac{\partial p}{\partial t} + \nabla \cdot \left[-\delta_K \frac{\kappa}{\eta}(\nabla p + \rho_f g \nabla D)\right] = \delta_Q Q_s \qquad [1]$$

where, *S* is the storage coefficient, κ is permeability, η is dynamic viscosity; ρ_f is the fluid density; *g* is acceleration of gravity; *D* is a vertical elevation; and Q_s is the volumetric flow rate per unit of porous medium for a fluid source.

Poisson´s Law (Revil and Abderrahim, 2013) describes the fundamental equation used to interpret self-potential signals in the quasi-statics regime of the Maxwell equations. The total macroscopic electric current density *J* (expressed in A m^{-2}) represents the flux of electrical charges; therefore, the amount of electrical charge passing per cross-sectional surface area of the porous material per unit time

(expressed in C m^{-2} s^{-1} or equivalently in A m^{-2}). It is given by sum of the terms, one conduction current density (described by the classical Ohm´s law) and a source current density J_s, The total current density is, given by

$$J = \sigma_0 E + J_S \qquad [2]$$

where E is the electric field (in V m^{-1}) (in the quasi-static limit of the Maxwell equations written as $E = -\nabla\psi$, where ψ is the electric potential expressed in V), σ_0 is the d.c. electrical conductivity of the porous material (in S m^{-1}), and J_s is a source current density (in A m^{-2}) associated with any disturbance that can affect the movement of charge carriers.

In addition to the constitutive equation, Eq. (2), we need a continuity equation for the current density in order to determine a field equation for the electrostatic potential ψ. In the magnetoquasi-static limit of the Maxwell equations, for which the displacement current is neglected, the continuity equation for the total current density is:

$$\nabla \cdot J = 0 \qquad [3]$$

Equation (3) means that the total current density is conservative (all the current entering a control volume must also exit in the absence of sources and sinks; there is no storage of electrical charges inside the control volume).

Combining Eq. (2) with the continuity equation for the charge, Eq. (3), the self-potential field ψ is the solution of the following elliptic (Poisson-type) equation:

$$\nabla \cdot (\sigma_0 \nabla\psi) = \nabla \cdot J_S \; [4]$$

where the source current density $\Im = \nabla \cdot J_S$ (in A m^{-3}) denotes a volumetric current density. Equation (4) is the fundamental field equation in the interpretation of (quasi-static) self-potential signals. It states that an electrical potential distribution is created by a source term, corresponding to the divergence of a source current density. The electrical potential distribution is also controlled by the distribution of the electrical conductivity σ_0.

Source mechanisms for the generation of spontaneous potentials are typically discussed in the framework of Onsager's relations for coupled flows (*Onsager*, 1931; *de Groot*, 1951; Nourtbehecht, 1963). Electric, hydraulic, chemical, or

thermal gradients provide a "forcing" term, represented by the ∇X_k that can generate any combination of cross-coupled flows ($\mathbf{q}_i$, i = 1:4):

$$q_i = -\sum_k L_{ik} \nabla X_k \qquad [5]$$

The Lik form a symmetric matrix that relates each flow to any combination of forces, where the diagonal elements of L are typical conductivities, such as those in Ohm's or Darcy's laws. In the simplest case we are interested in the total electric current density (j = q1) generated through coupling with one other phenomena in the Earth. In this case, equation (5) simplifies to:

$$j = -L_{11}\nabla X_1 - L_{1k}\nabla X_k = -\sigma\nabla\varphi - L_{1k}\nabla X_k \qquad [6]$$

where, $-\sigma\nabla\varphi$ is the conduction current density that flows throughout the Earth and $-L_{1k}\nabla X_k$ is a source current density related to the coupling process. In the absence of external sources of electric current, the conservation equation requires that the total current density is divergence-free (i.e., $\nabla \cdot \mathrm{j} = 0$) and thus:

$$-\nabla \cdot -\sigma\nabla\varphi = \nabla L \cdot \nabla \mathrm{x} + L\nabla^2 X \qquad [7]$$

The right-hand side of equation (3), which is related to the primary forcing process, provides a source term for the self-potential signal (e.g., Sill, 1983; Revil et al., 2002; Maineult et al., 2005). These sources, along with the resistivity structure and boundary conditions, determine the measured electric potential field. Typical boundary conditions require that $\phi \longrightarrow 0$ as the distance from the source region becomes large, and the normal component of the electric current density is zero at the Earth's surface, i.e., $\mathbf{n} \cdot \sigma\nabla\varphi = 0$ (Dey and Morrison, 1979).

The SP sources are sometimes described as localized "geobatteries" (*Bigalke and Grabner*, 1997; *Timm and Moller*, 2001) that are embedded within the Earth's resistivity structure. Self-potential measurements sample the electrical potential gradients that are created by current flow through the Earth generated by these sources. The self-potential data are therefore a function of the remote thermal/chemical/hydraulic gradient, as well as the resistivity and coupling coefficient structure of the medium.

The task of SP interpretation is to infer something about the location, magnitude, and mechanism of the source from a set of sparsely sampled and possibly noisy measurements. This deficiency of adequate sampling compounds the problem of

non uniqueness that is inherent to potential field methods. A set of surface measurements can be often explained equally well by several different combinations of source shape, depth, and magnitude. Other problems that plague SP measurements are mostly due to the influence of noise or other cultural/natural effects that mask the signal. These difficulties can be minimized through careful survey design but will always be present to some extent and should be accounted for when possible.

Using this approach, we give the parameters in COMSOL for this hydrogeological model:

Water Density: $\rho = 1000\ \mathrm{Kg} * \mathrm{m}^{-3}$;

Porosity (volumen liquid fraction): $\theta_s = 0{,}3$;

Saturated hydraulic conductivity: $K_s = 2 * 10^{-5}\ \mathrm{m} *\ \mathrm{s}$;

Storage coefficient: $s_s = 1{,}045 * 10^{-7}\ \mathrm{Pa}^{-1}$ (Bear, 1979);

Compressibility of soil: $\alpha_G = 0{,}45\ \mathrm{m}^{-1}$; (Gardner,1958)

Electrokinetic coupling coefficient: $C' = -8\ \mathrm{mV} * \mathrm{m}^{-1}$;

The parameters of Archie's law, which depend on the porosity, electrical conductivity and salinity of the rocks are:

Tortuosity: $a = 1$.

This coefficient have present: the variation of compaction, the geometric structure of the pores and the grain size;

Cementation exponent: $n = 1{,}82$.

Also, this is known as the degree of cementation, this increases with decreasing porosity:

Saturation exponent: $m = 1{,}55$.

This associated with the wettability of the rocks; when the rock is water-wet these values are around 2, and takes values between 3 or 4 if the rock is wetted with oil.

Degree of saturation S_w (Gardner,1958) depends on the behavior of α_G and hydraulics head H, this is described in two cases:

$$S_w = ((1 - 0.5 * \alpha_G * H) * e^{0.5*\alpha_G*H}))^{\frac{2}{0{,}5+2}} \quad \text{if} \quad H<0$$

$$S_w = 1 \qquad \text{if} \qquad H>0$$

Electrical conductivity of water:

$$\sigma_W = 103{,}2 * 10^{-4}\ s * m^{-1};$$

Electrical conductivity in saturated conditions:

$$\sigma_{sat} = \sigma_W * \ {\theta_s}^m [s * m^{-1}];$$

Electrical conductivity in function of saturation

$$\sigma(S_w) = \frac{\sigma_{sat} * S_w^{n_{Archie}}}{a_{Archie}}\ [s * m^{-1}];$$

Excess charge in liquid phase under saturated conditions:

$$Q_{v_{sat}} = -\sigma_{sat} * \frac{C\prime}{K_s}\ [c * m^{-3}];$$

Excess charge in liquid phase in function of saturation degree:

$$Q_v(S_w) = \frac{Q_{v_{sat}}}{S_w}\ [c * m^{-3}];$$

The equivalent flow to rainfall on the domain:

$$Q_{rainfall} = 0{,}58\ l * s^{-1}.$$

Model calibration

The hydraulic head variation monitored by the pressure transducers placed in the wells, has been used to calibrate the water flowrate generated by the rain. The estimation of this latter, has been performed through the minimization of the residual between observed and simulated hydraulic heads by an inverse modeling procedure which relies on coupling a transient groundwater flow model with the optimization code Spars Nonlinear OPTimizer (SNOPT) (Gill et al., 2005). The SNOPT solver uses a gradient-based optimization technique to find optimal solutions to a very general class of optimization problems.

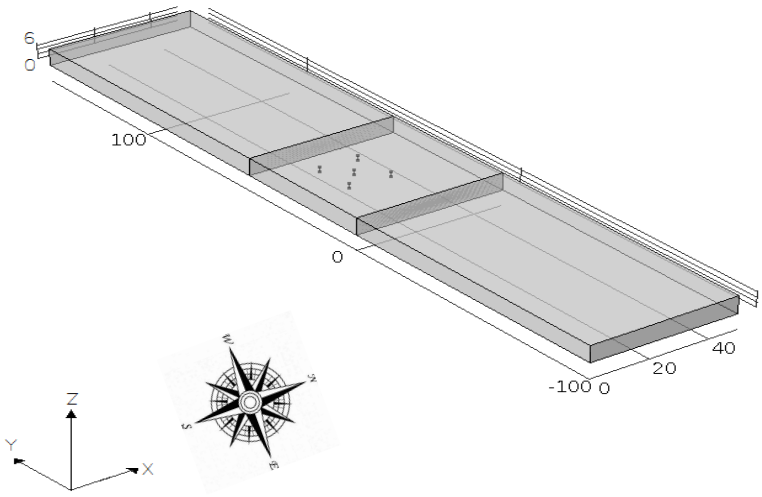

Figure 2. 41: Wells in the model domain

The calibration of the groundwater flow has provided a good superimposition between observed hydraulic heads (red curves) and simulated hydraulic heads (in blue)

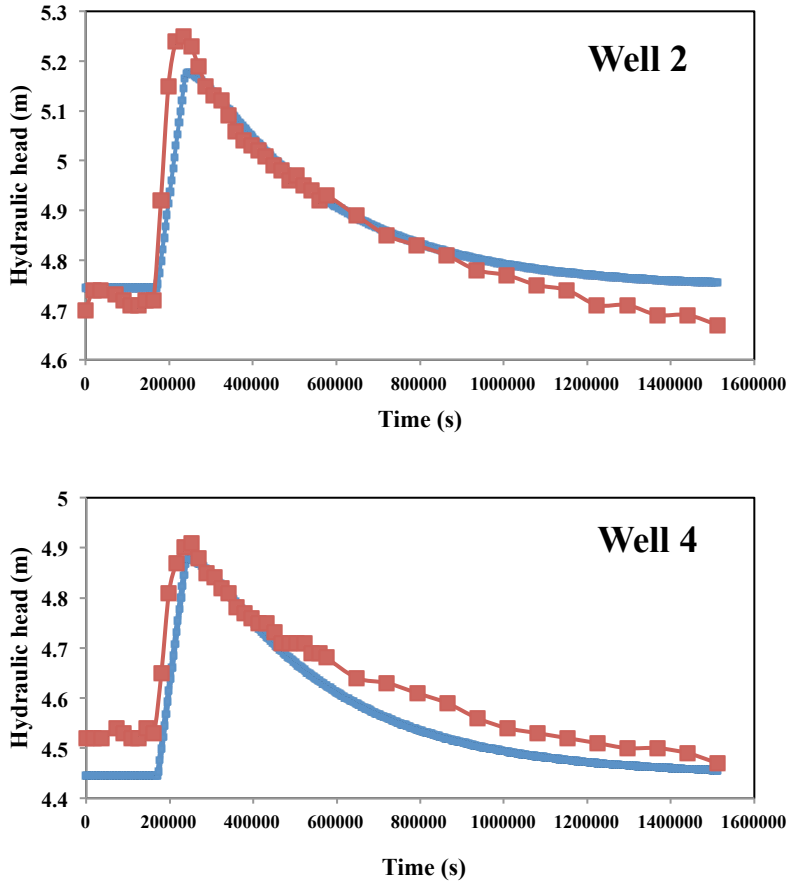

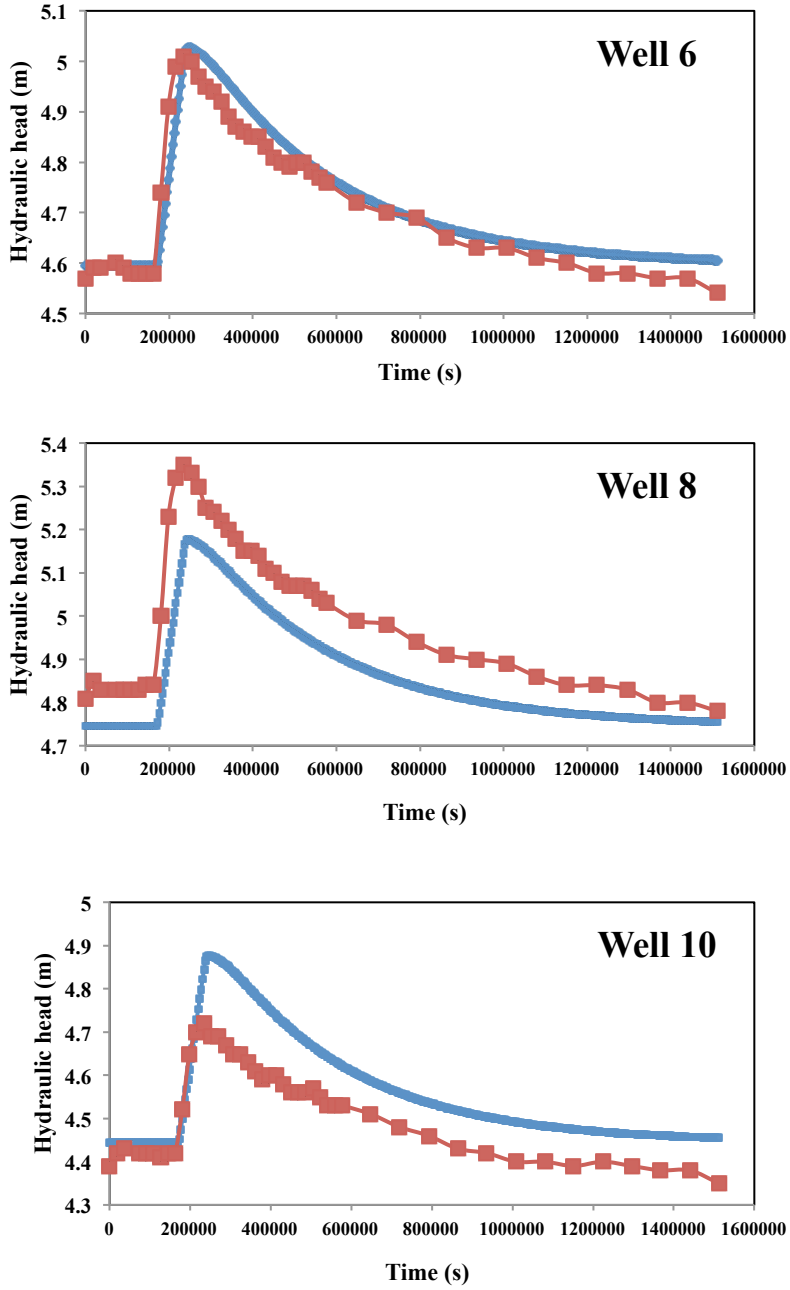

Figure 2. 42: Hydraulic head (5 wells) with respect to time

The calibration of the groundwater flow has provided a value of net infiltration 0.00058 m^3/s. Therefore, we proceed to simulate the electrical flow to calculate the SP signals in the model, and then compare SP signals measured in the field.

Self-Potential (SP) calculation

The self potential calculation has been performed on the domain and the 50 measurements point have been recreated in the model (Figure 2.43).

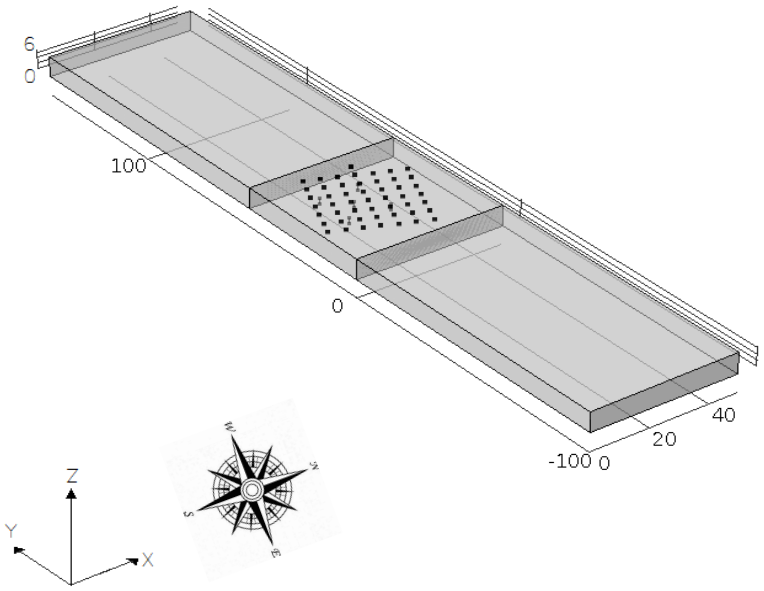

Figure 2. 43: SP signal points in the model domain

The simulation results show that the points have the same tendency. These results don''t show any disturbances, because the model is free form interferences (i.e. wells, pipes, manholes and other metallic parts) (Figure 2.44):

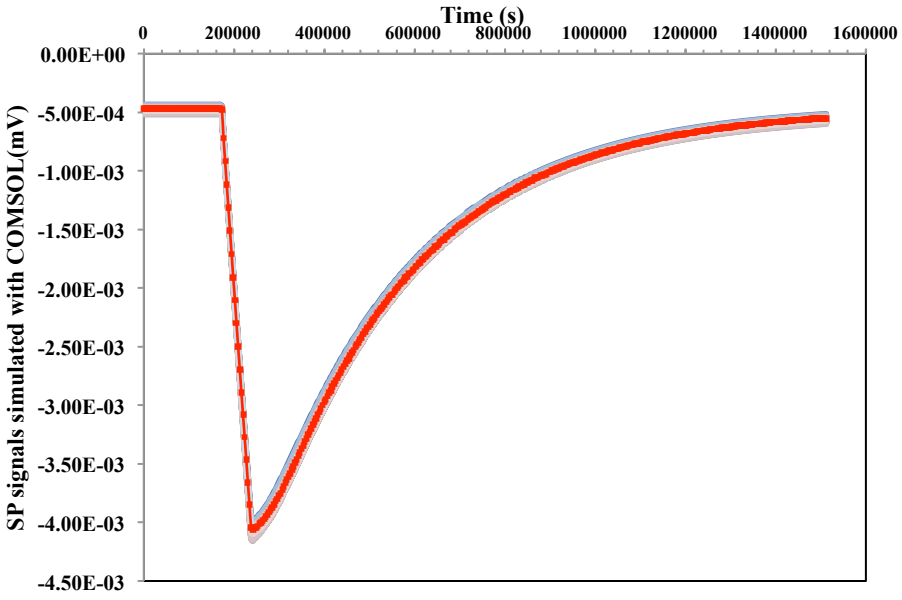

Figure 2. 44: SP signal in all the observation points

However, in order to compare these values of SP signals with hydraulic heads, we use a double axis graphs (Figure 2.45).

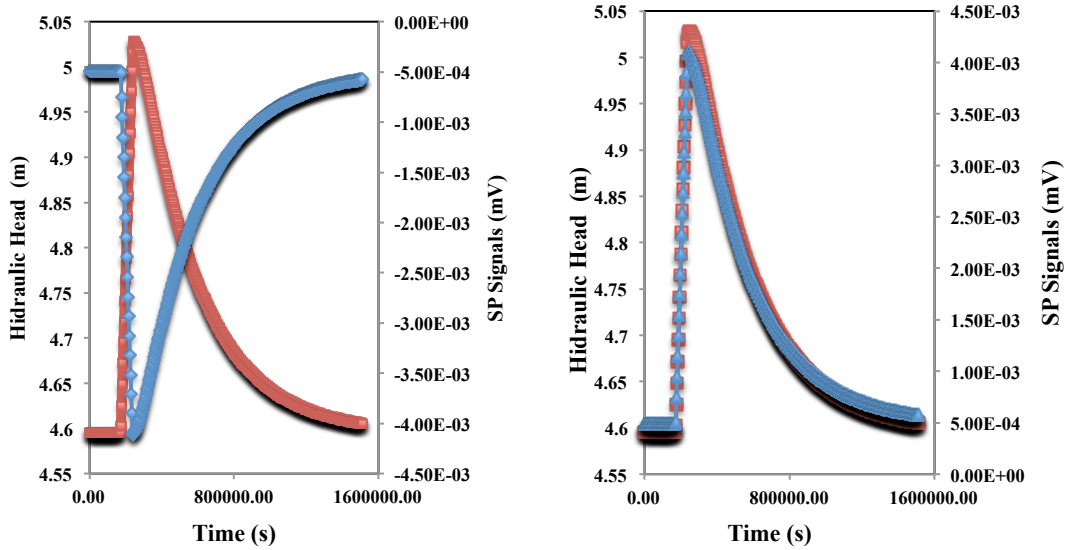

Figure 2. 45: Confrontation between SP and hydraulic head (Piezometer 6 in red, Point 2 in blue)

The function used gives a similar interpretation of the elaborated with COMSOL, but not for all points: This is due to the presence of the metallic casing of the wells that produces heavy electric currents (anomalies) in the field. In order to take in account only the electric signal related to the groundwater flow, we decided to eliminate points which show no consistent values compared to those obtained in COMSOL (Figure 2.46).

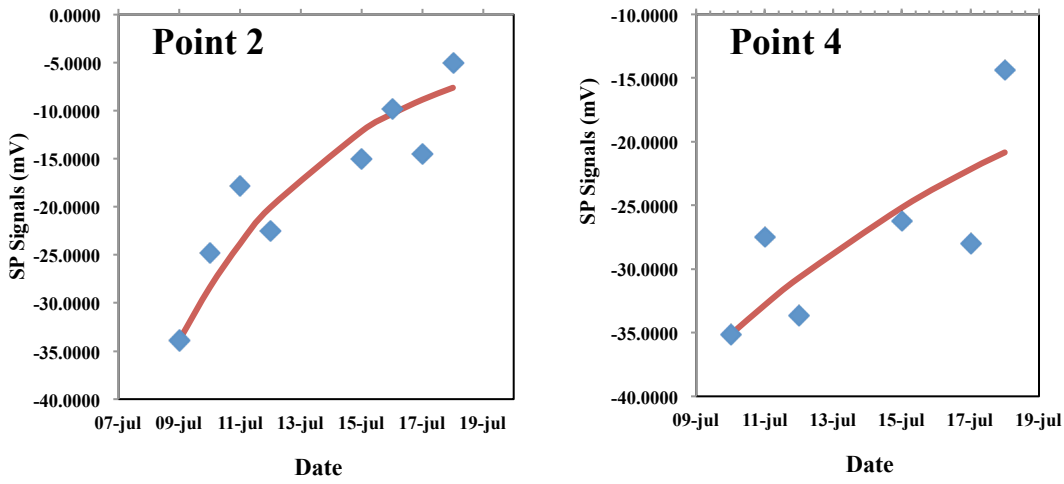

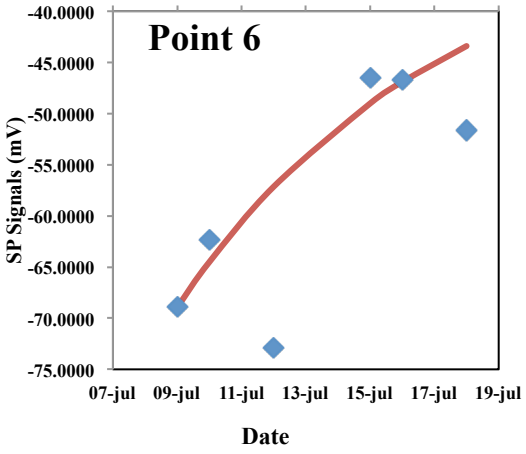
Point 6
SP Signals (mV)
-40.0000
-45.0000
-50.0000
-55.0000
-60.0000
-65.0000
-70.0000
-75.0000
07-jul 09-jul 11-jul 13-jul 15-jul 17-jul 19-jul
Date

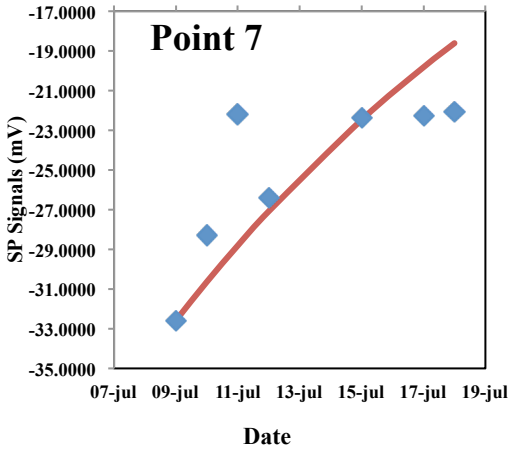
Point 7
SP Signals (mV)
-17.0000
-19.0000
-21.0000
-23.0000
-25.0000
-27.0000
-29.0000
-31.0000
-33.0000
-35.0000
07-jul 09-jul 11-jul 13-jul 15-jul 17-jul 19-jul
Date

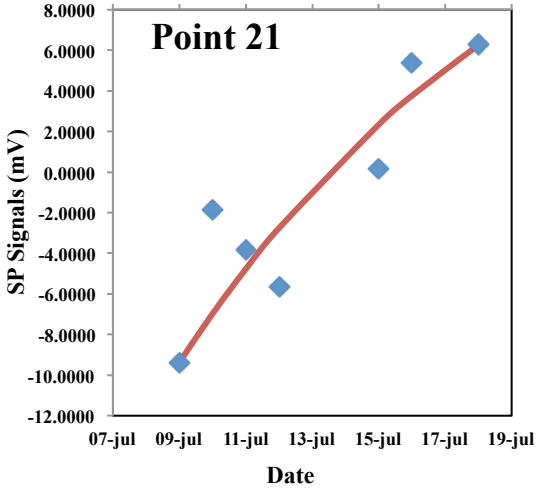
Point 21
SP Signals (mV)
8.0000
6.0000
4.0000
2.0000
0.0000
-2.0000
-4.0000
-6.0000
-8.0000
-10.0000
-12.0000
07-jul 09-jul 11-jul 13-jul 15-jul 17-jul 19-jul
Date

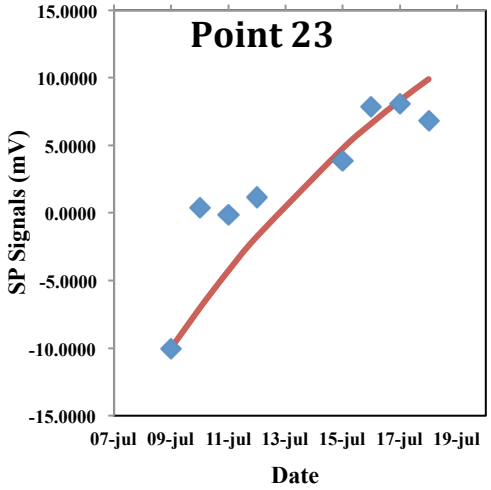
Point 23
SP Signals (mV)
15.0000
10.0000
5.0000
0.0000
-5.0000
-10.0000
-15.0000
07-jul 09-jul 11-jul 13-jul 15-jul 17-jul 19-jul
Date

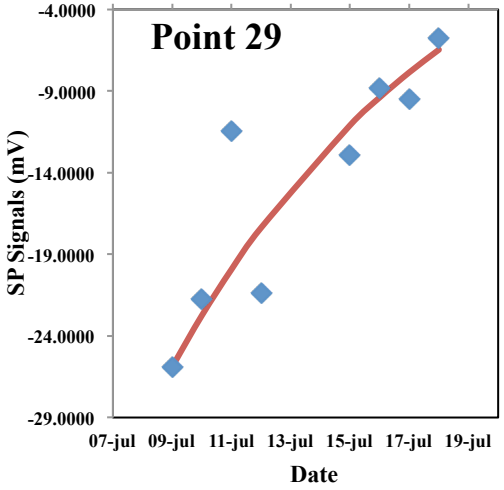
Point 29
SP Signals (mV)
-4.0000
-9.0000
-14.0000
-19.0000
-24.0000
-29.0000
07-jul 09-jul 11-jul 13-jul 15-jul 17-jul 19-jul
Date

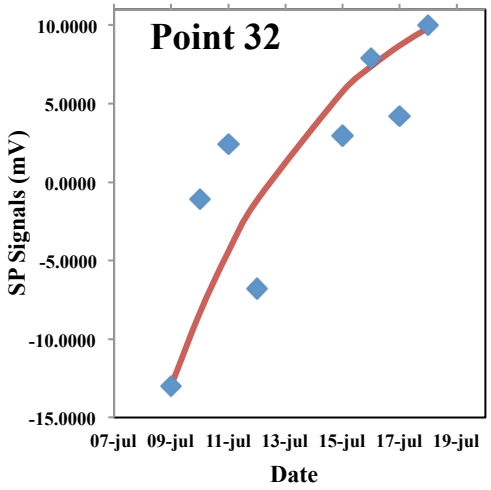
Point 32
SP Signals (mV)
10.0000
5.0000
0.0000
-5.0000
-10.0000
-15.0000
07-jul 09-jul 11-jul 13-jul 15-jul 17-jul 19-jul
Date

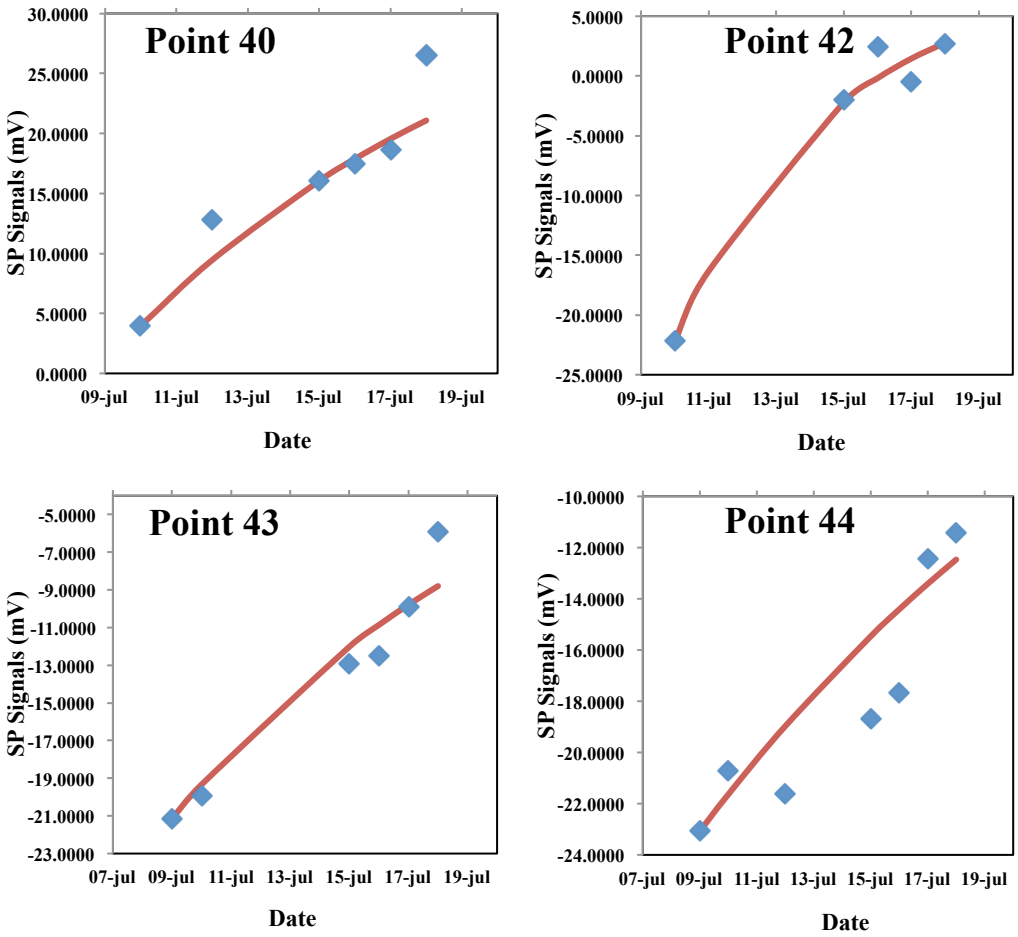

Figure 2. 46: Confrontation between SP smoothed (blue) and simulated (red)

We present methods for detecting groundwater, in particular, we have tried to identify a correlation between the hydraulic heads and signals SP generated by the flow of water passing through porous media under natural stimuli.

From the field measurements we can see how increasing the hydraulic head influences the SP signals; however, when the hydraulic head decreases there are changes in the signals SP but these are not uniform.

The conceptual model realized in COMSOL simulates the variations in time for hydraulic heads and SP signals. This model shows the theoretical correlation between these two variables. The correspondence between the observed SP with the modeled SP curves prove the possibility to guess the position of the water table by means of SP measurements on the field.

CHAPTER 3

3.1 AQUIFER CASE STUDY: Characterization of the Chambo Aquifer – Ecuador

3.1.1 Introduction

The Chambo River basin is located on the highland to the north-west of the Amazon River, in the Chimborazo district. It is characterized by areas with both a low water availability, as well as, a high population density. The increase of the already large population, and the consequent rise of water demand together with the reduction of rain phenomena in the last years, have led to a conflictual relationship between the various communities of the area, due to the uncertainty on the exploitable stock of water. The drinkable water system of the cities located within the basin (Riobamba and Guano), is supplied only by the groundwater coming from the Chambo aquifer. The hydrologic studies performed on the area have only led to conclusions on the superficial water balance without taking into account the groundwater contribution, causing a lack of information affecting the decisional capacity of the authorities responsible of the care and preservation of the basin. Moreover, a study performed on a small portion of the aquifer by means of radioactive isotopes (^{14}C) (Bigo, 2012), states that the groundwater in the aquifer, dates back to 8000 years ago. This result lead the community to think that the aquifer is fossil; and thus, the water reserve is limited due to the lack of lateral and vertical recharge.

The aim of this study is to demonstrate that the aquifer is refilled in time, and to estimate the amount of water coming from the melting of the glacier located on the Chimborazo volcano. A three-dimensional mathematical model of the basin has been developed, in which the information coming from the water balance has been adopted. The hydraulic conductivity distribution has been derived from the interpretation of several pumping tests performed on the basin. The estimation of the water amount coming from the volcano has been obtained by means of an inverse procedure based on the capacity of the model to reproduce the hydraulic heads observed in wells, sources and ponds.

3.1.2 Study area

The Chambo River sub-basin is located on the top of the Pastaza River Basin, its main affluent is the Chambo River, and covers a total area of 3589.55 Km^2 with a perimeter of 339.38 Km. This sub-basin lies entirely in the Chimborazo province - Ecuador (Figure 3.1).

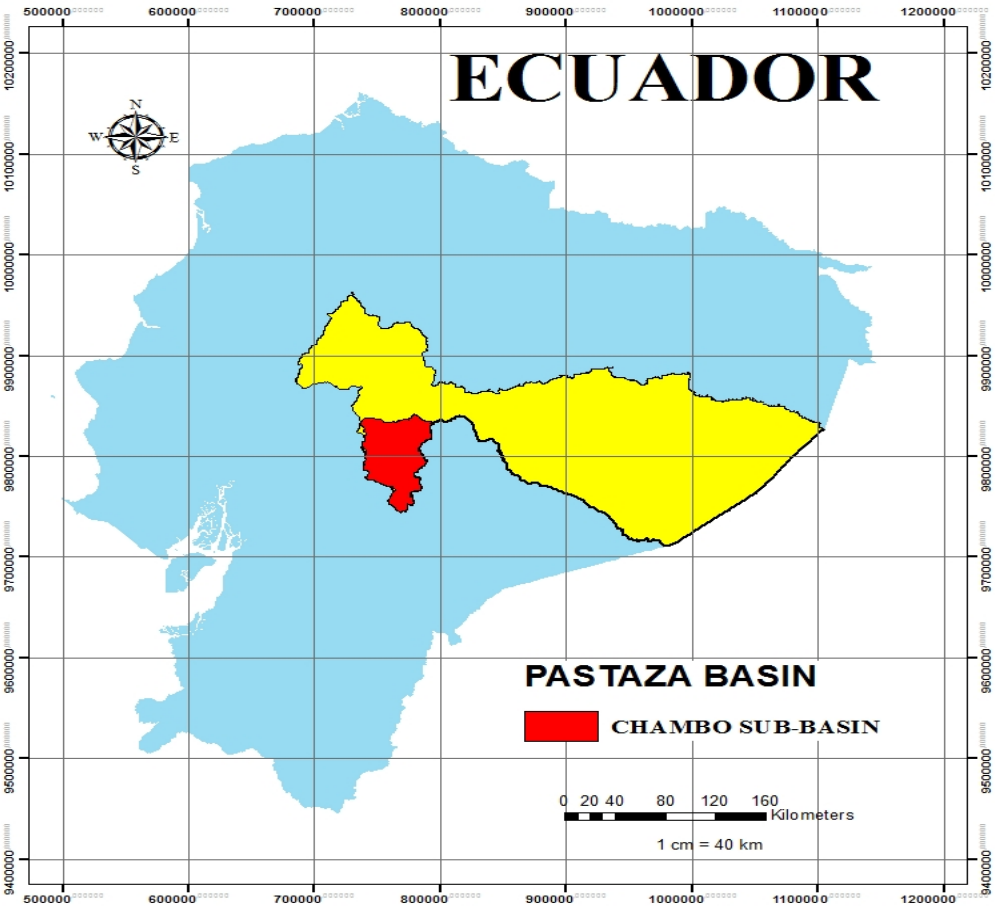

Figure 3. 1: The Chambo Sub-basin in Ecuador

The main river is the Chambo River, which flows from south to north with a length (LRP) of 144.49 Km. The sub-basin is made up by 21 micro basins; the most important micro-basins are Cebadas, Guamote Chibunga, Guano, Puela, Alao, White and Uldán (Figure 3.2).

Figure 3. 2: Micro-basins of the Chambo Sub-basin (Naranjo, 2013)

The elevations of the Chambo river basin varies from 2000 m.a.s.l. at the Chambo River outfall, up to 6280 m.a.s.l. at the top of Chimborazo volcano. As it is located in the inter-Andean zone, it has a hilly topography which also presents steep slopes up to 80% in the foothills of the "Real and Occidental" ranges.

The vegetation depends on height, climate, soil, and human activities. The Chambo sub-basin includes: the Andean wastelands (Palmira desert and Chimborazo sands), the inter-Andean grasslands between 2500 and 3000 m, while the upper part of the mountains is predominated by shrubs, wild plants, forests and pastures (Naranjo, 2013).

3.1.3 Geology and hydrogeology

Geology

The study area is located in the northern Andes; this area is formed by two mountain ranges, which limit the Andean valley: the Real Cordillera made-up by metamorphic and volcanic rocks of the Paleozoic – Cretaceous era(Litherland, 1994; Spikings, 2000 & 2001), And the Western Cordillera of Ecuador, which consists of allochthonous oceanic blocks, developed against the South American plate during the late Cretaceous to Eocene era (Hughes & Pilatasig, 2002; Jaillard, 2004; Spikings, 2005; Vallejo, 2006), and the volcanic arcs of Pallatanga (Vallejo, 2009). The narrow inter-Andean valley is largely composed by volcanic deposits (Neogene - Quaternary), and it's bounded to the East by the Peltetec fault, and to the west by the Pallatanga-Pujilí-Calacalí fault.

Geomorphology

The Chambo River sub-basin is bounded to the north by the Chimborazo-Igualata-Tungurahua junction, and to the south by the Tiocajas junction, where two or more mountain ranges are brought together (López, 1980). It is bordered to the east by the Cordillera Real sources and to the west by the Western Cordillera sources .

Several volcanic formations are located in this sub-basin : Chimborazo (6310 m) and Carihuairazo (5020 m) in the Cordillera Occidental; El Igualata (4430 m) on the inter-Andean basin; El Altar (5.319 m) and Tungurahua (5.023 m) located in the Cordillera Real, characterized by steep slopes and deeply marked by Quaternary glacial erosion.

The upper mountain ranges of the Occidental and Real, stand out for their glacial landscapes. The sequence of moderate and steep reliefs is the result of ice erosion, lava

flows and moraines. Moving down, at a lower altitude, a set of hills with wide and rounded tops, steep slopes, made by Pliocene pyroclastic rocks, apparently seem to jointhe mountain slopes. These volcanic formations can be often accompanied by colluvial-alluvial deposits. Glaciers, alluvial fans with moderate slopes, weak to moderate dissections topped by strong and continuous pyroclastic layers cemented in cangagua, are prevalent to the south and southeast volcanic formations of Igualata and Chimborazo (Winckell, Zebrowski, & Sourdat, 1997).

The Chambo River flows from south to north from Guamote to Riobamba, in a wide valley with multi-slope terraces. A small gorge, between the Igualata and Tungurahua volcanoes is observed in the Penipe area (Winckell, Zebrowski, & Sourdat, 1997).

Local Geology

The geology map (Figure 3.3) shows the geo-materials of the Chambo River sub-basin:

Agoyán Unit (Pzla) (Paleozoic).- This unit of pelitic schist and paragneiss has a typical lithology of garnet schists, medium grain muscovite and gneiss.

Tres Lagunas Unit (TrL) (Triassic).- This unit includes biotite granites and gneisses, some blue quartz, muscovite and garnet. The granite shows evidence of deformation, metamorphism and recrystallization; ranging from incipient alterations in massive rocks with preserved igneous textures (monzogranite - granodiorite), to the formation of gneiss, mylonitic granite and augen gneiss.

Alao - Paute Unit (JAA) (Jurassic - Early Cretaceous).- This unit shows a sequence of massive to sheared green-rocks and schistose andesitic. Minor lithologies include greenschists (metatuffs), graphitic schist, pelitic schist, and dark marble.

Maguazo Unit (JAM) (Jurassic - Early Cretaceous).- This unit shows a sequence of slightly metamorphosed turbidites and basaltic andesites. The turbidites are fine-grained silica with graded stratification. Typically, the andesites are massive rocks with some alteration to compact green rocks; other lithologies are green metatuffs, black slate, marble, orthoquartzites and cherts.

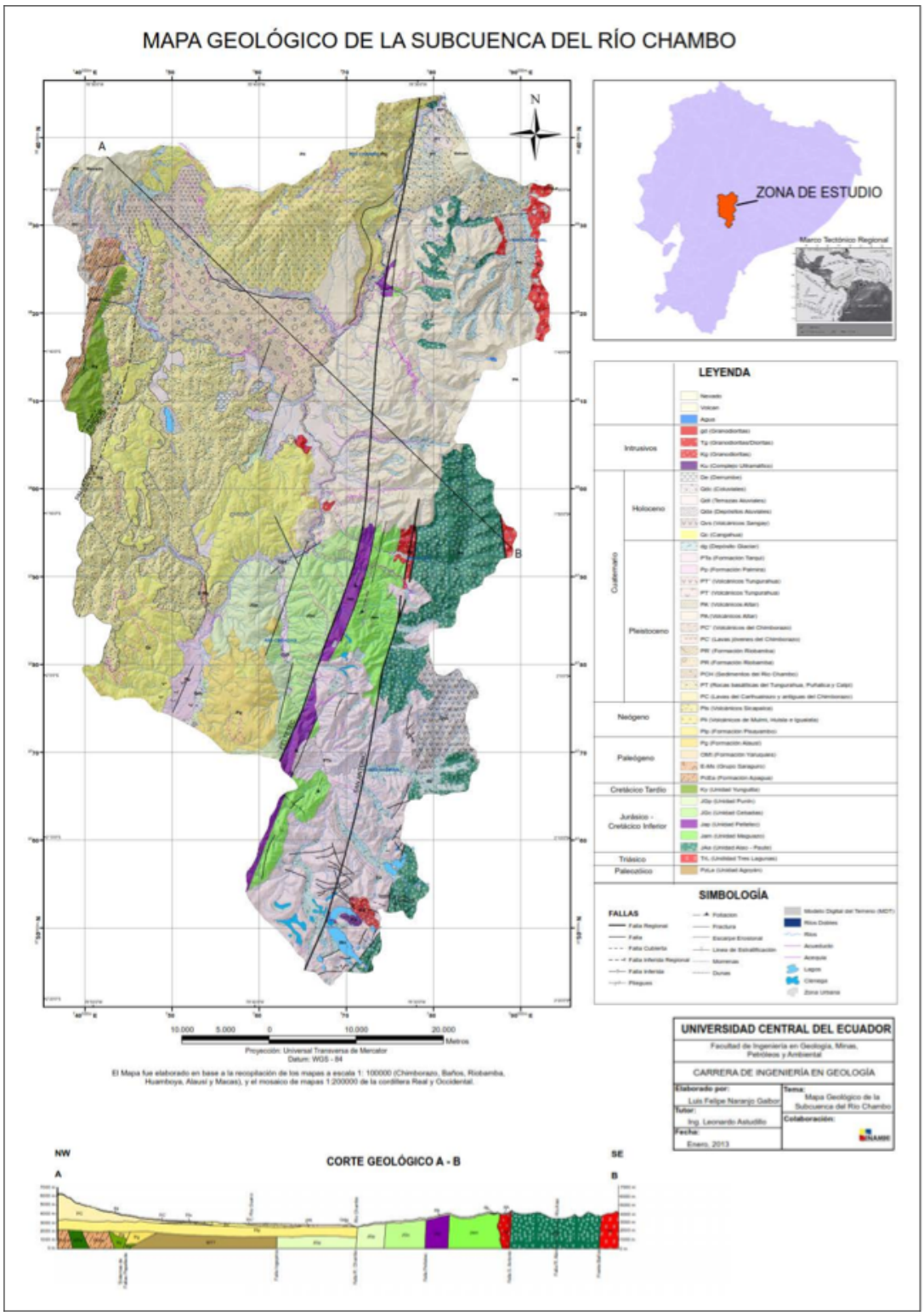

Figure 3. 3: Geologic map of the Chambo Subbasin (Naranjo, 2013)

Peltetec Unit (JAp) (Jurassic - Early Cretaceous).- This unit shows a sequence of metabasalts, serpentinites, pyroxenites, hornblendites, black phyllites, volcanoclastic rocks, undisturbed plutonic rocks such as gabbros of melanocratic olivine and

peridotites. The Peltetec area rocks are considered to be part of the sedimentary oceanic crust.

Punín Unit (JGP) (Jurassic - Early Cretaceous).- This unit includes quarzites presenting a color range going from a pale white to grey or from pink to red with a variable granulometry from medium-grained (feldspar) to coarse-grained, interspersed with shales presenting a color range going from black to grey. Ferruginous sandstone and clay concretions can also be present, .

Cebadas Unit (JGP) (Jurassic - Early Cretaceous).- This unit includes shales presenting a color range going from grey to black; and subordinate quartzite, fine to medium grained, with a color range going from black to grey.

Yunguilla Unit (Ky) (Maastrichtian).- This unit is defined the Yunguilla Formation and it's characterized by a sedimentary series of dark grey turbiditic siltstones and sandstones exposed to the west of the Nono village. (Thalmann, 1946).

Apagua Formation (PCEA) (Paleocene to Middle Eocene).- The Apagua Formation consists of medium-grained sandstones, dark grey siltstones and mudstones, and siliceous silty mudstones deposited within turbiditic facies. The sandstones are typically feldspathic and contain abundant quartz and micas, and are classified as feldspathic litharenites and sublitharenites (Vallejo, 2007).

Saraguro Group (E-Ms) (Oligocene).- This group includes a sequence of andesitic porphyritic lavas with a greenish grey color, breccia and andesitic tuffs, unconformably overlying the Apagua formation; and is overlain by the group Zumbagua (Dunkley & Gaibor, 1997).

Yaruquíes Formation (OMT) (Tertiary).- This formation is composed at its base by fine reddish-yellow sandstones, and on top by andesitic conglomerates and quartzite layers with interbedded layers of medium-grained reddish sandstone. While at the top, the conglomerates are unconformably composed by clay layers.

Alausí Formation (Pg) (Paleocene).- Lithologically consists of: andesites, pyroxene andesites, hornblende, and porphyritic rhyolite. Although on a smaller scale, rhyolitic tuffs and andesitic agglomerates are also present. The thickness of this formation exceeds 1500 m (Longo & Sosa, 1972-1973).

Pisayambo Formation (PLP) (Pliocene).- This formation includes layers of agglomerates and andesitic lavas. The agglomerates include andesite blocks placed in a very compact matrix (Lozada & Randel, 1973).

Mulmi, Igualata and Huisla volcanics (PLI) (Pliocene).- The pyroclastic rock of these volcanic formations is common and varies from fine-grained tuff to coarse tuff pumícea. The andesites are abundant in this volcanic area (Lozada & Randel, 1973).

Sicalpa Volcanics (Pls) (Pliocene).- This volcanic area consists of tuffs and agglomerates. The tuffs are fine-grained with presence of some medium-sized clasts. The agglomerates have an intermediate composition and are predominantbetween a depth of 10-15 m (Lozada & Randel, 1973). In some places, andesitic lava flows show up between the agglomerates.

Carihuairazo lavas and ancient lavas of the Chimborazo (PC) (Pleistocene).- The volcanic activity of the Carihuairazo and Chimborazo volcanoes date backto the Pleistocene. The volcanic formations are responsible of the production of fine grain mesocratic porphiritic andesites

Basaltic rocks of Tungurahua, Calpi and Puñalica (PT) (Pleistocene).- TUNGURAHUA: the volcanic activities of Tungurahua volcano produce basaltic mesocratic lava flows with fine grain; moreover, basaltic tuffs extend along the Chambo River. PUÑALICA: includes fine-grained melanocratic basaltic lava , basaltic andesite flows and porphyritic olivine basalts. CALPI: includes basaltic ash deposits associated to the volcanic activities of Yanaurcu and Tulabug craters.

Chambo River sediments (PCH) (Pleistocene).- The sediments are composed by conglomerates, sandstones and fine clays, with fine ash banks. Conglomerates include rounded pebbles, and boulders of andesitic composition, with metamorphic fragments and unconsolidated coarse-grained sandstones of andesitic composition. These sediments were deposited in a lake which was formed when the Chambo River was blocked by Tungurahua lava flows .

Riobamba Formation (PR & PR') (Pleistocene).- This formation constitutes the lahars of the Chimborazo volcano. It is composed by rounded and angular gravel; the thickness does not exceed 100 m (Sosa & Guevara, 1973). In the same formation there is another group of sedimentary rocks, partially covered by the lahars, such as clays,

tuffs and ashes which alternate irregularly between perfectly stratified layers. Their thickness is about 40 to 50 m.

Young Lavas of the Chimborazo (PC) (Pleistocene).- These young lava flows are located to the south and southwest sides of the mountain and include fine-grained rocks made up by pyroxene andesitic, mesocratic, porphyritic and vesicular (Sosa & Guevara, 1973).

Volcanic Chimborazo (PC'') (Pleistocene).- The final volcanic activity phase of Chimborazo is characterized by pyroclastic eruptions. These pyroclastic rocks include coarse-grained pumiced tuffs horizontally stratified (Lozada & Randel, 1973). The andesitic tuff fragments are also common, their thickness do not exceed 15 m.

Volcanic of Altar (PA & PA') (Pleistocene).- The Ulpán river subdivide this area in north and south pyroclastic lavas. The pyroclastic rocks are composed primarily by pumice and andesitic fragments and some sectors presented pseudo-stratifications with insertions of sandy tuff layers (Sosa & Guevara, 1973). However, the lavas have an intermediate and basic composition.

Volcanic of Tungurahua (PT '& PTT'') (Pleistocene).- The Tungurahua volcano is largely composed by porphyritic andesites (oldest lavas) and basaltic rocks (young lavas), these rocks are discordant with the metamorphic and volcanic rocks of the Altar volcano (Malo & Mortimer, 1978-1979)

Palmira Formation (Pp) (Pleistocene).- This volcanic-sedimentary formation covers the areas of Alausí and Riobamba. These formations are composed fundamentally of clayey sediments and insertions of tuffaceous strata-diatoms. At the top, the sediment layers alternate with conglomerate layers, and the thickness reaches a few hundred meters (Sosa & Guevara, 1973).

Tarqui Formation (PTa) (Pleistocene).- The rocks of this formation are essentially pyroclastic: agglomerates, tuffaceous agglomerates and tuffs of intermediate and acidic composition, presenting a quite horizontal stratification(Sosa & Guevara, 1973).

Glacial Deposit (dg) (Pleistocene).- These deposits are located in a U-shape valley, and includes: tillites, sand, gravel and sedimentary blocks of variable composition (Sosa & Guevara, 1973).

Cangagua (Qc) (Quaternary).- This coffee-colored tuffs forms a surface almost located under all the formations of the sub-basin. The tuffs are fine-grained with coarse-grained banks, and the thickness varies from 1 to 5 m (Sosa & Guevara, 1973).

Volcanic of Sangay (Qvs) (Holocene).- Their deposits are composed byandesitic gray-green lavas, pumiced, pyroclastic and masses of compact molten lava (Marín & Verset, 1986-1988).

Superficial Deposits (Holocene).- The alluvial deposits (Qda) are limited by the valleys of the Chambo, Blanco, Guano and Puela rivers (Lozada & Randel, 1973).

The alluvial terraces (Qdt) were developed in the Pallatanga between: Blanco, Chambo, Ulpán , Guasuntos-Zula, Alao rivers; and Chalhuaicu ravine. There are two levels of terraces in the Riobamba valley, the first is fully covered by cangagua; and the second level of terraces are formed by gravel layers which alternate with tuffs and lahar materials arranged almost horizontally (Sosa & Guevara, 1973).

The colluvial deposits (QDC) can be found in the foothills of the steep slopes mountains , especially on the Yunguilla formation and in the pyroclastics of the Yaruquies formation (Sosa & Guevara, 1973).

Intrusive.- These formations are intrusive bodies of the Cretaceous-Tertiary age with different composition, their outcrop are mainly located on the Cordillera Real and include: ultramafic complexes (Ku), granodiorite (Kg), granodiorite/diorite (Tg), tonalite (Tn)

Structural Geology

The tectonic of the area is mainly characterized by regional faults in the following directions NNE - SSW, NE - SW, N - S. The sub-basin is dominated to the east by the fault of the Cordillera Real. The San Antonio fault is inside the area of Alao, this fault divides the unit arc of Alao-Paute islands, with the metaturbiditas of the Maguazo unit. The Peltetec fault separates the lands of Guamote and Alao and is interpreted as a suture (Aspend, 1992). In the Alao land are identified numerous foliations parallel to the direction of the regional faults.

Pangor, Pallatanga, Bulubulu failures are located to the West of the sub-basin with NNE direction. These are part of the regional fault system bordered to the east by the oceanic cretaceous rocks of the Pallatanga unit (McCourt, 1997).

The Tambillo fault, in the NW of the sub-basin, extends up to the Chimborazo volcano showing the tectonized basic rocks of the Pallatanga unit in contact with the black shales of the Yunguilla unit (McCourt, 1997). In the Apagua and Yunguilla units, folds with similar directions can be identified at the regional faults.

The sub-basin is considered as an area of neotectonic activity, related to the reactivation of deep faults.

Historical Geology

The metasediments of the Agoyán unit were intruded by S-type granites of the Tres Lagunas units related to Tres Lagunas event.

During the Jurassic-Early Cretaceous, in the Thethis ocean, there was a subduction zone along the South American margin (Jaillard, 1990), which generated the island's arc (Alao-Paute), the ante-arc basin (Maguazo unit) and the basin of back-arc (Pan unit). While the Guamote ground (Punín and Barley units) is interpreted as a sequence of passive margin of Jurassic-Lower Cretaceous age. The rocks of the Jurassic-Early Cretaceous of the Cordillera Real were affected by the Peltetec event as is shown in the melanges of the Peltetec unit.

During the Late Cretaceous, the collision of oceanic allochthonous field of the Pallatanga in the South American margin occured. During the Late Eocene the Macuchi arc was obliquely formed, and as a result Apagua-Yunguilla units were lithologically deformed; the fragments of the Pallatanga unit were tectonically emplaced within them (Pilatasig & Duke, 1997). During the accretion event, the Macuchi arc was deformed, partitioned and transferred to the North.

During the Oligocene, a margin of the continental calc-alkaline arc was developed along the Ecuadorian Andes,(Saraguro Group) (Pilatasig & Duke, 1997). The fracture of the Farañón plate and the formation of Nazca and Cocos plates occurred about 25-22 Ma ago (Pliger, 1983), this event may have caused the opening of the inter-basin (Noblet, 1988).

The geological evolution of Ecuador, during the Miocene-Pliocene, was dominated by the formation of intramontane basins and subaerial volcanism. "(Lavenu, 1990 & 1993).

Thus, the Pisayambo formation was developed in the Pliocene (fissure eruptions) and later the centers of Mulmi, Huisla, Igualata, Sicalpa.

In the late Pliocene about 2 Myr ago, there was a further reorganization of the Pacific plate system, probably because the dorsal Carnegie came into contact with the active subduction zone (Pilatasig & Duke, 1997). As a result, ancient structures in the Cordillera Occidental re-emerged and the formation of large andesitic volcanoes occurred to the N 2° 30' S.

During the Pleistocene there was volcanic activity at the Chimborazo, Tungurahua, Altar, Carihuairazo volcanoes giving origin to the formation cones of Calpi and Puñalica. The lahars of the previous eruption of the Chimborazo created the Riobamba formation and the development of glacial deposits.

The deposition of the Cangahua formation (Quaternary), the surface deposits (Holocene), the eruptions of Tungurahua and Sangay (Holocene) were the final geological events in the formation processes.

Hydrogeology

The fundamental objective of the hydrogeological characterization is the identification of the significant geomaterials defining the stuctureof the aquifers. A qualitative characterization of the Chambo sub-basin was performed through the hydro-geological information, the hystorical series of water level measurements and literature permeability values of the exposed geological formations. The characterization shows that the 26% of the sub-basin area, includes permeable formations with intergranular porosity (Naranjo, 2013).

a) Permeable lithologic units with intergranular porosity

Medium to High Permeability: Includes 6% of the surface of the sub-basin. Within this group the following formations are considered:

- Alluvial terraces (Qdt) Alluvial (Qda), colluvial (Qdc), which include gravels, boulders of varying size and consolidated sands; these are included in the valleys of the Chambo, Blanco, Guano and Puela rivers. The Riobamba valley has two levels of terraces formed at the base of gravel layers alternating with lahar materials and tuffs arranged almost horizontally.

- Palmira Formation (Pp) (Pleistocene).- This volcano-sedimentary formation covers the Alausí and Riobamba areas. These formations are composed fundamentally of clayey sediments and insertions of tuffaceous strata-diatoms. At the top, the sediment layers alternate with conglomerate layers, and the thickness reaches a few hundred meters.

Lower to Medium Permeability: Includes the 6% of the surface of the sub-basin, within this group the following formations are considered:

- Yaruquíes Formation (OMT) (Tertiary).- This formation is composed by fine reddish-yellow sandstones, surmounted by layers of andesitic conglomerates and quartzite with interbedded layers of medium-grained reddish sandstone. While at the top the conglomerates are unconformably made up by clay layers. the formation is located to the South of the Yaruquies area.
- Riobamba Formation (PR & PR') (Pleistocene).- This formation constitutes the lahars of the Chimborazo volcano and stands up between the Chambo and the Chibunga rivers. It is composed by rounded and angular gravels, which, in some areas, are stratified as a result of deposition in water. The thickness does not exceed 100 m (Sosa & Guevara, 1973). In the same formation there is another group of sedimentary rocks as clays, tuffs and ashes, alternating irregularly between perfectly stratified layers. Their thickness is about 40 to 50 m. They are oftenin contact with lahar partially covering them. The formation includes aquifers located in zones generally exploitable through deep wells.
- Chambo River sediments (PCH) (Pleistocene).- These sediments emerge between the Licto, Chambo and Punín towns and include conglomerates, sandstones and fine clays, with fine ash banks. Conglomerates include rounded pebbles, and boulders of andesitic composition, with metamorphic fragments and unconsolidated coarse-grained sandstones of andesitic composition. In this area aquifers of relative importance may be present.
- Apagua Formation (PCEA) (Paleocene to Middle Eocene).- this formation appears SW on the slopes of the Chimborazo volcano. Because of its locationno wells have been drilled , even if it could represent great source

of groundwater.It includes fine-grained sandstones belonging to middle and fine strata, interspersed with black silicified siltstones, and coarser sandstones.

Low permeability: Approximately the 14% of the area of the sub-basin include units with low permeability, as follows:

- Glacial deposit (of) (Pleistocene).- includes a series of U-shaped valleys formed by tillites, sand, gravel and blocks. Based on their characteristics do not have hydrogeological interest.
- Cangagua (Qc) (Quaternary).- It appears practically in all the surfaces of the sub-basin; its lithology includes tuffs with particle size from mean to fine, and low permeability. The hydrogeological importance of these layers is reduced; usually, they form aquitards, which allow water infiltration to the lower layers through dripping.

b) Permeable lithological units by fissuration

Includes 56% of the area of the sub-basin, within this group the following formations are considered.

Lower to Medium Permeability: Includes 9% of the surface of the sub-basin, within this group the following formations are considered:

- Yunguilla Unit (Ky) (Maastrichtian).- Lithologically includes shales, black-gray siltstones, fine-grained mafic sandstone and gray bioclastic limestones. It presents a high degree of fracturing, therefore, has a medium to low permeability.
- Deposits of Saraguro Group (Oligocene) and Pisayambo Formation (Pliocene).- This area includes a high degree of fracturing and generally the groundwater can be exploited by springs.
- Chimborazo, Carihuairazo, Altar and Sangay Lavas (Quaternary).- These units of volcanic origin include sheet lavas, agglomerates and fine-grained pyroclastic material. These are surface materials, which include a secondary permeability due to their fissuring. These units are associated with the recharge area, allowing filtration through discontinuities; groundwater in these units may be exploited mainly by springs. Llío is the major hydrogeological area interest, and includes young lavas of

Chimborazo; in this area are present 7 bored wells, with an approximate flow rate of 520 l/s.

Low Permeability: This group includes all the volcanic formations from which pyroclastic deposits over lava mantles predominate and are not being affected by important tectonic phenomena; generally they can act as aquitards, occupying approximately the 47% of the sub-basin area, therefore there are:

- Deposits of the Alausí formation (Paleogene), the Mulmi, Huisla e Igualapa volcanoes (PLI) (Pliocene).- isolated springs are located over these formations. Hydrogeologically this unit can be considered a semi-impermeable underlying rock of the lava from the Chimborazo.
- The Sicalpa (Pls) (Pliocene).- located to the south of the Chibunga river, does not represent a hydrogeological area of high interest, generally springs associated to regional guidelines are present.
- The agglomerates, tuffaceous agglomerates and intermediate, acidic composition tuffs of the Tarqui formation do not represent hydrogeological interest, given its sparse fracturing.

c) Impermeable Lithological Units

All the metamorphic sequence (Loja Terrain, Alao, Guamote, Chaucha), at the Real mountain range, that extends towards east of the Chambo riverbed and the intrusive bodies, that surface towards the southern end of the sub-basin, have been considered as practically impermeable units covering approximately the 18% of the sub-basin. The hydrogeological map of the Chambo river sub-basin can be seen in Figure 3.4.

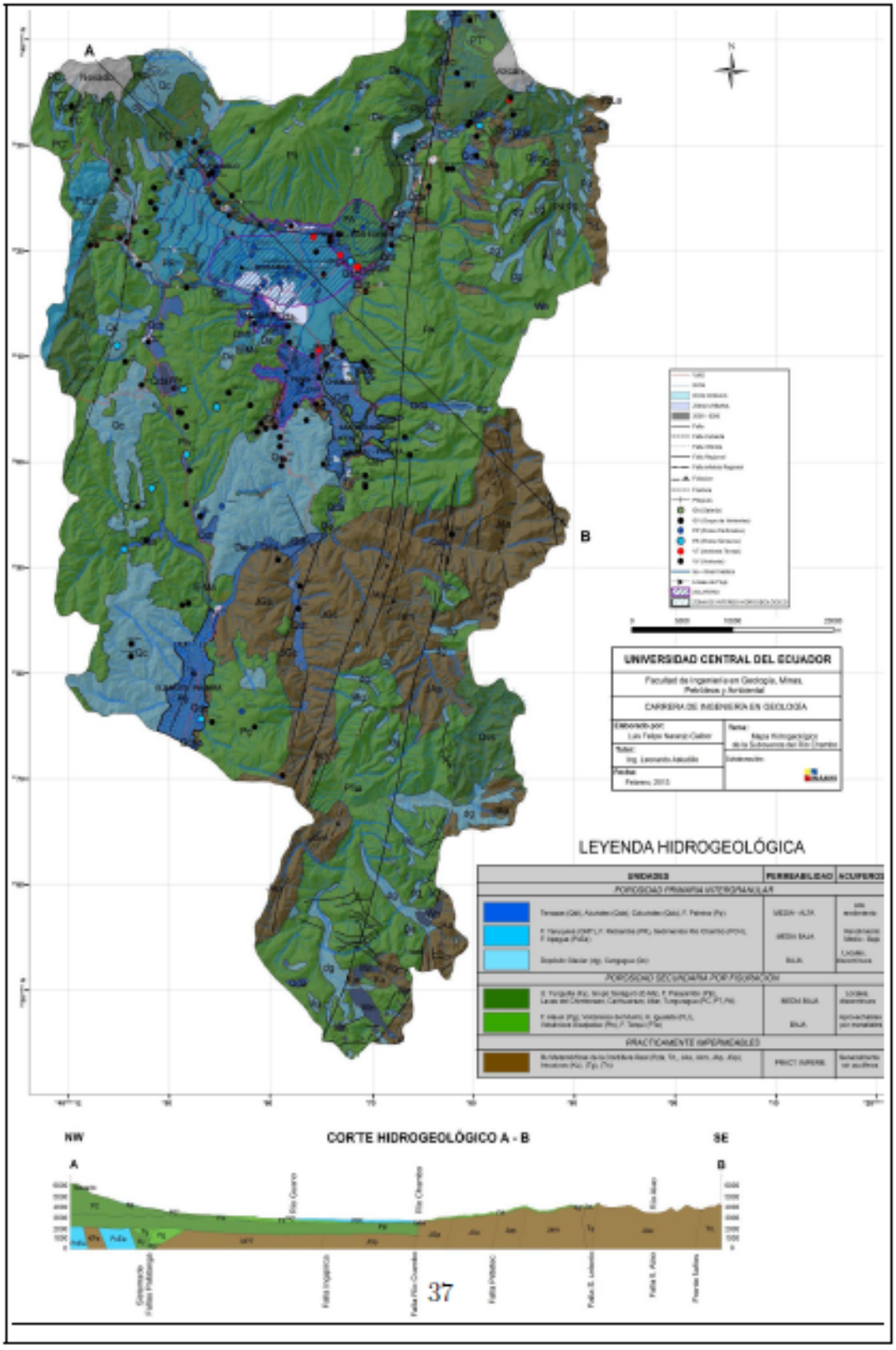

Figure 3. 4: Hydrogeological map of the Chambo River Sub-basin (Naranjo, 2013)

Based on the hystorical series of the water level measurements, monitored by the INAHMI and DGGM (1983), a piezometric map was made for the Chambo river sub-basin. According to the Hydrogeological and Piezometric map of the Chambo river sub-basin, the main areas of hydrogeological interest are located towards the West of the Chambo River (going North towards the river mouth of the Uldán at the Chambo river):

d) Chambo Aquifer in Riobamba

The area is limited to the North by the Guano River, to the South by the Chibunga River, to the Est by the Chambo River and to the West by the snow-capped Chimborazo. The area is characterized by a relatively flat topography, poor drainage and low flow.

Geological Synopsis. The volcanic deposits of the Riobamba formation are characterized by two sedimentary facies: A blockage and a matrix facie. The blockage facie consists in a mono lithological clast deposit. The main geomaterials are: andesite with pyroxenes, andesitas and dacitas with hornblende. The matrix facie consists in a variety of volcanic lithologies mixed in with a limo–sandy base. These deposits according to Beate & Hall, 1989, date back to 50 - 60 Myr. The Riobamba formation lies beneath the volcanic deposits of the Pisayambo formation that consists of agglomerate mantles and andesitic lava of the Neogene. Figure 3.5 shows a geological section crossing the Riobamba aquifer.

Hydrogeological Synopsis. The area is characterized by the presence of 8 springs and 16 monitoring wells.

The Chambo aquifer in Riobamba has an exploitation flow rate of 208.43 l/s, from which 174 l/s withdrawn by the wells and 34 l/s supplied by the springs. Based on the analysis of the drilling and electrical registries of SP (Spontaneous Potential) and resistivity, the present study did two correlations for the Chambo aquifer in Riobamba:

- **Correlation (A - B) crosswise (SW - NE),**
- **Correlation (C - D) lengthwise (NW – SE).**

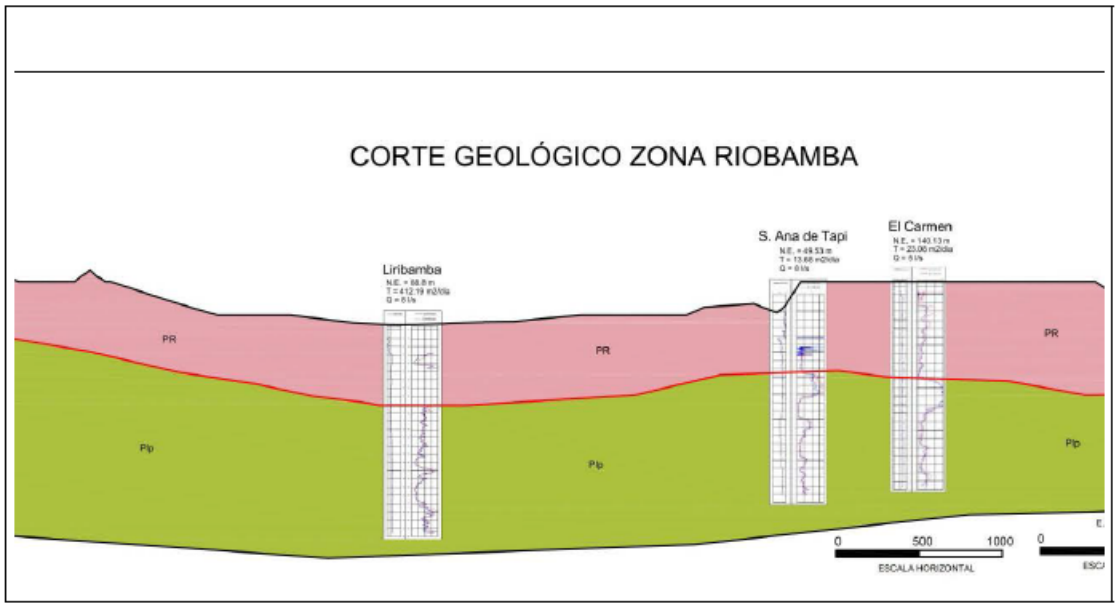

Figure 3. 5: Geological cut in the Riobamba area (Naranjo, 2013)

Figures 3.6, 3.7 and 3.8 show the performed correlations and their hydrogeological interpretation.

The aquifer ,in the Riobamba area, is generally located over the volcanic deposits of the Pisayambo formation. According to correlation (A - B) the aquifers are located starting from a depth of 90 m.

Going NE in the wells of Santa Ana de Tapi and El Carmen, at a depth of 250 m, up to four overlapped aquifer were identifiedand considered as local and discontinuous. The upper one is the most important with a thickness that varies between 30 and 40 m.. A relatively shallow aquifer, at a depth of 25 m and with a thickness of about 15 m, was identified by the well of El Carmen, . This aquifer can be seen as a confined aquifer within the Riobamba formation. Going SW, the Licán well, showed two overlapped aquifers ata depth of 240 m. The author believes that these aquifers are not connected with the one identified in the areas of Santa Ana and El Carmen. The most important aquifer in this area, is the upper one with an approximate potency of 60 m, while the deepest level has a thickness of 30 m.

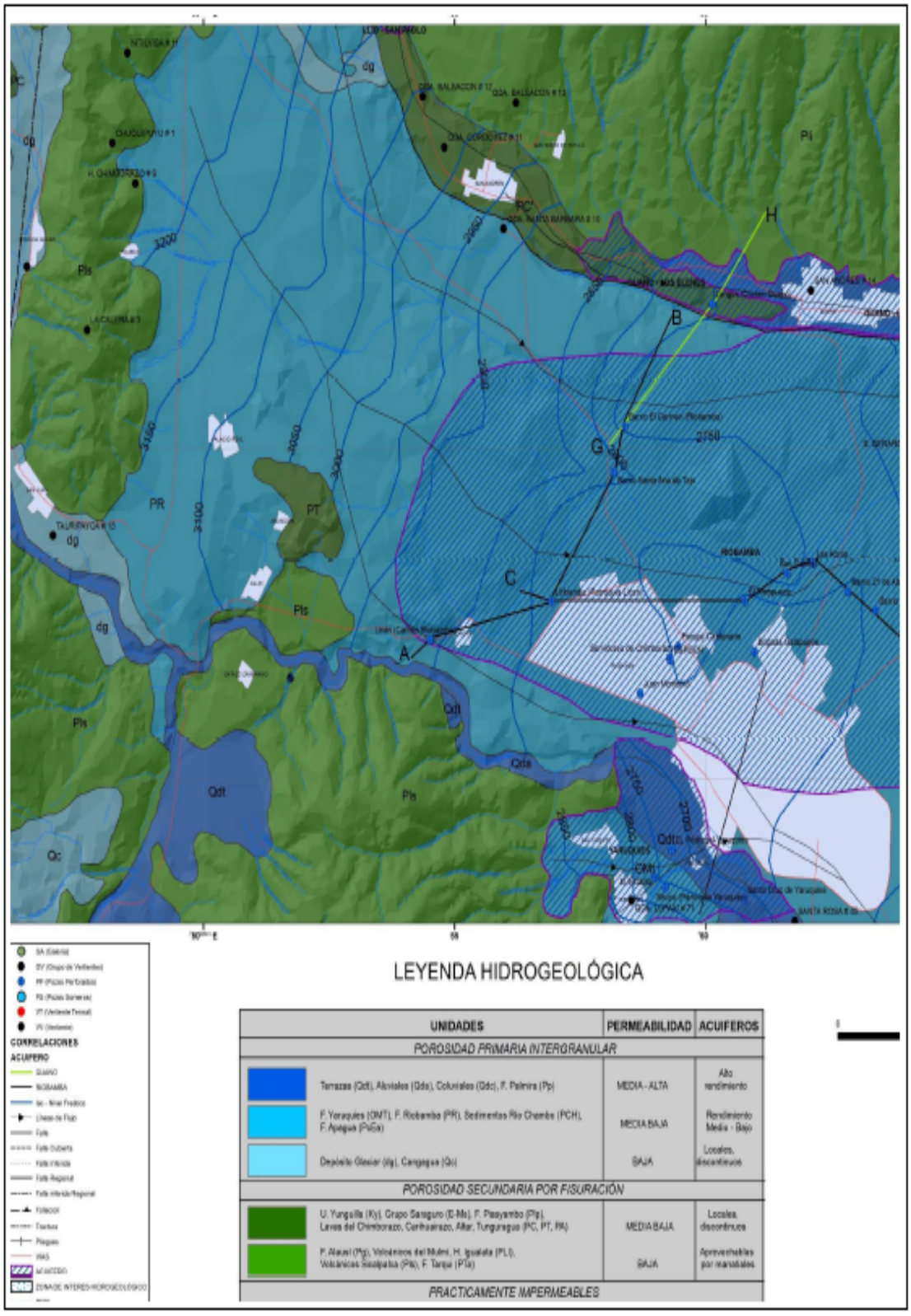

Figure 3. 6: Map with the locations of all the geological correlations performed at the Chambo Aquifer in Riobamba (Naranjo, 2013).

Type	X	Y	Elevation (msnm)	Location Name	N.E. (m)	Depth (m)	Volume (l/s)
PP	754519	9817112	2901	Licán (Cantón Riobamba)	46.56	221.00	5.00
PP	764359	9816828	2768	San Martín de Veranillo	51.40	222.00	8.00
PP	758178	9819647	2881	Barrio Santa Ana de Tapi	49.53	243.00	8.00
PP	758401	9820331	2887	Barrio El Carmen (Riobamba)	140.13	243.90	6.00
PP	763392	9817550	2746	Barrio San Antonio vía a Baños	34.19	0.00	8.00
PP	756937	9817682	2871	Liribamba (Parroquia Licán)	88.80	255.00	8.00
PP	760979	9816928	2833	Brigada Galápagos	49.43	200.00	8.33
PP	761626	9818110	2814	San Gabriel	81.05	204.00	12.00
PP	759284	9816835	2814	Servidores de Chimborazo	47.02	215.00	32.00
PP	758768	9816361	2817	Huertas	-	200.00	-
PP	759458	9817011	2814	Parque Centenario	108.00	188.00	30.00
PP	762841	9817832	2771	Barrio 21 de Abril	2.80	200.00	10.00
PP	762145	9818262	2791	Las Abras	30.00	194.00	10.00
PP	758700	9816300	2809	Juan Montalvo	48.84	219.00	10.30
PP	759300	9816800	2800	ESPOCH	38.30	190.00	10.30
PP	760790	9817687	2788	El Aeropuerto	22.00	175.00	8.00
VT	764327	9821304	2610	BALNEARIO LOS ELENES # 16	0.00	0.00	15.00
VV	751275	9827469	3390	HDA. CHUQIPOGYO # 3	0.00	0.00	10.00
VV	752514	9830289	3380	NITILVISA # 10	0.00	0.00	-
VV	761933	9811317	2720	O.D. RIO MOCHA # 23	0.00	0.00	-
VV	755980	9823316	3040	QDA. SANTA BARBARA # 10	0.00	0.00	5.00
VV	764570	9819921	2590	S. GERARDO BARRIO UNION # 18	0.00	0.00	0.50
VV	765336	9817774	2710	SAN FRANCISCO # 20	0.00	0.00	-
VT	766975	9819608	2700	YUIGAN # 17	0.00	0.00	4.00

Table 3. 1: Water levels monitoring at the Riobamba aquifer (Naranjo, 2013).

The analysis of the water level values and their spatial distribution in the Riobamba and Pisayambo formations, lead the author to believe that the deposits of the Riobamba formation is an unsaturated zone with the presence of small aquifers towards the N of Riobamba, while the main water reservoir are represented by the lava mantles and agglomerates of the Pisayambo formation.

The (C - D) correlation allowed us to identify the distribution of the aquifer levels in (NW - SE) direction. In the NW (Liribamba well) two overlapped aquifer were identified, whereas in the SE (San Antonio and San Martín de Veranillo wells), four overlapped aquifer were identified: In the SE (San Antonio and San Martín de Veranillo well) the shallowest aquifer, hosted in the Riobamba formation has a lesser potency at 20 m, which probably overlooks the top soil towards the E, giving origin to the springs of San Francisco.

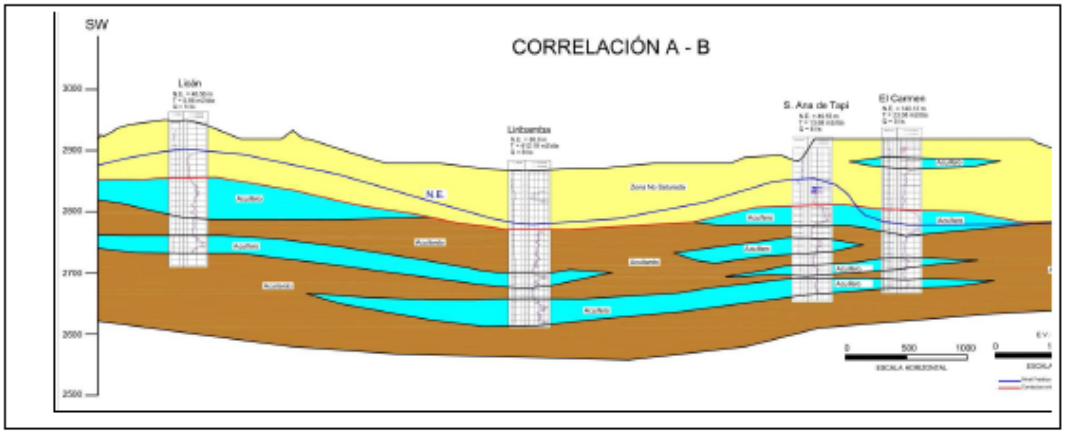

Figure 3. 7: Correlation wells in the Riobamba area in a SW–NE direction (Naranjo, 2013).

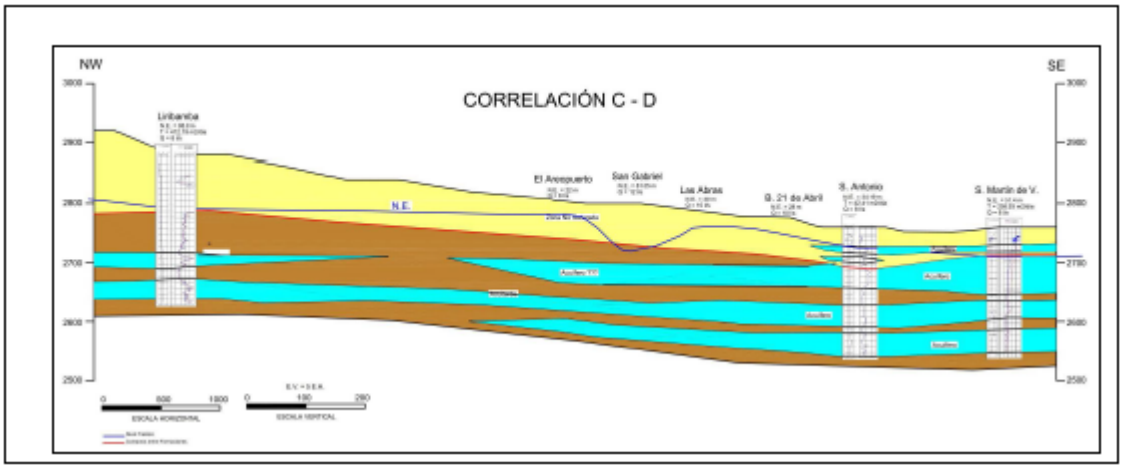

Figure 3. 8: Correlation Wells within the Riobamba area in a NW-SE direction (Naranjo 2013).

The aquifers identified in the Liribamba well are hosted over the rocks of the Pisayambo formation and are found starting at a depth of 160 m, while to the SE in the San Antonio and San Martín de Veranillo wells, three aquifers were identified in the Pisayambo formation, starting from a depth of 90 m. The Riobamba formation is interpreted as a non-saturated area with the presence of certain local

and discontinuous aquifers, whereas in the Pisayambo formation, 3 aquifers have been identified.

The distance between Liribamba and San Antonio wells on the way to Baños (6 km), the lack of information on the Airport, San Gabriel, Las Abras and Barrio 21 de Abril wells, and the heterogeneity of the Riobamba and Pisayambo formations, do not allow to determine the continuity of these aquifers in the NW to SE direction.

Hydrogeological Parameters. The hydrogeological properties (Transmissivity T, storage coefficient S, and permeability K) of the aquifers in the Riobamba area, have been determined by some pumping tests information performed on 7 wells. The pumping tests were performed through the Jacob and recovery methods. In table 3.2, the hydrogeological properties of the mentioned wells are indicated. Figure 3.9shows the transmissivity map of the Riobamba aquifer.

The values of the storage coefficient S depict the Riobamba aquifer, as a semi-confined and confined aquifer. The permeability (K) values vary in a range of 0.08 – 6.88 m/day. The permeability increases from NW to SE; in this way the Licán, El Carmen and Santa Ana de Tapi wells located to the NW of the aquifer, have a permeability of 0.08 – 1.01 m/day, whereas the San Martín de Veranillo, Liribamba, Brigada Galápagos located at the SE of the aquifer, have a permeability of 4.39 – 6.88 m/day.

Location Name	N.E (m)	Depth (m)	b (m)	Q (m3/day)	Tj (m2/day)	Tr (m2/day)	(S)	K (m/day)
Licán (Cantón Riobamba)	46.56	221	45	259.2	3.58	5.96	5.48E+02	0.08
San Martín de Veranillo	51.4	222	54	691.2	295.58	258.93	5.77E-06	5.47
Barrio Santa Ana de Tapi	49.53	243	66	691.2	55.35	13.68	9.76E-03	0.84
Barrio El Carmen (Riobamba)	140.13	243.9	60	432	60.59	23.08	2.19E-07	1.01
Barrio San Antonio vía a Baños	34.19	222.5	66	633.31	79.92	42.41	2.17E-12	1.21
Liribamba (Licán church)	88.8	255	60	633.31	413.09	412.69	2.15E-24	6.88
Brigada Galápagos	49.43	200	43	719.71	188.89	142.94	3.30E-06	4.39

Table 3. 2: Hydrogeological properties of the the Riobamba area

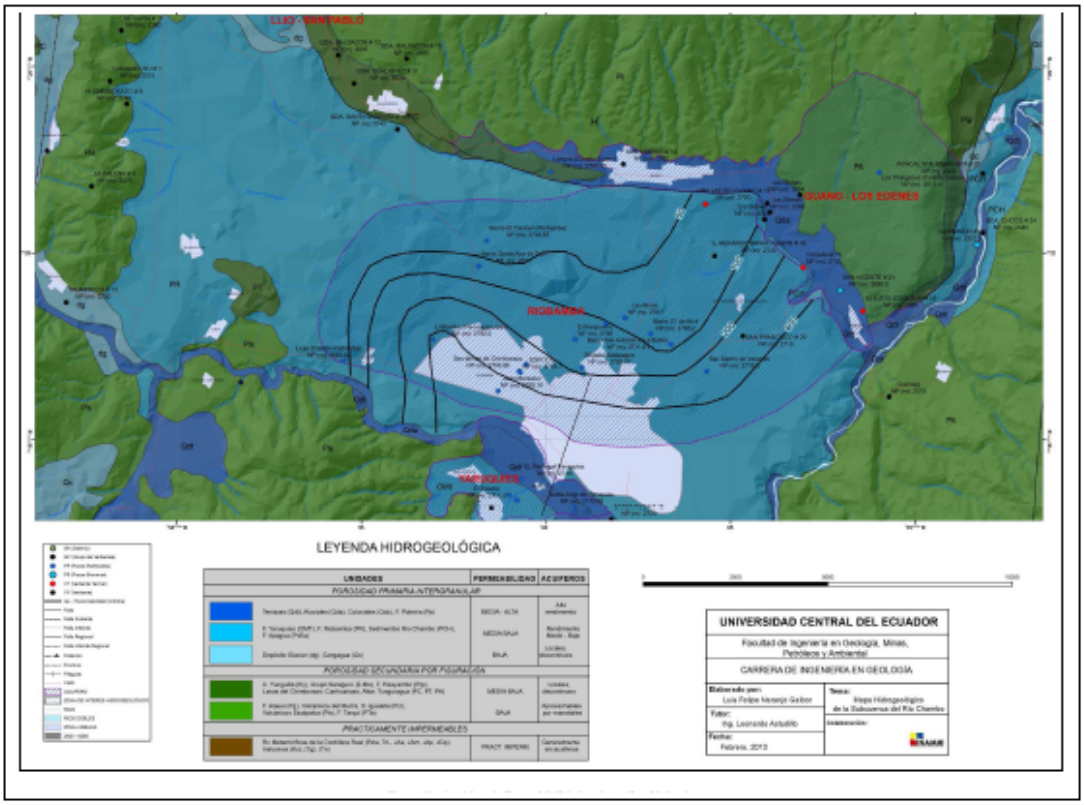

Figure 3. 9: Transmissivity map of the Chambo aquifer in Riobamba (Naranjo, 2013).

e) Chambo Aquifer in Llío – San Pablo

The area is limited to the West and South by the Guano river and to the Est by the Pichán waterfall. This area is characterized by a corrugated topography with the presence of rounded hills and U-shaped valleys, poor drainage and low flow.

Geological Synopsis. The area is characterized on the top by volcanic sediments of the Cangagua formation, made up by layers of sandy ash and clayed tuffs. Flows of andesitic lava correspondent to the young lavas from the Chimborazo cross these deposits. Under the young lava, pyroclastic deposits from the Igualata are found, while the bottom of the aquifers system is made by the volcanic deposits from the Neogene (Pisayambo formation). Figure 3.10 shows a geological section of the Chambo aquifer at Llío – San Pablo, derived from the geoelectrical investigation, in the NW - SE direction .

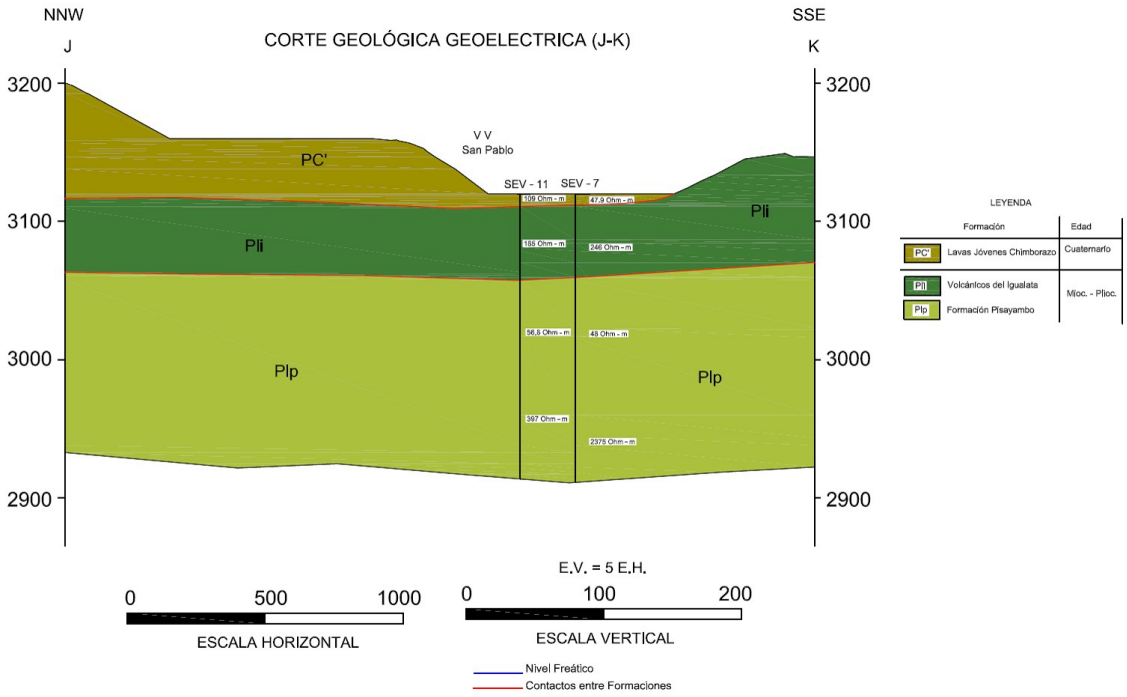

Figure 3. 10: Geological section of the Chambo aquifer at Llío San Pablo, derived from the geoelectrical investigation, (Naranjo, 2013).

Hydrogeological Synopsis. According to the water level measurements, 3 springs (VV) and 7 wells (PP) are present in this aquifer . Generally speaking and depending on the topography, the piezometric level, in the Llío area, is estimated to be at a depth of 18 m from the top soil, while the medium altitude is about 3100 masl.

The groundwater exploitation ,in the Chambo aquifer at Llío – San Pablo, consists in an withdrawn of approximately 500 l/s, divided in 200 l/s pumped from wells , and 280 l/s supplied by the San Pablo spring located approximately at 1km to the SW of the wells area. This represent the main source of water for the city of Riobamba.

Figure 3.11shows the location of the watertable and wells in the Chambo aquifer at Llío – San Pablo. The Chambo aquifer at Llío – San Pablo, presents two overlapped aquifers separated by a semi-impermeable clayed tuff from the Igualata volcanoes. The top of the upper aquifer is made by a rock of the young lavas from the Chimborazo, which in the Llío – San Pablo area tend to wedge over the Igualata volcano. The groundwater which mainly comes from the Chimborazo glaciers , travels through the cleats of andesitic lava, which have a preferential direction W - E, with sub vertical dips. In the Llío – San Pablo area, the clayed tuffs from

Igualata, are the sealing rocks that give place to a damming of groundwater and subsequent rise of the same water creating the springs of San Pablo.

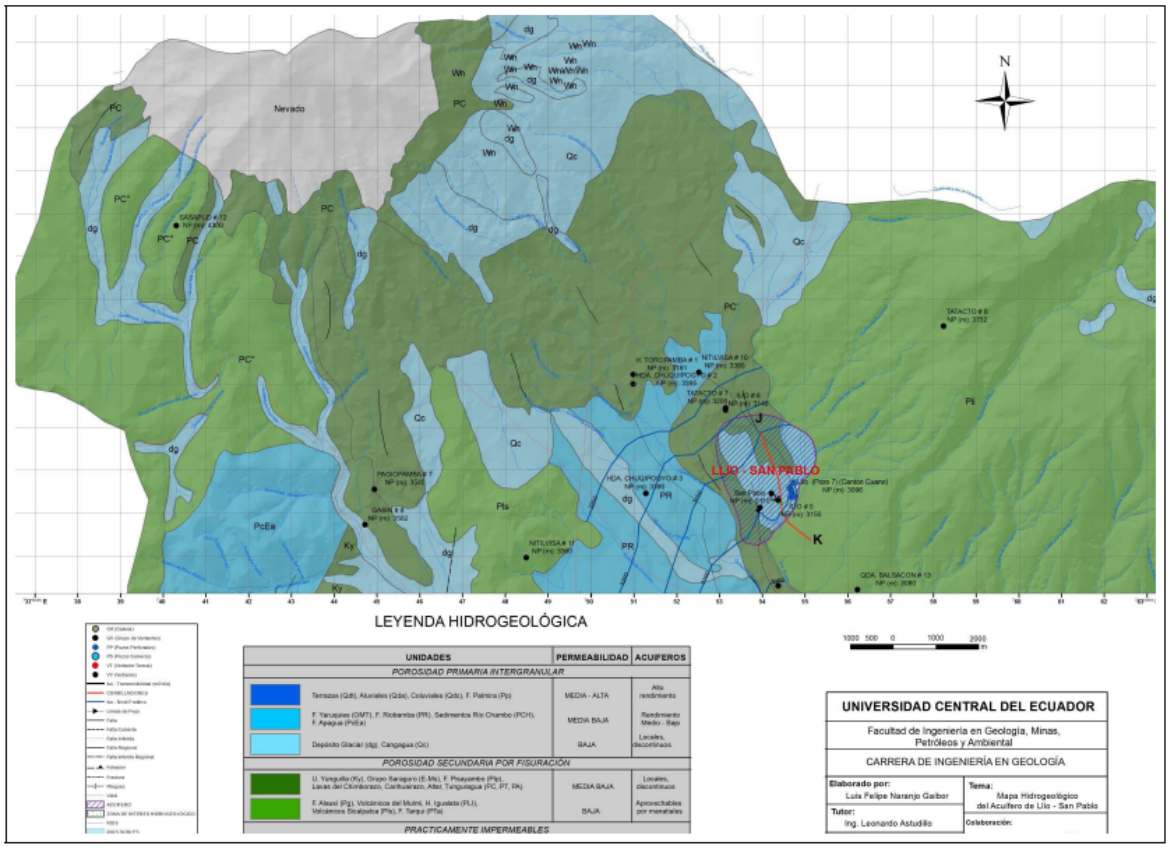

Figure 3. 11: Location map of the Llío – San Pablo aquifer (Naranjo, 2013).

The lower aquifer lies approximately at a depth of 65 m and has a thickness of approximately 75 m.This aquifer is hosted in the agglomerates and lava mantles of the Pisayambo formation. The hydrogeological interpretation of the Llío – San Pablo aquifer is shown in Figure 3.12.

f) Chambo aquifer in Yaruquíes

The area is limited to the NE by the Chibunga river, to the South and Est by the volcanic deposits of Sicalpa. The area is characterized by a relatively flat topography. Two terracing levels were identified; to the S the topography tends to be more rugged. The Chambo aquifer in Yaruquíes is drained by the Puctus waterfall from SW – NE, whereas going towards the North the main drainage is the Chibunga River.

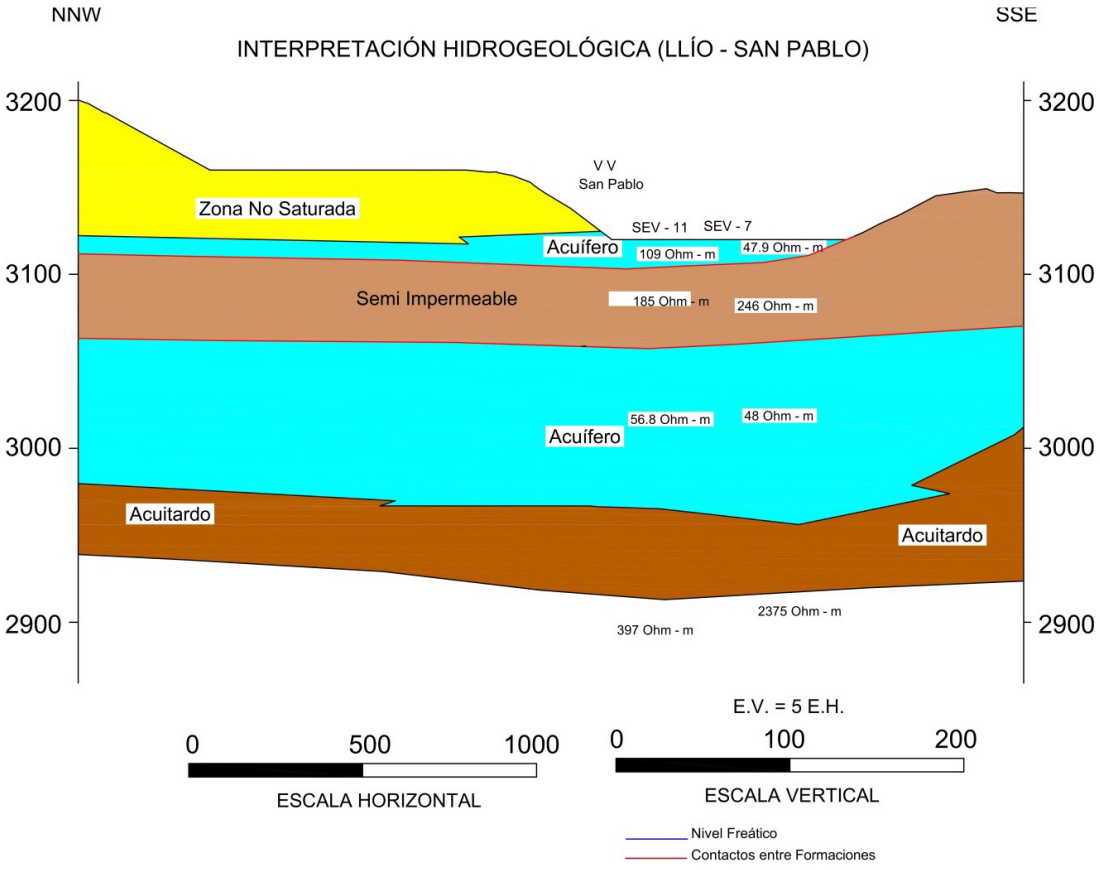

Figure 3. 12: Hydrogeological interpretation of the Chambo aquifer at Llío – San Pablo. (Naranjo, 2013).

Geological Synopsis. The bottom of the Chambo aquifer in Yaruquíes, is represented by the agglomerates and lava mantles from the Pisayambo formation, over which the deposits of the Yaruquíes formation lie. The lower part of the aquifer is comprised by layers of andesitic and quartzite conglomerates with medium-grained reddish sandstone interbedded, while in the upper part we have clay layers interspersed with sand strata.

The Yaruquíes formation is wedged towards the NE (Ciudad de Riobamba). In this area the deposits of the Riobamba formation are underlined by the Yaruquíes formation. To the south of the Chibunga river, we have the development of alluvial terraces and deposits over the Yaruquíes formation.

Hydrogeological Synopsys. The water level inventory, shows that 2 springs (VV) and 4 wells (PP) are present in this area.. The static level of the Chambo aquifer in Yaruquíes was foundd at a depth of 50 m. The piezometric level varies from 2850 msnm in the S to 2700 msnm to the NE, the preferential direction of the flow is SW - NE.

The Chambo aquifer in Yaruquíes has a groudwater exploitation of about 48 l/s withdrawn from 4 wells.. The present study performed a correlation (E – W) for the Chambo aquifer in Yaruquíes, based on the analysis of the drilling operations and the SP electrical registries (Spontaneous potential) and resistivity. Figure 3.13 shows the performed correlation and its hydrogeological interpretation. Two aquifers were identified in the Shuyo well (150 m of drilling) and up to four aquifers in the Santa Cruz well.

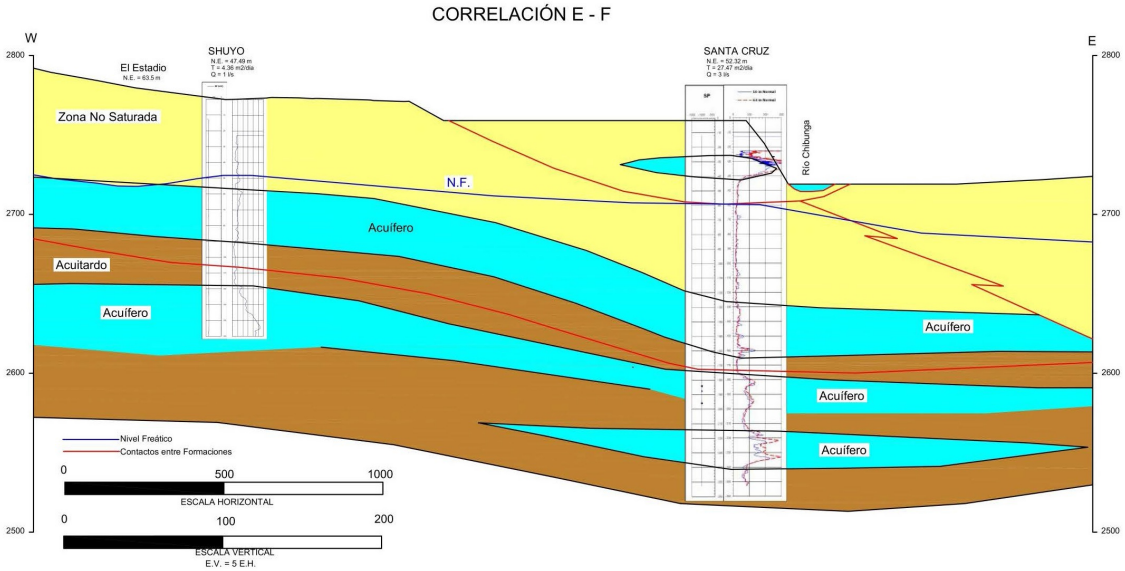

Figure 3. 13: Boreholes correlation in the Yaruquíes' aquifer in a (W-E) (Naranjo, 2013**)**

At a depth of 25 m, in the Santa Cruz well (alluvial terraces), a superficial aquifer with an approximate thickness of 15 m was identified . In the andesitic and quartzite conglomerates of the lower part of the Yaruquíes formation, an aquifer with an approximate thickness of 30 m is housed, evidenced in both Shuyo and Santa Cruz wells.

The deepest aquifers are found in andesitic agglomerates with a silty base, probably belonging to the Pisayambo formation. These aquifers are cosidered as local and discontinuous aquifers. Two aquifers were identified in the Santa Cruz well at a depth of 160 m , , hosted in volcanic agglomerates with an approximate thickness of 25 m each. A new aquifer was found in the Shuyo well starting at a depth of 120 m and continuing up to 150 mwere the drilling operations stop.

Hydrogeological Parameters. To determine the hydrogeological properties (Transmissivity T, Storage coefficient S and permeability K) of the Chambo aquifer

in Yaruquíes, the information coming from some pumping tests performed on 2 wells have been used.

Type	X	Y	Elevation (msnm)	Location Name	NE (m)	Depth (m)	Volume (l/s)
PP	759209	9813371	2804	Shuyo (Parroquia Yaruquíes)	47.49	151	1
PP	760772	9813185	2763	Santa Cruz de Yaruquíes	52.32	258.5	3
PP	759335	9813936	2794	EL Pedregal-Yaruquíes	50	225	15
PP	758994	9813514	2815	El Estadio	63.5	200	30
VV	758528	9813169	2820	QDA. LUPAXI # 71	0	0	-
VV	761779	9812855	2720	SANTA ROSA # 45	0	0	-

Table 3. 3: Water level measurements in the Chambo River at Yaruquíes.

The pumping tests were performed through the Jacob's and recovery methods. The Transmissivity (T) vary in a range of 4.26 – 20.40 m^2/day. The transmissivity increases from SW (Shuyo well) to the NE (Yaruquíes), meaning that in the Shuyo area the hydraulic gradient is greater than in the Santa Cruz area. The permeability varies from 0.10 until 0.31 m/day, increasing from SW to NE.

g) Chambo Aquifer in Punín

The area is limited to the NE by the Chibunga River, to the Est by the Chambo River and to the South by the Sicalpa volcanic deposits, metamorphic rocks from the Real mountain chain (Guamote terrain) and granodiorites. The area is characterized by a relatively flat topography in terraces, towards the S the landscape tends to be more rugged. The Punín area aquifer is drained by the Guaslán and Monjas waterfalls from SW to NE.

Geological Synopsis. The bottom of the Chambo aquifer in Punín, is made by black slates, quartzite from the Punín unit and intrusive granodiorites, which rise to the SE of the aquifer. These deposits are overlaid by alluvial terraces, as it was evidenced by the cores drilled for the realization of the Quebrada Colorada well (Punín church). The deposits in the alluvial terraces are made up of quartz conglomerates wrapped in a silty base (supporting grain), interspersed with layers of clayed silt of brown, white and gray.

Hydrogeological Synopsis. Based on the SP and resistivity measurements performed at the Punín aquifer, 6 aquifers are hosted in the quartz conglomerate strata embedded in a silty matrix. These aquifers are separated by layers of coffee colored clayed silts considered as aquicludes and layers of clay matrix clusters considered as aquitards. The piezometric level varies from 2700 msnm in the SW

to 2600 msnm in the NE, the flux lines have a SW to NE direction. In the Punín aquifer there is only one well (up to a depth of 192 m) located at the Colorada waterfall, in which the exploitation flow rate is of 8.33 l/s, and the static level is at 16 m.

Hydrogeological Parameters. The Colorada waterfall well has a transmissivity of 201.22 m^2/day, a total saturated thickness of 51 m, and a permeability of 3.95 m/day. The analysis of the pumping tests of the Colorada waterfall well were done through the Jacob and recovery methods. In Figure 3.14, the hydrogeological map of the aquifer is shown.

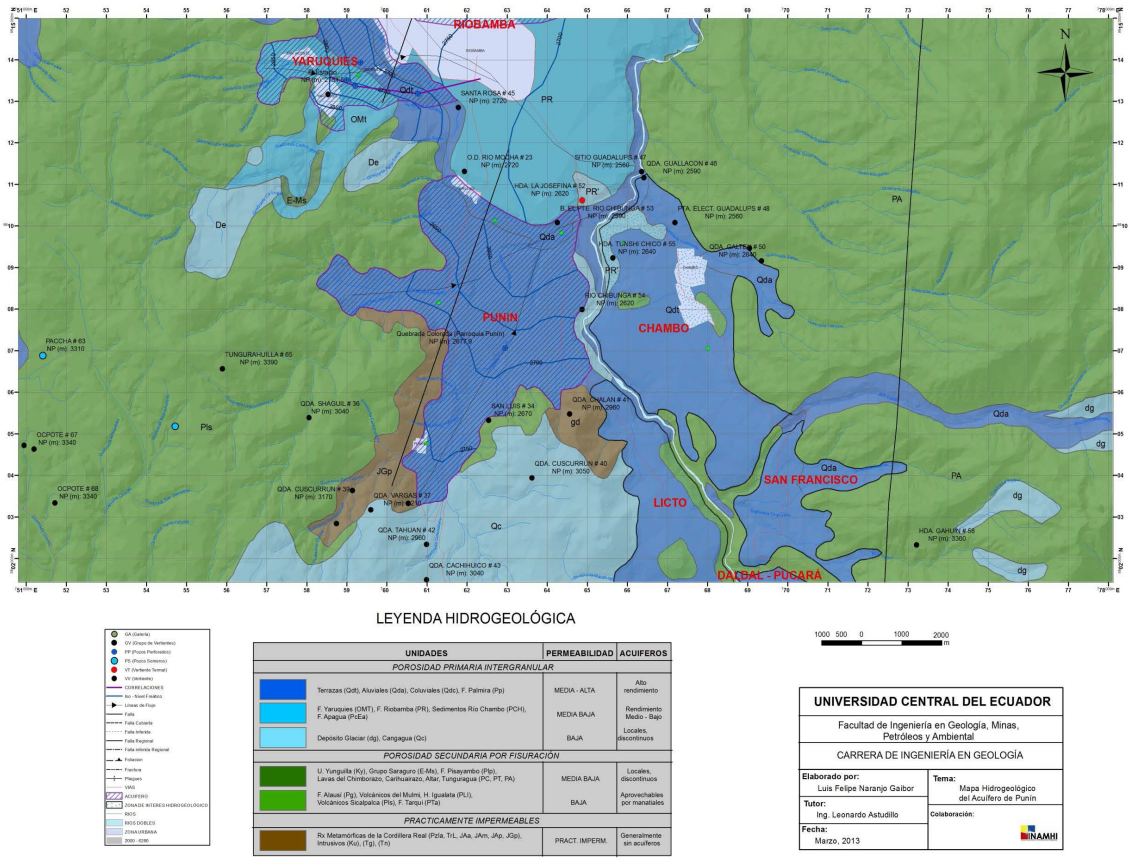

Figure 3. 14: Hydrogeological map of the Chambo aquifer at Punín (Naranjo, 2013).

h) Chambo Aquifer in Guano – Los Elenes

The Chambo aquifer in Guano – Los Elenes is limited to the South by the Guano River, to the Est by the Chambo River and to the North by the volcanic deposits of Igualata. Geomorphologically the area is characterized by a relatively flat topography in the Guano area, whereas to the North, the topography is more rugged in the areas of the volcanics of Igualata.

Geological Synopsis. The main geomaterial, in the West side of the Guano area, is the young lavas of the Chimborazo . This lava is formed by the deposits of the Riobamba and Igualata formations, having an approximate thickness of 40 m. The bottom of the Chambo aquifer in Guano – Los Elenes is constituted by the Pisayambo formation. Figure 3.15 shows the geological section SW - NE of the Chambo aquifer in the Guano area. Towards the West the young lavas of the Chimborazo are wedged in and we have the development of potent alluvial terraces. Towards the Chingazos area the young lavas of the Chimborazo vanish and volcanic deposits from the Altar overlay the Pisayambo area.

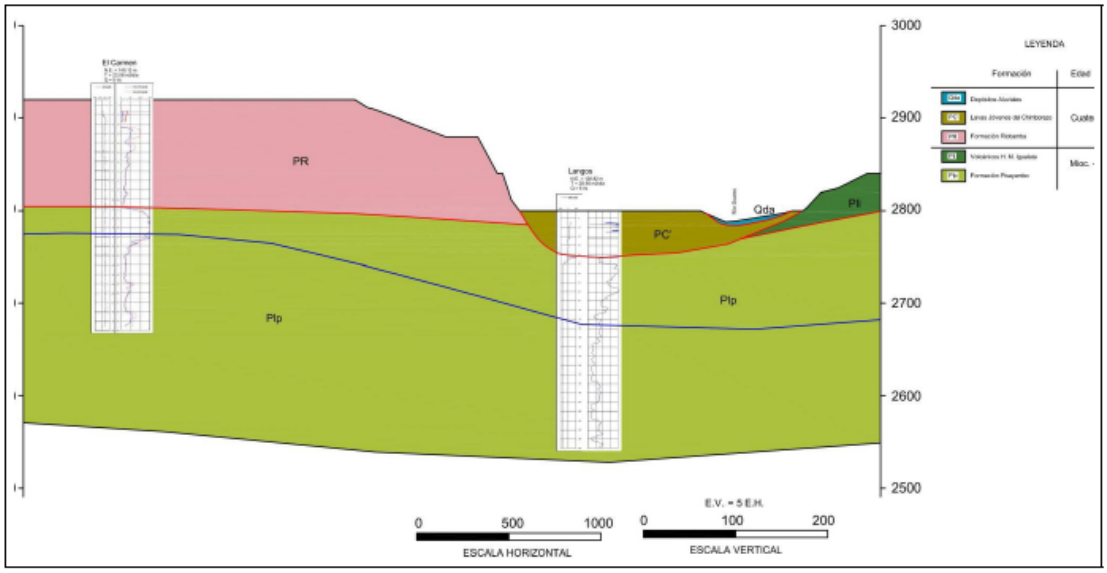

Figure 3. 15: Geological section of the Guano area (Naranjo, 2013).

Hydrogeological Synopsis. 6 springs and 3 wells (PP) are present in this aquifer according to the water level inventory, . The exploitation of the Chambo aquifer in Guano – Los Elenes, is performed through a flow rate of approximately 47 l/s.

The piezometric levels of the Chambo aquifer in Guano – Los Elenes, varies from 2850 masl to the West up to 2500 masl to the Est, while in the Chingazos area we have a piezometric system that varies from 2650 masl to the NNE up to 2550 to the SSW. The flux lines follow the regional lines (W – E) which in this area join with the lines of the Chingazos piezometric system that go from (NE – SW). Based on the electrical investigations (SP and resistivity), a SW – NE correlation was performed where the aquifer levels were measured in the (Guano – Los Elenes) aquifer. According to this correlation, up to 4 saturated aquifers were identified starting at a depth of 60 m. the shallowest aquifer is the most important with an

approximate thickness of 40 m. The second aquifer was found starting at a depth of 110 meters with a saturated thickness of 30 m. These aquifers may have a certain hydraulic connection with the deepest aquifer of El Carmen well of Riobamba. The third and fourth aquifers are located starting at a depth of 190 m and both of them have a saturated thickness of 20 m. These aquifers are hosted in the volcanic agglomerates of the Pisayambo formation. The alluvial terraces to the Est of Guano, host shallow aquifers which have a lateral recharge from the Guano River, and give place to springs formation.

Hydrogeological Parameters. The hydrogeological properties (Transmissivity T, storage coefficient S, and permeability K) of the Yaruquíes aquifer came out from the pumping tests performed on 2 wells (Langos y Los Chingazos). The transmissivity in the Langos well is about 13.20 m^2/day, with a saturated thickness of 53 m and a permeability of 0.25 m/day, whereas Los Chingazos well has a transmissivity of 161.53 m^2/day, with a total saturated thickness of 48 m and a permeability of 3.37 m/day.

Hydrometeorology

The Chambo river sub-basin is constituted by 21 micro-basins from which the most important are the ones crossed by Cebadas, Guamote, Chibunga, Guano, Puela, Alao, Blanco and Uldán rivers. The following image shows the micro-basins that occupy approximately 85% of the sub-basin. The main river in this sub-basin is the Chambo river which runs from south to north with a length (L_{RP}) of 144.49 km, the sub-basin area (A) is of 3589.55 km^2, the perimeter (P) is of 339.38 km with an axial length (L) of 106.77 km, with an average width (B) of 33.62 km. The total drainage length (L_TD) is of 4604.14 km. Figure 3.16 shows the Chambo river micro basins.

Table 3.4 shows the area (A), perimeter (P), axial length (L), main river length (LRP), main river valley length (LVRP), and medium width (B) of the Chambo river sub basin and its micro basins. Table 3.5 shows the shape indexes (compactness coefficient (K_c), shape coefficient (K_f)), drainage density (D_d), and the sinuosity of the main drain (S) for the Chambo river subbasins and its microbasins.

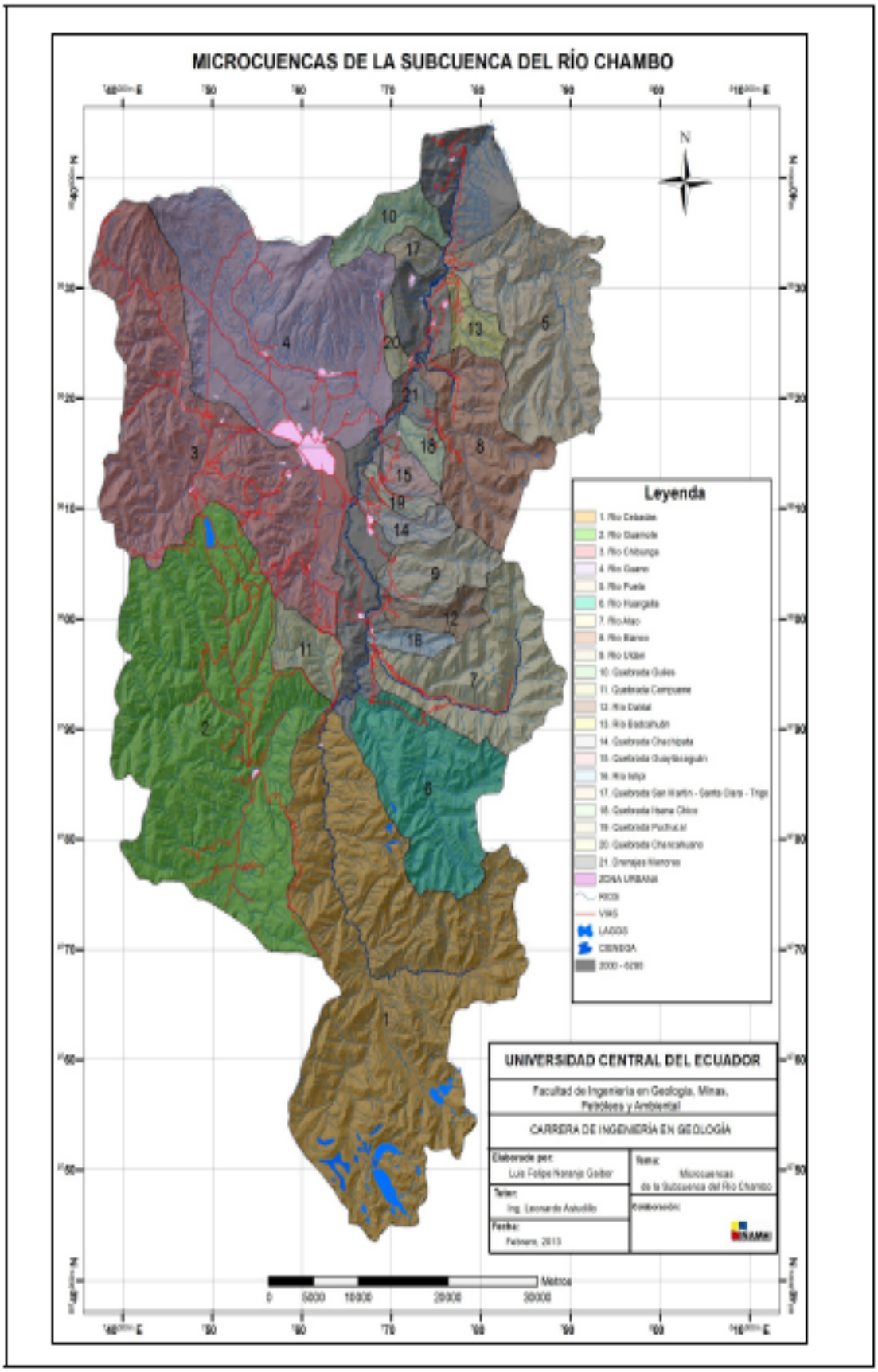

Figure 3. 16: Micro-basins at the Chambo River sub-basin.

No	SUBBASIN	A (Km^2)	P (Km)	L (Km)	L_{RP} (Km)	L_{VRP} (Km)	L_{TD} (Km)	B (Km)
1	Chambo River	3589.55	339.38	106.77	144.49	127.89	4604.145	33.62
No	**MICRO BASINS**	**A** (Km^2)	**P (Km)**	**L (Km)**	**L_{RP} (Km)**	**L_{VRP} (Km)**	**L_{TD} (Km)**	**B (Km)**
1	Cebadas River	711.73	154.94	46.75	66.05	51.92	1047.88	15.22
2	Guamote River	618.28	129.41	35.8	45.3	38.7	752.34	17.27
3	Chibunga River	481.76	133.41	43.9	55.95	47.25	603.3	10.97
4	Guano River	418.73	94.79	31.76	43.77	36.41	443.01	13.18
5	Puela River	231.05	74.4	26.28	33.84	31.54	316.72	8.79
6	Huargalla River	189.78	64.98	21.74	29.41	26.31	272.89	8.73
7	Alao River	185.09	68.85	29.31	37.71	32.82	185.09	6.31
8	Blanco River	145.47	60.19	20.72	24.01	22.63	141.39	7.02
9	Uldan River	63.98	35.71	14.5	16.08	15.12	60.21	4.41
10	Quebrada Guilles	46.65	37.81	14.49	17.1	15.77	47.87	3.22
11	Quebrada Compuene	42.83	30.32	11.86	15.1	14.32	53.6	3.61
12	Daldal River	33.07	32.34	12.52	13.14	12.48	22.68	2.64
13	Badcahuán River	29.56	26.11	9.49	11.37	11.01	32.94	3.11
14	Quebrada Chachipata	26.46	27.05	11.53	12.31	11.85	31.55	2.3
15	Quebrada Guayllacaguán	22.29	21.42	9.07	10.75	10.36	27.47	2.46
16	Ishpi River	18.62	22.33	10.23	10.89	10.63	20.19	1.82
17	Quebrada San Martín - Santa Clara - Trigo	17.47	18.19	6.28	7.1	6.91	31.13	2.78
18	Quebrada Itsana Chico	17.43	19.31	7.84	8.25	7.77	15.26	2.22
19	Quebrada Puchucal	13.77	21.45	9.71	9.91	9.42	17.9	1.42
20	Quebrada Chancahuano	13.68	19.48	7.82	9.25	8.87	13.98	1.75
21	Small Drains	262.43	184.14	-	-	-	-	-

Table 3. 4: Sub-basin and micro basin dimension from the Chambo River (Naranjo, 2013).

The shape index (K_c) and (K_f), indicate that the Chambo river sub-basin and its main micro-basins have oval to rectangular shapes and are slightly or very elongated. The analysis of the drainage density (D_d) within the Chambo sub-basin is based on Manosalve´s criteria (1995) "D_d usually takes values from 0.5 km/km^2 for river basins with poor drainage up until 3.5 km/km^2 for exceptionally well drained river basins". The analysis of drainage density values (D^d) fluctuate from 0.69 – 1.18 km/km^2 that correspond to the basins with poor to intermediate drainage. The micro-basin of the Daldal River has the poorest drainage, while the San Martín – Santa Clara – Trigo waterfall micro-basin has the best drainage of the Chambo river sub-basin. The sinuosity (S) values are analyzed according to Manosalve's criteria (1995) "A sinuosity value equal to or less than 1.25 indicate low sinuosity; therefore, it is defined as a basin with a straight feed". The (S) values of the drainage of the Chambo sub-basin are less than 1.27, thus having a straight alignment.

The elevations within the Chambo sub-basin vary between the 2000 m (at the mouth of the Chambo River) and 6280 m (at the eastern slope of the snow-capped Chimborazo). The elevation of the Real and Eastern mountain range exceeds 3000 m, whereas in the Riobamba Guamote area the elevations vary between the 2600 – 3000 m. Fromthe mouth of the Guano river throughout the Chambo river the elevations vary from 2600 to 2000 masl. Figure 3.17 shows an elevation model that allows to identify the distribution of the elevations within the Chambo river sub-basin.

No	SUB BASIN	K_c		K_f		Dd Km/Km^2	S
1	Chambo River	1.6	Elongated oval to elongated	0.31	Slightly elongated	1.28	1.13

No	MICRO BASINS	K_c		K_f		Dd Km/Km^2	S
1	Cebadas River	1.64	Elongated oval to elongated rectangular	0.33	Slightly elongated	1.47	1.27
2	Guamote River	1.47	Elongated oval to elongated rectangular	0.48	Lightly widened	1.22	1.17
3	Chibunga River	1.71	Elongated oval to elongated rectangular	0.25	Elongated	1.25	1.18
4	Guano River	1.31	Rounded oval to elongated oval	0.42	Neither enlarged nor elongated	1.06	1.2
5	Puela River	1.38	Rounded oval to elongated oval	0.33	Slightly elongated	1.37	1.07
6	Huargalla River	1.33	Rounded oval to elongated oval	0.4	Neither enlarged nor elongated	1.44	1.12
7	Alao River	1.43	Rounded oval to elongated oval	0.22	Very elongated	1	1.15
8	Blanco River	1.41	Rounded oval to elongated oval	0.34	Slightly elongated	0.97	1.06
9	Uldan River	1.26	Rounded oval to elongated oval	0.3	Slightly elongated	0.94	1.06
10	Quebrada Guilles	1.56	Elongated oval to elongated rectangular	0.22	Elongated	1.03	1.08
11	Quebrada Compuene	1.31	Rounded oval to elongated oval	0.3	Slightly elongated	1.25	1.05
12	Daldal River	1.59	Elongated oval to elongated rectangular	0.21	Very elongated	0.69	1.05
13	Badcahuán River	1.35	Rounded oval to elongated oval	0.33	Slightly elongated	1.11	1.03
14	Quebrada Chachipata	1.48	Rounded oval to elongated oval	0.2	Very elongated	1.19	1.04
15	Quebrada Guayllacaguán	1.28	Rounded oval to elongated oval	0.27	Elongated	1.23	1.04
16	Ishpi River	1.46	Rounded oval to elongated oval	0.18	Very elongated	1.08	1.02
17	Quebrada San Martín - Santa Clara - Trigo	1.23	Compact or rounded to rounded oval	0.44	Neither enlarged nor elongated	1.78	1.03
18	Quebrada Itsana Chico	1.3	Rounded oval to elongated oval	0.28	Elongated	0.88	1.06
19	Quebrada Puchucal	1.63	Rounded oval to elongated oval	0.15	Very elongated	1.3	1.05
20	Quebrada Chancahuano	1.49	Rounded oval to elongated oval	0.22	Elongated	1.02	1.04
21	Small Drains	-	-	-	-	-	-

Table 3. 5: Form, drainage densities, and sinuosity coefficients from the sub-basin and micro-basins of the Chambo River (Naranjo, 2013).

In the following Figure 3.18, a map of the springs in the Chambo river sub-basin is shown. The slopes in the Chambo river sub-basin, vary from 0% up until 81.54%. The

extremely steep slopes 75 – 81.54 % represent 0.08% of the total sub-basin area. The 4.54% corresponds to very steep slopes 45 – 75 % and are generally located in the adjacent basin areas of the Chambo, Alao and Blanco rivers; and in the springs from the snow-capped Chimborazo and the Tungurahua volcano. The abrupt slopes (25 - 45) % represent 24.10% whereas the 29.84% of the subbasin is influenced by moderate slopes (15 - 25) %.

The soft slopes (5 - 15) % and very soft (0 - 5) % are approximately 32.93% and 8.91% of the subbasin and are located in the flat topography of the Guano – Riobamba – Guamote and in the Palmira area. Based on a topographic cut throughout the Chambo, Cebadas and Atillo rivers, main drainage systems at the Chambo river subbasin, the river watershed were obtained in sections.

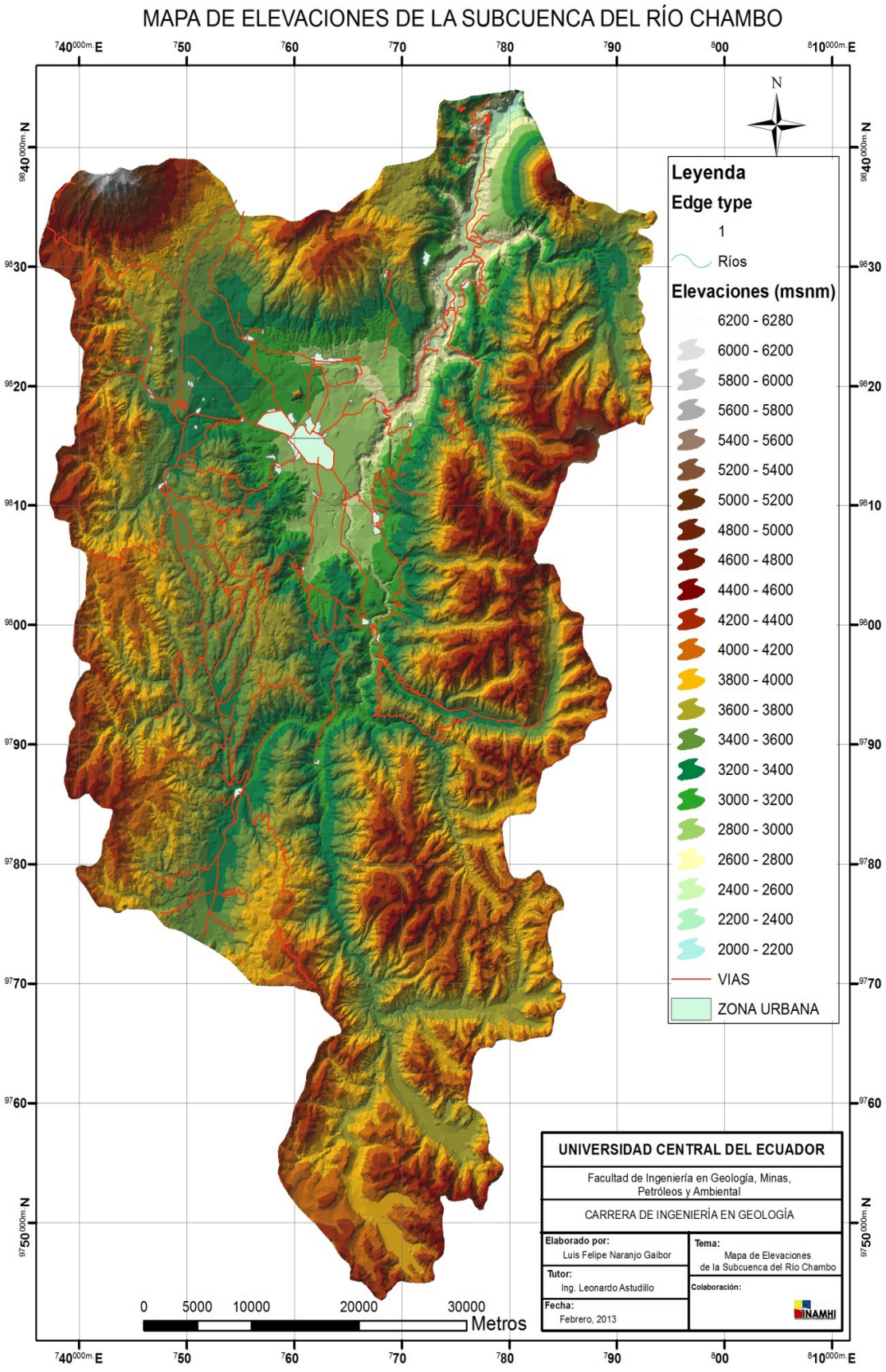

Figure 3. 17: Elevation map of the Chambo River sub-basin (Naranjo, 2013).

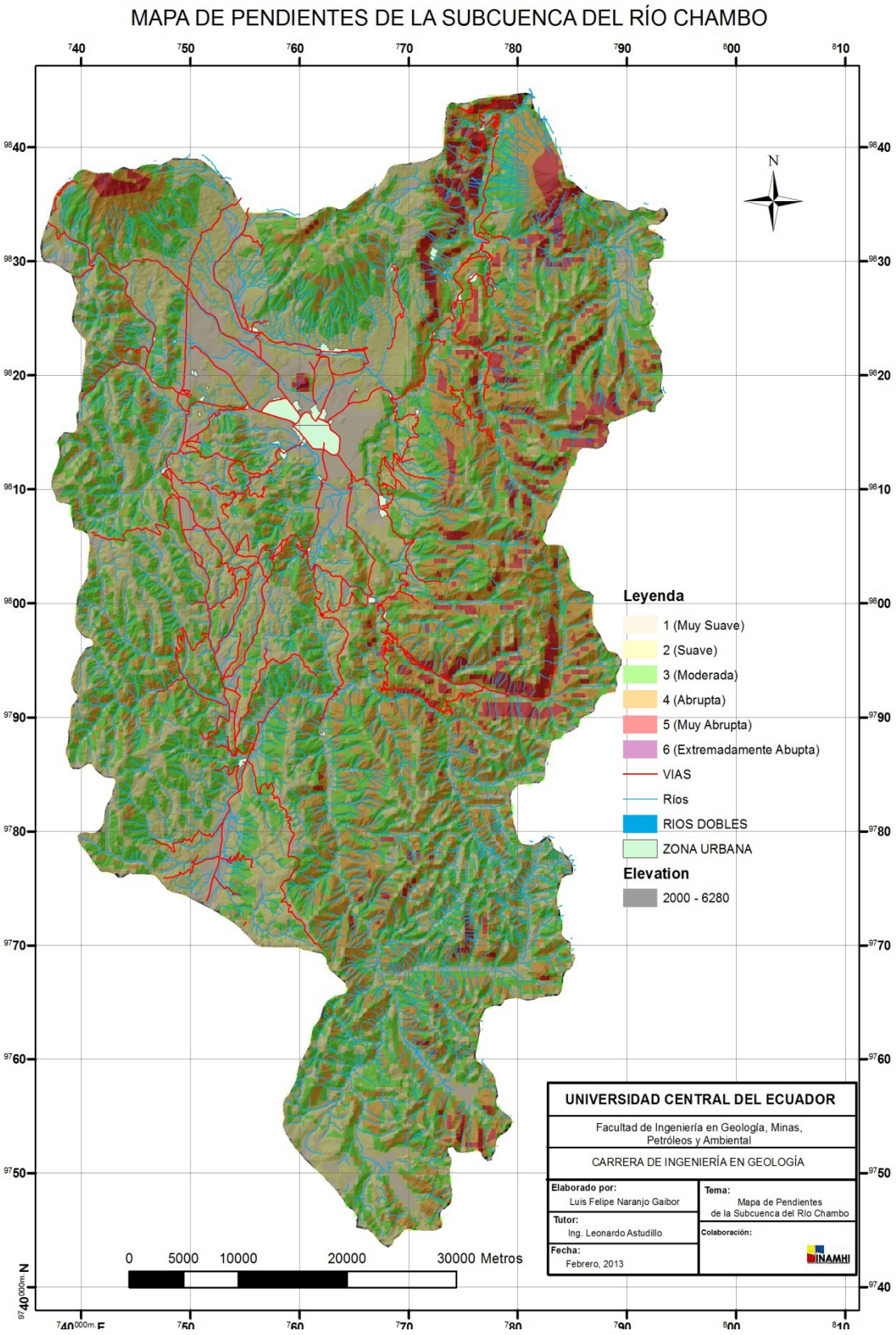

Figure 3. 18: Elevation map from the Chambo river sub-basin (Naranjo, 2013).

Intervalo	RANGO (%)	Pmr (Km)	Ap (Km^2)	% Ap	% Acumulado Ap	Pmr*Ap
1	0-5	2.5	305.11	8.51%	100.00%	762.775
2	5-15	7.5	1180.82	32.93%	91.49%	8856.15
3	15-25	20	1070.16	29.84%	58.56%	21403.2
4	25-45	35	864.22	24.10%	28.72%	30247.7
5	45-75	60	162.73	4.54%	4.61%	9763.8
6	75-81.54	78.27	2.72	0.08%	0.08%	212.8944
		$\sum A_p$	3585.76		$\sum Pmr * A_p$	71246.519

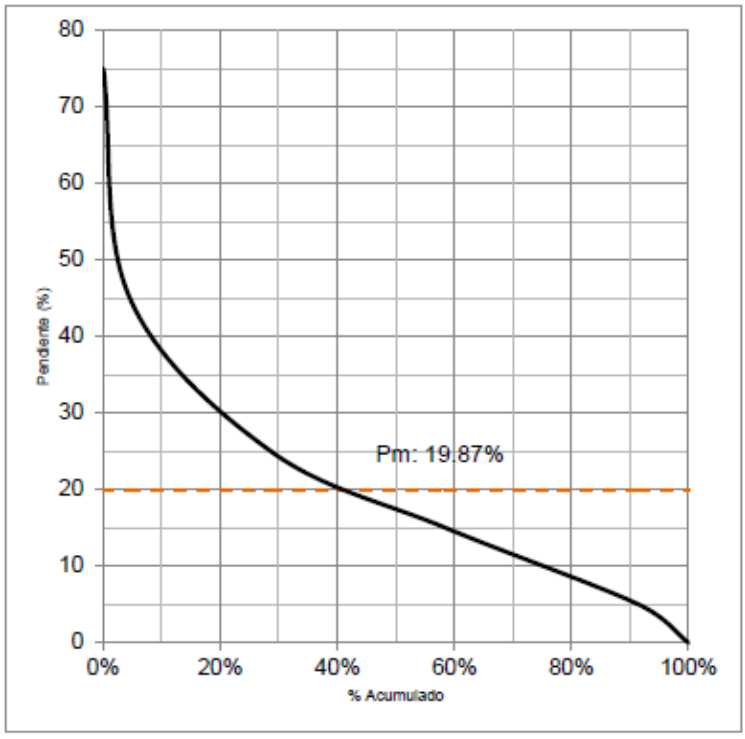

Figure 3. 19: Curved distribution of the slopes at the Chambo river sub basin (Naranjo, 2013).

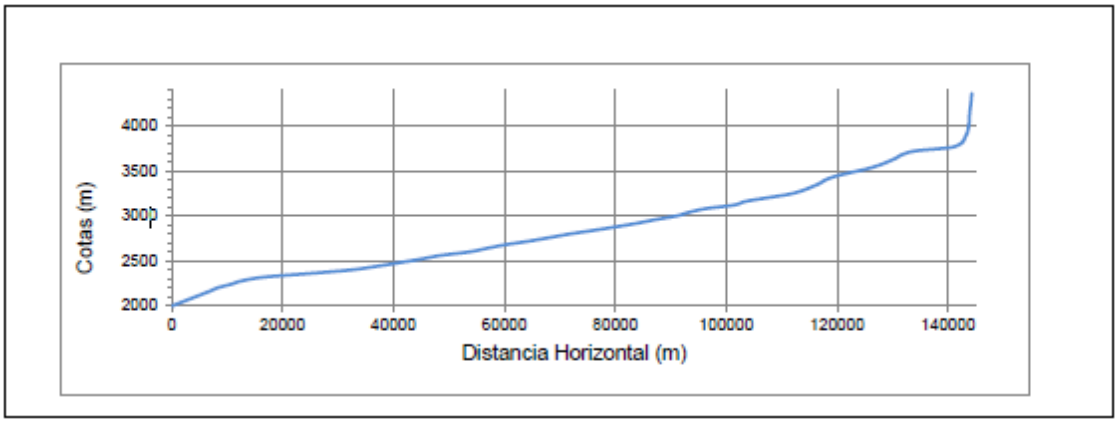

Figure 3. 20: Topographic cut through the Chambo, Cebadas and Altillo rivers (Naranjo, 2013).

Starting at 4320 m to 4360 m of height, the river manifests moderate slopes, in the area from (4120 - 4320) m, the river slope becomes really abrupt, starting the 4120 m up until the 4040 m. From the 4000 m up until Patate river mouth at 2000 m over the sea level, the Chambo River has slopes that vary from moderate to very soft. The constant equivalent value of the slope is of 1.088%.

The hypsometric curve and equivalent rectangle show that between the 4000 and 6280 msnm, is hardly 2% of the sub basin area, a situation that contrasts with the 90% of the subbasin area contained between 2800 and 4000 msnm, whereas between 2800 and 2000 msnm we have 8% of the subbasin. Associating this hypsometric curve with the ages of the river, the drainage of the Chambo river subbasin is classified as young to mature rivers. The highest length (L_{REC}) of the equivalent rectangle is of 146.48 km, while the shortest length (l_{REC}) is of 24.51 km, ratifying the elongated shape of the Chambo river subbasin.

3.1.4 The Water Balance

The water balance is the implementation of the principle of the conservation of water mass over a spatial domain (hydrological domain) in a time interval. This principle stipulates that the incoming flow mass in the system is equal to that leaving the system, unless there is a change in mass over time. The components of this mass balance are expressed in terms of average flow. The water balance in discrete terms is expressed mathematically by the following equation of continuity:

$$P = E_{tr} + R + N + A \qquad (1)$$

Where: P rainfall (mm), Etr real evapotranspiration (mm), R runoff (mm), N Vertical Infiltration (mm) and A variation of the water holding capacity of the soil (mm). The securities described have a time interval of the referenced month.

The Real Evapotranspiration is the quantity of water consumed by the evaporation power of the atmosphere (evaporation) and biological activity (transpiration); the thermal method to Thornthwaite (1948) is based on exponential relationship between potential evapotranspiration and average monthly temperature.

$$E_{tp}^{i} = K^{i}\left[1.6\left(\frac{10T^{i}}{I}\right)^{a}\right] \qquad (2)$$

Where: E_{tp}^{i} is the potential evapotranspiration in the ith month; K^{i} is the latitude correlation coefficient based on the ith month, and equal to the relationship between daytime and half overall hours, T^{i} is the average monthly of air temperature, R is the annual heat index equals:

$$I = \sum_{i=1}^{12} \left(\frac{T^{i}}{5}\right)^{1.514} \qquad (3)$$

and a is a coefficient which equals to:

$$0.49239 + 1.792x10^{-2}I - 771x10^{-7}I^{2} + 675x10^{-9}I^{3} \qquad (4)$$

Studies of U.S.D.A. have found the runoff exists when the rainfall is greater to 20% of the maximum hydric holding capacity in surface soil layers, and this process is described by infiltration curve method (Caziani and Cossu, 1985):

$$R = \frac{(P-I)^{2}}{P-I+C} \qquad (5)$$

Where: I is the initial losses (surface accumulation, intercepted water for vegetation, winter infiltration) and C is the field capacity, i.e. the maximum capacity for water storage in the soil layer. The value of I has been experimentally verified and can be considered equal to 0.2C; this changes the equation precedent to:

$$R = \frac{(P-0.2C)^{2}}{P+0.8C} \qquad (6)$$

The water capacity of the ground can be represented as a sponge; when it is bathed with water, it retains the water until when the forces prevent water runoff. The ground behaves in the same way, the water that does not drain and evapotranspires, infiltrates into the ground. Plants will use this water in the period in which the rainfall water does not satisfy their requirements. The water reserve, then increases during rainfall according to the relationship:

$$RI_{a} = RI_{p} + (P - R) - E_{tp} \qquad (7)$$

When the net rainfall (P – R) is less than the potential evapotranspiration; we use the depletion law and RI changes to:

$$RI_{a} = Ce^{-P_{ac}/C} \qquad (8)$$

Water loss accumulated P_{ac} is a function that only exists when it is in the integration phase of the RI, this is a relationship of the type:

$$P_{ac} = P_{acp} + \left[(E_{tp} - (P - R)\right] \qquad (9)$$

Infiltration N is obtained by difference between the Reserve Water RIa and field capacity C.

$$N = RI_a - C \qquad (10)$$

Estimation of Water Balance through ArcGIS

The Geographic Information system (GIS) of the Chambo sub-basin was built using ASTER satellite images and the information provided by the Ecuadorian Central Agricultural Services (CESA). As a result the area of the basin was estimated to be 3589.55 km^2 (Figure 3.21).

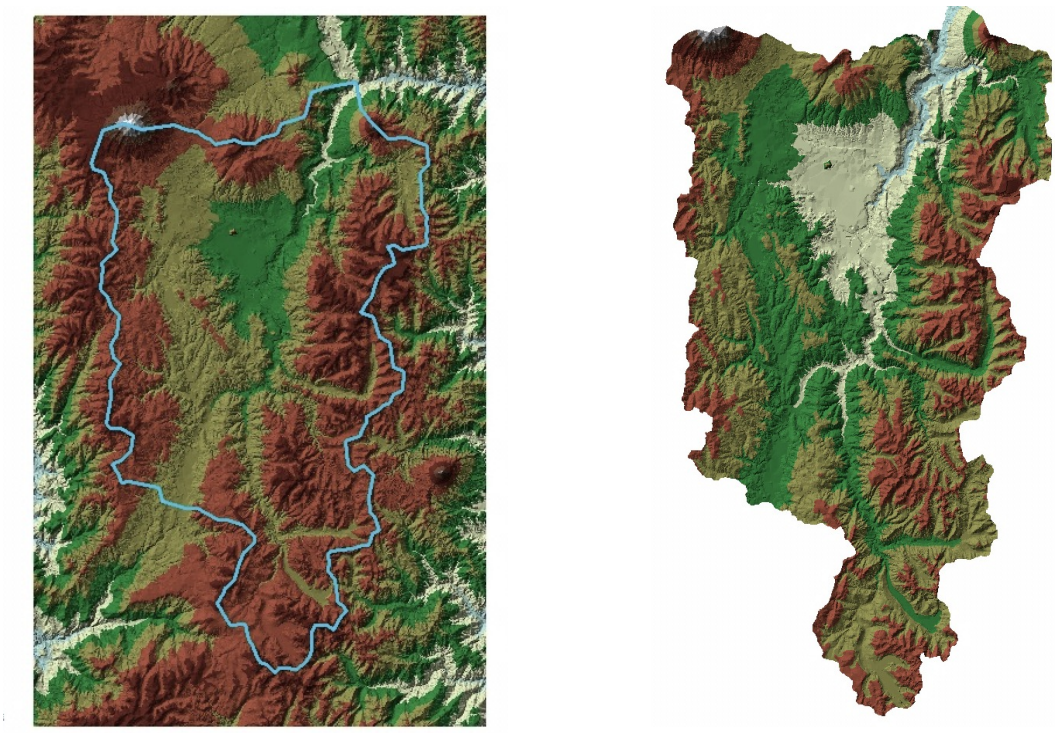

Figure 3. 21: Chambo river basin boundaries.

The hydrographic basin system (Figure 3.16) has thirty three tributaries that flow in all directions feeding the Chambo River. The main rivers are: Cebadas fed by the Atillo and Yasipan rivers that originate at the southern limits of the basin, and the Guano River coming from the North . Other important tributaries are the Chibunga, Sicalpa, San Juan, Blanco and Guargualla rivers.

Using the GIS, as well as the Temperature and Precipitation data obtained from Meteorological annual directories at the National Institute of Meteorology and

Hydrology (INAMHI), we applied the methodology for the evaluation of the water balance through monthly average values over the course of a year, showing the results below from a point in the basin Table 3.6.

Month	Etp (mm)	R (mm)	N (mm)	A (mm)	P (mm)
January	5.56692	1.13582	0.465919	37.679841	44.8485
February	5.17427	7.77698	0.00	56.87365	69.8249
March	5.73043	26.4765	25.5244	51.92167	109.653
April	5.57439	26.4765	27.7388	49.86331	109.653
May	5.60642	13.0453	13.9743	50.33408	82.9601
Jun	5.11072	3.53871	1.51854	46.08823	56.2562
July	4.98117	1.13148	0.00	38.70825	44.8209
August	5.05643	0.098764	0.00	29.807106	34.9623
September	5.21836	0.060408	0.00	28.811532	34.0903
October	5.85237	6.80348	0.00	54.39725	67.0531
November	5.52377	7.91765	4.08191	52.69037	70.2137
December	5.8202	4.33843	0.931839	48.101131	59.1916

Table 3. 6: Water Balance at the Chambo basin at a point (mm/month)

Figure 3.22 shows the behavior of the rainfall at one point during the entire year, an increase in rainfall may also be noted during the months of March and April, and a decline during September and October, this is always a cyclical process. Figure 3.23 shows the behavior of the rainfall in the Chambo sub-basin for the entire year.

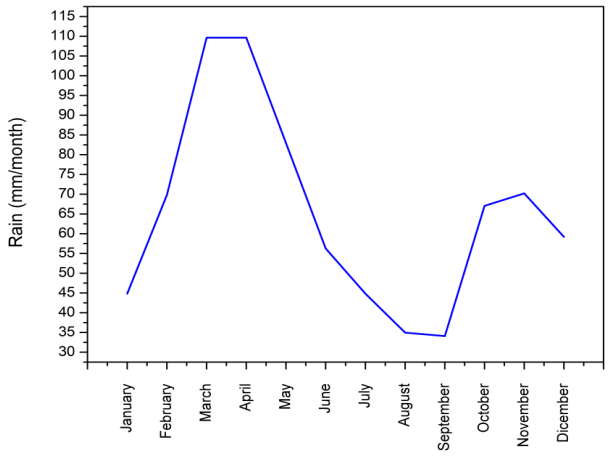

Figure 3. 22: Rainfall at one point in the Chambo sub-basin

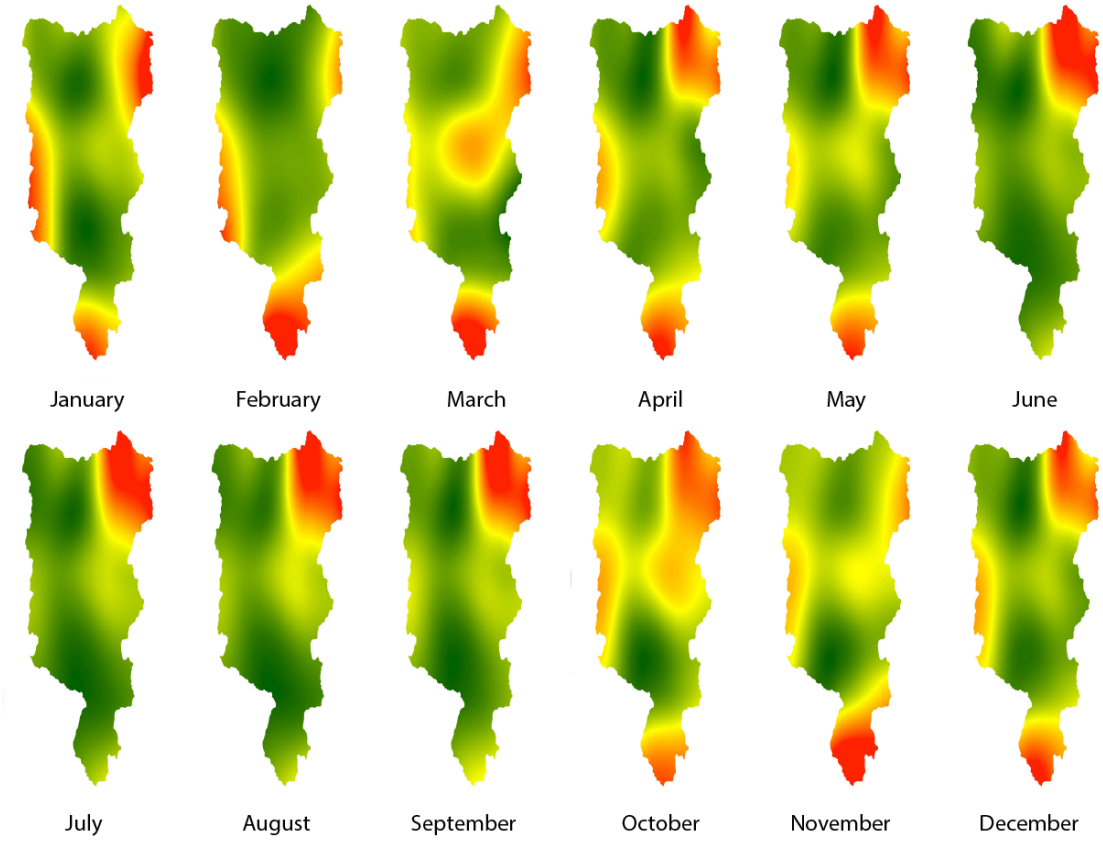

Figure 3. 23: Rainfall in Chambo the sub-basin for the entire year.

Figure 3.24 a) shows the behavior of the evapotranspiration in one point during one year, an increase in evapotranspiration values may also be noted during the month of March, a decline during July, and increases again in September, this is a cyclical process. Figure 3.24 b) shows the evapotranspiration at the Chambo River subbasin for January.

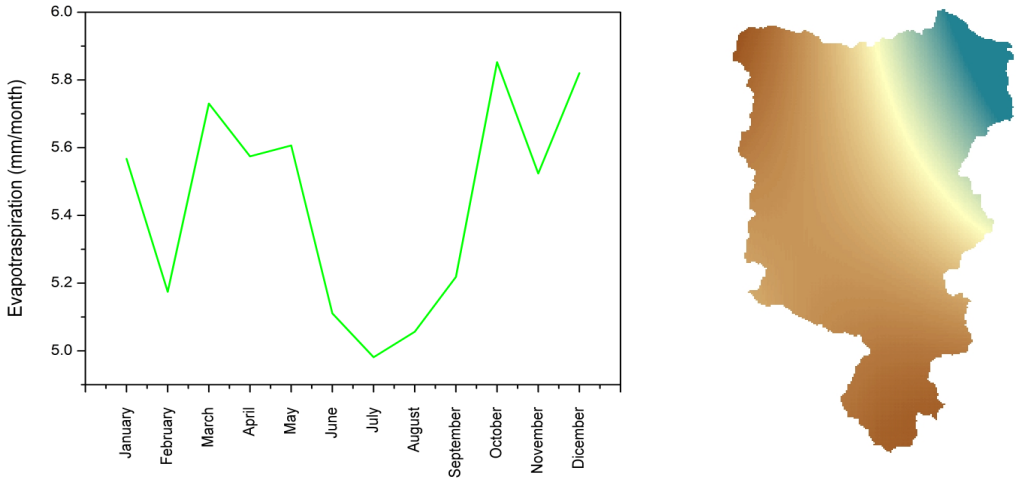

a) **b)**

Figure 3. 24: a) Evapotranspiration at one point in the subbasin of the Chambo River year round b) Evapotranspiration in the Chambo sub-basin during January.

Figure 3.25 a) shows the behavior of the runoff in one point during the entire year, an increase in values may also be noted during the months of March and April, a decline during August and September, and increases again in November, this is a cyclical process. Figure 3.25 b) shows the runoff at the sub-basin of Chambo River and the change of values between January and March.

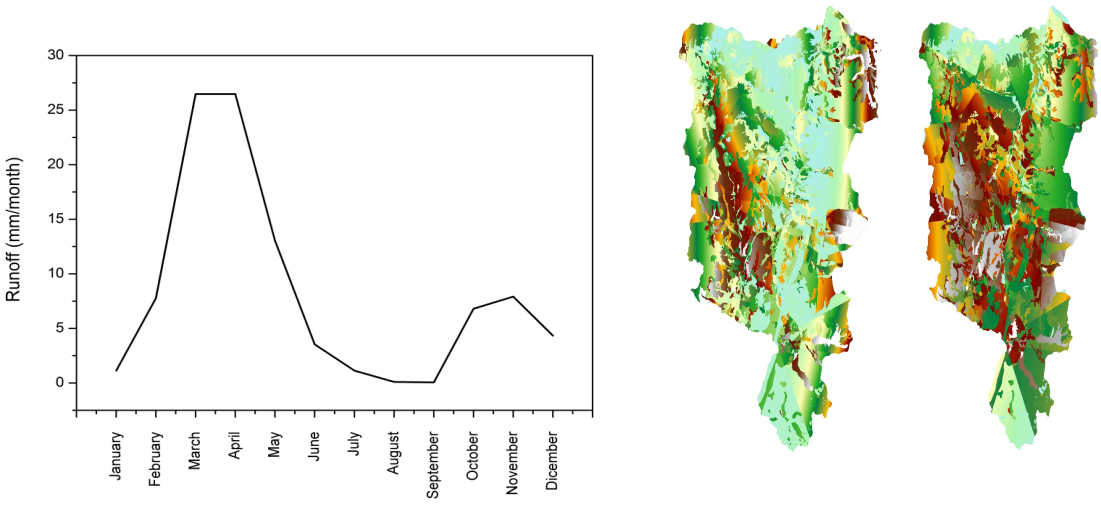

a) **b)**

Figure 3. 25: a) Runoff at one point in the Chambo sub-basin during one year b) runoff at the Chambo sub-basin and the change of the values between January and March.

Figure 3.26 a) shows the behavior of the infiltration at one point over the entire year, an increase in values may also be noted during the months of March and April, a decline during July until October, and increases again in November, this is a cyclical process. Figure 3.26 b) shows the infiltration at the Chambo sub-basin and the change in values between February and March.

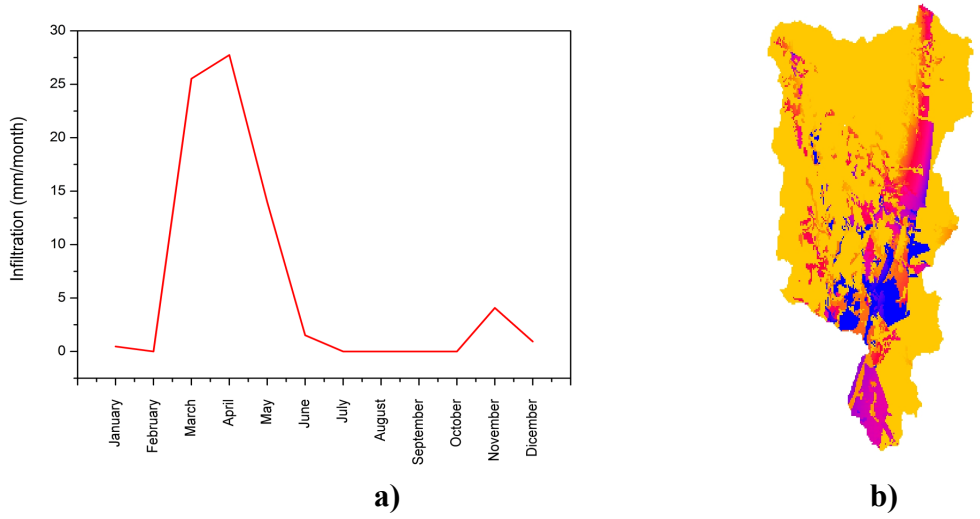

Figure 3. 26: a) Infiltration at one point in the Chambo sub-basin over the course of a year b) Infiltration at the Chambo sub-basin and the change of values between February and March.

The main result is the infiltration in the aquifer area. Figure 3.27 shows the behavior of the values of infiltration in the Chambo aquifer for the entire year. The infiltration values range, during the year, from 0.0 mm (red areas) to 50 mm (green areas).

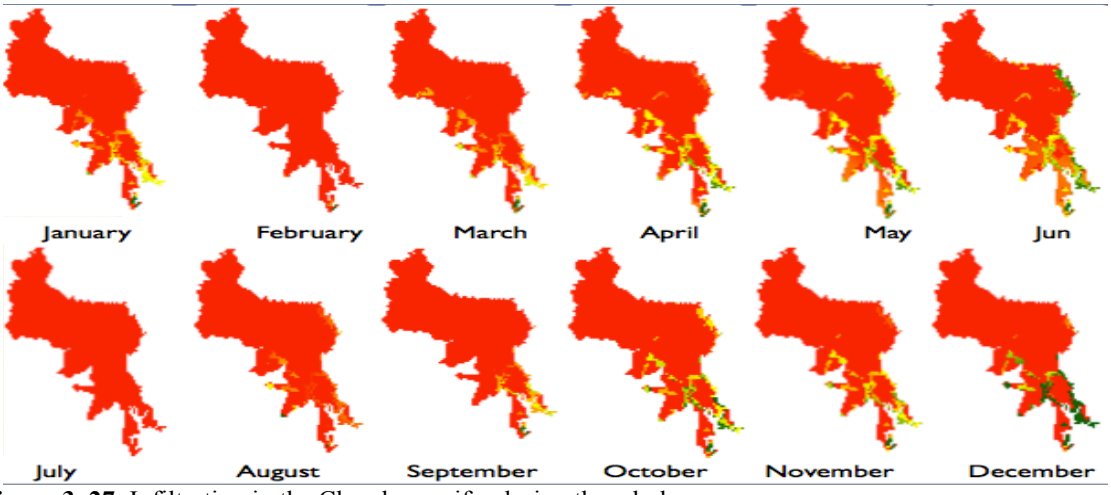

Figure 3. 27: Infiltration in the Chambo aquifer during the whole year.

3.1.5 Hydrogeological Balance

An aquifer is an underground layer of water-bearing permeable rock or unconsolidated materials (gravel, sand, or silt) from which groundwater can be extracted using a water well. The aquifer is a hydrologic and hydrodynamic system, identified by five quantifiable characteristics:

1. This is a reservoir, with a defined space, characterized by the contour conditions, dimensions or configurations, internal organization or structure. Identified as a hydrogeological formation.
2. Some internal processes in the case of hydrodynamic, hydrochemical and hydrobiological mechanisms allow for: storage, transport (transfer of water and energy quantities) and a means of geochemical exchange.
3. A sequence of water cycle with some interactions with the environment, manifested by three behaviors: hydrodynamic, hydrochemical and hydrobiological. This sequence is characterized by the relationship impulse/response expressed as a ratio or transferring function.
4. The variability of these characteristics in space.
5. The variability of hydrogeological forces over time. The latter is based on a time series that allows for making predictions.

The aquifer can be represented with a conceptual model. The configuration and management of the aquifer is given by their size, geologic and hydrodynamic characteristics or contour conditions. The bottom of the aquifer (substrate) is constituted by an impermeable hydrological formation, and the upper limit is of three types:

1. Hydrodynamic with free fluctuations: unconfined aquifer or water table;
2. Geological waterproof: confined aquifer;
3. Geological semipermeable: semiconfined aquifer.

General equations of groundwater flow

The continuity equation derived from the principle of mass conservation, establishes that the inbound mass flow is equal to the outbound mass flow unless there is a change

in mass over time. The hypotheses by the continuity equation are: a) degree of saturation unitary, b) fluid with homogeneous density.

Moreover, if we consider a parallelepiped elementary volume, the inbound mass flow on one side of the generic face is $\rho q_n A_n$, and q_n is the specific flow which cross through section A_n, of normal $\hat{n}$. This flow is developed through the Taylor series in relation to the gravity center of the elementary volume, the inbound and outbound mass is obtained:

$$I_x = \rho q_x \Delta y \Delta z - \frac{\partial}{\partial_x}(\rho q_x)\Delta y \Delta z \frac{1}{2}\Delta x$$

$$O_z = \rho q_z \Delta y \Delta z - \frac{\partial}{\partial_x}(\rho q_x)\Delta y \Delta z \frac{1}{2}\Delta x$$

Obtaining such expressions for all directions and applying the principle of mass conservation, we have:

$$-\left[\frac{\partial}{\partial_x}(\rho q_x) + \frac{\partial}{\partial_y}(\rho q_y) + \frac{\partial}{\partial_z}(\rho q_z)\right]\Delta x \Delta y \Delta z = \frac{\partial}{\partial_t}(\rho n \Delta x \Delta y \Delta z) \qquad (11)$$

As from the principle of mass conservation, and consequently the continuity equation, the volume under consideration is irrelevant; this can be neglected. Therefore, the continuity equation becomes:

$$-\nabla \cdot (\rho \boldsymbol{q}) = \frac{\partial}{\partial t}(\rho n) \qquad (12)$$

Undeformable media: by replacing the specific flow q with the general form of Darcy's law; assuming the fluid is incompressible, and the solid part is non-deformable, we obtain the general groundwater equation in non-deformable porous media:

$$\nabla \cdot (K \nabla h) = \frac{\partial n}{\partial t} \qquad (13)$$

Deformable media: The variations of porosity and density in deformable porous media over time, due to variations in the internal pressure of the medium caused by external actions (pumping, recharge, drainage, etc.). Given the previous definition, the deformability of the porous medium must be applied only in a vertical direction. The grain direction (vertical) is dz/dt therefore the velocity vector is: $v_g = [0,0,dz/dt]$. The position in space at time t of the centroid is provided by: $z = \xi + \int_0^t w_g dt$ with ξ position of the centroid at time $t = 0$. Given the displacement volume V', the average

velocity is given by the sum between the Darcy velocity and the fluid solid velocity with $V'(nw_g\hat{k})$, Darcy is relative to the volume V', the continuity equation is:

$$-\nabla \cdot \left(\rho \boldsymbol{q_D} + \boldsymbol{\rho} n w_g \hat{k}\right) = \frac{\partial}{\partial t}\,(\rho n) \qquad (14)$$

and also

$$-\nabla \cdot (\rho \boldsymbol{q}) - n w_g \frac{\partial \rho}{\partial z} - \rho w_g \frac{\partial n}{\partial z} - \rho n \frac{\partial w_g}{\partial z} = n \frac{\partial \rho}{\partial t} + \rho \frac{\partial n}{\partial t} \quad (15)$$

the partial derivatives are transformed through the Eulerian derivation rule:

$$-\nabla \cdot (\rho \boldsymbol{q}) = n \frac{\partial \rho}{\partial t} + \rho \frac{\partial n}{\partial t} + \rho n \frac{\partial w_g}{\partial z} \qquad (16)$$

The first term of the second member represents the temporal variation of the fluid as a function of elastic behavior; and is defined as the coefficient of fluid compressibility:

$$\beta = -\frac{1}{V_w}\frac{dV_w}{dp}$$

with $V_w = \frac{m}{\rho}$

replacing and deriving

$$\frac{\partial \rho}{\partial t} = \beta \rho \frac{\partial p}{\partial t} \qquad (17)$$

The second term of the second member represents the variation of the porosity of the solid, for determining this quantity the continuity equation is applied again, but this time only in the solid part:

$$-\nabla \cdot \rho_s (1-n) w_g \hat{k} = \frac{\partial}{\partial t}\left(\rho_s (1-n)\right) \qquad (18)$$

For the undeformability hypothesis $(\rho_s = cost)$:

$$(1-n)\frac{\partial w_g}{\partial z} - w_g \frac{\partial n}{\partial z} = \frac{\partial n}{\partial t} \qquad (19)$$

and the passing to total derivatives

$$(1-n)\frac{\partial w_g}{\partial z} = \frac{\partial n}{\partial t} \qquad (20)$$

The third term of second member represents the variation of the velocity of the grains in function to the compressibility of the solid part, the coefficient of fluid compressibility of the solid part:

$$\alpha = -\frac{1}{\Delta z}\frac{d(\Delta z)}{d\sigma_z}$$

$$\alpha\frac{d\sigma_z}{dt} = -\frac{1}{\Delta z}\frac{d(\Delta z)}{dt}$$

such as $\sigma_z + p = cost$, we have then:

$$\alpha\frac{\partial h}{\partial t} = \frac{\partial}{\partial z}w_g \qquad (21)$$

Substituting the explanatory term of equation (16) is obtained:

$$-\nabla\cdot(\rho\boldsymbol{q}) = \rho(\alpha + n\beta)\frac{dp}{dt} \qquad (22)$$

Because the speed of the grains is very small, we change the total derivative to partial derivative, the term $w_g\,\partial p/\partial z$ can be ignored compared to $\partial p/\partial t$ therefore can be written (de Marsily, 1986):

$$-\nabla\cdot(\rho\boldsymbol{q}) = \rho(\alpha + n\beta)\frac{\partial p}{\partial t} \qquad (23)$$

There are some problems in groundwater, therefore, the spatial variation of the density is much smaller than the variation of the fluid velocity and can be ignored. May also explain the pressure in function of hydraulic head:

$$-\nabla\cdot(\boldsymbol{q}) = \rho g(\alpha + n\beta)\left(\frac{\partial h}{\partial t} - w_g\right) \qquad (24)$$

the specifics storage is: $S_s = \rho g(\alpha + n\beta)$ obtain:

$$-\nabla\cdot(\boldsymbol{q}) = S_s\left(\frac{\partial h}{\partial t} - w_g\right) \qquad (25)$$

The term w_g can be ignored because it is small respect to velocity of Darcy's Law; therefore, we obtain the general equation of groundwater flow by undeformable media:

$$-\nabla\cdot(K\nabla h) = S_s\frac{\partial h}{\partial t} \qquad (26)$$

Groundwater flow Equation at regional scale

It may be assumed that the flow is essentially horizontal for very large spatial and temporal scales, or that the vertical component of the velocity vector can be ignored,

because it is equivalent to assuming that the hydraulic gradient along the vertical is zero (Dupuit hypothesis) and also assume that the axes of the reference system (X, Y, Z) are principal axes of anisotropy. For Dupuit hypothesis, the hydraulic head is constant along the vertical, then there is variation only in the plane (h (x, y)) and also the problem can be considered two-dimensionally. Therefore, it is possible to integrate the general equation (tridimensional) of groundwater flow from vertical movement. These assumptions form the two classical equations of groundwater flow: the equation of motion for confined and unconfined aquifers.

Flow Equation for an unconfined aquifer: An unconfined aquifer is limited only in the lower part. The main difference between an unconfined and confined aquifer stands in the first released quantity of water, which is , in the latter case, a function of the compressibility of the fluid and the medium, while in the first case depends on the variations of the water surface and the water content in the pores. Consequently the general equation of groundwater flow should consider an elementary volume that intercepts the free surface of unconfined aquifer. In this case the integration in the thickness (which coincides to the hydraulic head), of the equation of motion for a undeformable aquifer produces the equation:

$$\frac{\partial}{\partial x}\left[\int_{z_0}^{h} K_x \frac{\partial h}{\partial x} dz\right] + \frac{\partial}{\partial y}\left[\int_{z_0}^{h} K_y \frac{\partial h}{\partial y} dz\right] = \int_{z_0}^{h} \frac{\partial n}{\partial t} dz$$

In the hypothesis of non-deformable porous medium, water may move by gravity; in the second member it may replace the post of the total porosity (n) the effective porosity (nd). If it is hypothesized that as the hydraulic head, it does not vary along the vertical; it behaves similarly to the hydraulic conductivity K_x and K_y, we obtain:

$$\frac{\partial}{\partial x}\left[K_x(h - z_0)\frac{\partial h}{\partial x}\right] + \frac{\partial}{\partial y}\left[K_y(h - z_0)\frac{\partial h}{\partial y}\right] = n_d \frac{\partial n}{\partial t}$$

These equations are not linear in h but can be linearized by using (Boussinesque linearized) $T_x = \int_{z_0}^{\overline{h}} K_x dz$ and $T_y = \int_{z_0}^{\overline{h}} K_y dz$, specifying with h the average hydraulic head, obtained from the groundwater equation for a confined aquifer:

$$\frac{\partial}{\partial x}\left[T_x \frac{\partial h}{\partial x}\right] + \frac{\partial}{\partial y}\left[T_y \frac{\partial h}{\partial y}\right] = n_d \frac{\partial n}{\partial t} \qquad (27)$$

Flow Equation for a confined aquifer: A confined aquifer is limited by the top and bottom through an impermeable substrate. The quantity of water that can be extracted

depends on the compressibility of the porous media and fluid; but not simply by the quantity of water contained in the pores. Assuming Dupuit, the equation of water movement in a confined aquifer is obtained by integrating the equation of groundwater flow for deformable porous medium (26) in the thickness (B) of the aquifer:

$$\frac{\partial}{\partial x}\left[\int_0^B K_x \frac{\partial h}{\partial x} dz\right] + \frac{\partial}{\partial y}\left[\int_0^B K_y \frac{\partial h}{\partial y} dz\right] = \int_0^B S_s \frac{\partial n}{\partial t} dz$$

With the assumption that in the hydraulic conductivity K_x and K_y there is no change along the vertical, and applying Leibnitz rule and using $T_x = \int_0^B K_x dz$ and $T_y = \int_0^B K_y dz$, obtain:

$$\frac{\partial}{\partial x}\left[T_x \frac{\partial h}{\partial x}\right] + \frac{\partial}{\partial y}\left[T_y \frac{\partial h}{\partial y}\right] = S \frac{\partial h}{\partial t} \qquad (28)$$

and with S as storage coefficient.

The boundary conditions

The boundary conditions are the requirements for hydraulic head and flow, as in this case we have:

Dirichlet conditions: it is present when to the contour is assigned the hydraulic head:

$$h(x, y, z, t) = h^*(t) \qquad (x, y, z, t) \in \Gamma_1$$

Neumann conditions: it is present when to the contour is assigned the flow values:

$$q \cdot n = -K\nabla \mathrm{h} \cdot n = g^*(x, y, z, t) \qquad (x, y, z, t) \in \Gamma_2$$

Cauchy conditions: it has when to the contour is assigned the flow values or the hydraulic head:

$$-K\nabla \mathrm{h} \cdot n = N_o + R_b(h_b - h) \qquad (x, y, z, t) \in \Gamma_3$$

Where N_o is an external flux independent of hydraulic, R_b is the external resistance [T^{-1}] and h_b external hydraulic head.

Hydrogeological Modeling

The Geological map was used to delimitate the aquifer (Figure 3.28). The Riobamba formation, mainly composed by sand and gravel, is the only geomaterial in the area, capable to guarantee a groundwater flow. ,.

For modeling purposes and because our objective is to determine whether or not there is a water entrance from the Chimborazo volcano, the following final modeling domain has been adopted (Figure 3.29 a and Figure 3.29 b): a) Starting from the geological boundaries of the aquifer b) we adjusted the domain boundaries, because of the presence of the Chambo river coming from the south towards the east, and Chibunga river which runs through the basin from the western sector. These rivers represent a Dirchlet baundary condition, so that the aquifer area which goes from these rivers towards the south direction has no influence on the estimation of the water amount coming from the North side of the domain. For this reason the model domain has assumed the aspect shown in figure 3.29b

The model surface was constructed through DTM data, and the bottom of the aquifer through an ordinary kriging of the information coming from an Vertical Electrical Sounding campaign (Figure 3.30).

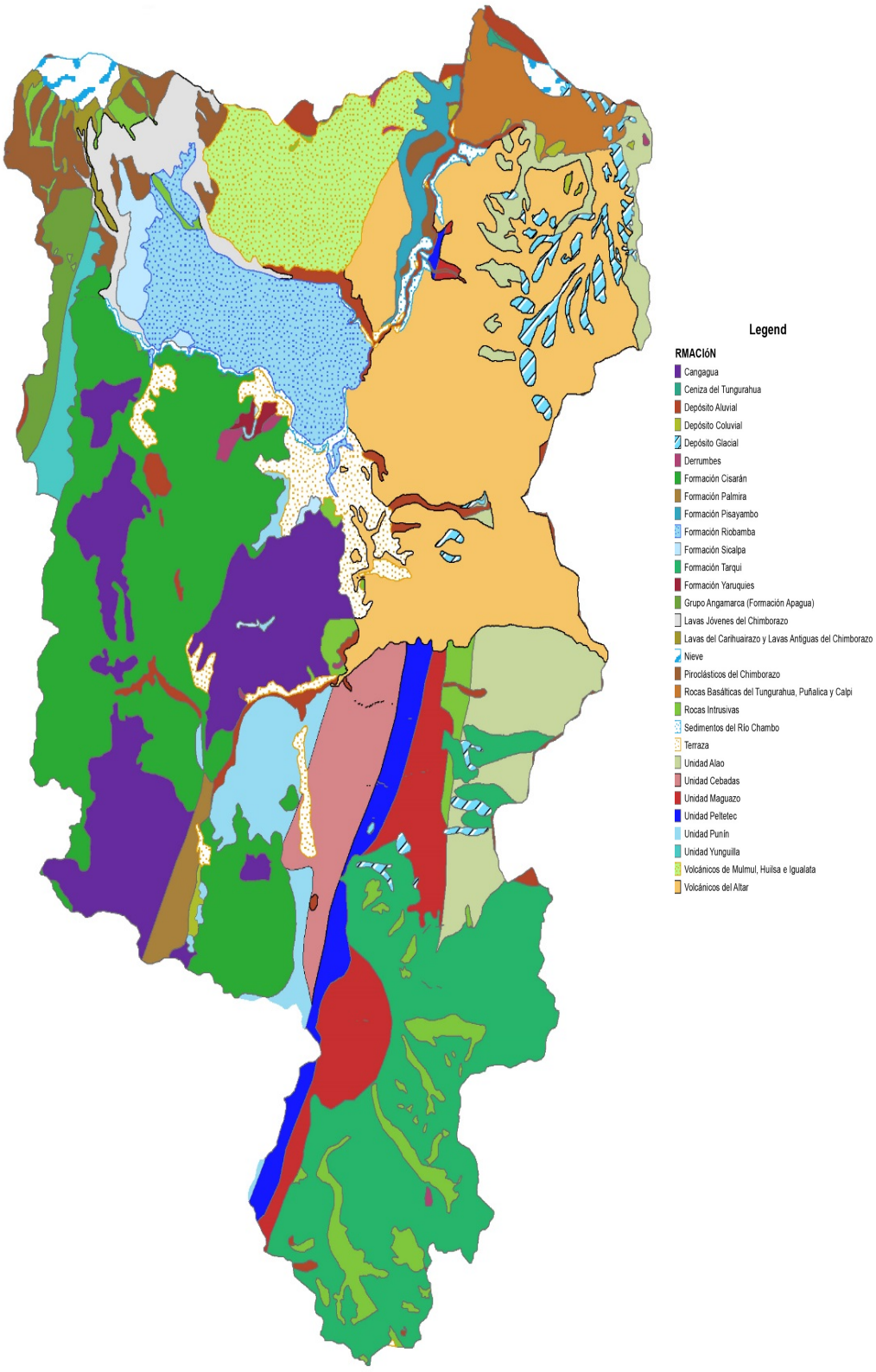

Figure 3. 28: Chambo river basin geology.

Figure 3. 29: a) Aquifer geological boundaries b) Aquifer modeling boundaries

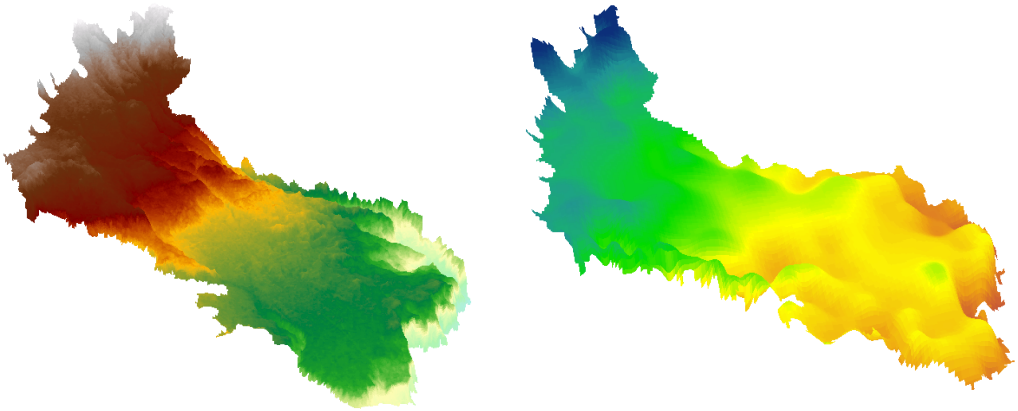

Figure 3. 30: a) DTM surface of the aquifer b) Kriging of the aquifer's bottom.

The distribution of the Hydraulic conductivity K (Figure 27) is derived from an ordinary Kriging of the information derived from the interpretation of various pumping tests performed in the basin (Table 10).

The hydrological forcings of the aquifer are: a) Guano river, Chibunga river, Chambo river in addition to the pumping wells withdrawing a flowrate of about 600 l/s for the Water Supply System of the cities of Riobamba and Guano and b) the infiltration rate calculated by the superficial water balance (Figure 28).

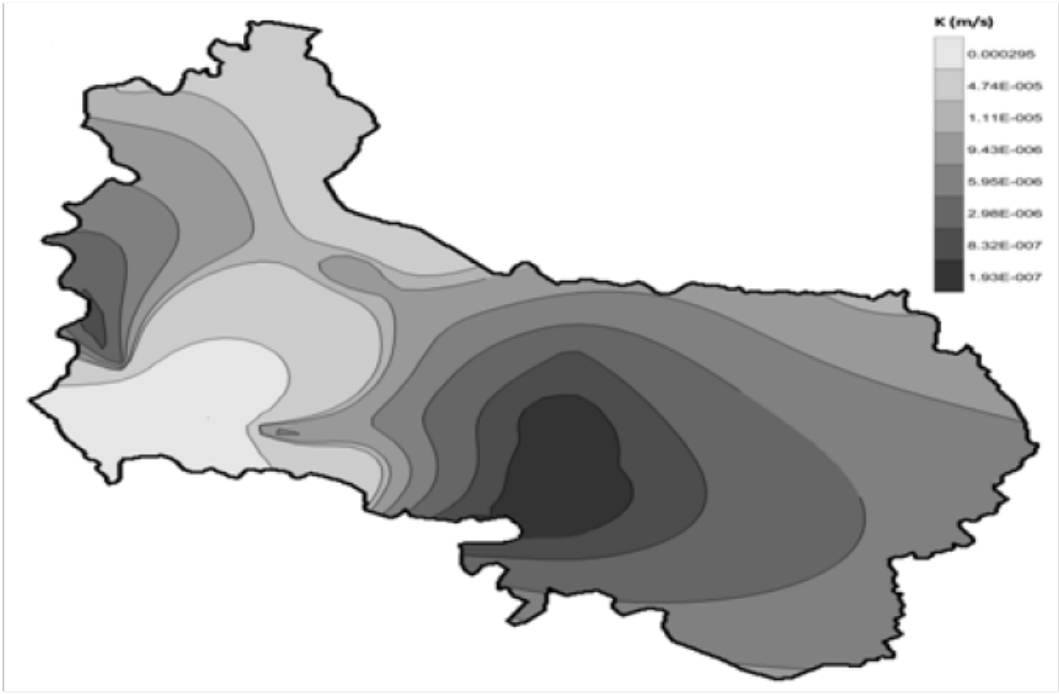

Figure 3. 31: Distribution of Hydraulic Conductivity K (m/s)

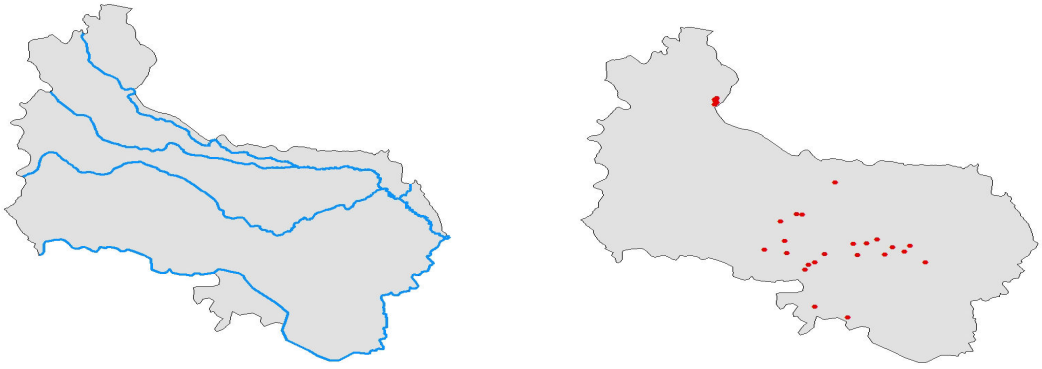

a)

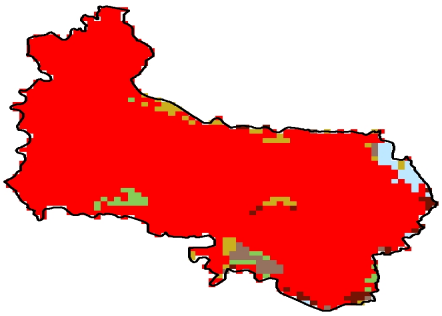

b)

Figure 3. 32: a) Rives and wells present at the aquifer b) infiltration (mm/month)

Location Name	X (m)	Y (m)	K (m/day)	K (m/s)
Licán	754519	9817112	0.017693	2.05E-07
Quebrada Colorada	762947	9807070	0.989412	1.15E-05
San Martín de Veranillo	764359	9816828	1.841023	2.13E-05
Santa Ana de Tapi	758178	9819647	0.257529	2.98E-06
El Carmen	758401	9820331	27.311492	3.16E-04
San Antonio – Vía a Baños	763392	9817550	0.514213	5.95E-06
Los Chingazos	769032	9822158	0.966644	1.12E-05
Langos	760132	9822180	0.0766	8.87E-07
Liribamba	756937	9817682	1.776854	2.06E-05
Shuyo	759209	9813371	0.016737	1.94E-07
Santa Cruz	760772	9813185	0.071897	8.32E-07
Brigada Galápagos	760979	9816928	0.906343	1.05E-05

Table 3. 7: Wells used for the reconstruction of Hydraulic conductivity spatial distribution

The boundary conditions are represented by Neuman baundary conditions along the side bordering the Chimborazo volcano, from which a probable lateral recharge occur (water amount we want to estimate) , and Dirichlet boundary conditions at the rivers bordering the south side of the domain; No flow boundary conditions elsewhere, where no existing hydraulic forcings are present. Once the model was implemented, The estimation of the water amount coming from the volcano has been obtained by means of an iterative inverse procedure based on the capacity of the model to reproduce the hydraulic heads observed in wells, sources and ponds (Figure 3.32). The parameter calibration process has been performed by two main base programs: the PEST optimization software and the ModFlow groundwater model. PEST uses a nonlinear estimation technique known as the Gauss-Marquardt- Levenberg method, while MODFLOW simulates steady and non-steady groundwater flow. Pest changes the beginning trial values of the parameters to be estimated, until the ModFlow code doesn't generate a hydraulic heads distribution which minimize the error between measured and calculated values in specific observation points.

The inversion procedure was run for twelve different monthly scenarios, and the results showed the existence of an flowrate of approximately 2 m^3/s coming from the northeastern side of the model (Figure 3.33), and so from the Chimborazo volcano;.

The modeling reliability is represented by the scattergraphs between observed and calculated Hydraulic head values (Figure 3.35). January is the month presenting the greatest margin error, with respect to those observed during the other months. The best calculated values are those from the month of March with an R^2 equal to 0,9998 and an annual average R^2 of 0,9952.

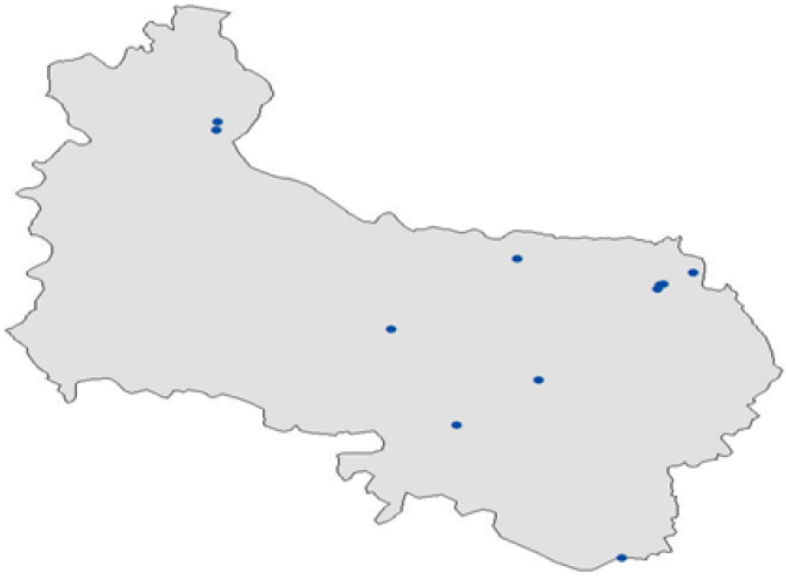

Figure 3. 33: Observation points

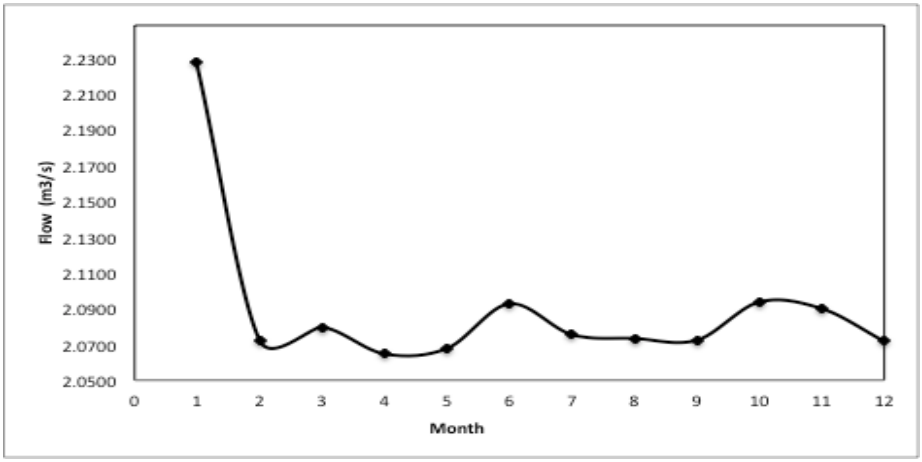

Figure 3. 34: Estimated flow rate variations coming from the Chimborazo.

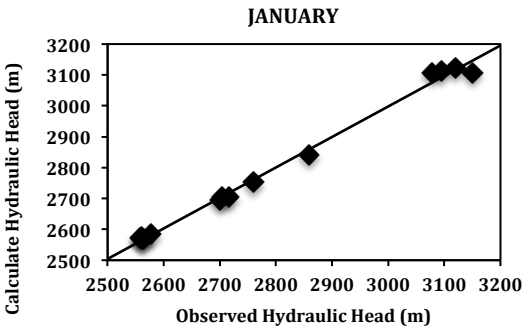
JANUARY
Calculate Hydraulic Head (m)
Observed Hydraulic Head (m)
2500 2600 2700 2800 2900 3000 3100 3200

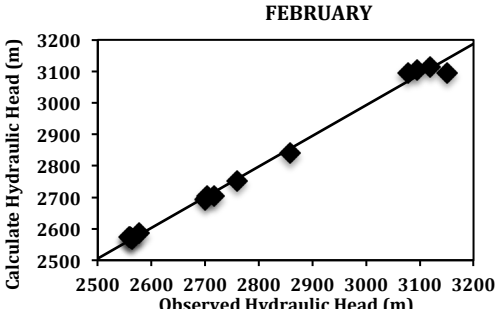
FEBRUARY
Calculate Hydraulic Head (m)
Observed Hydraulic Head (m)
2500 2600 2700 2800 2900 3000 3100 3200

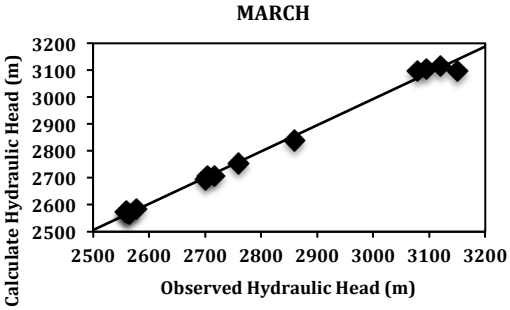
MARCH
Calculate Hydraulic Head (m)
Observed Hydraulic Head (m)
2500 2600 2700 2800 2900 3000 3100 3200

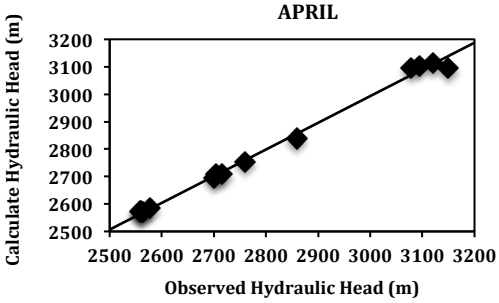
APRIL
Calculate Hydraulic Head (m)
Observed Hydraulic Head (m)
2500 2600 2700 2800 2900 3000 3100 3200

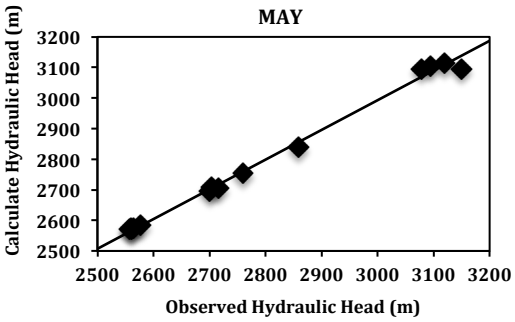
MAY
Calculate Hydraulic Head (m)
Observed Hydraulic Head (m)
2500 2600 2700 2800 2900 3000 3100 3200

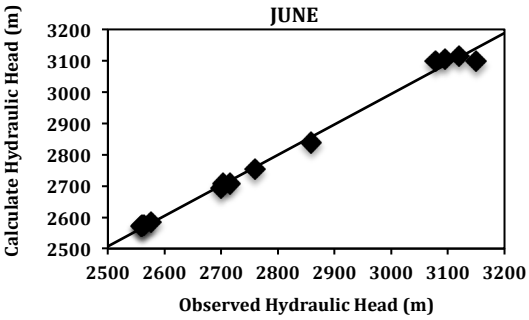
JUNE
Calculate Hydraulic Head (m)
Observed Hydraulic Head (m)
2500 2600 2700 2800 2900 3000 3100 3200

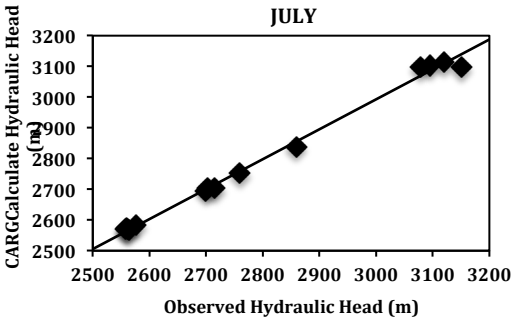
JULY
CARGCalculate Hydraulic Head (m)
Observed Hydraulic Head (m)
2500 2600 2700 2800 2900 3000 3100 3200

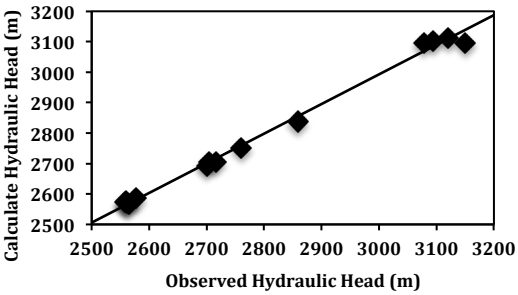
AUGUST
Calculate Hydraulic Head (m)
Observed Hydraulic Head (m)
2500 2600 2700 2800 2900 3000 3100 3200

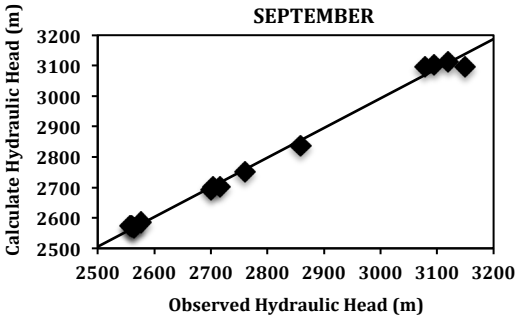
SEPTEMBER
Calculate Hydraulic Head (m)
Observed Hydraulic Head (m)
2500 2600 2700 2800 2900 3000 3100 3200

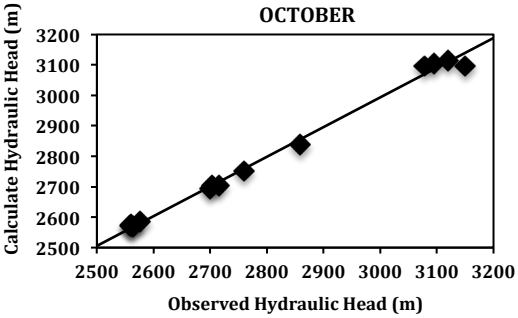
OCTOBER
Calculate Hydraulic Head (m)
Observed Hydraulic Head (m)
2500 2600 2700 2800 2900 3000 3100 3200

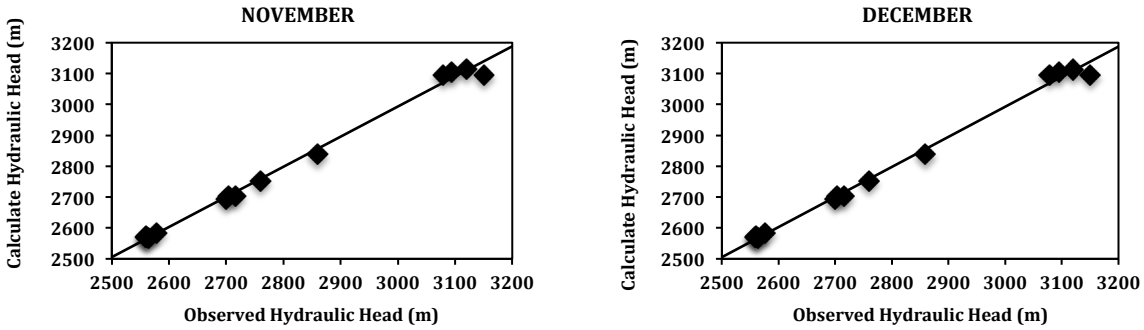

Figure 3. 35: Confrontation between observed and calculated hydraulic head

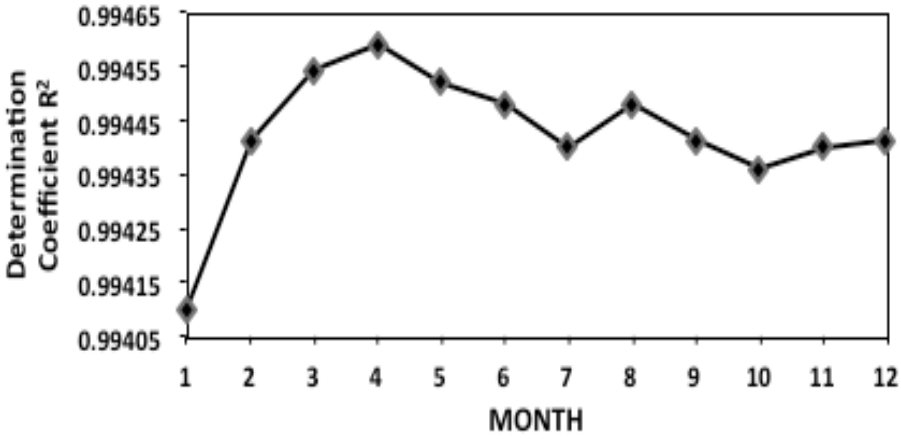

Figure 3. 36: Determination R^2 coefficient variation between observed and calculated values.

3.1.6 Conclusion

This study definitely demonstrates that the Chambo aquifer it's not fossil, but it's fed by a lateral recharge of about 2 m^3/s coming from the glacier of the Chimborazo volcano.

The results of this study, together with the ones coming from the ^{14}C analyses, suggest that the reserves of ancestral ice of the Chimborazo glacier are dissolving, highlighting the influence of the climate change in Ecuador and, hence, in the world.

This study can be seen as a starting point for possible future modeling improvements:

- Accurate characterization of the site: more pumping and slug tests spatially well distributed for a better representation of the aquifer heterogeneity.

- A larger observations database: more hydraulic heads measurements spatially and temporaly well distributed for a better conditioning of the inverse procedure
- The adoption of a fully-coupled modeling approach: the possibility to set up future climate scenarios, and to relate these latter with surface-water and groundwater phenomena could represent a powerful instrument to foresee the fate of the Chimborazo glacier and to plan in a wiser way the exploitation of the aquifer.

CONCLUSION

In this thesis, new approaches to improve aquifer characterization and monitoring by means of hydrogeophysical methodologies have been adopted. The developed methodologies have led to the following conclusions:

The solute transport in three different granular media (granite pebbles, gravel and Leca®), exhibiting similar particle sizes but different particle shapes, was analyzed in this study. Solute transport data, using chloride as a tracer, for 27 particle size fractions (9 for each material), at 6 different pore flow velocities (corresponding to a total of 324 breakthrough curves (BTC's)), were acquired during the analysis.

The measured BTC's were fitted to both single porosity and dual porosity models. Results of the fitting confirm that both models can be accurately fitted to the initial part of the breakthrough curves. However, as expected, significant deviations between measured and fitted values occur for the single porosity model when fitting the tail end of the BTC's, while the dual porosity model is able to achieve accurate fits for the entire curve. This suggests the presence of non-equilibrium solute mass transfer between a mobile and an immobile phase, as also often seen in previous studies. Among the three materials, BTC's for Leca® (having the most rounded particles) exhibit the largest amount of tailing while granite (having the least rounded particles) exhibit the smallest amount of tailing suggesting that particle shape has a significant impact on mass transfer.

Values of dispersion coefficient D were determined by fitting the single porosity model to the initial part of the BTC's. The D-values were then used in the dual porosity model together with the entire BTC's to estimate values of mass transfer coefficient k and mobile porosity (εm). Leca® showed the highest k-values (a consequence of the higher amount of tailing in the BTC's), while granite showed the lowest, values. This indicate that the more spherical the particles are, the greater the mass transfer between the mobile and immobile phases becomes. Round particles in fact expedite the exchange between mobile and immobile phases, while particles with more angular shapes (mainly granite) hinder it. The results further indicated that the slope could be predicted from particle size distribution characteristics and particle shape using a simple linear

expression. This means that dual porosity model parameters (k and εm) may be estimated using only the initial part of the BTC's, in combination with porous medium characteristics, which in turn mean that significant time can be saved as the time consuming measurements of the tail end of the curves can be excluded. As the quantity of data used in the analyses presented here are somewhat limited, however, additional measurements on other media, having different particle size distributions and particle shapes are needed to verify and improve the relationships presented in this study.

The reliability of GPR as a tool to detect near-surface contaminants is illustrated through a test representing diesel fuel infiltration in a saturated soil, carried out under controlled conditions in a hydro-geophysical laboratory of the University of Calabria. Lots of the performed tests show that GPR may provide an indication of NAPL saturation degree in the saturated zone. In fact, results show significant changes in the responses of electromagnetic measurements in presence of fuel contamination. Moreover, GPR can provide high-density, quantitative data for investigations of vadose zone contaminant hydrogeology. The experimental results show the capability of GPR to identify the contaminant dispersed in the subsoil.

The chemical analysis carried out on the samples, validate the technique of GPR in the study of infiltration process into the soil and provide basic data for the construction of empirical relationships for the estimation of the real amount of contaminants in the subsurface. For this reason, the future of this research will be the evaluation of the capability to estimate the real content of LNAPL from the values of permittivity by geophysical techniques.

The new methodology for the identification of aquifers watertable based on the correlation between hydraulic head values and SP signals generated by the water flow passing through porous media under natural stimuli gave back the following considerations:

From the field measurements, the influence of an increasing hydraulic head distribution on the SP signals was observed. When the hydraulic head decreases there SP signals change but not uniformly.

The conceptual model realized in COMSOL simulates the variations in time for hydraulic heads and SP signals. This model shows the theoretical correlation between these two variables. The correspondence between the observed SP with the modeled SP curves prove the possibility to guess the position of the water table by means of SP measurements on the field.

The Know-how acquired through laboratory and experimental field tests, has been than applied in a real problem, regarding the water supply of the Chambo Aquifer in the Province of Chimborazo – Ecuador. This study definitely demonstrates that the Chambo aquifer it's not fossil, but it's fed by a lateral recharge of about 2 m3/s coming from the glacier of the Chimborazo volcano.

The results of this study, together with the ones coming from the 14C analyses, suggest that the reserves of ancestral ice of the Chimborazo glacier are dissolving, highlighting the influence of the climate change in Ecuador and, hence, in the world.

This study can be seen as a starting point for possible future modeling improvements:

Accurate characterization of the site: more pumping and slug tests spatially well distributed for a better representation of the aquifer heterogeneity.

A larger observations database: more hydraulic heads measurements spatially and temporaly well distributed for a better conditioning of the inverse procedure

The adoption of a fully-coupled modeling approach: the possibility to set up future climate scenarios, and to relate these latter with surface-water and groundwater phenomena could represent a powerful instrument to foresee the fate of the Chimborazo glacier and to plan in a wiser way the exploitation of the aquifer.

REFERENCES

Ahn, I.S., Lion, L.W., and M.L. Shuler 1996. Microscale-based modeling of polynuclear aromatic hydrocarbon transport and biodegradation in soil. Biotechnol. Bioeng. 51(1):1-14.

Arango, C., 2005. Estudio Magnetotelúrico de la zona de Lluchmajor (Mallorca): Avances en el proceso de datos y modelo 3D, PhD Thesis, Dep. de Geodinàmica i Geofísica, Universitat de Barcelona.

Archie, G.E., 1942. The electrical resistivity log as an aid in determining some reservoir characteristics, Trans. Amer. Inst. Mining Metallurgical and Petroleum Engineers, 146, 54-62.

Atekwana, E.A., Sauck W.A., Werkema JR., D.D., 1998, Characterization of a complex refinery groundwater contamination plume using multiple geoelectric methods. Proc. of the Symposium on the Application of Geophysics to Environmental and Engineering Problems, EEGS, Chicago, 427-436.

Auken, E., A.V. Christiansen and K. Sørensen, 2006 a. Structural mapping of large aquifer structures, 19th SAGEEP, Seattle, USA.

Auken, E., L. Pellerin, A.V. Christiansen and K. Sørensen, 2006 b. A survey of current trends in near-surface electrical and electromagnetic methods, Geophysics, 71, 5, G249-G260.

Ball, W.P., and P.V. Roberts 1991. Long-term sorption of halogenated organic chemicals by aquifer material 2. Intraparticle diffusion. Environ. Sci. & Technol. 25(7):1237-1249.

Bear J., (1979). Hydraulics of Grandwater, McGraw-Hill

Bedrosian, P.A., 2006. MT+, Integrating Magnetotellurics to Determine Earth Structure, Composition and Processes. Invited review paper in 18th EMIW, El Vendrell, Spain.

Benfratello, G. (1961). Contributo allo studio del bilancio idrologico del terreno agrario. L'Acqua, (2).

Benson, A. K., 1995, Applications of ground penetrating radar in assessing some geological hazards: Examples of groundwater contamination, faults, cavities. J. Appl. Geophys., 33, 177–193.

Bermejo, J.L., Sauck, W.A. and Atekwana, E.A., 1997, Geophysical discovery of a new LNAPL plume at the former Wurtsmith AFB, Oscoda, Michigan. Ground Water Monitoring Remediation, 17, 131–137.

Bigo, A. (2012). Estudio hidrogeológico de la subcuenca del río Chambo. Technical report, AVSF – CESA.

Binley, A., and A. Kemna, 2005. DC resistivity and Induced Polarization Methods, in Hydrogeophysics (Y. Rubin and S. Hubbard Eds.), Water Science and Technology Library, Springer, 129-155.

Blakely, R. J., 1995. Potential Theory in Gravity and Magnetic Applications, Cambridge University Press, 441 p.

Cameron, D.R., and A. Klute 1977. Convective-dispersive solute transport with a combined equilibrium and kinetic adsorption model. Water Resour. Res. 13(1):183-188.

Carrera, J. 1993. An overview of uncertainties in modelling groundwater solute transport. J. Contam. Hydrol. 13(1-4):23-48.

Carrera, J., Sanchez-Vila, X, Benet, I., Medina, A., Galarza, G., and J. Guimera 1998. On matrix diffusion: formulations, solution methods and qualitative effects. Hydrogeol. J. 6:178-190.

Cavazza, L. (1981). Fisica del terreno agrario. UTET, Torino, Italy. Caziani, R. and Cossu, R. (1985). Valutazione della quantitá di percolato prodotta in uno scarico controllato. Ingegneria Ambientale, (14). de Marsily, G. (1986). Quantitative hydrogeology: groundwater hydrology for engineers. Academic Press, Orlando, FL.

Choudhury, K., and D. K. Saha 2004. Integrated Geophysical and Chemical Study of Saline Water intrusion, Ground Water, 42 (5), 671-677.

Coats, K.H., and B.D Smith 1964. Dead-end pore volume and dispersion in porous media. Soc. Pet. Eng. J. 4(1):73-84.

Comsol group S.r.l, Comsol Multiphysics user's guide, version 3.5 (2008)

Cortis, A., and B. Berkowitz 2004. Anomalous transport in classical soil and sand columns. Soil Sci. Soc. Am. J. 68(5):1539-1548.

Cortis, A., and C. Knudby 2006. A continuous time random walk approach to transient flow in heterogeneous porous media. Water Resour. Res. 42(10). doi: 10.1029/2006WR005227

Culver, T.B., Hallisey, S.P., Sahoo. D., Deitsch, J.J., and J.A. Smith 1997. Modeling the desorption of organic contaminants from long-term contaminated soil using distributed mass transfer rates. Environ. Sci. Technol 31(6):1581-1588.

Cunningham, J.A., and P.V. Roberts 1998. Use of temporal moments to investigate the effects of nonuniform grain-size distribution on the transport of sorbing solutes. Water Resour. Res. 34(6):1415-1425.

Cvetkovic, V., Shapiro, A.M., and G. Dagan 1992. A solute flux approach to transport in heterogeneous formations. 2. Uncertainty analysis. Water Resour. Res. 28(5):1377-1388.

Darnet, M., 2003. Caractérisation et suivi de circulations de fluides la mesure de Potentiels Spontanés (PS). PhD thesis, Université Louis Pasteur – Strasbourg I.

Darnet, M. and G. Marquis, 2003. Modelling streaming potential (SP) signals induced movement in the vadose zone, Journal of Hydrology, 285 (2004),114–124.

Delgado, J. M. P. Q. 2006. A critical review of dispersion in packed beds. Heat Mass Transf., 42(4):279-310.

Dentz, M., and B. Berkowitz 2003. Transport behavior of a passive solute in continuous time random walks and multirate mass transfer. Water Resour. Res 39(5):111. doi:10.1029/2001WR001163.

Deutsch, C.V., and A.G. Journel, 1998. GSLIB, Geostadistical Software Library and User's Guide, Oxford, UK: Oxford University Press.

De Carvalho, J.R.F.G., and J.M.P.Q. Delgado 2003. Effect of fluid properties on dispersion in flow through packed beds. AIChE J. 49(8):1980-1985.

Doherty, J. (2006). PEST Model-Independent Parameter Estimation. Manual.

Ebach, E.A., and R.R. White 1958. Mixing of fluids flowing through beds of oacked solids. AIChE J. 4:161-169.

Edwards, L.S., 1977. A modified pseudosection for resistivity and IP. Geophysics, 42 (5), 1020-1036.

Everett, M.E. and M. Meju, 2005. Near SurfaceControlled-Source-Electromagnetic Induction: Background and Recent Advances, in Hydrogeophysics, (Y. Rubin and S. Hubbard Eds.), Water Science and Technology Library, Springer, 157-185.

Falgàs, E., J. Ledo, T. Teixidó, A. Gabàs, F. Ribera, C. Arango, P. Queralt, J.L. Plata, F.M. Rubio, J.A. Peña, A. Martí, and A. Marcuello, 2005. Geophysical Characterization of a Mediterranean coastal aqüífer: the baixa Tordera fluvio-deltaic aqüífer unit (Barcelona, NE Spain), in Groundwater and Saline Intrusion, IGME (L. Araguás, E. Custodio and M. Manzano Eds.), 395-404.

Feehley, C.E., Zheng, C.M., and F.J. Molz 2000. A dual-domain mass transfer approach for modeling solute transport in heterogeneous aquifers: Application to the Macrodispersion Experiment (MADE) site. Water Resour. Res 36(9):2501-2515.

Fernández, L.C., Rojas, N.G., Rodán T.G., Ramírez, M.E., Zegarra, H.G., Uribe, R., Reyes, R.J., Flores, D. and Arce J.M., 2006, Manual de técnicas de análisis de suelos aplicadas a la remediación de sitios contaminados, México D.F., 89–108 , ISBN 968-489-039-7.

Ferré, T.P.A., A. Binley, J. Geller, E. Hill, and T. Illangasekare, 2005. Hydrogeophysical Methods at the Laboratory Scale, in Hydrogeophysics (Y. Rubin and S. Hubbard Eds.), Water Science and Technology Library, Springer, 441-463.

Fitterman, D.V., and M.T. Stewart, 1986. Transient Electromagnetic sounding for groundwater,

Geophysics, 51 (4), 995-1005.

Gabàs, A., 2003. Nous aspects metodològics en l'exploració elèctrica I electromagnètica, PhD thesis, Dpt. Geodinàmica i Geofísica, Universitat de Barcelona.

Galbiati, G. L. and Gruppo, M. (1979). Verifica della validità a livello locale di una legge di essiccamento del terreno agrario. In III Convegno Nazionale, Catania, volume 1, pages 7–13. AIGR.

Gallardo, L.A., and M. A. Meju, 2003. Characterization of heterogeneous near-surface materials by joint 2D inversion of dc resistivity and seismic data, Geophysical research letters, 30, 1658-1661.

Gehman, C., D. Harry, and W. Sanford, 2006. Measuring Groundwater Storage Change in an Unconfined Alluvial Aquifer Using Temporal Gravity Surveys, 19th SAGEEP, Seattle, USA.

Geonics, 1999. Selected Papers and examples, Groundwater Exploration Applications.

Gerke, H.H., and M.T. van Genuchten 1993a. A dual-porosity model for simulating the preferential movement of water and solutes in structured porous-media. Water Resour. Res. 29(2):305-319.

Gerke, H.H., and M.T. van Genuchten 1993b. Evaluation of a 1st-order water transfer term for variably saturated dual-porosity flow models. Water Resour. Res 29(4):1225-1238.

Golden Software, Inc. Surfer version 11 user's guide, (2012)

Goldman, M., U. Kafri and Y. Yechieli, 2003. Application of the Time Domain Elecrtromagnetic (TDEM) Method for Studying Groundwater Salinity in Different Coastal Aquifers of Israel, in Coastal Aquifers Intrusion Technology: Mediterranean countries, (A. Lopez-Jeta, J. de Dios, J.A. de la Orden, G. Ramos and L. Rodriguez Eds.) Publicaciones del Instututo Geologico y Minero de Espanya Serie: Hidrogeología y aguas subterranias nº8, tomo II, 45-56.

Goldman, M., and U. Kafri, 2004. The use of time domain electromagnetic TDEM method to evaluate porosity of saline water saturated aquifers, in Groundwater and Saline intrusion, IGME (L. Araguás, E. Custodio and M. Manzano Eds.), 327-339.

Gómez-Hernández, J., 2005. Geostatistics, in Hydrogeophysics (Y. Rubin and S. Hubbard Eds.), Water Science and Technology Library, Springer, 59-83.

Grathwohl, P., and S. Kleineidam 1995. Impact of heterogeneous aquifer materials on sorption capacities and sorption dynamics of organic contaminants. Groundwater Quality: Remediation and Protection. IAHS Wallingford, Oxfordshire, England, 79-86.

Grauch, V.J.S., M.R. Hudson, and S.A. Minor, 2001. Aeromagnetic expression of hydrogeologically important faults, Albuquerque basin, New Mexico SAGEEP, Denver Co., USA.

Guérin, R., M. Descloitres, A. Coudrain, A. Talbi and R. Gallaire, 2001. Geophysical surveys for

identifying saline groundwater in the semi-arid region of the central Altiplano, Bolivia, Hydrological Processes, 15, 3287-3301.

Guérin, R., 2005. Borehole and surface-based hydrogeophysics, Hydrogeology Journal, 13, 251-254.

Haber, E., U. M. Ascher, D. W. Oldenburg, 2004. Inversion of 3D Electromagnetic Data in Frequency and Time Domain Using an Inexact All-at-Once Approach, Geophysics, 69, 1216-1228.

Haber, E., 2005. Quasi–Newton Methods for Large-Scale Electromagnetic Inverse Problems, Inverse. Problems. 21, 305-323.

Haggerty, R., and S.M. Gorelick 1995. Multiple-rate mass-transfer for modeling diffusion and surface-reactions in media with pore-scale heterogeneity. Water Resour. Res 31(10):2383-2400.

Haggerty, R., and S.M. Gorelick 1998. Modeling mass transfer processes in soil columns with pore- scale heterogeneity. Soil Sci. Soc. Am. J. 62(1):62-74.

Haggerty, R., McKenna, S.A., and L.C. Meigs 2000. On the late-time behaviour of tracer test breakthrough curves. Water Resour. Res. 36(12):3467-3479.

Haggerty, R., Fleming, S.W., Meigs, L.C., and S.A. McKenna 2001. Tracer tests in a fractured dolomite. 2. analysis of mass transfer in single well injection-withdrawal tests. Water Resour. Res. 37(5):1129-1142.

Harbaugh, A. W. (2005). The u.s. geological survey modular ground-water model – the ground-water flow process. techniques and methods. Technical report, U.S. Geological Survey.

Harvey, C.F., and S.M. Gorelick 2000. Rate-limited mass transfer or macrodispersion: which dominates plume evolution at the macrodispersion experiment. Water Resour. Res 36(3):637-650.

Hashin, Z. and S.Strickman, 1962. A variational approach to the theory of effective magnetic permeability of multiphase materials, Journal of Applied Physics, 33, 3125-3131.

Hiby, J.W. 1962. Longitudinal dispersion in single-phase liquid flow thorough ordered and random packings. Interact between Fluid & Partcicles, London Instn. Chem. Engrs., 312-325.

Hill, M., Banta, E. R., Harbaugh, A. W., and Anderman, E. R. (2000).

Himi, M., J.V. Navarro, J.A. Sabadía, and A. Casas, 2000. Delimitación de la intrusión salina en el delta del río Tordera por métodos electromagnéticos. Technical report, Actualidad de las Técnicas Geofísicas Aplicadas en Hidrogeología, IGME.

Hollenbeck, K.J., Harvey, C.F., Haggerty, R., and C.J. Werth 1999. A method for estimating distributions of mass transfer rate coefficients with application to purging and batch experiments. J. Contam. Hydrol. 37(3-4):367-388.

Hunter, J.A., S.E. Pullan, R.A. Burns, R.M. Gagne, and R.S. Good 1984. Shallow seismic reflection mapping of the overburden-bedrock interface with the engineering seismographsome simple techniques, Geophysics, 49, 1381-1385.

INAMHI and DGGM (1983). Mapa hidrogeológico del ecuador. Technical report, Ministerio de Recursos Naturales y Energéticos, Quito.

Jachens, R.C., and B.C. Moring, 1990. Maps of thickness of Cenozoic deposits and the isostatic residual gravity over basement for Nevada, USGS Open-File Report, 90-404, 15p.

Jarvis, K. D., and R.J. Knight, 2002. Aquifer heterogeneity from SH-wave seismic impedance inversion, Geophysics, 67 (5), 1548–1557. doi:10.1190/1.1512800.

Kauffman, S.J., Bolster, C.H., Hornberger, G.M., Herman, J.S., and A.L. Mills 1998. Rate-limited transport of hydroxyatrazine in an unsaturated soil. Environ. Sci. Technol. 32(20):3137-3141.

Keating, K. and R. Knight, 2007. A laboratory study to determine the effect ofiron oxides on proton NMR measurements, Geophysics , 72 (1) E27–E32.

Julian, H.E., Boggs, J.M., Zheng, C.M., and C.E. Feehley 2001. Numerical simulation of a natural gradient tracer experiment for the natural attenuation study: flow and physical transport. Ground Water 39(4):534-545.

Keller, G.V., 1988. Rock and mineral properties, in Electromagnetic methods in applied Geophysics, (M. N. Nabighian Ed.), Society of Exploration Geophysicists.

Knight, R., and A. Nur, 1987. The dielectric constant of sandstones, 60 kHz to 4 MHz, Geophysics, 52, 664-654.

Knight, R., 2001. Ground penetrating radar for environmental applications, Annual Review of Earth and Planetary Sciences, 29, 229-255.

Korb, M., S. Mares and F. Paillet, 2005, Geophysical Well Logging: Borehole Geophysics for Hydrogeological Studies: Principles and Applications, in Hydrogeophysics, (Y. Rubin and S.S. Hubbard Eds.) Water Science and Technology Library, Springer, 291-333.

Krivochieva, S., and M. Chouteau 2003. Integrating TDEM and MT methods for characterization and delineation of the Santa Catarina aquifer (Chalco Sub-Basin, Mexico), Journal of Applied Geophysics, 52 (1), 23-43.

Ledo, J., P. Queralt, A. Martí, and A.G Jones, 2002 a. Two-dimensional interpretation of three-dimensional magnetotelluric data: an example of limitations and resolution, Geophysical Journal International, 150,127-139.

Legchenko, A.V. and O.V. Shushakov, 1998. Inversion of surface NMR data. Geophysics, 63, 75-8

Lesmes D. P., and S.P. Friedman, 2005. Relationships between the Electrical and Hydrogeological Properties of Rocks and Soils, in Hydrogeophysics, Y. Rubin and S.S. Hubbard Eds.) Water Science and Technology Library, Springer, 87-129.

Linde, N., and L. B. Pedersen, 2004 a. Evidence of electrical anisotropy in limestone formations using the RMT technique, Geophysics, 69, 909-916, doi:10.1190/1.1778234.

Linde, N., 2005. Characterization of Hydrogeological Media Using Electromagnetic Geophysics, PhD thesis, Uppsala Universitet, Sweden

Linde, N., A. Binley, A. Tryggvason, L.B. Pedersen, and A. Revil, 2007. Improved hydrogeophysical characterization using joint inversion of crosshole electrical resistance and ground penetrating radar traveltime data, Water Resources Research, 42, W12404, doi:10.1029/2006ER005131.

Loeffler, O., 2005. Módelisation géoradar de la proche surface estimation de la teneur en eau et influence d'un pulluant. PhD thesis, Université Louis Pasteur, Strasbour-I.

Longino, B.L. and Kueper, B.H., 1999, Non-wetting phase retention and mobilization in rock fractures. Water Resources Research, 35(7), 2085-2093.

Longo, R. and Sosa, H. (1972). Hoja geológica de alausí escala 1:100000. Technical report, Dirección General de Geología y Minas, Quito.

Lozada, F. and Randel, P. (1973). Hoja geológica de Chimborazo escala 1:100000. Technical report, Direccio´n General de Geología y Minas, Quito.

López, C. H. (1980). Estudio hidrogeológico de la cuenca del río Chimborazo. Aguas subterráneas, INAMHI.

Lubczynsky, M., and J. Roy, 2003. Hydrogeological interpretation and potential of the new magnetic resonance sounding (MRS) method, Journal of Hydrology, 283, 19-40.

Lucius, J.E., Olhoeft, G.R., Hill, P.L. and Duke, S.K., 1992, Properties and hazards of 108 selected substances -1992 Edition, U.S. Geological Survey Open-File Report 92-527.

Malo, G. and Mortimer, C. (1978). Hoja geológica de baños escala 1:100000. Technical report, Dirección General de Geología y Minas, Quito.

Manzella A., G. Volpi, A. Zaja and M. Meju, 2004. Combined TEM-MT investigation of shallow-depth resistivity structure of Mt Somma-Vesuvius. Journal of Volcanology and Geothermal Research, 131, 1-2, 19-32.

Marín, M. and Y, V. (1986). Hoja geológica de macas escala 1:100000. Technical report, Dirección

General de Geología y Minas, Quito.

Martí, A., P. Queralt, and E. Roca, 2004. Geoelectric dimensionality in complex geological areas: application to the Spanish Betic Chain, Geophysical Journal International, 157, 961-974.

Martinez, A., Carr, T., Beaty, D., Byrnes, A. and Stiles, J., 1999. Abstract: Comparison of ground-penetrating radar response and rock properties in a sandstone-dominated incised valley-fill deposit. In Society of Exploration Geophysicists Annual Meeting Expanded Abstracts, 582–585.

Mazác, O., M. Císlerová, W. E. Kelly, I. Landa, and D. Venhodová, 1990. Determination of Hydraulic Conductivities by Surface Geoelectrical Methods, in Geotechnical and Environmental Geophysics (2), (S.H. Ward Ed.), Environmental and Groundwater, Society of Exploration Geophysicists.

McKenna, S.A., Meigs, L.C., and R. Haggerty 2001. Tracer tests in a fractured dolomite 3. Double-porosity, multiple-rate mass transfer processes in convergent flow tracer tests. Water Resour. Res. 37(5):1143-1154.

McPhee, D.K., B. A. Chunchel, and L. Pellerin, 2006, Audiomagnetotelluric data from Spring, Cave, and Coyote Spring Valleys, Nevada, USGS Open-File Report 2006-1164, 41p.

Meju, M.A., 2000. Environmental Geophysics: tasks ahead, Journal of Applied Geophysics, 44, 63-65.

Melisenda, I. (1964). Sui calcoli idrologici per il terreno agrario: influenza del clima. L'acqua, (4).

Melisenda, I. (1970). Stima delle perdite per evapotraspirazione. In Atti del I Convegno Intern. Acque Sott, Palermo. IAH.

MODFLOW-2000, the U. S. Geological Survey modular groundwater model-User guide to theobservation, sensitivity, and parameter estimation processes and three post-processing programs. Open File Rep.

Mota, R., F.A. Monteiro Santos, A. Mateus, F.O. Marques, M.A. Gonçalves, J. Figueiras, and H. Amaral, 2004. Granite fracturing and incipient pollution beneath a recent landfill facility as detected by geoelectrical survey, Journal of Applied Geophysics, 57, 11-22.

Mualem, Y., 1976, A new model for predicting the hydraulic permeability of unsaturated porous media. Water Resources Research, 12, 513-522.

Naranjo, L. F. (2013). Caracterización hidrolgeológica de la Subcuenca del Río Chambo. Universidad Central del Ecuador, Tesis de Grado.

Neuman, S.P., and D.M. Tartakovsky 2009. Perspective on theories of non-Fickian transport in heterogeneous media. Adv. Water Resour. 32(5):670-680.

Olhoeft, G. R., 1986, Direct detection of hydrocarbon and organic chemicals with ground penetrating

radar and complex resistivity. In Proceedings of the NWWA/API Conference on Petroleum Hydrocarbons and Organic Chemicals in Ground Water—Prevention, Detection and Restoration, Dublin, OH, 284–305.

Pedersen, L.B., M. Bastani, and L. Dynesius 2005. Groundwater exploration using combined controlled-source and radiomagnetotelluric techniques, Geophysics, 70, G8-G15, doi:10.1190/1.1852774.

Pedit, J.A., and C.T. Miller 1995. Heterogeneous sorption processes in subsurface systems. 2. Diffusion modelling approaches. Environ. Sci. Technol. 29(7):1766-1772.

Pellerin, L., 2002. Applications of electrical and electromagnetic methods for environmental and geotechnical investigations, Surveys in Geophysics, 23, 101-132.

Pelton, J.R., 2006. Near-surface Seismology: Surface-Based Methods, in Near-Surface Geophysics (D.K. Butler Ed.), Investigation in Geophysics nº13, Society of Exploration Geophysicists, 219-136.

Plata, J., and F. Rubio, 2002. MRS experiments in a noisy area of a detrital aquifer in the south of Spain, Journal of Applied Geophysisics, 50,83–94.

Pugliese, L., Poulsen, T.G., and R.R. Andreasen 2012. Relating gas dispersion in porous media to medium tortuosity and anisotropy ratio. Water, Air and Soil Pollution 223(7):4101-4118.

Pugliese, L., Poulsen, T.G., and R.R. Andreasen 2013a. Biofilter media gas pressure loss as related to media particle size and particle shape. Journal of Environmental Engineering. doi:10.1061/(ASCE)EE.1943-7870.

Pugliese, L., Poulsen, T.G., and S. Straface 2013b. Gas-solute dispersivity ratio in granular porous media as related to particle size distribution and particle shape. Water Air and Soil Pollution 224(1691). doi:10.1007/s11270-013-1691-1.

Pugliese, L., and T.G. Poulsen 2013c. Linking gas and liquid pressure loss to particle size distribution and particle shape in granular filter materials. Submitted to Water Air and Soil Pollution. Submitted to Water Air and Soil Pollution Journal.

Purvance, D. T., and R. Andricevic, 2000. On the electrical-hydraulic conductivity correlation in aquifers, Water Resources Research, 36, 2905-2913.

Radzevicius, S. J., Daniels, J. J., Guy, E. D., and Vendl, M. A., 2000, Significance of crossed-dipole antennas for high noise environments. In Proceedings of the Symposium on the Application of Geophysics to Environmental and Engineering Problems, Washington, DC, 407–413.

Rao, P.S. C., Rolston, D.E., Jessup, R.E., and J.M. Davidson 1980. Solute transport in aggregated porous-media - theoretical and experimental evaluation. Soil. Sci. Soc. Am. J. 44(6):1139-1146.

Redman, J.D., DeRyck, S.M. and Annan, A.P., 1994, Detection of LNAPL pools with GPR: Theoretical modelling and surveys of a controlled spill. Proceedings, Fifth International Conference on Ground Penetrating Radar, June 1994, Kitchener, Ontario, 1283–1294.

Revil, A., and P.A. Pezard, 1999. Streaming potential in porous media 1. Theory of the zeta potential. Journal of Geophysical Research. 104,20033–20048.

Rodi, W. and R. Mackie, 2001. Nonlinear conjugate gradients algorithm for 2-D magnetotelluric inversion, Geophysics, 66 (1), 174-187.

Roy, A., and A. Apparo, 1971. Depth of investigation in direct current methods, Geophysics, 36 (5), 943-959.

Rubin, Y., G. Mavko, and J. Harris, 1992. Mapping permeability in heterogeneous aquifers using hydrologic and seismic data, Water Resources. Research, 28, 1809-1816.

Rubin, Y., and S. Hubbard, 2005. Stochastic forward and inverse modeling: the hydrogeophysical challenge, in Hydrogeophysics (Y. Rubin and S.S. Hubbard Eds.) Water Science and Technology Library, Springer, 487-511.

Rugner, H., Kleineidam, S., and P. Grathwohl 1999. Long term sorption kinetics of phenanthrene in aquifer materials. Environ. Sci. Technol. 33(10):1645-1651.

Sailhac, P.and G. Marquis, 2001. Analytic potentials for the forward and inverse modeling of SP anomalies caused by subsurface fluid flow, Geophysical Research Letters, 28, 1643-1646.

Sanchez-Vila, X., and J. Carrera 2004. On the striking similarity between the moments of breakthrough curves for a heterogeneous medium and a homogeneous medium with a matrix diffusion term. Journal of hydrology 294(1-3):164-175.

Sánchez-Vila, X., A. Guadagnini and J. Carrera, 2006. Representative Hydraulic Conductivities in Saturated Groundwater Flow, Reviews of Geophysics, 44, RG3002.

Santamarina, J.C., Fam, M., 1997, Dielectric permittivity of soils mixed with organic and inorganic fluids (0.02 GHz to 1.30 GHz). J. Environmental and Engineering Geophysics, 2(1), 37-51.

Sardin, M., Schweich, D., Leij, F.J., and M.T. van Genuchten 1991. Modeling the nonequilibrium transport of linearly interacting solutes in porous media, a review. Water Resour. Res. 27(9):2287- 2307.

Sauck W.A., 2000, A model for the resistivity structure of LNAPL plumes and their environs in sandy sediments. Journal of Applied Geophysics, 44(2-3), 151–165.

Sen, P.N., Scala, C. and Cohen, M., 1981, A self similar model for sedimentary rocks with application to the dielectric constant of fused glass beads. Geophysics, 46, 781–795.

Sheriff, R.E., 1984, Encyclopedic Dictionary of Exploration Geophysics. Soc. Explor. Geophys., Tulsa, OK, 2nd ed., 323 pp.

Sharma, P., and T.G. Poulsen 2010. Gas dispersion and immobile gas content in granular porous media: effect of particle size nonuniformity. Soil Science 175:426-431.

Silva, O., Carrera, J., Dentz, M., Kumar, S., Alcolea, A., and M. Willmann 2009. A general real- time formulation for multi-rate mas transfer problems. Hydrol. Earth Syst. Sci. 13(8):1399-1411.

Simpson, F. and K. Bahr, 2005. Practical Magnetotellurics, Cambridge Univesity Press.

Singha, K., and S.M. Gorelick, 2005. Saline tracer visualized with three-dimensional electrical resistivity tomography: Field-scale spatial moment analysis, Water Resources Research, 41, W05023, doi:10.1029/2004WR003460.

Slater, L., and D. Lesmes, 2002. IP interpretation in environmental investigations, Geophysics, 67, 77-88.

Slater, L., R. Knight, K. Shinga, A. Binley, and E. Atekwana, 2006. About AGU, Near Surface Geophysics: A New Focus Group, EOS, 87, 25.

Sørensen, K, 1996. Pulled array continuous electrical profiling, First Break, 14, 85-90.

Sosa, H. and Guevara, S. (1973). Hoja geológica de Riobamba escala 1:100000. Technical report, Dirección General de Geología y Minas, Quito.

Spichak, V., and I. Popova, 2000. Artificial Neural Network Inversion of Magnetotelluric Data in Terms of Three-Dimensional Earth Macroparameters, Geophysical Journal International 142, 15-26.

Spies, B.R. and F.C. Frischknecht,1991. Electromagnetic sounding, in Electromagnetic Methods in Applied Geophysics, Vol. 2 (M.N. Nabighian Ed.), Society of. Exploration. Geophysicists, 285-425.

Steeples, D.W., and W.E Miller, 1990. Seismic-reflection methods applied to engineering, environmental, and ground-water problems, in Geotechnical and Environmental Geophysics vol.1, (S. Ward Ed.), Society of. Exploration. Geophysicists, 1-30.

Straface, S., T.-J. Yeh, J. Zhu, S. Troisi, and C. H. Lee (2007), Sequential aquifer tests at a well field, Montalto Uffugo Scalo, Italy,Water Resour. Res., 43, W07432, doi:10.1029/2006WR005287

Szymczyk, A., B. Aoubiza, P. Fievet, and J. Pagetti, 1999. Electrokinetic phenomena in homogeneous cylindrical pores, J. Colloid Interface Sci., 216, 285– 296.

Tezkan, B., P. Georgescu and U. Fauzi, 2005. A radomagnetotelluric survey on an oilcontaminated area near the Brazi Refinery, Romania, Geophysical Prospecting, 53, 311-323.

Thornthwaite, C. W. (1948). An approach towards a rational classification of climate. Geogr. Rev.

Americ. Geoph. Soc, 55(94).

Topp, G.C., Davis, J.L. and Annan, A.P., 1980, Electromagnetic determination of soil water content: Measurements in Coaxial Transmission Lines. Water Resources Research, 16(3), 574–582.

Trad, D.O., and J.M. Travassos, 2000. Wavelet filtering of magnetotelluric data. Geophysics, 65 (2), 482-491.

Tullen, P., O. Turberg, and A. Parriaux, 2006. Radiomangetotelluric mapping, groundwater numerical modelling and 18-Oxygen isotopic data as combined tools to determine the hydrogeological system of a landslide prone area, Engineering Geology, 87, 195-204.

Turc, L. (1978). Evaluation des besoins en eau d'irrigation, evapotranspiration potentielle. Ann. Agron., (1).

Unsworth, M.J., X. Lu, M.D. Watts, 2000. AMT exploration at Sellafield: Characterization of a potential radioactive waste disposal site, Geophysics, 65, 1070-1079.

Valocchi, A.J. 1985. Validity of the local equilibrium assumption for modeling sorbing solute transport through homogeneous soils. Water Resour. Res. 21(6):808-820.

Valocchi, A.J. 1990. Use of temporal moment analysis to study reactive solute transport in aggregated porous media. Geoderma 46(1/3):233-247.

Van Genuchten, M.T., and P.J. Wierenga 1976. Mass transfer studies in sorbing porous-media. 1. Analytical solutions. Soil Sci. Soc. Am. J. 40(4):473-480.

Van Genuchten, M.T., 1980, A closed-form equation for predicting the hydraulic conductivity of unsaturated soils. Soil Science Society of America Journal, 44, 892-898.

Wadell, H. 1935. Volume, shape and roundness of quartz particles. Journ of Geology 43(3):250- 280.

Wempe, W.L., 2000. Predicting Flow Properties Using Geophysical Data: Improving Aquifer Characterization, PhD Thesis, Stanford University, CA ,USA.

Werth, C.J., Cunningham, J.A., Roberts, P.V., and M. Reinhard 1997. Effects of grain-scale mass transfer on the transport of volatile organics through sediments. 2. Column results. Water Resour. Res. 33(12):2727-2740.

Winckell, A., Zebrowski, C., and Sourdat, M. (1997). Las Regiones y paisajes del Ecuador. IGM, Quito, Ecuador.

Wilson, S.R., M. Ingham, J.A. McConchie, 2006. The applicability of earth resistivity methods for saline interface definition, Journal of Hydrogeology, 316, 301-312.

Yaramanci, U., A. Kemna, and H. Vereeckens, 2005. Emerging technologies in Hydrogeophysics, in Hydrogeophysics (Y. Rubin and S. Hubbard Eds.), Water Science Technology and Library, Springer, 467-486.

Zhang, Y.Q., Liu, H.H., Zhou, Q.L., and S. Finsterle 2006. Effects of diffusive property heterogeneity on effective matrix diffusion coefficient for fractured rock. Water Resour. Res. 42(4). doi:10.1029/2005WR004513.

Zhang, Z.H., and M.L. Brusseau 1999. Nonideal transport of reactive solutes in heterogeneous porous media. 5 Simulating regional-scale behaviour of a trichloroethene plume during pump-and-treat remediation. Water Resour. Res. 35(10):2921-2935.

Zinn, B., and C.F. Harvey 2003. When good statistical models of aquifer heterogeneity go bad: a comparison of flow dispersion, and mass transfer in connected and multivariate Gaussian hydraulic conductivity fields. Water Resour. Res. 39(3). doi: 10.1029/2001WR001146

Zonge, K.L., J. Wynn and S. Urquhat, 2006. Resistivity induced polarization and complez resistivity, in Near-surface Geophysics, (D.K. Butler Ed.), Investigations in Geophysics, Society of Exploration Geophysicists, 13, 265-300.

ACKNOWLEDGEMENTS

Dios fuente de sabiduría de paz y amor en todo este tiempo he sentido tu presencia todos los días, te doy gracias porque siempre estás en mi vida y me acompañas en mis propósitos y sobre todo me iluminas.

Agradezco a mi país Ecuador a través de la Secretaría Nacional de Educación Superior Ciencia, Tecnología e Innovación (SENESCYT) por brindarme la oportunidad de cumplir mis sueños de superación a través de mis estudios.

Agradezco a la Universidad de la Calabria, a la Escuela de Doctorado "Pitagora" y al Departamento de Ingeniería para el Ambiente, el Territorio e Ingeniería Química, por haberme acogido en tan noble institución y permitido realizar mi proyecto de investigación durante este periodo de tiempo.

Al Profesor Salvatore Straface, gracias por la impartirme sus conocimientos, por la serenidad y confianza que transmite, pero sobre todo la confianza y paciencia, lo que ha permitido culminar este objetivo.

A Francesco (Kidiz) mi gratitud es infinita no solo por los momentos compartidos entre laboratorio, oficina, cálculos, tesis, traducciones, italiano y dialecto. Sino por la amistad que haz sabido brindarme hicieron que lo que he aprendido lo haya hecho con alegría. Dios bendiga siempre tu familia.

A Michele (Miky) mi querido hermano en Italia, tuve que llegar tan lejos para conocer una persona con tenacidad, inteligencia y locura al mismo tiempo, te agradezco a ti y tu familia por haberme hecho sentir a mi y a los míos que la casa está donde se encuentran las personas que te quieren. Dios te bendiga a ti y a tu familia.

A Francesco (Saraceni), te agradezco por la amistad, por esas conversaciones profundas y técnicas en este tiempo.

A mis amigos tesistas Daniela, Gianni, Pasquale, Giuseppe, por su ayuda prestada en la investigación y sobre todo con el italiano, sin olvidarme de mi amigo Francesco (Ciccio Altomare) un pequeño grande de Rogliano.

Querido hijo, amigo, cómplice te agradezco por esa valentía que siempre me haz demostrado, eres mi inspiración porque aun siendo pequeño no te dejas vencer y sobre todo gracias por tu amor.

A mi esposa, que con paciencia y amor me acompañó en este sueño, gracias de corazón.

A mi padre, gracias por creer en mi y en lo que puedo hacer y sobre todo por tu confianza, preocupación y ayuda han hecho posible este objetivo.

A mi mamita, describir cuanto es al amor y la gratitud que tengo hacia no me alcanzarían las estrellas para hacerlo, gracias por tus oraciones.

A mis amigos ecuatorianos en Italia, Oscarito, Alfonso, Lito, Lucho, Don J, Tir, Migue y a los demás gracias por esos momentos de felicidad que ayudaron a cumplir con esta meta.